Low-Speed Model Support Interference

Elements of an Expert System

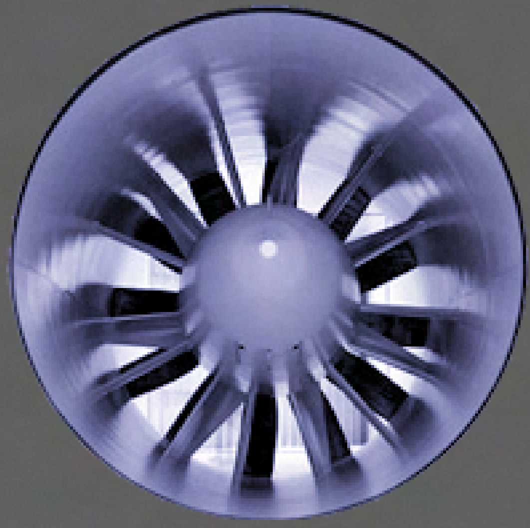

B.J.C. Horsten

Stellingen

behorend bij het proefschrift:

LOW-SPEED MODEL SUPPORT INTERFERENCE

ELEMENTS OF AN EXPERT SYSTEM

B.J.C. Horsten

1. Een hoge nauwkeurigheid en lage implementatie-inspanning van een correctiemethode voor de bepaling van model ophangings-interferentie zijn momenteel onverenigbaar indien een breed toepassingsgebied is gewenst. *dit proefschrift*
2. In het belang van het verbeteren van correctiemethoden voor de bepaling van ophangings-interferentie worden windtunnelgebruikers aangemoedigd de gemeten data vrij te geven aan de wetenschappelijke gemeenschap. *dit proefschrift*
3. Het is slechts een kwestie van tijd voor experimenten in de windtunnel overbodig zullen worden
4. Magnetische model-ophangingen hebben geen toekomst in commerciële windtunnel toepassingen
5. Expert systemen zullen nooit leiden tot redundantie van experts op eigen vakgebied
6. Als de huidige stijging van de brandstofprijzen aanhoudt zal het onderwerp van ophangings-interferentie in de komende jaren herleven
7. De relatie tussen wetenschapper en zijn resultaten is een functie van zijn integriteit
8. Promovendi zouden aangespoord moeten worden hun communicatieve vaardigheden te verbeteren
9. Balans-metingen hebben een wetenschappelijke waarde; zij kunnen eveneens bevorderend zijn voor het algemeen welzijn

Deze stellingen worden opponeerbaar en verdedigbaar geacht en zijn als zodanig goedgekeurd door de promotor, prof. Dr.-Ing. G. Eitelberg.

Propositions

belonging to the dissertation:

LOW-SPEED MODEL SUPPORT INTERFERENCE

ELEMENTS OF AN EXPERT SYSTEM

B.J.C. Horsten

1. High accuracy and low implementation effort of a correction method for determining model support interference are currently incompatible when a wide range of applicability is desired. *this thesis*
2. For the benefit of improving support interference correction methods, wind tunnel users are encouraged to release their data to the scientific community. *this thesis*
3. It is only a matter of time untill wind tunnel experiments will become redundant
4. Magnetic model suspensions have no future in commercial wind tunnel applications
5. Expert systems will never lead to a redundancy of experts in their own area of expertise
6. If the current rise of the fuel prices continues, the subject of model support interference will revive in the years to come
7. The relation between a scientist and his results is a function of his integrity
8. PhD candidates should be encouraged to improve their communication skills
9. Balance measurements have a scientific value; they can also promote the general wellbeing

These propositions are regarded as opposable and defendable, and have been approved as such by the supervisor, prof. Dr.-Ing. G. Eitelberg.

Low-Speed Model Support Interference

Elements of an Expert System

Low-Speed Model Support Interference

Elements of an Expert System

PROEFSCHRIFT

ter verkrijging van de graad van doctor
aan de Technische Universiteit Delft,
op gezag van de Rector Magnificus prof. ir. K.C.A.M. Luyben,
voorzitter van het College voor Promoties,
in het openbaar te verdedigen op vrijdag 24 juni 2011 om 12.30 uur

door Bart Josephus Carolus HORSTEN
ingenieur luchtvaart en ruimtevaarttechniek
geboren te Montfoort

Dit proefschrift is goedgekeurd door de promotor:
Prof. Dr. -Ing. G. Eitelberg

Samenstelling promotiecommissie:

Rector Magnificus,	Voorzitter
Prof. Dr. -Ing. G. Eitelberg,	Technische Universiteit Delft, promotor
Dr. ir. L.L.M. Veldhuis,	Technische Universiteit Delft, copromotor
Prof. dr. ir. drs. H. Bijl,	Technische Universiteit Delft
Prof. dr. ir. M.J.L. van Tooren,	Technische Universiteit Delft
Prof. dr. H. Babinsky,	Cambridge University
Prof. ir. J.P. van Buijtenen,	Technische Universiteit Delft
Dr. ing. S. Schaber,	Airbus Germany GmbH, Bremen
Prof. dr. F. Scarano,	Technische Universiteit Delft, reservelid

ISBN: 978-90-8891-294-8

To Maaike

Summary

Low-Speed Model Support Interference
Elements of an Expert System

Wind tunnel support interference is one of the constraints affecting the quality of wind tunnel measurements. Several methods to determine the interference are experimental- empirical- and numerical methods. Experimental methods are often time consuming and costly. This also holds for empirical methods as they are founded on a vast number of experimental data sets. CFD is also found to be time consuming and sometimes computationally expensive. Future guidelines for the treatment of support interference aim at providing engineers more alternatives. Such alternatives require however an extensive knowledge on experiments and CFD: it requires the engineer to be an expert in the field, something that is often impossible. Engineers should therefore be guided by an expert system (a computer program that represents and reasons with knowledge of some specialist subject with a view to solving problems or giving advice) in their dealings with support interference. In this thesis such an application-based expert system is considered. The system focuses on low-speed model support interference on single sting mounted models carrying an internal balance.

The research objective of this thesis is stated as: "To identify the necessary elements for the design of an expert system for support interference on sting mounted models carrying internal balances applicable to low-speed wind tunnels."

In this thesis the necessary components of such an expert system are identified through a study on the elements of its knowledge base and a study on a feasible structure of the system in terms of its applications.

Considering the study on the elements of its knowledge base, experimental- and numerical research is carried out to gain intelligibility on support interference.
It is shown that a support break down facilitating the treatment of disturbances of individual support parts spanning a certain setup is a systematic method to analyze support interference. The order of magnitude and the nature of the disturbances are not compromised when this approach is adopted provided that the amount of separate parts is kept to a minimum. This approach enables the crucial study on the disturbances of the model sting that causes the complete spectrum of support disturbances.

Advantages of studying the sting include the possibility to generalize the research results to a wider class of support structures, allow for a qualitative analysis on the nature of near-field and far-field effects but also a qualitative and quantitative validation of several methods applied to determine support interference.
Comparing measurements (balance measurements and 5-hole probe measurements) to calculations (panel code- and Euler calculations) on model sting near-field and far-field effects shows that without knowing the specific details of a complex interference flow field, it is not justified (from the viewpoint of accuracy) to determine model sting near-field and far-field effects using methods at low levels of complexity and intrinsic accuracy. Significant calculation offsets (out of the bounds of experimental accuracy) are caused by the action of the balance cavity and slit, vorticity and viscosity. In depth understanding of the limitations of these numerical methods (panel code, Euler) can only be developed when the interference flow field itself is understood both qualitatively and quantitatively. Navier-Stokes calculations are used for this purpose. Calculations provide a qualitative image of the interference flow field that complies with measurements. Quantitatively, the Navier-Stokes calculations are not able to determine the values of the interference with the right trends and within typical measurement (balance) accuracy.
Gained near-field flow knowledge is used for an assessment of the potential of various numerical and experimental methods in determining the near-field and far-field model sting effects on wind tunnel models at low speed for various sting placements. This knowledge is generalized such as to cover the treatment of the remaining support for typical sting mounted setups.
Considering the numerical and experimental treatment of support disturbances of any support part it is concluded that classification parameters “accuracy” and “effort” (classifying the various methods for the determination of the interference) oppose each other: accurate methods demand a lot of implementation effort and vice versa.
This opposition can not be solved by designing a custom-made model (that is both accurate and requires a low amount of implementation effort) for calculating model support interference. Such a model should calculate the disturbance effects fast (by incorporating only the disturbance factors of primary quantitative interest) with the right trends and magnitude. Solving for the confinements of such models implies an inevitable reduction in the applicability range of the model. Typical custom-made models are unsuitable for implementation in the expert system. They reveal the following rule of thumb: “High accuracy (at a minimum equal to typical balance Δ-measurement accuracy) and low implementation effort (total measurement effort or modeling effort and computational effort) of a correction method for determining model support interference are currently incompatible when a wide range of applicability (freestream conditions, setups) is desired”.
This rule of thumb necessitates a more elaborate definition of the expert system’s requirements on speed and accuracy, resulting in an expert system with an application-based structure. The applications with given accuracy and speed assist in four stages defining a typical commercial wind tunnel measurement: negotiations at the client, test preparation phase, performing the measurements and finally the post test corrections.

Next a closer look is taken at a feasible structure of the expert system. The proposed application-based structure fulfills the expert system’s main requirements: advise on

the test setup/correction methods, calculate the interference fast enough and accurate enough pre-test and on-line, correct for the interference on-line and off-line and allow easy plug-in of modules dealing with the problem of wall interference. Additional requirements relate to the use of the system (meet computer platform standards and be user friendly with professional interfaces). Typical necessary system elements are identified: the expanded knowledge base on model support interference has resulted in two basic expert applications (ESI and ASID, directly applicable for measurements in the LLF of DNW for which they are customized) and new methods (VOLAER and MVL) to approach the problem of wind tunnel wall- and support interference. These products are seen as basic elements of an expert system (generalizable to other wind tunnels).
MVL (a method combining both uncorrected wind tunnel measurements and vortex-lattice calculations) proves to be particularly valuable as it predicts the interference of wind tunnel walls, support and includes secondary interference (when e.g. the support is traversed close to the wind tunnel walls). MVL is suitable for all support setups in all types of wind tunnels provided a vortex-lattice method is used enabling an accurate representation of the model aerodynamic derivatives (preferably including the effects of viscosity). MVL's prediction capabilities necessitates the use of multiple boundary conditions (interference values) in order to guarantee a stable solution thereby categorizing it as an interpolation tool with the potential of decreasing the amount of necessary experimental balance Δ-measurements.

Currently, a very basic variant of an expert system is presented in this thesis and its necessary elements are identified. This is seen as a good initiative towards meeting the future needs. It is believed that the future needs can be met when further development of this expert system is stimulated. Increasing data availability and updating the applications is of utmost importance in this matter. To the authors opinion, the data availability can be expanded to exceed the companies thresholds and to span multiple companies and countries. In this light, cooperation might very well be seen as the most important future need of all.

Samenvatting

Lage-Snelheids Model Ophangings-Interferentie
Elementen van een Expert Systeem

De stoorinvloeden veroorzaakt door windtunnel model ophangingen is een beperking die de kwaliteit van de meting in de windtunnel negatief beïnvloedt. Verscheidene methoden om deze interferentie te bepalen zijn experimentele- empirische- en numerieke methoden (CFD). Experimentele methoden zijn vaak tijdrovend en duur. Dit geldt tevens voor empirische methoden aangezien deze de basis ontlenen aan een substantiële hoeveelheid experimentele data. CFD is tevens tijdrovend en kan behoorlijke numerieke rekenkracht vereisen. Toekomstige richtlijnen voor de aanpak van de interferentie richten zich op het kunnen bieden van meer alternatieven aan ingenieurs. Zulke alternatieven vereisen echter een omvangrijke kennis van experimenten en CFD: het vereist de ingenieur om een expert te zijn op alle velden, iets wat vaak onmogelijk is. Om deze reden zouden ingenieurs geleid moeten worden door een expert systeem (een computer programma dat kennis representeert en redeneert met kennis over een specialistisch onderwerp met het doel problemen op te lossen of advies te bieden) gedurende het omgaan met het interferentie probleem. In deze dissertatie wordt zo'n applicatie-gebaseerd expert systeem beschouwd. Het systeem richt zich op ophangings-interferentie (vanaf hier genoemd: interferentie) op windtunnel modellen met een interne balans die opgehangen zijn met een enkele staak in een lage-snelheids windtunnel.

De doelstelling van het onderzoek in dit proefschrift is: “Het vaststellen van noodzakelijke elementen voor het ontwerp van een expert systeem voor interferentie op modellen met interne balans opgehangen met een modelstaak in een lage-snelheids windtunnel.”

In dit proefschrift zijn de noodzakelijke elementen van zo'n expert systeem geïdentificeerd door middel van een studie naar de elementen van de kennis-basis (“knowledge base”) en een studie naar een mogelijke structuur van het systeem in termen van applicaties of elementen.

Met betrekking tot de studie naar de elementen van de kennis-basis: experimenteel- en numeriek onderzoek is uitgevoerd om meer kennis te vergaren op het gebied van ophangings-interferentie. Er wordt aangetoond dat de behandeling van verstoringen

van individuele delen van de ophanging een systematische methode is om interferentie te analyseren. De orde van grootte en aard van de verstoringen worden niet gecompromiteerd met deze aanpak als het aantal afzonderlijke, te bestuderen delen van de ophanging tot een minimum worden beperkt. Deze aanpak staat de cruciale studie naar de verstoringen van de modelstaak toe, welke het complete spectrum van verstoringen veroorzaakt. Voordelen van het bestuderen van de modelstaak zijn onder andere de mogelijkheid om de onderzoeksresultaten te generalizeren naar een grote klasse van ophangingen, het toestaan van een kwalitatieve analyse naar de aard van de "near-field" en "far-field" verstoringen maar ook een kwalitatieve en kwantitatieve validatie van verscheidene methoden toegepast voor de bepaling van de interferentie.
Wanneer metingen (balansmetingen en 5-gats-buismetingen) op near-field en far-field effecten van de model-staak worden vergeleken met berekeningen (panelen code- en Euler-berekeningen) wordt het duidelijk dat zonder de specifieke details te weten van een complexe-interferentie stroming, het niet is gerechtvaardigd (uit het oogpunt van nauwkeurigheid) deze effecten te bepalen met methoden met een laag niveau van complexiteit en intrinsieke nauwkeurigheid. Significante rekenfouten (buiten de grenzen van experimentele nauwkeurigheid) worden veroorzaakt door het effect van de balansholte, vorticiteit en viscositeit. De limitaties van de panelen-code en Euler-berekening kunnen slechts worden vastgesteld als het interferentie-veld zelf wordt begrepen, zowel kwalitatief als kwantitatief. Voor dit doel zijn Navier-Stokes berekeningen ingezet. De berekeningen leveren een kwalitatief beeld van het verstorings-veld dat overeenkomt met eigen metingen. De Navier-Stokes berekeningen zijn echter niet in staat om de verstoringen met de juiste trends en met balans-nauwkeurigheid te bepalen.
De verworven kennis van de lokale verstoring wordt aangewend voor een beoordeling van verscheidene numerieke en experimentele methoden voor het bepalen van near-field en far-field modelstaak verstoringen voor verschillende posities van de staak in het model. Deze kennis wordt gegeneralizeerd naar de behandeling van de overige onderdelen van de ophanging.
Met betrekking tot de numerieke en experimentele analyse van interferentie van een bepaald ophangings-onderdeel wordt geconcludeerd dat de classificatie parameters (welke de verscheidene methoden classificeren) "nauwkeurigheid" en "inspanning" (denk aan bijvoorbeeld rekenkracht) tegenstrijdig zijn. Nauwkeurige methoden vereisen een hoge implementatie-inspanning en vice versa.
Deze tegenstrijdigheid kan niet worden weggenomen met een op maat gemaakt rekenmodel (welke zowel nauwkeurig is en een lage implementatie inspanning kost) voor de bepaling van de interferentie. Een dergelijk model zou de verstoringen snel moeten kunnen berekenen (door alleen de verstoringen te modelleren die een kwantitatief significant effect tonen) met de juiste trends en grootte. Typische beperkingen van zulk soort modellen leiden tot een reductie in het toepassings gebied van het model. Typische op maat gemaakte modellen zijn ongeschikt voor implementatie in het expert systeem. Ze verhullen de volgende vuistregel: "Een hoge nauwkeurigheid (minimaal gelijk aan de nauwkeurigheid van typische Δ-metingen met een balans) en lage implementatie-inspanning (totale meet-inspanning of modellerings- en rekeninspanning) van een correctiemethode voor de bepaling van ophangings-interferentie zijn momenteel onverenigbaar indien een groot toepassingsgebied (stromings condities, model ophangingen) is gewenst".
Deze vuistregel noodzaakt een uitvoerige definitie van de gestelde eisen aan het expert

systeem op gebied van snelheid en nauwkeurigheid, resulterend in een expert systeem met een modulaire-, applicatie-gebaseerde structuur. Deze applicaties met gegeven nauwkeurigheid en snelheid assisteren in vier fases die een typische commerciële windtunnel meting definiëren: onderhandelingen met de klant, de test-voorbereidings fase, het uitvoeren van de metingen en correcties tijdens en/of na het testen.

Vervolgens wordt een mogelijke structuur van het expert systeem bestudeerd. Die voldoet aan de voornaamste eisen aan het expert systeem: adviseren ten aanzien van de experimentele opzet van de test/correctiemethoden, het snel genoeg en nauwkeurig genoeg berekenen van de interferentie (zowel voor de test als tijdens het meten), corrigeren voor de interferentie zowel tijdens als na de test, en het invoegen van extra modules voor de bepaling van windtunnel wandinterferentie faciliteren. Additionele eisen zijn gerelateerd aan het gebruik van het systeem (compatibel zijn met een standaard platform en gebruiksvriendelijk zijn met professionele interfaces). Typische benodigde elementen van het expert systeem worden geïdentificeerd: de uitgebreidde kennis-basis op het gebied van interferentie heeft geleid tot twee elementaire expert applicaties (ESI en ASID, direct toepasbaar voor metingen in de LLF van DNW) en nieuwe methoden (VOLAER en MVL) om het probleem van windtunnel wand- en ophangings-interferentie te kunnen analyseren. Deze producten kunnen gezien worden als fundamentele elementen van een expert systeem (te generalizeren voor het gebruik in andere windtunnels).
MVL (een methode welke ongecorrigeerde windtunnel-metingen en vortex-lattice berekeningen met elkaar combineert) blijkt bijzonder waardevol aangezien de methode de interferentie van de windtunnelwanden en model ophanging berekent en eveneens het effect van secundaire interferentie (in het geval dat bijvoorbeeld de ophanging de windtunnelwanden nadert) in beschouwing neemt. MVL is geschikt voor alle model ophangingen in alle typen windtunnels onder het voorbehoud dat een vortex-lattice methode wordt gebruikt die een nauwkeurige berekening toestaat van de afgeleiden van aerodynamische coefficiënten van het windtunnel model (en die bij voorkeur de effecten van viscositeit meeneemt). MVL noodzaakt het gebruik van meerdere randvoorwaarden (interferentie-waarden) om een stabiele oplossing te kunnen garanderen. Hierdoor kan de methode worden geclassificeerd als interpolatie-methode om de hoeveelheid noodzakelijke experimentele balans Δ-metingen te reduceren.

In deze thesis wordt een eerste eenvoudige variant van een expert systeem gepresenteerd en de noodzakelijke elementen daarvan worden geïdentificeerd. Dit kan worden gezien als een goed initiatief naar het kunnen voldoen aan de toekomstige richtlijnen op het gebied van interferentie bepaling. Aan deze richtlijnen kan worden voldaan als verdere ontwikkeling van het expert systeem wordt gestimuleerd. Toenemende beschikbaarheid van data en het updaten van de diverse expert-applicaties zijn hierin van groot belang. Naar de mening van de auteur zou de beschikbaarheid van data verder moeten strekken dan de grenzen van bedrijven en zelfs landen. In dit opzicht kan samenwerking tussen deze wellicht gezien worden als de grootste toekomstige behoefte.

Acknowledgements

The content of the research presented in this thesis is based on support interference. The support of the people I would like to acknowledge here can however hardly be called interfering. Their support has proven to be very valuable to me in accomplishing this work. For that, I would like to thank all of them.

First of all, I would like to thank the people of DNW that made this research possible. In particular I would like to express my gratitude towards Georg Eitelberg for his mentoring during the research and our interesting discussions on the research topic. Furthermore Sinus Hegen and Dieter Eckert for their guidance during the project and for tutoring me the ways of low-speed wind tunnel testing and its constraints during my stay at DNW.

At the high-speed and low-speed laboratories of the faculty of Aerospace Engineering there have been several people committed to my day-to-day supervision and assistance. I would like to thank Leo Veldhuis and Hester Bijl for their guidance, participation and enthousiasm. Furthermore the practical assistance at the laboratories is also greatly acknowledged. For that I would like to thank Erik de Keizer, Peter Duyndam, Nico van Beek, Frits Donker Duyvis, Leo Molenwijk and Stefan Bernardy.

During the last months of finishing the thesis I have started up a career at Dockwise Shipping in Breda. At Dockwise my supervisors Michel Seij and Ralph Postma have given me the opportunity and space to finish this work for which I am truly grateful.

Besides all professional help from the abovementioned people it is certain that a big part of the support has been the encouragements of family and friends. On a more personal note, I would like to thank these people as well for being there when I needed them the most: mom, dad and Noortje as my biggest fans from the beginning, this work is a bit yours as well. Your unconditional companionship, love and support has helped me incredibly. I would like to thank Frank, Roger en Roeland for their neverending interest in my work and the good company over a drink discussing science. Ger and Maria, thanks for all the pats on the shoulder and heartwarming encouragements. Ger, thank you very much for making this thesis an eye-catcher on anyone's bookshelf!

Robert and Erik, I will never forget the bar-sessions for blowing off some steam when things got rough. Your friendship means a lot to me. Jack, our friendship goes back for some 30 years already and I hope it will go on for many years to come. Thank you so much for all the good times and the laughter.

Last my Maaike. My love, thank you for always being there for me, encouraging and supporting me. Thank you for being the person that made me put things in the proper perspective if they were not. Thank you for being you and thank you for being mine. This work is dedicated to you.

Delft, May 2011.

Contents

List of Figures

Chapter 1

Introduction

Obtaining useful experimental data to assess aerodynamic characteristics in aerospace engineering may be performed in a number of ways. Amongst these are performing flight tests (both scaled- and full scale models) and wind tunnel tests, two main classes each bearing advantages and disadvantages from a practical and theoretical point of view. According to Barlow et al. [1] wind tunnels are seen as the most rapid, economical and accurate means for conducting aerodynamic research and obtaining aerodynamic data to support certain design decisions. Wind tunnels enable the use of models that can be prepared early in design cycles. Including the complexity of real fluid flow during a test and realizing the acquisition of large amounts of reliable data are also appealing advantages. Compared to flight tests, wind tunnels save both money and lives worldwide. Typical disadvantages of wind tunnel testing are the corrections that need to be applied in order to correct the measurement results to free-flight data. Besides corrections for geometric scale effects, Mach number effects, Reynolds number effects and wind tunnel wall interference, wind tunnel support disturbance corrections are unavoidable for guaranteeing the integrity of the free-flight data.

This thesis focuses on the fundamentals of low-speed model support interference on sting mounted models carrying internal balances as one of the above mentioned constraints of wind tunnel testing. The goal of this focus is to identify the necessary elements for designing an expert system for the treatment of low-speed wind tunnel support interference.

In this chapter a short historical review is given on low-speed wind tunnel testing revealing that above mentioned constraints have always played an important role in the development of wind tunnels and wind tunnel tests. After this review, the constraints are discussed. Besides touching upon geometric scale effects, Mach number effects and Reynolds number effects, wind tunnel wall interference is treated. The problem of wind tunnel support interference is more thoroughly treated as it is the focus of this thesis. A break-down of interference effects, correction methods and accuracy requirements are discussed. Defining the future needs for support interference treatment will lead to the thesis aim and objectives: to identify the necessary elements for designing an expert system for the treatment of low-speed wind tunnel support interference on sting mounted models carrying internal balances.

1.1 Wind tunnels: a historical context

Wind tunnels have always been an important engineering tool both from the viewpoint of scientific research as well as practical engineering. Although the first wind tunnel as we know it today was built some 30 years before the first controlled, powered and sustained manned flight at Kitty Hawk by the Wright Brothers in 1903, scientists (or "experimenters" as they were called in those days) from all over the world have designed and constructed "aerodynamic test devices" far before that time.

As Leonardo da Vinci (1452 - 1519) and Isaac Newton (1643 - 1727) realized during their experiments, the flow of air around any object can be studied when either the object moves through the air at a certain velocity or when the model would remain stationary. In the latter case the air would have to be blown past the stationary model. From the viewpoint of experimental controllability this poses constraints on the experimental setup. In the centuries to come, these constraints have become clear to the scientists that build aerodynamic test devices.

According to Baals et al. [2] the first documented experiments have been carried out with a stationary model. For creating a flow of air over the model, the natural wind source was chosen. This put constraints on the test setup because the model was to be attached above wind-swept ridges and in the mouths of blowing (drafting) caves (this situation seems to resemble the modern open jet wind tunnel facilities). Because of the various uncertainties that were present during such experiments mostly related to the incoming flow properties, the experimenters turned to more controllable experiments where the object to be studied moved through still air. This shift in philosophy led to the invention of the "whirling arm".

It was the British mathematician and engineer Benjamin Robins (1707 - 1751) who was the first to employ this mechanical centrifugal device where the model was given a rotational velocity in still air. A schematic of this device is shown in Figure 1.1. The whirling arm is spun by a falling weight. Via a wire and pulley, the vertical force exerted by the weight is transferred to a spindle. The rotating spindle then initiates the motion of the test-object, attached to the end of an arm. Velocities of only a few feet per second could be reached.

Using this setup, various shapes have been studied by Robins (blunt objects such as pyramids but also plates) by attachment to the tip of the whirling arm. His work concentrated on the resistance of certain bodies in a flow of air. He concluded:

> "all the theories of resistance hitherto established are extremely defective"

His statement was based on the observation that different objects with the same frontal area did not always have the same value of air resistance, or drag. His statement was an indication of the complex relationship between drag, model shape- and orientation

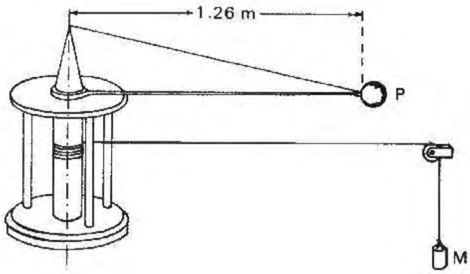

Figure 1.1: A schematic of Robins' whirling arm

and air velocity.

Another scientist to use the whirling arm was George Cayley (1773 - 1857). He measured lift and drag forces on various airfoil resembling shaped objects. The whirling arm used was larger than Robins' and the tip speeds at the whirling arm tip also increased. The data that was gathered by his research was used by Cayley himself to build a glider. This glider is believed to be the first successful "heavier-than air" vehicle in history and shows the rise of early aerodynamic research applied for aeronautical purposes. In the years to follow, Cayley designed various glider configurations (an example of one of his creations is shown in Figure 1.2).

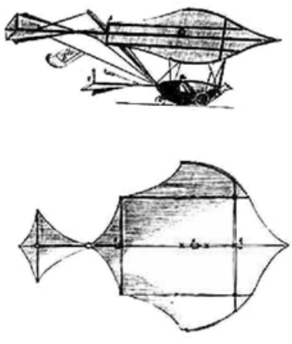

Figure 1.2: An example of one of George Cayley's gliders (from top to bottom: side- and top view)

Manned and powered flight would however take another 50 years. Besides Cayley's contribution to aerodynamic research and practical engineering, he was also able to shine a new light on future successful airplane configurations that were able to fly both manned and powered. Scientists before his time believed that the airplane propulsion system would serve two purposes: to create both forward motion (or, thrust) and lift. This idea was inspired on nature's solution (birds). Cayley however had a different viewpoint. He proposed to use a power plant in order to create forward motion and to let this motion develop the lift via the wings. His revolutionary idea to separate propulsion and lift have finally led to manned powered flight.

Although the whirling arm used by Robins and Cayley has contributed to quite some extent to the aerodynamic data gathered in the late 1800's, the disadvantages of using the whirling arm became obvious. It seemed that in order to create more reliable data that was to be used for manned powered airplane design, a more accurate facility enabling the use of more accurate measurement instruments was necessary. The amount of turbulence generated by the whirling arm was severe and the flow around the object was influenced by this turbulence and on top of this the influence of its own wake. This turbulence made the determination of relative velocity between model and air almost impossible for the experimenter. Mounting measurement equipment on the whirling arm to measure the small forces on the model that was spinning at high speeds was also difficult. These disadvantages led again to a shift in test philosophy. As in the olden days the idea to keep the model stationary and let the flow pass the object seemed attractive again.

These findings have finally led to the design of the first wind tunnel as we know it today. The first of these was designed and operated by Frank H. Wenham (1824 - 1908), a Council Member of the Aeronautical Society of Great Britain. Although the exact configuration of wind tunnels used today is different from the tunnel as designed by Wenham, the basic components of this type of wind tunnel and the operating principle are more or less the same: the wind tunnel consists of an enclosed passage through which air is driven by an appropriate drive system. The heart of the wind tunnel is the test section, housing and supporting the wind tunnel model under study. This model is held in the controlled air stream. This produces the flow over the object of study, duplicating the behavior of the full-scale object. Appropriate test instrumentation (such as balances) are used in order to measure the characteristics of the model and its flow field. The fact that a new method for studying the aerodynamics over an object was found that incorporated controlled flow and systematic testing using instrumentation with pre-defined accuracy levels, quickly obsoleted the use of the whirling arm. There was still an important issue that kept the experimenters busy: the problem of model scale. Is it possible to translate the object characteristics attained using the wind tunnel to the characteristics of the full scale model? This question had to be addressed if a scale model of an airplane configuration would be used for full scale design purposes.

The answer to this problem was solved by Osborne Reynolds (1842 - 1912), a "professor of engineering" at the University of Manchester. In a set of experiments Reynolds demonstrated that the flow pattern over a test object was the same as the flow pattern over the full scale model as long as the ratio of inertial forces and viscous forces in both flows corresponded. This ratio is known today as the "Reynolds number".

From this historical note it is concluded that the wind tunnel developed to an important engineering tool that was absolutely crucial in the gathering of scientific knowledge if manned powered flight was ever to be accomplished. This has proven to be the case as the Wright Brothers based their design on knowledge gathered during their wind tunnel tests. After centuries of development, the aerodynamic test devices evolved in to what is known today as the low-speed wind tunnel. During the development of the low-speed wind tunnel then and in the years to come a lot has changed, ranging from exact wind tunnel layout to instrumentation and test. These are changes that have mostly been inspired by the current technological standard (think of the development of the main power source driving the wind tunnel but also the development of different types of measurement equipment and their increasing accuracy that contributed to the designs of different types of wind tunnels because flow quality also became an issue).

Today, two basic types of low-speed wind tunnels along with three types of test sections can be distinguished: open circuit and closed circuit tunnels with a closed test section, open test section or a slotted test section. Various combinations on these basic types exist. Consider a closed circuit wind tunnel with a closed test section. A typical example of such a tunnel is given in Figure 1.3.

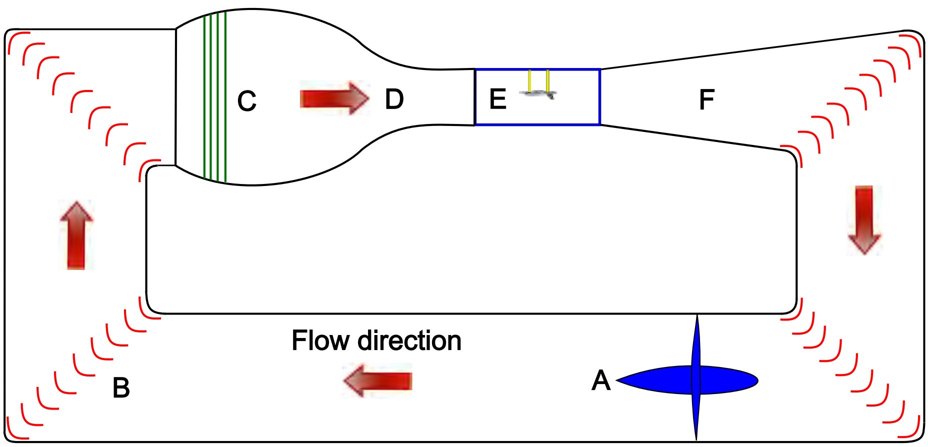

Figure 1.3: A typical example of a closed circuit low-speed wind tunnel with closed test section

This tunnel consists of a few basic elements that are representative for low-speed wind tunnels:

1. A propulsion system (e.g. a fan) that drives the air through the wind tunnel adding momentum to the flow (marked as “A” in the figure),

2. Corner vanes to redirect the flow through turns in the wind tunnel while minimizing the amount of turbulence and accompanying viscous losses (marked as “B” in the figure),

3. A settling chamber including turbulence screens to straighten the flow and fragment large eddies into smaller eddies (marked as “C” in the figure),

4. The contraction to increase the flow velocity and break down the eddies by the mechanism of vortex stretching (through viscous dissipation) (marked as “D” in the figure),
5. The test section housing the wind tunnel model and accommodating measurement equipment and/or optical/mechanical access for measurement equipment (marked as “E” in the figure),
6. The diffuser decreasing the flow velocity before it is fed back to the fan (marked as “F” in the figure).

Studying a typical low-speed wind tunnel as given in Figure 1.3 it seems that the resemblance with Robin’s whirling arm (Figure 1.1) is poor. Although the way to drive a stream of air along the object of study and the way measurements are performed with the accompanying equipment have shown a major evolution in the last centuries, most of the important constraints on the quality of measurement results have not changed. These constraints have- and will in the future affect the quality of wind tunnel measurements. They are:

1. Geometric scale effects, Mach number effects and Reynolds number effects,
2. Wind tunnel wall interference,
3. Wind tunnel support interference.

With increasing measurement accuracy, these factors that constitute the main differences between a measurement in a “wind tunnel environment” and a “true freestream event” have become even more important. They are discussed in the following sections.

1.2 Correcting wind tunnel measurements to free-flight data

In this section, the prominent constraints are discussed that affect the quality of wind tunnel measurements. These constraints affect the flow around the object of study, thereby complicating the extrapolation of measurement results to an “undisturbed freestream value”. Accurate extrapolation from the wind tunnel environment to a full scale free-flight event is of utmost importance in order to prevent costly steps back to earlier design stages to correct for potential mistakes. According to Rolston [3] erroneously predicted corrections implying a drag increase of 1% for an ultra high capacity aircraft would equate to a reduction in range of 120 [km] for a constant maximum take-off weight.

1.2.1 Geometric scale-, Mach number- and Reynolds number effects

Geometric scale effects occur due to differences in model geometric fidelity or aeroelastic properties between the wind tunnel model and its full scale design. Wind tunnel models are typically not designed with the same level of detail as the full scale design (think of leaving out antennas, gaps etc. in the production of a wind tunnel model). This affects the measured drag in the wind tunnel causing an offset compared to the free-flight value. Because the aeroelastic properties of the wind tunnel model differ from the full scale design, different aeroelastic behavior is measured in the wind tunnel.

Mach number effects manifest when the test Mach number in the wind tunnel differs from the free-flight value. Depending on the Mach regime this might result in a difference in flow behavior: at incompressible Mach numbers (typically ≤ 0.3) small differences in Mach number are corrected to lead to equivalent static- and dynamic pressures as in free-flight. At transonic conditions however, offsets might also lead to differences in flow topology by means of shock formation.

A distinct classification of Reynolds number effects is given by Pettersson et al. [4]:

1. Direct Reynolds number effects: these are associated with a constant pressure distribution for varying Reynolds numbers. Typical characteristics that are dependent on direct Reynolds number effects are boundary layer transition and separation, shock wave- boundary layer interaction, buffet boundary and viscous drag,

2. Indirect Reynolds number effects: these are associated with a change in pressure distribution for varying Reynolds numbers. Characteristics dependent on indirect Reynolds number effects are shock strength and position, wave drag and drag divergence, lift and pitching moment.

As an example, the following typical Reynolds number effects are seen between a measured and free-flight lift polar of an airfoil: when the Reynolds number is increased (extrapolating from the wind tunnel experiment to the free-flight value), the slope of the lift polar (C_{L_α}) increases as does the maximum value of the lift-coefficient ($C_{L_{max}}$). Increases in C_{L_α} are attributed to the fact that at higher Reynolds numbers, the thickness of the boundary layer decreases. This increases the effective camber of the airfoil and hence the value of C_{L_α}. When the Reynolds number increases, the boundary layers transit from laminar to turbulent (only when transition is not triggered artificially) thereby energizing the boundary layers. These turbulent boundary layers are less prone to flow separation than laminar boundary layers. This causes an increase of $C_{L_{max}}$.

Correcting wind tunnel measurements for above mentioned effects is a difficult and cumbersome task. Methods used are often described with empirical relations based on the extrapolation between measurements, CFD calculations and free-flight data. The last necessity is usually what makes correcting difficult. If free-flight data exist they are usually confidential and not accessible for everybody. For the engineer this implies performing more wind tunnel tests and/or CFD calculations consuming a lot of time and being expensive.

1.2.2 Wind tunnel wall corrections

Wall interference in the test section is caused by the presence of the wind tunnel walls. To obtain equivalence of the measured data with the undisturbed free-flight values wind tunnel wall corrections need to be carried out. As described in the AGARDograph 336 [5] a rigorous definition of equivalence is complicated by the fact that wall interference varies over the model and its wake. If the wall interference were uniform the equivalent free-air conditions could be defined as the values of Mach number, angle of attack and angle of sideslip which in free-air at the same total pressure and temperature would give the same forces and moments as those measured in the tunnel. The existence of the spatial variations in the wall-induced velocities implies that this equivalence cannot be obtained precisely. Therefore, some corrections are needed for these variations.

Four factors govern the aerodynamic interference of wind tunnel walls on a model:

1. The nature of the aerodynamic forces generated by the model (lift, drag, pitching moment), the constitution of the drag and contributions of simulated power units (rotors, propellers, fans and jets),
2. The Mach number,
3. The size of the model relative to the size of the test section,
4. The type of test section walls.

The standard correction approach is to correct the Mach number as measured in the wind tunnel to the free-flight value thereby obtaining the equivalent static- and dynamic pressures. Angles of attack and angles of sideslip also need to be corrected. These corrections are referred to as the "wind tunnel wall primary corrections". Besides these, residual variations in wall interference velocities (interpreted as wall induced distortions of the model flow and its wake) are customary to correct for.

Typical examples of wall interference corrections that are carried out are:

1. Blockage corrections (residual): corrections on the freestream value of the Mach number, velocity, Reynolds number, dynamic pressure, static pressure, density and temperature are necessary to correct for the blockage effects of the wind tunnel model, its wakes and the slipstream of model engines. The presence of the model and its wakes induce a local increase in dynamic pressure according to the law of mass conservation. Therefore the model encounters a dynamic pressure that is higher than the "freestream" value used to calculate the aerodynamic coefficients. As for the engine slipstreams, the presence of locally higher velocities in the slipstream leads to a lower value of the dynamic pressure outside the slipstream (mass conservation). This is felt by the model and should be compensated for by a blockage correction as well. A blockage correction frequently applied during ground-proximity testing of aircraft is lift-blockage: this blockage is the consequence of an off-center location of the model wing. Blockage corrections are frequently determined for all the parts spanning the model configuration and then summed in order to calculate the value of the total blockage,

2. Lift interference: a correction on the angle of attack of the lifting surfaces (wing, horizontal tailplane) is carried out because of two disturbance factors:
   - Wall interference on the direction of the effective wind speed. This is lift-dependent up wash interference (residual),
   - Wall interference on the streamline curvature along the wing mean chord (primary),
3. Drag interference:
   - The drag is affected by the rotation of the effective wind speed vector (residual),
   - A slight buoyancy force will work on the model induced by a wake blockage gradient (residual). This necessitates an additional correction.

Methods to determine wall interference

Determining the values of primary corrections and residual variations can be based on:

1. A mathematical representation of the wind tunnel model according to classical theory. In the AGARDograph 336 [5] the term "classical" refers to the results of the earliest analysis of wind tunnel boundary interference. The assumptions underlying classical theory include:
   - The flow in the tunnel is regarded as a linear potential flow,
   - The flow at the tunnel boundaries is a perturbation flow,
   - Model dimensions are relatively small (typically the ratio of model span to test section width is ≤ 0.5 for a negligible spanwise variation of lift interference) compared to the tunnel, and its wakes (viscous- and vortex wakes) extend straight downstream,
   - The tunnel of constant cross-sectional area extends far upstream and downstream of the model. Its boundaries are parallel to the direction of the flow far upstream of the model. Its boundary condition is either no flow normal to the wall (flow tangency condition) or a constant pressure at the wall.
2. Measurements of pressures at the wind tunnel walls ("two-variable methods" as described by Ashill [6]),
3. A combination of the above mentioned ("one-variable"- and "wall-signature" methods as described by Ashill [6]).

For solid-wall wind tunnels, the wall boundary conditions are well defined facilitating the calculation of e.g. wall induced velocities. In ventilated tunnels the primary corrections and residual variations are not determined easily or accurately due to uncertainties arising in the representation of the wall boundary conditions. The required data can sometimes be obtained experimentally by extrapolation of data between tests in facilities with different walls.

Generally speaking, wind tunnel engineers are people that are experimentally minded. They are not easily inspired by Computational Fluid Dynamics. Besides the limited availability of computational resources this is the reason that the adoption of CFD in practical wind tunnel engineering has been slow at first. Correction routines formulated by for instance Prandtl, Glauert, Durant and Maskell have been used for quite some time, even in high quality tunnels. During this period, a substantial amount of research has been performed (both theoretical and experimental) on wind tunnel wall interference. Combined with the fact that during this period the quality and quantity of computing power has increased tremendously, some computer based methods have been developed such as panel methods, boundary measurement methods and more advanced CFD methods (discretizing the complete volume inside the wind tunnel). Although the quality of these methods has improved throughout the years (especially the advanced CFD methods used to determine the wall interference of ventilated- or slotted wall wind tunnels) fairly little has been done to provide a systematic validation of these methods. This is mainly caused by the fact that there is no readily available calibration standard.

Accuracy requirements on wind tunnel wall correction methods

The choice of a correction method (or the choice whether corrections should be carried out at all) depends besides available resources on required data resolution and available accuracy. According to Steinle et al. [7], required data resolution is dictated by industry sources. For commercial- and transport-type aircraft, drag is considered the most important aerodynamic parameter. The following accuracy requirements are given for the longitudinal aerodynamic coefficients (lift-, drag- and pitching moment-coefficient) of such aircraft with Mach numbers between 0.5 and 0.85:

$$\begin{aligned} \Delta C_L &= 0.01, \\ \Delta C_D &= 0.0001, \\ \Delta C_m &= 0.001. \end{aligned} \tag{1.1}$$

These numbers are based on the requirement to resolve the interference to within one drag count (a distinguishable 0.0001 in drag-coefficient) at cruise conditions (considering attached flow). According to Luijendijk [8] the drag-coefficient of a typical commercial aircraft in cruise condition at a Mach number of 0.85 is approximately 0.03. Resolving the drag-coefficient to within one count equals roughly 0.33% of the complete aircraft drag. The reduction of aircraft drag with 0.33% equals a corresponding reduction in fuel consumption. On a yearly basis, this might lead to a significant reduction in operational costs, especially for an entire fleet. The reason that the requirement on resolving for the drag-coefficient is so strict is thus based on fuel-saving economics. Based on the parameters in Equation set (1.1) required data resolution of additional parameters can be derived. These are summarized in Table 1.1.

Similar requirements are mentioned by Krentz et al. [9] for the Mach regime $0.2 \leq \text{Mach} \leq 0.95$ (including the transonic regime). For low-speed high-lift scenarios when e.g. take-off and landing are simulated, requirements point towards an accurate determination of the maximum lift $C_{L_{max}}$ and the lift- to drag ratio L/D. In these cases

Table 1.1: Required data resolution (based on Steinle et al. [7]) for resolving low-speed wind tunnel wall interference based on the accuracy requirement of resolving the drag-coefficient of a typical commercial-/transport-type aircraft to within 1 drag count. Results are valid for cruise Mach numbers between 0.5 and 0.85

Description	Value
Mach number	0.001
Stream wise Mach gradient	$\leq 0.0006 \cdot M$
Flow angle	≤ 0.01 [deg]
Stream wise flow curvature	≤ 0.03 [deg/chord]
Spanwise variation in flow angle	≤ 0.1 [deg]

typical required data resolution is in the order of $\Delta C_L = 0.03$ (approximately 1% of $C_{L_{max}}$) and $\Delta C_D = 0.0005$.

Besides the latter values for high-lift scenarios, typical values as presented in Equation set (1.1) and Table 1.1 provide benchmarks against which the accuracy of correction methods for low-speed wind tunnel wall interference on typical aircraft configurations can be evaluated.

1.2.3 Wind tunnel support corrections

When the problem of model support disturbances is addressed, an accurate description of the disturbances of interest is necessary. Generally speaking, model support disturbances can be defined as "... all the disturbances in the model flow field induced by the presence of its supporting members ...". Generally speaking it is difficult to separate model support interference and wall interference. According to Carlin et al. [10] simulating the interference of the support system without the tunnel wall constraints is found to result in erroneous magnitudes and gradients of the interference at subsonic conditions.

In the present work the manifestation of the disturbances of the model support on the flow field of interest (a volume bounded by wind tunnel walls containing the wind tunnel model) are divided in two main classes (illustrated in Figure 1.4) according to Horsten et al. [11]:

1. Support near-field effects: near-field effects consist of viscous and inviscid disturbances manifesting in the direct vicinity of the protrusion of model support and wind tunnel model (on the fuselage of the model). The near-field effects are caused by the support member protruding the fuselage boundary layer (such as a sting or bayonet). Typical effects include a streamline displacement on the model, a carry-over of the support pressure distribution onto the model and model boundary layer disturbances caused by the protrusion and presence of the support,

2. Support far-field effects: far-field effects are inviscid disturbances expressed in a buoyancy effect on the wind tunnel model fuselage and inviscid disturbances that

influence the local flow properties at the lifting surfaces of the model. Generally speaking, these disturbances are expressed in local changes of angle of attack α, angle of sideslip β and dynamic pressure q.

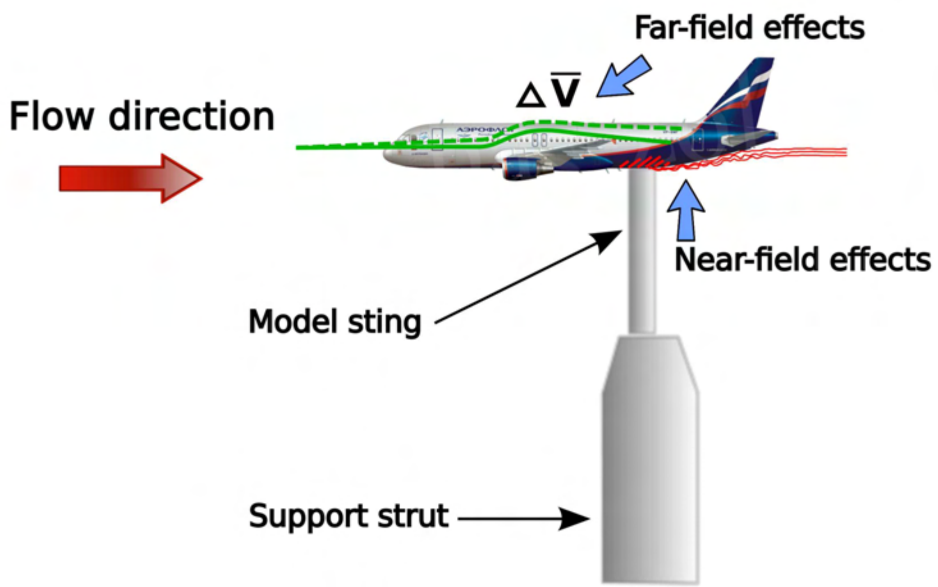

Figure 1.4: An example of support near-field and far-field disturbances on a typical sting-mounted wind tunnel model. The far-field effects are indicated at the wing as a disturbance on the local velocity vector

Of course there are exceptions to these definitions: a model support may contain a part that does not protrude the boundary layer of the model but is close enough to the model surface so that its pressure distribution affects the model significantly. Such support setups are however not desirable because they are likely to provide large disturbances on the model. For that purpose they are not considered in this thesis.

The support member protruding the model boundary layer will cause both a near-field and a far-field effect on the wind tunnel model. It will be clear that the magnitude of its far-field effect is dependent on the magnitude of its near-field effect: large local disturbances at the protrusion of support and model will also affect the flow at the lifting surfaces. Support members that do not protrude the model boundary layer only cause far-field effects.

The values of near-field and far-field effects depend on the disturbance ability of the model support. This disturbance ability is influenced by a number of factors:

1. The geometrical characteristics of the support and model,

2. The placement of the support with respect to the model according to Veldhuis [12],

3. Incoming flow conditions of model and support.

Changing wind tunnel model geometries and/or support placements with respect to the model will cause the disturbance ability of the model support to change. The reason for this is that the local boundary layer properties at the support protrusion location and local pressure gradients determine the effectiveness of the support in interfering with the model flow field. Adjusting the geometrical characteristics of the support will lead to a change in disturbance ability seen as a local and global increase or decrease of the disturbance. When the inflow conditions of model and support change (velocity magnitude and/or direction) this will have an effect on its disturbance signature as well. Changing this signature, the near-field and far-field effects will change in magnitude.

According to the author a second classification of model support interference including above mentioned definitions of near-field- and far-field effects can be recognized. The total disturbance of a certain support configuration on one of the aerodynamic coefficients of a wind tunnel model can be given by:

$$\Delta C_i = \Delta C_{i_{primary}} + \Delta C_{i_{secondary}}. \tag{1.2}$$

According to Equation (1.2) the total disturbance is a composition of a primary and a secondary disturbance. The primary disturbance consists of the summation of near-field and far-field effects of the members spanning the model support setup in a wind tunnel at given freestream conditions. Secondary disturbances are *additional* disturbances caused by a change in disturbance ability of the support thereby influencing the primary near-field and far-field effects. According to Horsten et al. [13] examples of secondary disturbances are:

- Wind tunnel wall proximity effects: when during a wind tunnel test the support geometry is traversed close to the wind tunnel walls, both the pressure signatures on the walls and on the support change. This leads to a change in disturbance ability of the model support leading to a change in primary near-field and far-field effects,

- Engine power effects: when powered wind tunnel tests are performed, the model support can be influenced by the slipstream of the engine(s). This will result in a local change of the disturbance ability of the support, causing changes in the values of the primary near-field and far-field effects.

In Appendix A the author illustrates the determination of typical primary support disturbances experimentally. For this purpose, results of low-speed (freestream Mach number of approximately $M_\infty \approx 0.20$) wind tunnel measurements on a typical four-engine turboprop aircraft in the Large Low-Speed Facility (LLF) of the German-Dutch

Wind Tunnels (DNW) are used. The nature and order of magnitude of such disturbances are discussed. **In Appendix B** the author demonstrates the experimental and numerical determination of a significant secondary support disturbance (engine power effects) for a similar setup. Nature and order of magnitude of such disturbances are again evaluated. Typical methods used for the assessment of support disturbances are discussed in the following section.

Support interference effects have to be accounted for when correcting wind tunnel data to free-flight conditions. The only exception to this rule is when the wind tunnel data is used to determine incremental effects or relative effects of the model configuration on its performance. Even then it is of utmost importance that the model support does not interfere (or at least minimally) with the configuration parts of interest. Dealing with support interference is therefore a combined action of choosing an “appropriate” model support (that minimizes the disturbances) while applying a correction technique that determines the interference with the desired accuracy. Such methods are treated in the next section.

Examples of methods to correct for support interference

The choice of a correction method used to determine model support interference is governed by a desirable balance between accuracy, implementation effort and costs. Based on these requirements, three main categories can be pointed out for the choice on the correction technique:

1. Experimental methods,
2. Empirical methods that extrapolate available interference data to the support setup of interest,
3. Computational Fluid Dynamics (CFD).

Experimental determination of support interference is time consuming and costly. Various support configurations are used to mount the model. Subtraction of the measurement results (measured by e.g. balances) of these configurations provides the support correction of the configuration of interest. This means that the measurement matrix of a certain test is at least tripled by the fact that all measurement points should be covered by at least three support configurations. This experimental technique is referred to by the author as performing “Δ-measurements”. As part of the Δ-measurements, dummy setups are included. This is clarified in Figure 1.5 that demonstrates the basics of a Δ-measurement on a typical aircraft configuration carrying an internal balance. When external balance systems are implemented, additional tare corrections are necessary compensating for the aerodynamic forces and moments on the support parts that connect the model and balance. Examples of support corrections attained by Δ-measurements are given by Poole et al. [14], Kirby [15], Elsenaar et al. [16], Lynch et al. [17], Eckert [18], Ericsson [19], Lee et al. [20], Loving et al. [21], Dietz et al. [22] and Canning et al. [23]. Δ-measurements can also be used with other equipment than balances. Far-field effects can for instance be measured in

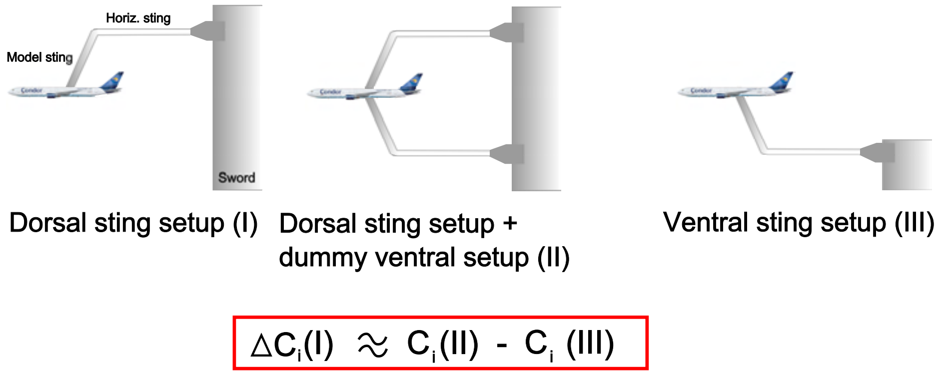

Figure 1.5: A typical example of performing a Δ-measurement on a sting-mounted wind tunnel model with an internal balance. It is shown how subtraction of the aerodynamic characteristics of various setups (including the dummy setup II) leads to the support interference of the setup of interest. The approximate sign (≈) is put in the formula because in the calculation of the interference of the dorsal setup (I), a small part of the sword is not included

a Δ-measurement using a 5-hole probe (discussed later on).

Using empirical methods to determine corrections for similar support systems is proposed by Eckert [18]. This method implies that model support corrections can be used for the determination of support interference of models showing distinct similarities in geometry and test setup, e.g. models of the same aircraft family. The corrections are found by data extrapolation of available interference results. This makes this method relatively fast and cheap. It however requires a substantial data-base of support interference measurements and/or calculations.

CFD calculations are becoming more and more applicable these days because of the substantial increase in computational resources. Multiple numerical methods are applied to solve the problem of model support interference. On the whole, for every test condition in the wind tunnel (angle of attack, angle of sideslip, Mach number) two calculations should be performed: one calculation including the model support and one calculation excluding the model support. Subtracting the forces and moments of these calculations (referred to as a "Δ-calculation") leads to the determination of model support interference.

With increasing computing power and the development of advanced CFD methods (RaNS models closed by advanced turbulence modeling for example) the detail of geometrical and physical modeling has also increased over the years. Typical numerical methods that are applied rely on a distribution of singularities (elementary solutions to the Laplace equation) as shown by Quemard [24], vortex-lattice calculations as shown for example by Vaucheret [25] and panel code calculations according to Mokry [26], Willaume et al. [27], Almosnino [28], Quemard [24], Carlin et al. [10], Steinbach [29], Fiddes et al. [30], Steinbach [31], Amtsberg [32], Elsenaar et al. [16] and Lynch et al. [17]. CFD methods that rely on a volumetric discretization of the flow typically solve for the Navier-Stokes equations as shown by Lynch et al. [17] and Pettersson et al. [4], [33]. Whatever method is chosen to calculate the model support interference, generally speaking its determination is a time consuming and sometimes computationally expensive task. This is due to mainly two factors:

1. For every test condition two calculations have to be performed (including- and excluding the discretization of the support),
2. Every test condition usually requires a remodeling of the configuration because the orientation of the support structure changes relative to the model and/or the test section walls (that have to be taken into account in the calculation).

Because existing methods to determine model support interference are expensive the question arises whether methods exist to avoid the complete problem of support interference. Such a method is magnetic suspension demonstrated by Britcher et al. [34] and Higuchi et al. [35]. By creating a magnetic field in the wind tunnel surrounding the model, the model can be kept in place without the use of supporting members. The magnetic field strength can even be used in order to determine the various forces and moments on the models. Although such methods seem ideal at first, the advantages are no even match for the disadvantages:

1. The wind tunnel models tested in large facilities weigh over tons of kilos. This would imply the generation of tremendous magnetic field strengths in order to keep the model at the desired position,
2. The integrity of the data collected by the equipment stored in the model should be safeguarded from the magnetic field by shielding the equipment thereby adding more weight to the model,
3. When powered wind tunnel tests are performed, pressurized air and cooling water/oil need to provide the model with the means of controlling the engines. This is usually realized by internal pneumatic-, hydraulic- and cooling lines that run through the support to- and from the model in order to minimize the amount of obstacles in the flow field. This is not possible when magnetic suspension is implemented.

Typical problems as mentioned above lead to the recognition that model supports will be an unavoidable part of the scenario of wind tunnel testing for the coming years. This leaves engineers with the challenge to find methods that are able to determine model support interference within a specified amount of time and within a specified budget, requirements that are often determined by the clients outsourcing a wind tunnel measurement. On top of this certain standards regarding the accuracy of these methods should be met that justify the application of the support corrections. These accuracy requirements are discussed in the following section.

Accuracy requirements on the determination of model support interference

Considering the fact that wall interference and support interference are closely related (Carlin et al. [10]) it seems only fair to relate the accuracy requirements on their determination as well. In this case, reference is again made to Table 1.1. Dictated by industry, these requirements are based on fuel-saving economics.

These requirements are only justified when they are exceeded by typical values of support interference. Consider a low-speed wind tunnel test (with a Mach number of ≈ 0.20) of a typical sting-mounted aircraft configuration shown in Figure 1.6(a) and (b). The disturbances induced by the support structure on such models can be calculated by means of performing Δ-measurements. These disturbances are given in terms of the longitudinal coefficients, for instance ΔC_L and ΔC_D for the disturbance on the lift- and drag-coefficient respectively. For typical models shown in Figure 1.6(a) and (b), disturbances on these coefficients for zero angle of sideslip are of the order of 10 counts (0.01 and 0.001 for the lift- and drag-coefficient respectively), the exact magnitude depending on support placement and flap/control surface settings. The disturbances on the longitudinal coefficients can be used to calculate model spanwise averaged values of the disturbances on the angle of attack. For tests shown in Figure 1.6(a) and (b) these parameters are typically of the order of 0.1 [deg].

(a) (b)

Figure 1.6: Two examples of a low-speed measurement on a typical sting-mounted aircraft configuration (courtesy of DNW (a) and NASA (b))

It is seen from these numbers that for a typical low-speed test the interference values exceed the accuracy requirements by approximately a factor 10. Therefore support interference corrections are of importance and should be included in the data processing of a wind tunnel test.

Considering the determination of support interference effects, the general consensus seems to be that people are more confident with and rely on experimental techniques than on numerical techniques. This is partly caused by the fact that nowadays more and more complex wind tunnel tests are carried out (including the deflection of high lift devices, thrust reverser simulations etc.). Such configurations are not always amenable to CFD assessment and if they are, their results are likely to have a larger error bandwidth than e.g. a Δ-measurement. Generally speaking the most accurate and widely applicable method for the determination of support interference is the Δ-measurement. When companies outsource a wind tunnel measurement and they want the model support determination to be "as accurate as possible", Δ-measurements are most likely to be performed with an accuracy defined by the balance system. Almost every wind tunnel is facilitated with one or more internal or external balance systems.

Summarizing, when relating accuracy requirements on the determination of model support interference to the problem of wall interference, support corrections of typical low-speed wind tunnel tests are justified. The most accurate determination of support interference to live up to these requirements is currently the Δ-measurement. The question now becomes: "Are Δ-measurements accurate enough in order to meet the accuracy targets?" Unfortunately the answer to this question is no. This is illustrated by Table 1.2 showing typical Δ-measurement accuracy for a variety of wind tunnel facilities.

Table 1.2: Δ-measurement accuracy of typical wind tunnels covering the low-speed and high-speed regime (Low Speed Tunnel, Low Turbulence Tunnel, Large Low-speed Facility and High Speed Tunnel). Reynolds numbers are based on the characteristic length $0.1\sqrt{S}$ where S is the test section cross-sectional area. Accuracies (given in counts) are given for tests on typical aircraft shown in Figure 1.6

Facility	M_1	M_2	Re_1	Re_2	ΔC_L	ΔC_D
LST (Marknesse)	0.10	0.25	$6{\cdot}10^5$	$1.5{\cdot}10^6$	13	12
LTT (Delft)	0.10	0.35	$3{\cdot}10^5$	$1{\cdot}10^6$	4	3
LLF (Marknesse)	0.10	0.45	$2.5{\cdot}10^6$	$6{\cdot}10^6$	2	8
HST (Amsterdam)	0.10	1.30	$2{\cdot}10^5$	$9{\cdot}10^6$	3	5

Comparing typical values in Table 1.2 with the accuracy requirements given e.g. in Equation set (1.1) it is seen that even the Δ-measurement accuracy is not sufficient to meet the standards. Still, the accuracy level of the Δ-measurements is generally perceived as "high". Clients will choose without a doubt a method with similar prediction capabilities if it would be more attractive from a financial point of view. The balance accuracy is therefore an ideal reference for the accuracy of new methods for the determination of support interference: it indicates the "state of the art" standard to comply with. In this thesis, the balance accuracy is used as a reference for the evaluation of methods to determine model support interference.

1.3 Future needs for support interference treatment

If future wind tunnel tests are to be used for providing pre-flight estimates of aircraft characteristics, it is of utmost importance that support interference can be determined with ample accuracy. Accurate determination of support interference is becoming more and more important with the increasing demand for high Reynolds number testing according to Lynch et al. [17]. In addition to increasing the model size, higher Reynolds- and Mach numbers will be attained. Consequently, model loads will increase substantially. This means that the support systems will grow accordingly leading to larger support interference effects to be accounted for. An example of two support systems for low- and high Mach number tests on a typical aircraft configuration are shown in Figure 1.7.

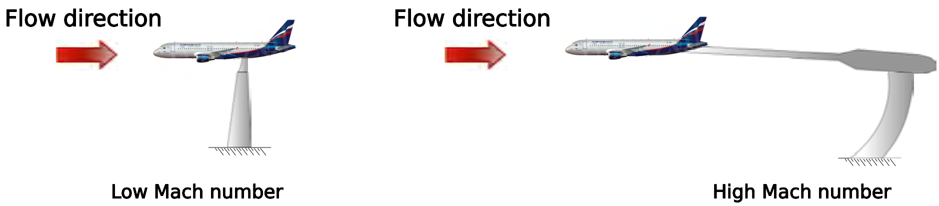

Figure 1.7: An example of the support structure used for a low Mach number test and high Mach number test of a typical aircraft configuration

On top of this, methods to determine the interference should be fast enough in order to reduce design cycle times. According to Lynch et al. [17] future needs regarding support interference are:

1. **An establishment of guidelines for the design of support installations that minimize the total amount of interference and are amenable to CFD analyses,**

2. **Development, refinement and a more extensive calibration/validation of advanced CFD methodologies (like Navier-Stokes) that are easily applicable to a wide range of support system installations,**

3. **The development of empirically-based methods for rapidly estimating support interference effects for installations not amenable to accurate CFD assessment (such as those involving multi-element high-lift systems).**

According to the author, above mentioned needs are vague as no need is quantified. The needs seem to originate from a general consensus that support interference is a poorly understood, unavoidable and growing problem (considering the growing need for high Reynolds number testing) that needs to be dealt with to ensure quality of measurements. The needs aim at providing engineers with more alternatives in dealing with support interference. Besides being able to judge various support systems on the magnitude of their interference providing alternatives for the design of support systems, alternatives are also desirable for the determination of interference. Such alternatives are however based on extensive knowledge of the problem of support interference, measurement techniques and advanced CFD. It would typically require an expert to deal with this.

To provide engineers with a tool for the treatment of support interference an expert system is desirable. The definition and interpretation of such a system for the problem of low-speed wind tunnel support interference is given in the following section.

1.4 Towards more alternatives: the expert system for support interference

A clear definition of an expert system is given by Jackson [36]:

"An expert system is a computer program that represents and reasons with knowledge of some specialist subject with a view to solving problems or giving advice."

The technology of expert systems derives from the discipline of Artificial Intelligence (AI). This is a branch of computer science that is concerned with the design and implementation of programs capable of emulating human cognitive skills such as language understanding, visual perception but also problem solving. Expert systems can be implemented to completely fulfill a function normally requiring human expertise. It may however also be used to play the role of assistant to some human decision maker. This implies that the user of the expert system may interact with the program directly, or interact with a human expert who interacts with the program. The key to successful expert system deployment is to obtain the right allocation of function between user and machine. This is facilitated by a clear and understandable user-interface making use of an interactive dialog.

Although sometimes the distinction between an expert system and a conventional applications program seems vague, Jackson [36] points out distinguishable factors:

1. An expert system simulates the reasoning about a specific problem domain instead of simulating the domain itself,

2. An expert system performs reasoning over representations of human knowledge in addition to performing calculations and data retrieval. All the knowledge in the program is expressed in some language and kept separate from the code that performs the reasoning. These distinct program modules are referred to as the *knowledge base* and the *inference engine* respectively,

3. An expert system can solve problems by heuristic or approximate methods which (unlike for example algorithmic solutions) are not guaranteed to succeed. A heuristic is essentially a rule of thumb encoding a piece of knowledge. These methods are approximate in a sense that the solutions that are derived by the system may be proposed with a degree of uncertainty.

Some general advantages and disadvantages can be stated for expert systems. Amongst the advantages are:

- Expert systems provide consistent answers for repetitive decisions, processes and tasks,
- The system holds and maintains significant amounts and levels of information,
- Expert systems encourage organizations to clarify the logic of their decision-making.

Amongst the disadvantages are:

- An expert system can not make creative responses as a human expert would in unusual circumstances,
- Domain experts are not always able to explain their logic and reasoning,
- Errors may be included in the knowledge base leading to erroneous decisions,
- The system can not adapt to changing environments unless the knowledge base is updated (this can for instance be achieved automatically by a self-learning system).

Designing an expert system is a process called knowledge engineering. Knowledge engineering aims at constructing mainly two components: the knowledge base (seen as a problem dependent set of data declarations) and a problem independent program called the inference engine (that is highly dependent on the data structure).

Mentioned in the last sections, future needs aim at providing engineers with more alternatives when dealing with the problem of wind tunnel support interference. According to the definition an expert system is the ideal solution to fulfill these needs as "solving problems" and "giving advice" are its main tasks. Such a system could be able to calculate the values of wind tunnel support interference (the specific problem domain), give advice on desirable test setups but also on methods to correct for the interference. The knowledge base of the system could be filled with experimental, numerical and empirically derived data. The inference engine could partly be based on heuristic methods such as valuable rules of thumb. Speed and accuracy would play a very important role in the design of the expert system inasmuch as speed determines the way in which the expert system can be used (during what stage of a wind tunnel measurement) and accuracy of the expert system solutions and advice on accuracy of attainable methods provides with a transparent image of the problem of interest. Engineers would benefit from such an expert system. Identifying the necessary elements for designing an expert system for the treatment of low-speed wind tunnel support interference is the topic of this thesis.

1.5 Thesis aim and objectives

Based on considerations regarding the problem of wind tunnel support interference as presented in the last sections, the research objective of the current work is stated as:

"To identify the necessary elements for the design of an expert system for support interference on sting mounted models carrying internal balances applicable to low-speed wind tunnels". Note that only single sting setups are considered in this thesis (ignoring various exotic support variants). Requirements on the expert system are:

1. The system should facilitate the engineer in making choices (by means of advice) on:
   - the test setup considering support interference effects,
   - the methods to correct for such effects.
2. The system should enable the calculation of support interference fast enough and accurate enough (to be defined later on) both pre-test and on-line,
3. The system should correct for above mentioned effects on-line and off-line,
4. The design of the expert system should allow easy plug-in of modules dealing with the problem of wind tunnel wall interference.

Identifying the necessary components of an expert system requires:

1. A study on the elements of its knowledge base. More intelligibility on support interference is necessary. **Part I** of this thesis focuses on the fundamentals of low-speed model support interference on sting mounted models for this purpose,
2. A study on a feasible structure of the system in terms of its applications (or, elements). This is presented in **Part II** of this thesis.

1.6 Thesis outline

The outline of this thesis is as follows: part I focuses on the elements of the knowledge base of the expert system by focusing on the fundamentals of low-speed model support interference. In Chapter 2 a starting point for the study on the fundamentals of low-speed model support interference on sting mounted models accommodating internal balances is given: the model sting. Focusing on the sting is justified by a validated support break down that facilitates the treatment of disturbances of individual support parts spanning a certain support structure. This approach enables the study on the disturbances of the model sting alone, the support member protruding the fuselage. The model sting is an essential object for further study as it causes the complete spectrum of support disturbances. Besides practical advantages another advantage of studying the sting is the possibility to generalize the research results to a wider class of support structures. A study on the disturbance behavior of the model sting allows a qualitative analysis on the nature of near-field and far-field effects but also a qualitative and quantitative validation of several methods applied to determine the interference. As a starting point "exploratory" measurements and calculations are performed on model sting interference assessing the complexity of the interference field. Their results are presented in Chapter 3. In this chapter the following question is answered:

"Without knowing the specific details of a possibly complex interference flow field, is it justified (from the viewpoint of accuracy) to determine model sting near-field and far-field effects using methods at low levels of complexity and intrinsic accuracy?" This question aims at identifying low-cost computational methods for the determination of model sting interference implementable in the expert system once labeled as "good enough" (to within accuracy requirements). It will be shown that limitations of such calculations are only truly understood if an in depth understanding of the interference flow field is created. To this end Navier-Stokes calculations are carried out. The setup and analysis of these calculations are treated in Chapter 4. Besides clarifying the interference flow topology, a more decisive answer is given in this chapter for all numerical methods applied (panel code calculations, Euler calculations and Navier-Stokes calculations) on how well they perform qualitatively and quantitatively in determining model sting interference effects and why. This provides an overview of the restrictions of these methods for calculating model sting interference for the configuration under study. This knowledge is extrapolated to other support setups. Experimental and numerical methods for the determination of support interference of various setups are classified using the parameters "accuracy" and "effort". These classification parameters however seem to oppose each other. This opposition might be cleared by designing a custom-made model for calculating model support interference (that is both accurate and requires a low amount of implementation effort), implementable in the expert system. In order to test the potential of such a model, a simplified 2D case is setup and tested revealing typical disadvantages. This is discussed in Chapter 5. A discussion on the performance of such models will lead to a more elaborate definition of the expert system's requirements on speed and accuracy.

Part II of this thesis will focus on a feasible structure of the expert system in terms of its applications (or, elements). In Chapter 6 a feasible application-based structure of the expert system is discussed in more detail after summarizing its requirements. Typical applications are studied in more detail. It is shown that the proposed structure fulfills the expert system's requirements. Two new hybrid methods (developed by the author) for the determination of wall- and support interference are introduced: VOLAER (VOrtex-LAttice/EuleR) and MVL (Measurement/Vortex-Lattice) implementable during a typical commercial wind tunnel measurement. The principle and evaluation of characteristics of these methods is demonstrated in Chapter 7 on hybrid methods. Chapter 8 recapitulates on the research presented in this thesis. It will become clear that the research objective is met. Windows of opportunity for the development of the expert system by means of knowledge base expansion and the development of new expert applications/elements will be highlighted. This will result in a discussion on future prospects of the expert system. Finally in Chapter 9 the main conclusions of the work presented in this thesis are given followed by some future recommendations.

Part I

A Study on Model Support Interference

Chapter 2

Defining a Research Starting Point: The Model Sting

In this chapter a starting point is defined for the research on support interference: the model sting. It is shown that the sting can be separately treated from the remaining support parts of a typical support structure without compromising the nature and order of magnitude of its disturbances.

2.1 Introduction

Generalizing on the order of magnitude and nature of support disturbances is complicated because the disturbance ability of the support depends on the exact geometry of the support setup. Model support structures exist with a variety of geometrical descriptions. Besides this, some support structures change in layout when angle of attack and/or angle of sideslip traverses are performed in the test section during a measurement. This variety in setups complicates the generalization of approaches towards the problem of support interference. It necessitates the break down of the problem to packages that can be individually analyzed.

In this chapter a support break down is proposed that facilitates the treatment of disturbances of individual support parts spanning a typical support structure. A proof of concept is given by measurement results of DNW. This approach enables the study on the disturbances of the model sting alone, the support member protruding the fuselage. It is concluded that the model sting is an essential object for further study on model support interference as it causes the complete spectrum of manifesting support disturbances. As a starting point for further research, the model sting will allow for:

- The generalization of research results to a wider class of support structures,
- A qualitative analysis on the nature of the disturbance effects,
- Validation of methods to determine support interference.

2.2 Individual treatment of support parts

It is proposed by the author to divide the support structure of interest in parts whose interference can be treated separately, or in general terms:

$$\Delta C_{i_{total}} = \sum_{k=1}^{N} \Delta C_{i_k}. \tag{2.1}$$

In Equation (2.1) the total disturbance is equal to the summation of disturbances of separate parts spanning the support structure. According to Luijendijk [8] it can be argued that physics is lost when the mutual interference between the support members is neglected. This approach therefore proposes that the break down of the support structure is kept to a minimum number of separate parts (to minimize the loss in physics). It is recommendable to split the support geometry into packages of the "same type of disturbance" (near-field and/or far-field) such that these packages can be analyzed using similar methods. An example of a typical break down and an experimental validation of this method are given in the next sections.

2.2.1 Example: support structure break down

A typical low-speed support configuration is considered. A schematic of such a support setup including its degrees of freedom is shown in Figure 2.1.

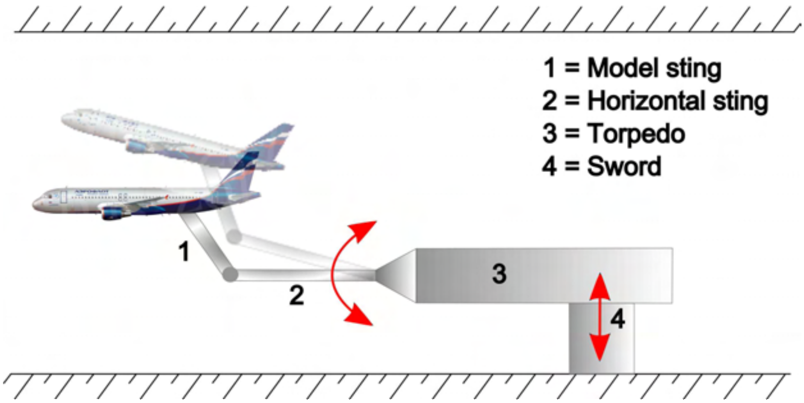

Figure 2.1: An example of a typical low-speed wind tunnel model support structure

The support structure shown in Figure 2.1 typically consists of the following parts:

1. The model sting,
2. The horizontal sting,
3. The torpedo,
4. The sword.

The support interference of these type of setups could be divided into the separate contributions delivered by all of its support members. However in this case, a division in only two parts is proposed (validated in the next section): because the model sting is the only part that causes near-field effects and the other members only introduce far-field effects, the model sting is separated from the rest of the support structure. The near-field and far-field effects of the model sting can be analyzed as also holds for the far-field effects of the other members. Their interference contributions are finally added to form the total disturbance package.

The question arises whether above mentioned approach is valid or not. Is the nature of the support disturbance preserved when this break down is performed? The answer to this question is given by analyzing results of low-speed measurements performed by DNW on the wind tunnel model shown in Figure 2.2. DNW's model support structure in the LLF is very comparable to the configuration shown in Figure 2.1. Separate determination of the disturbance effects of the model sting and the rest of the support structure are performed. Recombining these disturbance effects and comparison to the results of Δ-measurements provides an experimental validation of the break down method.

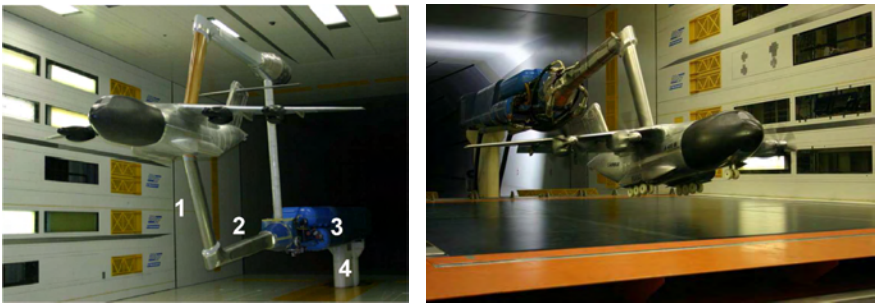

(a) (b)

Figure 2.2: Setup of a low-speed measurement on a typical four-engine turboprop aircraft in the LLF of DNW showing (a) The dummy dorsal setup. The model is supported by a ventral support (penetrating the model belly) while a dummy dorsal setup (penetrating the model back) is installed. The numbers in the figure correspond to the model sting (1), the horizontal sting (2) the torpedo (3) and the sword (4) (b) A dorsal setup (courtesy of DNW)

2.2.2 Experimental validation of the break down method

Measuring the disturbances of the model sting

The research on the near-field and far-field disturbances caused by the model sting is carried out on a wire-mounted model in the Low-Speed Tunnel (LST) of DNW as described by Eckert et al. [37]. The disturbance effects are evaluated by placing (both in ventral as in dorsal position) and removing a dummy model sting (see Figure 2.3(a)).

The sting effects on the aerodynamic coefficients found by this Δ-measurement are indicative for the values of the near-field and far-field disturbances of the model sting.

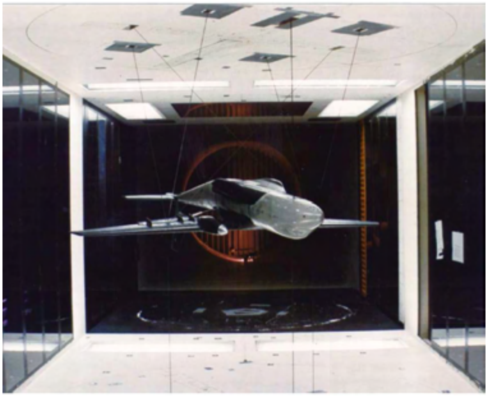

(a)

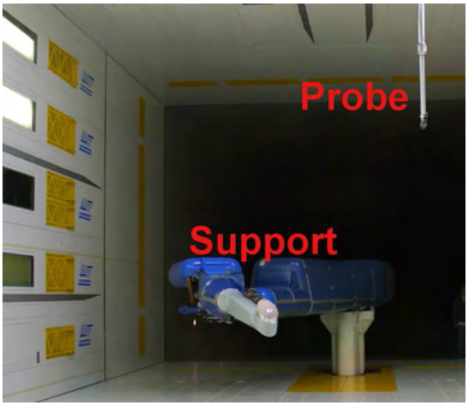

(b)

Figure 2.3: (a) Sting interference measurements on a typical turboprop aircraft in the LST of DNW using a wire-mounted model (b) The 6-hole probe setup in the LLF of DNW to measure the far-field disturbance effects of the remaining support structure. The 6-hole probe is attached to the ceiling thereby enabling the measurement of the flow disturbances for a ventral setup

Measuring the disturbances of the remaining support structure

The far-field disturbance effects of the remaining support structure (parts 2, 3 and 4 in Figure 2.1) are measured in the LLF [1]. An example of the measurement setup is given in Figure 2.3(b). Measurements involve employing a dedicated 6-hole probe. The support structure (without model sting and model) is moved in a similar way as if regular measurements take place. For the measurements, the 6-hole probe is positioned to specific points representing the location of the aircraft nose, tail, wing and stabilizer. The results of these measurements indicate the disturbances of the support structure on local angle of attack, angle of sideslip and dynamic pressure. These disturbances are translated to offsets in the values of the aerodynamic coefficients (using for instance Equation set (A.2) and adding additional disturbance corrections for the tail based on local disturbances in α, β and q. A buoyancy correction is also deduced from the results). One aspect of this measurement could raise particular concern: the end effects

[1] Instead of measurements, less intrusive methods can be adopted to calculate the far-field effects of the support structure, for example by performing calculations. RaNS calculations are performed on several angles of attack and angles of sideslip of the support structure. At the location of model specific points (the model nose, certain spanwise wing positions and model tail), the disturbances are calculated. Validation of the results of these calculations leads to the conclusions that the far-field effects are calculated to within measurement accuracy of the dedicated 6-hole probe for locations at the nose and wings of the aircraft configuration. For evaluation points close to the support (at the tail of the aircraft configuration) the RaNS calculations perform poorly according to Horsten [38]

of the horizontal sting. Because no vertical sting is included in the measurements, end effects such as excessive separation of the horizontal sting exist that affect the probe measurements. In order to reduce these effects, the horizontal sting is provided a fairing. The absolute value of the resulting end effect is however not evaluated.

Recombining the disturbances

Support corrections resulting from the separate determination and recombination method as proposed in this section can be compared to the results of Δ-measurements on the setup shown in Figure 2.2. Results of such a comparison are given in Figures 2.4 and 2.5 for corrections of dorsal- and ventral setups on both longitudinal coefficients (lift-coefficient C_L, drag-coefficient C_D and pitching moment-coefficient C_m) and lateral coefficients (side force-coefficient C_Y, rolling moment-coefficient C_l and yawing moment-coefficient C_n). The configuration of interest is a clean (no flap/control surface deflections) tail-on configuration.

Although no interference effects between the model sting and the rest of the support structure are included in the "break down" method, the corrections are very similar according to Figure 2.4 and 2.5. The most significant differences between the corrections (e.g. for the pitching moment) are attributed to the fact that two different wind tunnels are utilized in the measurements and that the wind tunnel model used in the LST is not completely geometrically identical to the model used in the LLF (the LST model is more simplified).

From these results it is concluded that the order of magnitude and the nature of the support correction is not influenced when educated choices are made for the break down of the support structure in parts that are separately analyzable. Considering the complex support setup of the validation case, the author believes that these results can be generalized to all support setups where the mutual interference between the support parts is minimized. This conclusion provides the starting point of the current research: the study on model sting interference.

2.3 Starting the study on sting interference

The model sting is responsible for causing both near-field and far-field effects on the wind tunnel model. This makes it an essential object of study. Because it is shown in the last section that the model sting can be decoupled from the rest of the support structure without compromising the order of magnitude and nature of its disturbance, the disturbance of the model sting can be studied separately. An advantage of this is that when research is performed on the model sting (both numerically and experimentally), the configuration of the remaining support structure attached to the model sting can be left unconsidered. This facilitates wind tunnel tests in various tunnels. It also enables the research results to be generalized to a wider class of support setups.

Model stings of various shapes exist such as bayonets, blade stings etc. For the current research a model sting is selected that is used in typical low-speed wind tunnel tests where the wind tunnel models contain an internal balance. The design of such a model

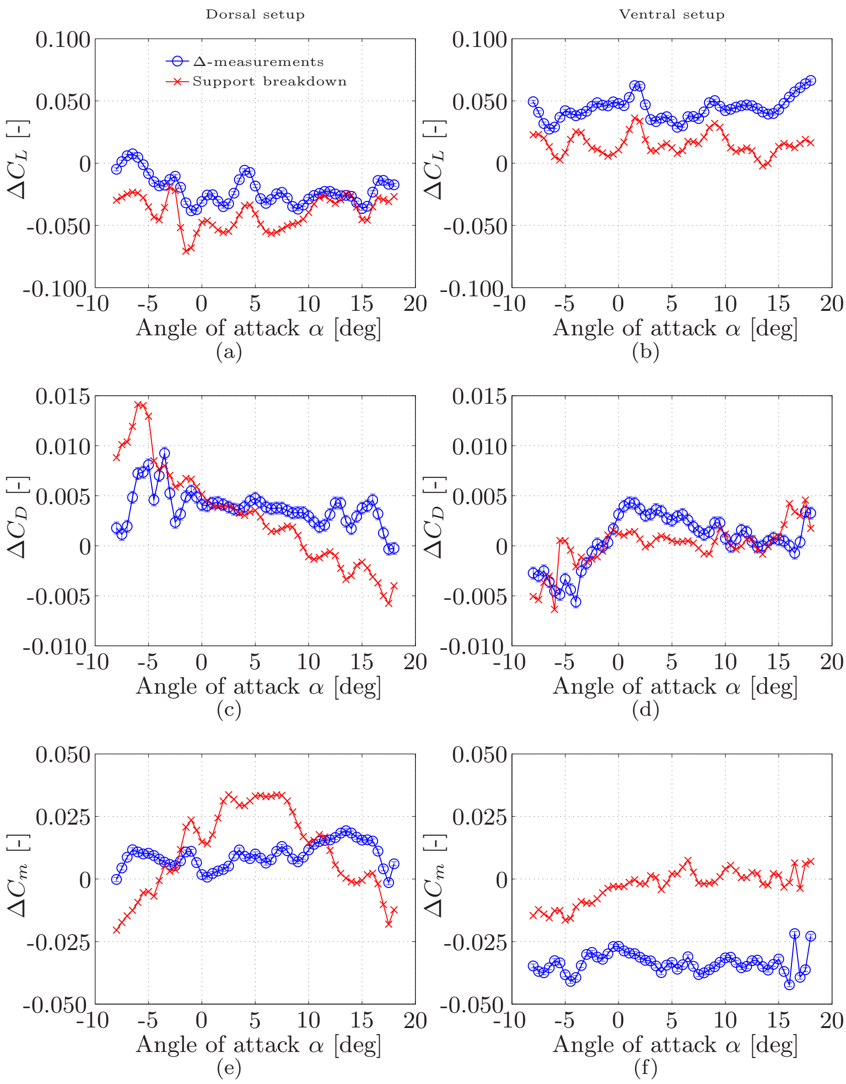

Figure 2.4: A comparison of corrections for the dorsal- and ventral setup of the configuration shown in Figure 2.2: Δ-measurements are compared to the recombined corrections for the various support parts. Corrections shown are for the longitudinal coefficients

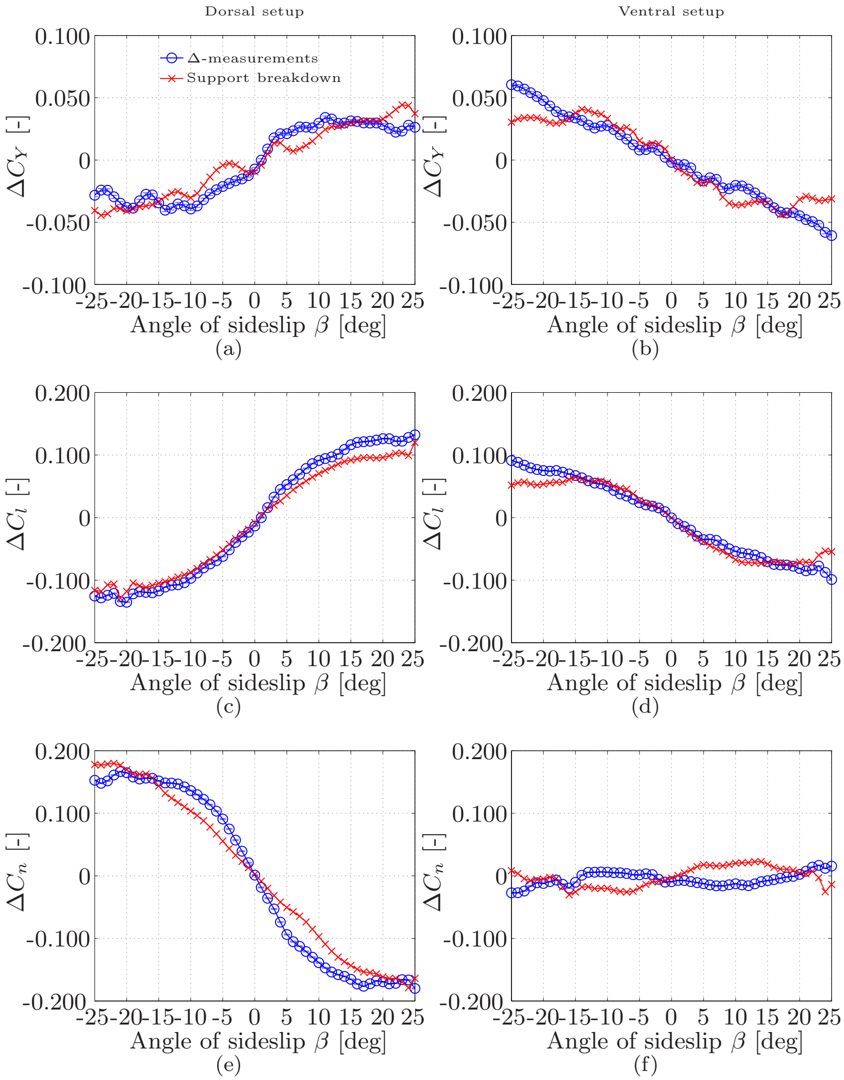

Figure 2.5: The same as shown in Figure 2.4 but now for the lateral coefficients

sting is based on typical support design rules pointed out by Eckert et al. [37]. The choice on the model sting as a starting point for further research is explained in the next section.

2.4 Choosing a representative model sting for further study

According to Eckert et al. [37], designing a support arrangement means looking for the best compromise in fulfilling two main requirements:

1. Safe mechanical bearing of the model without oscillations that could disturb the flow and complicate the measurement,
2. No disturbance of the model flow field by support effects in a non-correctable way.

The second requirement indicates that no direct influence of support solid volumes and support wakes should occur on the model parts of main interest during a wind tunnel test: neither the boundary layer condition (laminar, turbulent or separated) nor vortex structures may be essentially changed at these model parts. Eckert et al. state that experience with various low-speed models has led to a few basic rules for the design of model supports that reduce the amount of interference:

- No intrusion of support parts into the boundary layer of a high-lift wing is allowed,
- Intrusion of the fuselage boundary layer by a model sting is preferred at the cylindrical part of the model,
- The cross section of the model sting should be as small as possible (as small as safe mechanical bearing allows),
- The distance of the support elements to the model should be as large as stiffness of construction allows,
- Different support arrangements with the same model are encouraged for different types of investigations.

Focusing on the model sting it is seen that its design is governed by practical considerations and considerations that lead to the reduction of its interference on the model flow field. An exemplary cross-section of a model sting used in low-speed (powered) wind tunnel tests on models accommodating an internal balance is given in Figure 2.6.

It is seen in Figure 2.6 that such a typical model sting resembles a truncated symmetric wing profile. Reasons for this include:

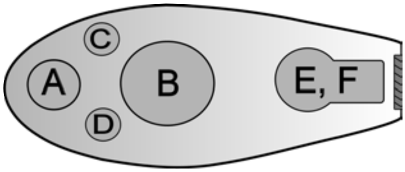

Figure 2.6: An exemplary cross-sectional shape of a model sting used for low-speed (powered) wind tunnel tests on models accommodating an internal balance

- In order to minimize the disturbances, streamlined model stings are recommendable thereby keeping the thickness of the model sting at bay. The sting should however be capable of carrying the loads from the model attached to it. This necessitates a certain sting thickness. Besides this, model stings are ideal for the transfer- and housing of e.g. compressed air and/or hydraulics, instrumentation cabling and reference pressure tubes to and from the model as shown in Figure 2.6. This is facilitated by a certain sting thickness as well,
- Truncating the profile is recommendable for the following reasons:
  - Because the model sting cross-section behaves as a 2D wing profile, angles of sideslip will induce large side-forces at the model sting posing constraints on its structural design. This side force is minimized by truncating the profile,
  - To avoid large wake variations at angles of sideslip. These wake variations are expressed in a large sidewash interference of the model sting as described by Eckert et al. [37].

The model sting used for further study on interference effects is based on the model sting presented by Eckert et al. [37]. It is representative for typical low-speed (powered) measurements on aircraft configurations. It concerns a truncated RA-28-Y profile according to Goedegebuure [39]. Measurements described by Eckert et al. [37] indicate an optimal truncation of 65% of the wing profile as investigated using a 5-hole probe to study the wake. The effect of boundary layer transition on the flow behavior around the model sting is also assessed: tripping the flow with zig-zag tape results in a more 2D flow pattern. At angles of sideslip it is seen that tripping delays the upstream movement of boundary layer separation points.

A tripped 65% truncated RA-28-Y profile (with a typical shape as shown in Figure 2.6) is used for research presented in this thesis on model sting disturbances where the models accommodate an internal balance.

2.5 Summary

In this chapter a starting point for the study on the fundamentals of low-speed model support interference on sting mounted models accommodating internal balances is given: the model sting. Focusing on the sting is justified by a support break down that facilitates the treatment of disturbances of individual support parts spanning a certain support structure. This break down should be such that the support members spanning a particular part deliver the same type of disturbance (near-field or far-field) and can be determined by the same method. A proof of concept is given by analyzing measurement results of DNW. It seems that the order of magnitude and the nature of the disturbances are not compromised when this approach is adopted provided that the amount of separate parts is kept to a minimum. This approach enables the study on the disturbances of the model sting alone, the support member protruding the fuselage. The model sting is an essential object for further study as it causes the complete spectrum of disturbances (both near-field and far-field). Besides practical advantages another advantage of studying the sting is the possibility to generalize the research results to a wider class of support structures.

The sting is a crucial starting point for further research on model support interference. It allows a qualitative analysis on the nature of near-field and far-field effects but also a qualitative and quantitative validation of several methods applied to determine the interference. As a starting point "exploratory" measurements and calculations are performed on model sting interference assessing the complexity of the interference field. Their results are presented in the next chapter.

Chapter 3

Exploratory Work on Model Sting Interference

In this chapter the complexity of the sting interference field is addressed by exploratory numerical and experimental analyses. Besides the need to create an experimental and numerical data base for the tuning of calculations and validation of numerical techniques, these exploratory measurements and calculations on model sting near-field and far-field effects answer the following question:

"Is it justified (from the viewpoint of accuracy) to determine model sting near-field and far-field effects using methods at low levels of complexity and intrinsic accuracy without knowing the specific details of a possibly complex interference flow field?"

This question aims at identifying low-cost computational methods for the determination of model sting interference implementable in the expert system once labeled as "good enough" (meaning to within accuracy requirements).

Comparing the results of the exploratory analyses it is concluded that it is not justified to implement these type of calculations (such as panel code and Euler calculations) for determining model sting disturbances to within measurement accuracy. Significant calculation offsets (out of the bounds of experimental accuracy) are caused by unknown characteristics of the interference flow field. The limitations of such calculations are only truly understood if an in depth understanding of the flow field is created. To this end Navier-Stokes calculations must be carried out.

3.1 Introduction: complex physics

3.1.1 Characteristics of juncture flow

Observing a typical model sting setup as shown in Figure 1.6(a) it can be noted that the interference flow field might show considerable agreements with the well known "juncture flow". Juncture flow occurs when a boundary layer encounters an obstacle that is attached to the same surface. Examples where this type of flow is found are: the encounter of water and bridge pillars at the bottom of rivers, the attachment of a boat keel to its hull, the attachment of the wing to an aircraft fuselage and last but not least, the attachment of a model support to a model in a wind tunnel. On the whole several components are present in the description of a juncture flow (see also Figure 3.1):

1. A base body: the viscous flow over a base body is considered. On this body a laminar or turbulent boundary layer develops. In most experimental and numerical work on juncture flow, a flat plate is taken for this base body,

2. An appendage attached to the base body: although in real life a wide variety exists in the shape of these bodies, the most frequently reported appendages in experimental and numerical aerodynamics are:

    - The famous "Rood" wing (Sung et al. [40], Devenport et al. [41], [42], [43], [44], Ölçmen et al. [45], Apsley et al. [46], Khan et al. [47], Jones et al. [48], Paciorri et al. [49]). This wing is named after its designer E.P. Rood. It consists of a 3:2 elliptical nose joined to a NACA 0020 profile at its maximum thickness,
    - The NACA 0020 wing profile (Sung et al. [40], Dickinson [50]),
    - The NACA 0015 wing profile (Bernstein et al. [51], [52], van Oudheusden et al [53]),
    - The NACA 0012 wing profile (Kubendran et al. [54], [55], Green et al. [56]),
    - A cylinder (Seal et al. [57], Constantinescu et al. [58], Pattenden et al. [59]),
    - A custom designed airfoil (Shabaka et al. [60], Mehta [61], Kubendran et al. [54], Peirce et al. [62]).

As shown by above references, both numerical and experimental work are performed on base bodies with laminar or turbulent boundary layers in order to understand the physics of juncture flows. On the whole the general consensus from literature is that juncture flow is dominated by a couple of phenomena (Figure 3.1): close to the actual juncture, the incoming two-dimensional boundary layer is transformed into a highly skewed three-dimensional boundary layer being forced around the juncture. In the region in front of the juncture nose, the flow is dominated by flow separation lines trailing along the juncture downstream. The flow is separated by the action of an adverse pressure gradient caused by the presence of the obstacle. The separation lines near the leading edge allow the rotated spanwise vorticity (rotated in streamwise direction due to the boundary layer skew and spanwise pressure gradients) to be concentrated into horseshoe vortices that trail downstream around the juncture. These horseshoe vortices determine to a great extent the flow properties in the juncture, especially the flow on the aft part where the position of flow separation on both base body and obstacle can change due to the position and the strength of the horseshoe vortices.

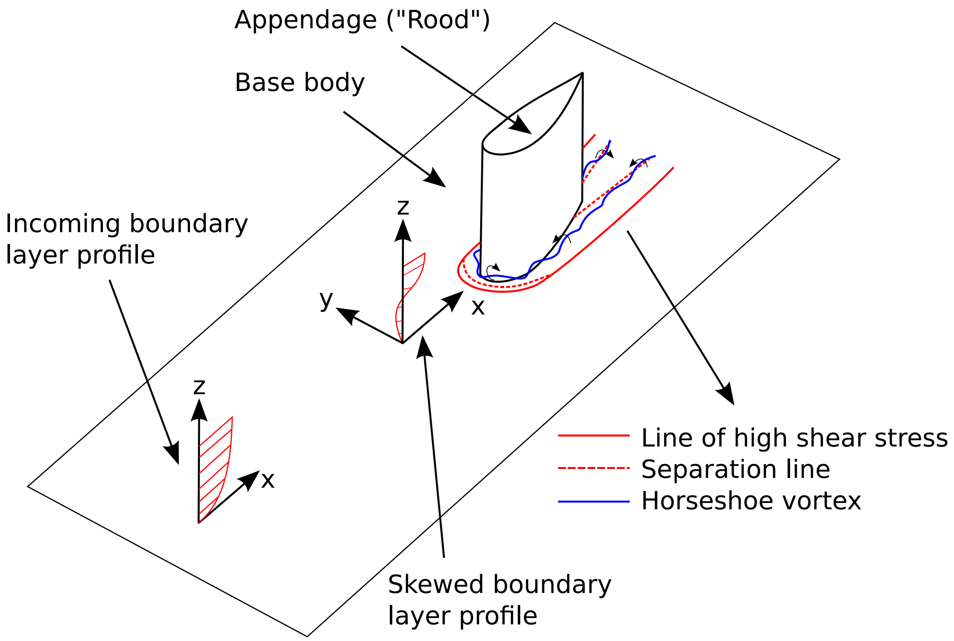

(a)

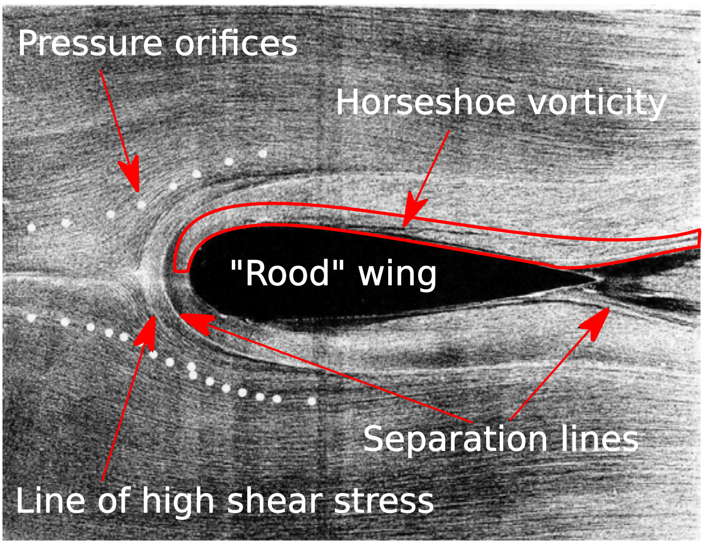

(b)

Figure 3.1: A typical example of a juncture flow field (around a "Rood" wing) (a) A schematic showing the most prominent features (b) A result from an experimental oil flow visualization (courtesy of Simpson ([63]))

The exact vorticity pattern in front of the juncture, the behavior of the vortices and the separation profile seem to be dependent on the flow Reynolds number. For laminar flow (for increasing Reynolds number), three types of behavior seem to establish according to Khan et al. [47]:

- A static system of vortices (only for very low Reynolds numbers),
- An oscillating system of vortices demonstrating highly unsteady flow,
- A shedding splitting system of vortices demonstrating highly unsteady flow.

In turbulent flow, highly unsteady behavior is detected as well, accompanied by high turbulence intensities, high heat transfer rates and high surface pressure fluctuations according to Simpson [63].

The exact juncture flow field characteristics are dependent on incoming boundary layer thickness and juncture angle of sweep as a measure for the "bluntness" of the obstacle. According to Bernstein et al. [51] some implications of this type of flow on the aerodynamic characteristics at the juncture are:

- The local lift of the appendage near the junction decreases,
- The local drag of the appendage near the junction increases.

Possible methods to reduce these effects aim at preventing flow separation in front of the juncture by means of applying a leading edge strake or fillet (e.g. Devenport et al. [44], Bernstein et al. [52] and Green et al. [56]) and by tempering the juncture flow disturbances by for instance boundary layer suction (e.g. Seal et al. [57]).

Because juncture flow is a very complex flow type and because of its many variants in practical engineering, it has been the subject of study for many years. Although the quality and variety of both experimental and numerical methods in analyzing the flow field has increased considerably during these years, juncture flow is still not fully understood. The extent of unsteadiness of the flow phenomena, the complex turbulent structures involved and the various dependencies of the flow field characteristics on e.g. Reynolds number, incoming boundary layer properties and juncture bluntness are the reason for this.

3.1.2 Classical juncture flow versus present configuration

The configuration of interest of the present study shows considerable agreements with the "conventional" juncture case. However the model sting penetrating a fuselage also shows three distinct geometrical differences:

1. The model sting does not have a sharp trailing edge but has a pronounced base,
2. A slit is present separating the base body (the fuselage) from the appendage (the sting),

3. An internal cavity in the fuselage (accommodating an internal balance) with an open connection (via the slit) to the freestream is present.

These differences might influence the topology of the near-field flow considerably from the turbulent juncture flow as frequently studied. It is therefore dangerous to solely rely on the results found for the juncture flow configuration and extrapolate these to some extent to the configuration of interest. This means that a new study on the sting disturbances is inevitable.

A study into the disturbance behavior of the sting necessitates the generation of a data base containing information on the magnitude of its disturbances. This information can be used for both calculation tuning and for validation purposes. To this end measurements are performed on model sting interference. Their setup and results are presented in this chapter. Besides these measurements, panel code- and Euler calculations are performed in order to answer the following question:

"Is it justified (from the viewpoint of accuracy) to determine model sting near-field and far-field effects using methods at low levels of complexity and intrinsic accuracy without knowing the specific details of a possibly complex interference flow field?"

This question aims at identifying low-cost computational methods for the determination of model sting interference that might be implementable in the expert system once labeled as "good enough" (implying to within accuracy requirements). The setup and results of these calculations are also discussed in this chapter.

Results of measurements and calculations reveal necessary subsequent steps in the analysis of model sting disturbances. Because of this, the measurements and calculations in this chapter are considered as "exploratory".

Experimental- and numerical results on model support interference presented in this and the following chapters focus only on the primary support disturbances.

3.2 Measuring model sting disturbances

The exploratory measurements are based on a typical model sting setup commonly applied in the LLF of DNW and simulate the measurements of an aircraft fuselage mounted with a ventral sting to the remaining support structure (horizontal sting, torpedo and sword schematized in Figure 2.1). The forces and moments on such configurations are measured by an internal balance (a type of balance frequently used nowadays). The wind tunnel facility, model and measurement equipment used for these measurements are described in the following sections.

3.2.1 The wind tunnel facility

The exploratory measurements are carried out in the Low Turbulence Tunnel (LTT) of Delft University of Technology. A schematic of this facility is given in Figure 3.2.

Table 3.1 gives a short description of the properties of this facility.

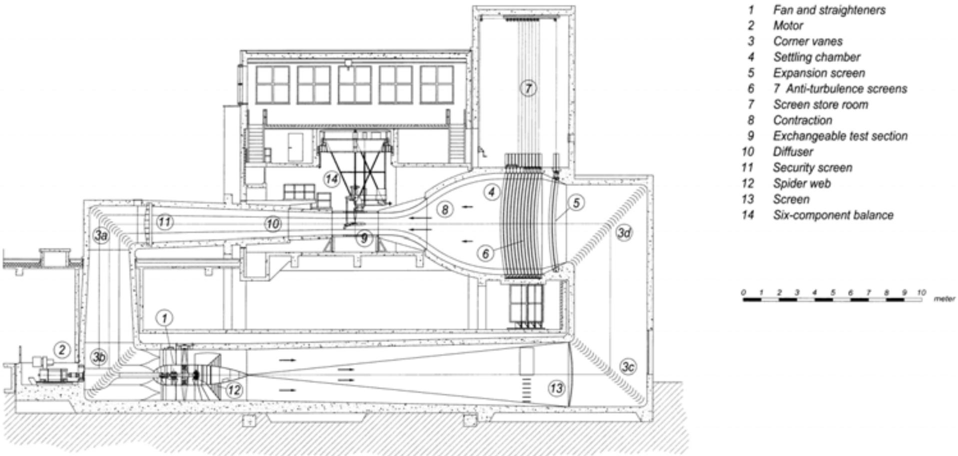

Figure 3.2: The Low Turbulence Tunnel (LTT) of Delft University of Technology (DUT) used for the exploratory measurements on model sting interference

Table 3.1: Description of main properties of the LTT of DUT used for the exploratory measurements on model sting interference

Parameter	**Value**
Type	Closed-throat, single return
Engine power	525 [kW]
Contraction-ratio	1:17.8
Test section cross-sectional shape	Octagonal
Test section dimensions (W x H x L)	1.80 x 1.25 x 2.60 [m]
Maximum test section velocity	120 [m/s]
Maximum Reynolds number for 2D testing	3.5×10^6
Turbulence level	0.015% - 0.07% (20 - 75 [m/s])

3.2.2 The wind tunnel model

In Figure 3.3 the test setup of the exploratory measurements is shown.

In the test section of the LTT a body resembling a generalized aircraft fuselage is mounted to the external balance system of the wind tunnel positioned above the test section by means of two struts. This external balance system enables angle of attack changes during measurements. The front “Y-shaped” strut is attached to a pivot point in the model. Up- and down movement of the back strut provides a rotation of the

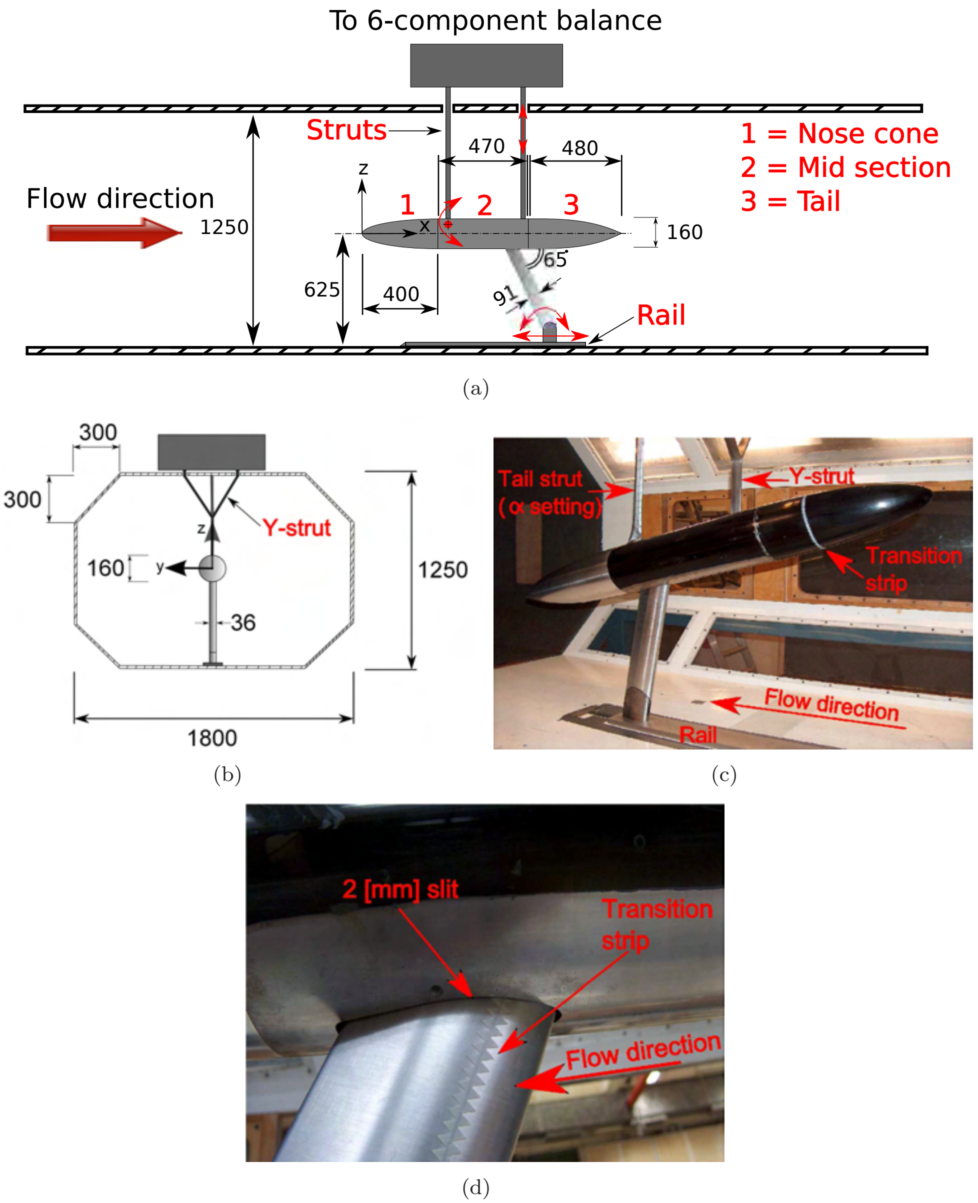

Figure 3.3: Layout and dimensions of the experimental setup in the LTT of DUT. Dimensions are in [mm]. (a) Schematic side view of the test setup. The degrees of freedom of the model are indicated (b) Schematic front view of the test setup (c) 3D view of the test setup (d) A close-up of the experimental setup near the protrusion of model sting and fuselage

model about this pivot point thereby controlling the angle of attack. The back strut is wound by a copper wire to decrease the amount of vortex shedding from this strut and terminate oscillatory motion of the model. The model under consideration is an axi-symmetrical fuselage of length 1.35 [m] and maximum diameter of 0.16 [m] (at the cylindrical part). It consists of a nose cone of length 0.40 [m], a cylindrical section of length 0.47 [m] and an ogive shaped tail of length 0.48 [m]. The coordinates of the nose cone are described by:

$$\begin{aligned} &0 \leq x \leq 400, \\ &z = 80\sqrt{1 - \left(\frac{400 - x}{400}\right)^2}, \end{aligned} \tag{3.1}$$

where the coordinates are given from the model nose in [mm]. For the after-body (that has a length/diameter ratio comparable to a Do-328 aircraft) the following can be written (coordinates are once again given from the model nose in [mm]):

$$\begin{aligned} &870 \leq x \leq 1350, \\ &z = 80\left(1 - \left(\frac{x - 870}{480}\right)^3\right). \end{aligned} \tag{3.2}$$

The boundary layer on the fuselage is tripped at 20% of the body length on the nose cone by a zig-zag tape of 0.32 [mm] thickness. Using Braslow's method it is calculated that at a reference speed of 40 [m/s] the boundary layer is tripped (according to Veldhuis [12]).

The model sting under consideration serves as a dummy support member during these measurements. Because forces and moments are measured using the external balance system the model sting is detached from the fuselage. An opening is machined into the hollow fuselage at the bottom side into which the dummy sting is inserted. The sting is only attached to the test section floor. Note that the support and fuselage remain separated by a slit as if the forces and moments would be measured by means of an internal balance. This slit has a width of 2 [mm]. The slit width is scaled down from a DNW measurement (at similar Mach number) on a typical large transport aircraft. It is based on the requirement that considering the bending of the model support under high loads (e.g. maximum lift), the sting and model are not allowed to connect. Angle of attack changes of the dummy sting are performed manually using a hinge at the support mount to the test section floor. This hinge is also free to translate in upstream and downstream direction along a small rail. This enables the sting to penetrate the fuselage at the right location and with the right angle relative to the model. The model sting is inserted into the fuselage at 54% of the body length measured from the nose of the model into the cylindrical part. The angle of the support trailing edge with the fuselage longitudinal axis is 65°. The placement and orientation of the sting in the model are chosen according to Veldhuis [12].

A schematic drawing of the model sting cross-section is given in Figure 3.4. The sting has an airfoil shaped cross-section. It resembles an RA-28-Y profile cutoff at 65% of the chord as discussed in section 2.4. The sting has a chord of 91 [mm], a maximum thickness of 36 [mm] and a base width of 17 [mm]. The trailing edges of the support are not sharp but rounded off with a radius of 3 [mm]. Zig-zag boundary layer transition strips with a thickness of 0.20 [mm] are applied at the quarter chord line of the model support.

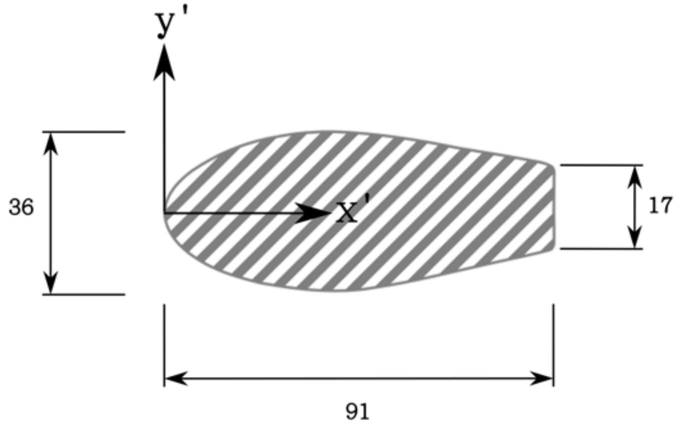

x'	y'
0.00	0.00
1.37	4.36
5.74	8.38
11.72	11.96
17.70	14.36
23.68	16.03
29.67	17.11
35.65	17.71
41.63	17.92
47.61	17.59
53.59	16.51
64.35	14.14
76.32	11.47
88.28	8.80
90.67	0.00

Figure 3.4: A schematic drawing of the RA-28-Y based model sting cross-section. Coordinates are in [mm]

3.2.3 Type of measurements performed

The setup discussed in the previous section is used to measure the near-field and far-field disturbances of the dummy model sting by means of a Δ-measurement:

- The near-field effects are measured on the fuselage using the external balance. At a certain angle of attack (no angles of sideslip are considered) the forces on the fuselage are measured using the external balance both including- and excluding the presence of the dummy sting. When the dummy sting is removed from the setup, the resulting gap in the fuselage is closed by a filling cap. After minor solid- and wake blockage corrections of the sting the subtraction of the measurement results provides the model sting near-field effects expressed in disturbances on the lift-, drag- and pitching moment-coefficients of the fuselage (the pitching moment is measured with respect to the pivot point of the model/attachment point of the front Y-strut). It is assumed that the struts connecting the fuselage to the external balance have a negligible influence on the disturbance ability of the dummy sting. Measurements are performed for an angle of attack range varying from -4 to 15° and at several freestream velocities of 40, 50, 60 and 80 [m/s] (or freestream Mach numbers of 0.119, 0.149, 0.179 and 0.237),

- The far-field disturbances of the sting are measured with a 5-hole probe. These disturbances manifest in changes of the local velocity vector at lifting surfaces (the buoyancy of the sting is negligible). In the setup, no lifting surfaces are present. On the whole this is not a problem as long as the disturbance ability of the model sting is not affected by the lifting surfaces (this would be the case when e.g. the sting would be positioned directly in the wake of the wing). Such setups are not considered here. This implies that the far-field effects of the model sting can be measured without the presence of the lifting surfaces at the location of the lifting surface's quarter- and three-quarter chord according to Eckert [18]. During the measurements, a volume near the fuselage is probed using a 5-hole probe (described in section 3.2.4) as shown by Luijendijk [8]. An impression of this volume relative to the fuselage is given in Figure 3.5. This volume covers a large range of wing configurations such as low-wing, mid-wing and high-wing but also wing placements from front placements to placements further to the rear of the fuselage. Measurements including and excluding (the remaining gap in the fuselage is closed with a cap) the dummy sting at $\alpha = 0$ [deg] and $V_\infty = 60$ [m/s] (or $M_\infty = 0.179$) are performed on the local values of angle of attack and dynamic pressure.

Characteristics of the external balance and dedicated 5-hole probe used to measure the model sting near-field- and far-field effects are described in the next section.

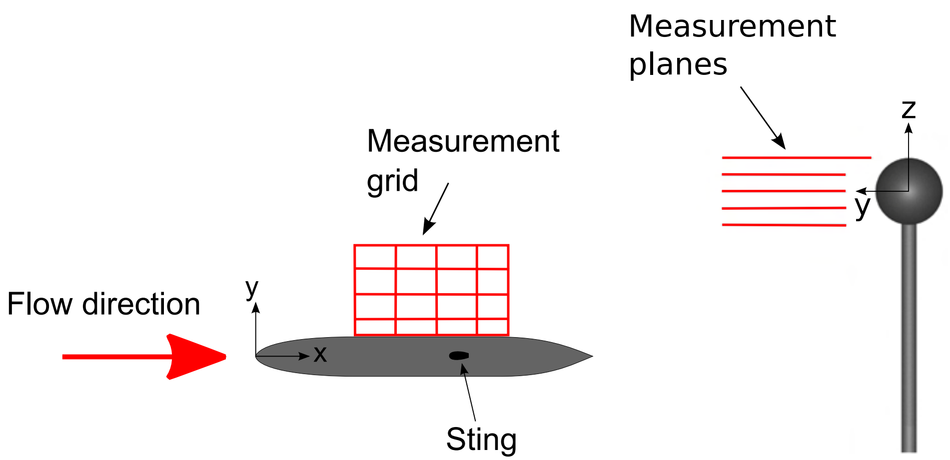

(a) (b)

Figure 3.5: 5-hole probe measurement grid relative to the fuselage (a) Top view (the position of sting entry at the fuselage is also indicated) (b) Front view

3.2.4 Description of measurement equipment

The external balance

The external balance used in the measurements of model sting near-field effects is a 6-component balance. The total forces and moments working on the model and struts in the test section are lead to six separate balances that are positioned on top of the tunnel. These mechanical balances are based on the “weighing arm principle” according to Dobbinga et al. [64]. Combining the balance readings leads to the aerodynamic forces and moments on the model and struts in the measurement axes system. Because Δ-measurements are carried out under the assumption that the effects of the dummy model sting on the struts are negligible, tare corrections on the latter do not need to be considered. The quality of the measurement is dictated by the governing accuracy of the balance system and uncertainties in the setup. These are quantified in lift- drag- and moment-counts and misalignment angles in degrees. The reference area and chord used to non-dimensionalize the forces and moments are based on a scaled DLR-ALVAST wing as described by Brodersen [65]). The accuracies and uncertainties of the balance measurement are given in Table 3.2.

Table 3.2: Accuracies and uncertainties of a Δ-measurement using the 6-component balance of the LTT of DUT

Parameter	**Value**
Wing reference area	0.15 [m^2]
Wing reference chord	0.14 [m]
Balance Δ-measurement accuracy: ΔC_L	$\pm$ 4 [counts]
Balance Δ-measurement accuracy: ΔC_D	$\pm$ 3 [counts]
Balance Δ-measurement accuracy: ΔC_m	$\pm$ 8 [counts]
Uncertainty in alignment of the model: α	$\pm$ 0.02 [deg]
Uncertainty in alignment of the model: β	$\pm$ 0.02 [deg]
Uncertainty in alignment of the sting	$\pm$ 0.02 [deg]

The 5-hole probe

5-hole probe measurements are carried out using a dedicated 5-hole probe with a conical head. The dimensions of the probe are given in Figure 3.6. To increase the accuracy of the 5-hole probe, it is re-calibrated before the actual measurement. A calibration sequence is implemented as proposed by Samuelsson [66]. The probe is calibrated for freestream velocities of 40 and 80 [m/s] for angles of attack and angles of sideslip ranging between -45 [deg] and 45 [deg]. An impression of the calibration setup is given in Figure 3.7(a). During the calibration, the angle of sideslip is changed using a turning table that is attached to the tunnel floor. The angle of attack of the probe is changed manually. At a given value of the angle of attack, angle of sideslip and freestream velocity, the pressures at the holes of the probe are measured using an electronic pressure transducer with a range of 1 [Psi] that is frequently calibrated during the measurements. The influence of Reynolds number variations on the calibration are negligible.

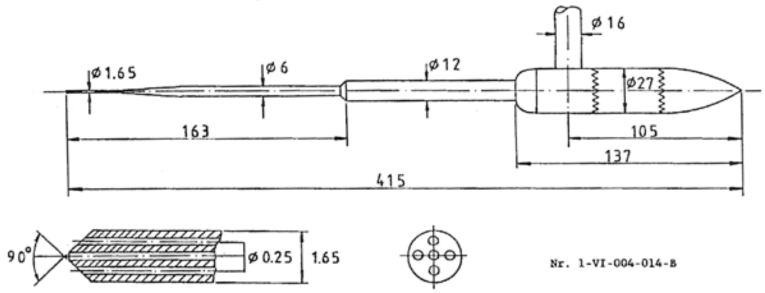

Figure 3.6: The dimensions (in [mm]) of the 5-hole probe used to determine the far-field model sting effects in the LTT of DUT

The calibration data is used during the actual measurements to determine the flow angles and velocity magnitude. An example of the measurement setup is given in Figures 3.7(b) and 3.7(c). The 5-hole probe is connected to three slender arms. Using these arms the angle of attack of the 5-hole probe can be adjusted such as to cause minimal interference of the setup with the fuselage. The angle of sideslip of the probe is adjusted by rotation around the vertically aligned rod directly connected to the probe. The back arm is fixed in a sledge that enables a translation of arms and probe as a whole in streamwise direction. This sledge is fixed to a rail in a slender horizontal beam enabling a transverse movement. This beam is located aft of the test section. It is connected to two vertically translating beams outside the test section that enable a vertical movement of the probe. These degrees of freedom enable a traverse of the 5-hole probe in a volume spanning a wing configuration with a fixed angle of attack and angle of sideslip of the probe. Accuracies and uncertainties of the probe Δ-measurement are given in Table 3.3.

Table 3.3: Accuracies and uncertainties of a Δ-measurement using the 5-hole probe in the LTT of DUT

Parameter	**Value**
Probe absolute accuracy: $\Delta\alpha$	$\pm$ 0.10 [deg]
Probe absolute accuracy: $\Delta\beta$	$\pm$ 0.10 [deg]
Probe absolute accuracy: $\frac{\Delta q}{q_\infty}$	$\pm$ 0.6 [%]
Probe repeatability: $\Delta\alpha$	$\pm$ 0.02 [deg]
Probe repeatability: $\Delta\beta$	$\pm$ 0.02 [deg]
Probe repeatability: $\frac{\Delta q}{q_\infty}$	$\pm$ 0.0 [%]
Uncertainty in alignment of the probe: α	$\pm$ 0.02 [deg]
Uncertainty in alignment of the probe: β	$\pm$ 0.02 [deg]

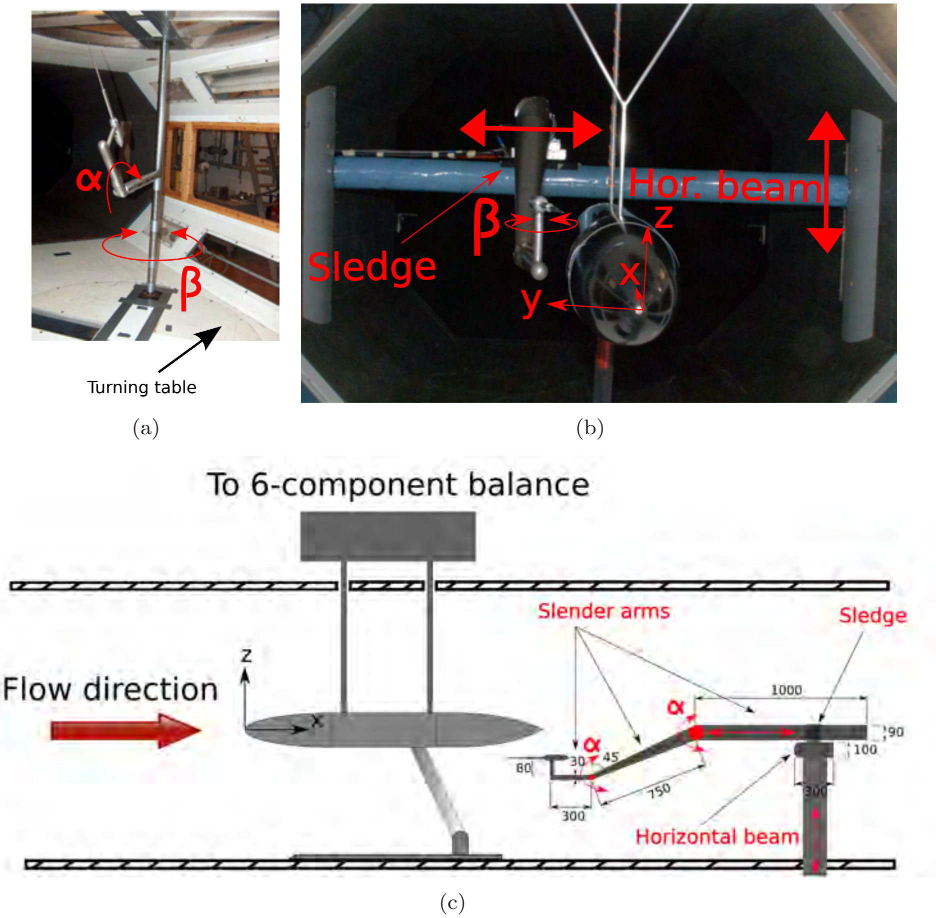

Figure 3.7: (a) The calibration setup of the 5-hole probe (b) A 3D-view of the measurement setup of the 5-hole probe used to measure model sting far-field effects in the LTT of DUT. In the figure, the degrees of freedom of the probe are indicated (c) A 2D (xz)-view of the measurement setup. In the picture the degrees of freedom of the 5-hole probe are included

In the next sections, the setup of the exploratory calculations is discussed.

3.3 Calculating model sting disturbances

Exploratory panel code calculations and Euler calculations are performed. These are calculations at low levels of complexity and intrinsic accuracy. It is recognized that the near-field of the model sting might be governed qualitatively by complex vorticity- and viscosity dominated phenomena. These phenomena (that are not resolved by the exploratory calculations) do not necessarily have a large quantitative influence on the values of near-field and far-field effects. The question that therefore arises is whether or not the exploratory calculations are justified from the viewpoint of accuracy without knowing the specific details of a possibly complex interference flow field. In the light of the expert system, identifying such methods leads to a considerable gain because the amount of costs for the determination of support interference can be reduced significantly (similar methods might be incorporated in the expert system without taking the risk of initiating calculations that are expensive from a computational point of view while unnecessary).

3.3.1 Panel code calculations

Panel code Δ-calculations are performed on a 3-dimensional representation of the fuselage, model sting and extended LTT test section (extended in order to guarantee the integrity of the inflow and outflow boundary conditions). The most important restrictions of these calculations are that they are applicable to incompressible ($M_\infty \leq 0.30$), inviscid and irrotational flows.

According to the concept of a Δ-calculation, two calculations are necessary at every freestream condition: one calculation includes the model sting and one calculation excludes the sting. In the calculations including the sting, the model sting is attached to the fuselage. The fuselage does not contain an internal balance cavity and slit. This is not possible from the viewpoint of numerical stability. This will however enable an assessment of significance of the disturbances induced by the internal cavity and slit when compared to the results of for instance Euler calculations where the internal cavity and the slit are modeled. The struts connected to the external balance are not modeled. In the calculation excluding the sting the fuselage is represented as a closed axi-symmetrical body. An impression of the computational domain is given in Figure 3.8.

The panel code calculations are performed using the commercial code $VSAERO^{TM}$ [67]. This program calculates the steady disturbance potential on all the panels spanning the geometry applying Green's Theorem to Laplace's differential equation for irrotational and incompressible flows. The position and distribution of panel collocation points depends on the type of panels used. In the current calculations both trilateral and quadrilateral panels are used in order to best represent the geometry of the fuselage and sting and thus increase the modeling accuracy (Figure 3.8(b)). The value of the disturbance potential over the panels is constant: VSAERO is a 0^{th} order method implying that the contribution of the linear and higher order terms of both the potential as the normal velocity at the collocation points can be neglected compared to the constant term. Boundary conditions enforced on the domain consist of:

1. Normal velocities are prescribed at the domain inlet. This velocity equals the freestream value. At the outlet, the normal direction is indicated whereas the velocity is calculated by the code such as to maintain conservation of mass in the computational domain,

2. Normal velocities are prescribed at the backside of the sting thereby prescribing a closing wake (as shown in Figure 3.9(a)). The flow separates at the sting trailing edge leading to a wake with a low velocity magnitude. The calculated afterbody

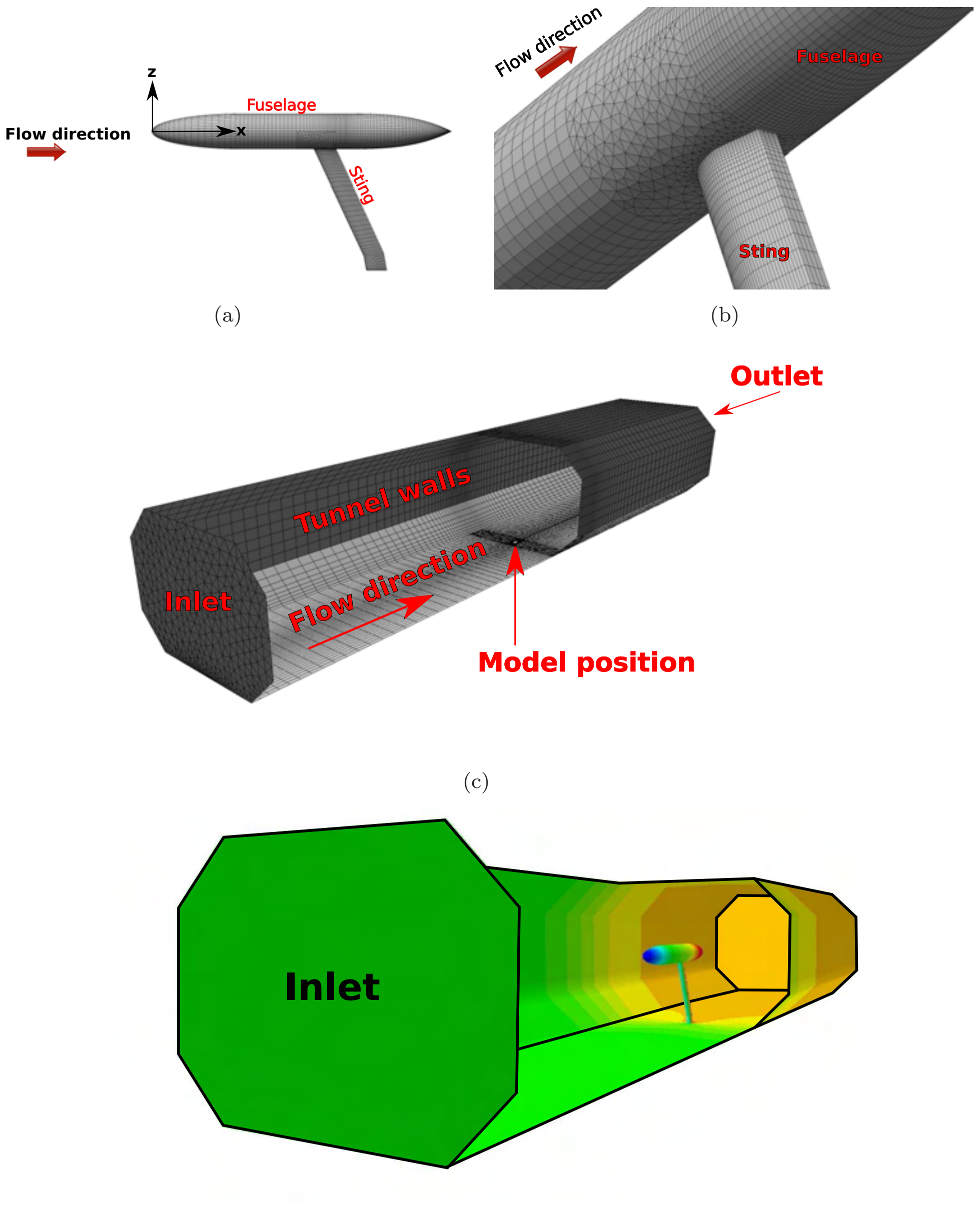

(a) (b)

(c)

(d)

Figure 3.8: An impression of the computational domain and panel-distribution applied in the exploratory panel code calculations (a) Side view of the fuselage including model sting (b) Perspective view showing the sting back and fuselage afterbody (c) Perspective view of the wind tunnel (a cut out is shown) indicating the model position (the model is not shown here) (d) The complete picture showing a cut out of the wind tunnel with the model installed. Contours of disturbance potential are shown for clarity

pressure distribution is matched to the measured results of Veldhuis [12] by means of tuning this boundary condition,

3. At the trailing edge of the fuselage the Kutta condition is enforced by placing a closed separation wake [68]. In this wake, the doublet distribution μ_w is linear in streamwise direction. The gradient is based on the velocity difference across the wake (as shown in Figure 3.9(b)). It is assumed that the velocity inside the wake is zero and outside the wake equal to the freestream value. The placement of the wake is based on experimental results by Veldhuis [12],

4. The tunnel walls, fuselage and sting are given the Neumann (flow tangency) boundary condition.

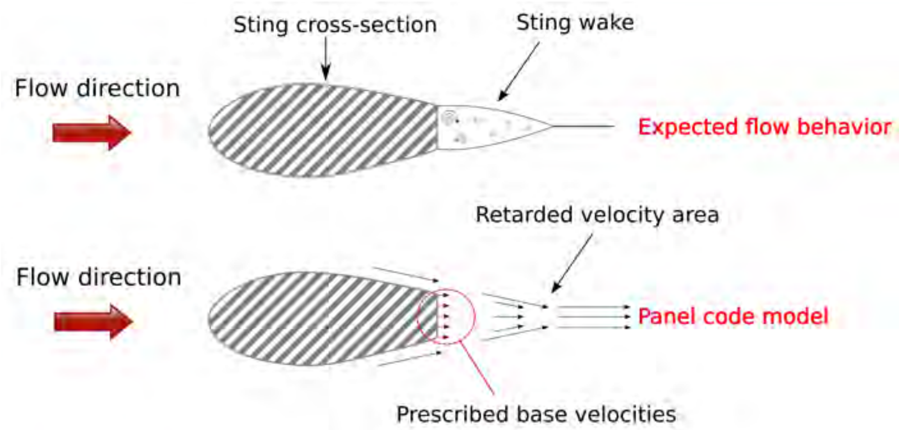

(a)

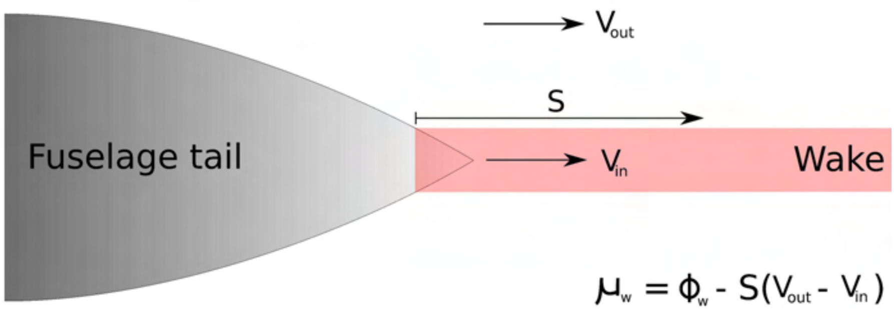

(b)

Figure 3.9: Examples of boundary conditions posed on the model fuselage and sting in the exploratory panel code calculations (a) Prescribing normal velocities at the sting back (b) Prescribing the Kutta condition by a closed separation wake at the fuselage tail

Δ-calculations at several angles of attack (0°, 4° and 8°) at zero sideslip and at a velocity of $V_\infty = 60$ [m/s] (or $M_\infty = 0.176$) are performed leading to the values of the near-field and far-field effects. Δ-calculations on the pressure integrals on the parts spanning the body lead to the value of the model sting near-field effects after minor solid- and wake blockage corrections. Δ-calculations on angle of attack and dynamic pressure at wing-specific points presented in section 3.4.2 lead to the values of model sting far-field effects. The results of these calculations are discussed in section 3.4.

3.3.2 Euler calculations

Euler calculations are restricted to inviscid flows whereas (contrary to panel code calculations) the fluid is also discretized. Δ-calculations are performed using an Euler model of the flow at the same freestream conditions as for the panel code calculations. Calculations are performed on a 3-dimensional representation of the test section, fuselage and model sting. In the calculations including the model sting, the balance cavity and slit are modeled (contrary to the panel model). This implies that the model sting is inserted into the fuselage's balance cavity without making contact to the fuselage shell. In the calculations excluding the model sting, the fuselage is modeled as a closed axi-symmetrical body. In both cases the struts attached to the external balance are excluded from the modeling. An impression of the computational domain is given in Figure 3.10.

The domain size chosen for the Euler calculations has a smaller streamwise extent than for the panel code calculations. This is caused by the fact that the choice of boundary condition treatment in the flow solver is much more divers. For all but the test section inlet and outlet planes, flow tangency is prescribed. The inlet is modeled as a mass-flow inlet (the variation of total pressure over the inlet plane matches typical 5-hole probe accuracy mentioned in Table 3.3) and the outlet is modeled as a pressure outlet (the air is modeled as an ideal gas). This choice proves to be particularly advantageous for convergence of the calculations.

The domains are meshed by an unstructured scheme using hexahedral elements. For this the commercial code $Hexpress^{TM}$ [69] is used. The cell density is increased in areas of interest where large gradients of flow field variables are expected (e.g. in front of the support near the fuselage). Considering the discretization of the sting wake, the following can be noted: when the "Euler-flow" at the sting side approaches the trailing edge of the sting it tries to "bend" around the trailing edge and create a stagnation point at the center of the sting trailing edge. When the trailing edge is sharp however (meaning that the angle between sting side at the trailing edge and sting base approaches 90°) this creates velocity gradients causing a substantial amount of artificial dissipation (as explained in more detail in section 4.4.3). This dissipation acts as "numerical viscosity". The dissipation does not only stabilize the calculation but also creates a flow pattern simulating separation at the sting trailing edge, recirculation of the flow aft of the trailing edge and an "Euler-wake" induced by the model sting. These phenomena are not with a completely physical background and dependent on the amount of dissipation (partly governed by the coefficients of the dissipation scheme).

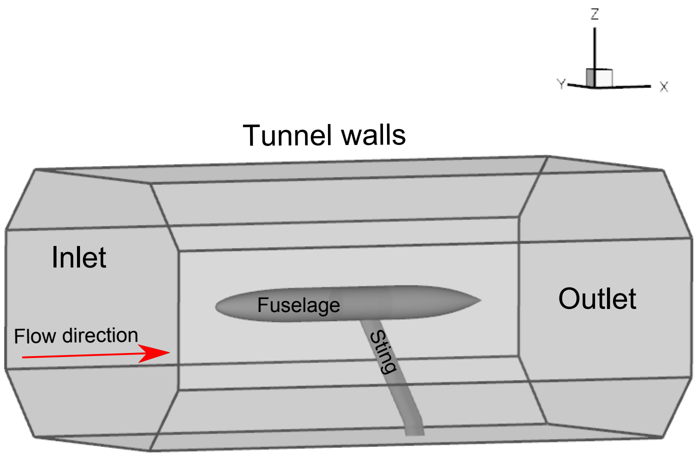

(a)

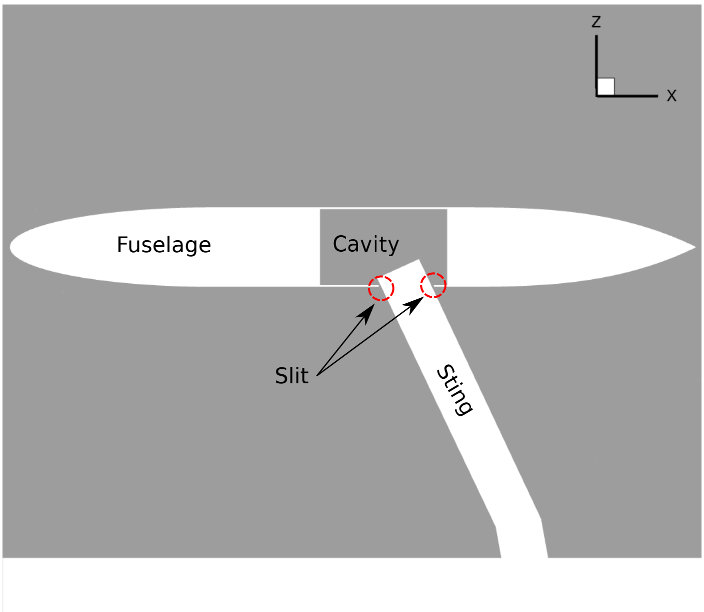

(b)

Figure 3.10: An impression of the computational domain used for the exploratory Euler calculations (a) A 3D view of wind tunnel and model (b) A longitudinal cross-section of the model (fuselage and sting) revealing typical features as internal cavity and slit

The commercial codes that are used in order to perform the calculations are $HexaNS^{TM}$ [70] and $FLUENT^{TM}$ [71]. HexaNS is used with both a second order upwind scheme (ROE) and a second order central scheme discretizing the governing equations describing the flow. The calculations in FLUENT use a second order upwind scheme. They are performed as a reference to the calculations performed by HexaNS.

For both panel code calculations and Euler calculations, errors caused by e.g. domain size and mesh density are evaluated by performing parametric studies. The resulting errors in the calculations presented are approximately one order of magnitude smaller than the balance accuracy given in Table 3.2. They are therefore regarded as insignificant.

Now that is explained how the exploratory measurements and calculations on model sting interference are setup, their results and comparison are discussed.

3.4 Measurements vs. calculations

3.4.1 Model sting near-field effects

The quantities ΔC_L, ΔC_D and ΔC_m provide an indication of the quantitative near-field effect of the model sting on the fuselage. The results of the balance measurements at $M_\infty = 0.179$ (or $V_\infty = 60$ [m/s]) are given in Figure 3.11. The trends shown comply to the trends found by Poole et al. [14]. These results are compared to the results of the panel code calculations and Euler calculations.

When the results in Figure 3.11 are considered, the following observations are made:

- From Figure 3.11(a), measurements indicate that the sting does not have a pronounced effect on the fuselage lift-coefficient. The pressure field on the body caused by the sting changes when the angle of attack is increased. This is due to the fact that the effective bluntness of the model sting increases (the mutual orientation of sting and fuselage does not change) thereby increasing its disturbance ability on the fuselage. The net quantitative effect on the lift-coefficient is however negligible. There is no discernible trend for the disturbance on the lift-coefficient within the measurement resolution. All calculations except the panel code calculation provide results within the accuracy bandwidth of the measurement,

- When the results of the interference on the drag-coefficient of the fuselage are considered (Figure 3.11(b)) it becomes clear that the sting does have a pronounced effect on the drag reaching beyond the balance accuracy (Table 3.2). The interference is more pronounced at lower angles of attack and increases the drag of the fuselage. When the angle of attack is increased the interference decreases until an angle of attack of approximately 10 [deg] is reached. At this angle, the interference is approximately zero. Increasing the angle of attack even more shows a decrease of the interference to negative values. None of the numerical methods applied is able to predict this interference to within balance accuracy. The trend

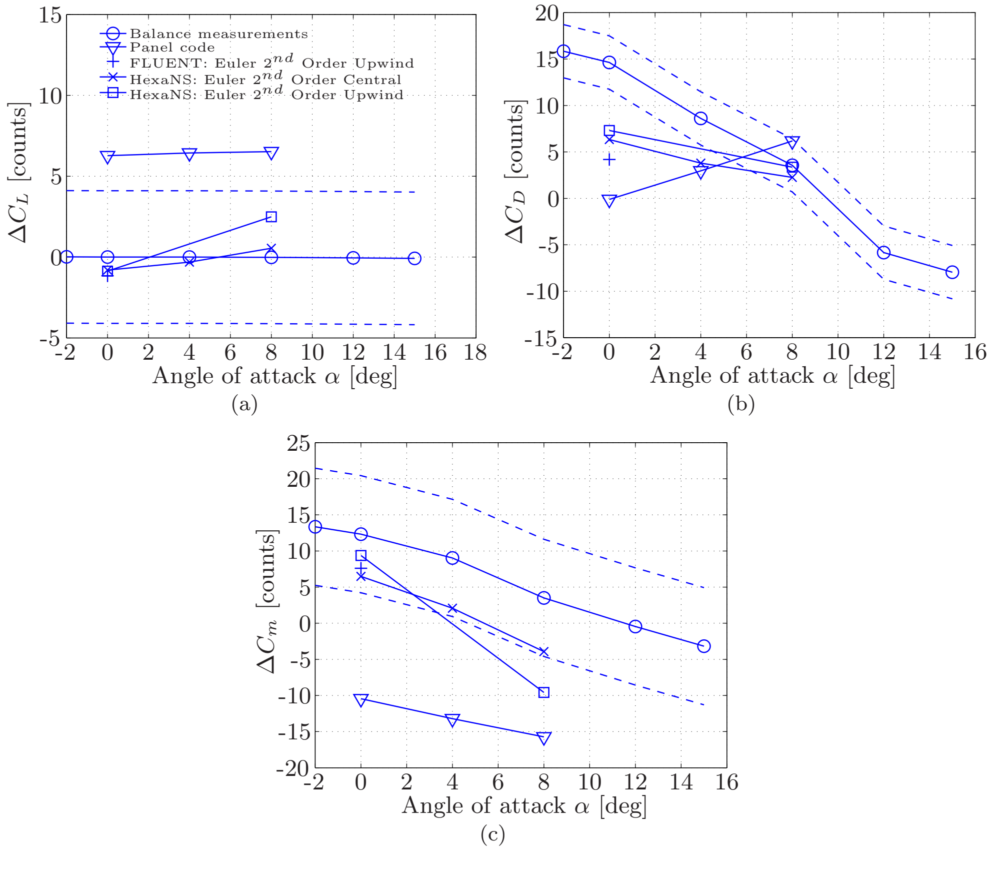

Figure 3.11: Measured and calculated model sting near-field effects on the (a) Lift-coefficient (b) Drag-coefficient (c) Pitching moment-coefficient on the fuselage shown in Figure 3.3 at $\beta = 0°$ and $M_\infty = 0.179$. The dashed line (– –) indicates the accuracy bandwidth of the measurements

calculated by the panel code is erroneous. The Euler calculations give the right trend, although the values of $\frac{\partial \Delta C_D}{\partial \alpha}$ are underestimated,

- Figure 3.11(c) shows the comparison of the measured and calculated pitching moment-coefficients. Measured trends are similar to the interference on the fuselage drag-coefficient. Allocating the interference on the pitching moment-coefficient to the interference on the drag-coefficient (thereby neglecting the lift-interference according to Figure 3.11(a)) it seems that the drag disturbance manifests at the backbody of the fuselage. To this end it is thought that the near-field interference is a local phenomenon. Although all the numerical methods seem to predict the right trend (not necessarily with a correct value of $\frac{\partial \Delta C_m}{\partial \alpha}$), the only method that is capable of calculating the interference to within balance accuracy is the Euler calculation, setup with a second order central scheme (the choice between a central- or an upwind scheme does not result in fundamental differences),

- Results in these graphs are discussed more extensively in Chapter 4.

The presented trends resemble results from tests performed at freestream velocities of 40, 50 and 80 [m/s] (freestream Mach numbers of $M_\infty = 0.119$, 0.149 and 0.237). Their results are closely related (same trends and order of magnitude) and show no distinct effects of Reynolds number variations. This is also found by Poole et al. [14] and Petterson et al. [4], [33]).

Conclusions that are drawn based on these results are:

1. Considering the fact that the Euler calculations predict the near-field effects with correct order of magnitude, it is concluded that the absolute value of the viscous near-field disturbance must be small for this configuration. This is in agreement with the findings of Veldhuis [12] where a similar placement of the model sting with respect to the body is considered,

2. Typical differences between the measurements and calculations fall outside the measurement accuracy. Referring back to Figure 3.11, it is seen that the panel code calculation is outperformed by the Euler calculation. The difference is a measure for the effects of vorticity and the disturbance effects of the internal cavity and slit. From the viewpoint of consistency this should also be noticeable in the calculation of the far-field disturbances: it is expected and shown that results of Euler calculations show a closer agreement with measurements than the panel code results. This is demonstrated in the next section.

3.4.2 Model sting far-field effects

The disturbance parameters indicating the value of model sting far-field effects are $\Delta\alpha$ and $\frac{\Delta q}{q_\infty}$. Experimental results revealing typical far-field effects are given in Figure 3.12 for the case $\alpha = 0°$ and $V_\infty = 60$ [m/s].

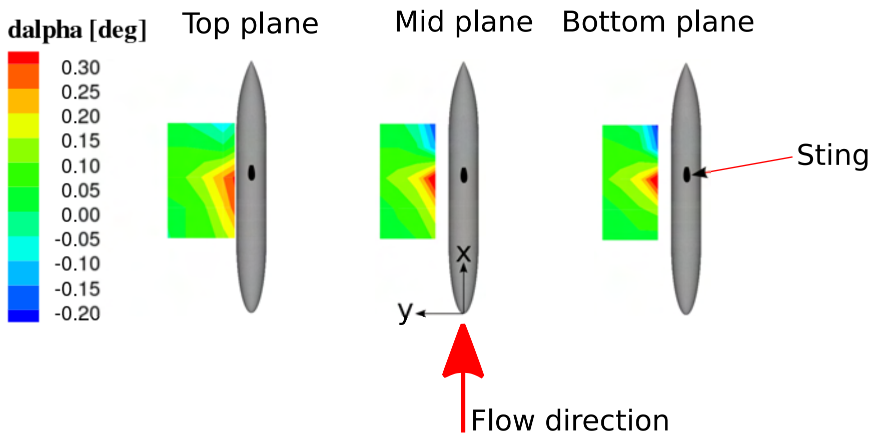

(a)

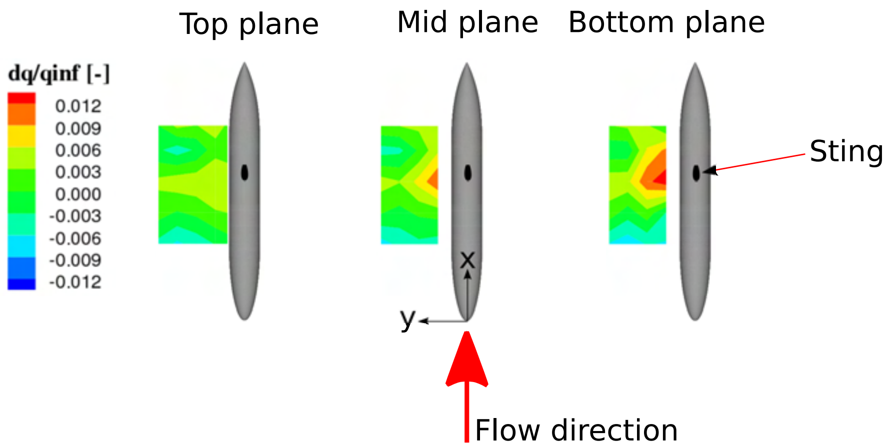

(b)

Figure 3.12: Model sting far-field disturbances on the (a) Local angle of attack α (b) Local non-dimensionalized dynamic pressure $\frac{q}{q_\infty}$ near the fuselage at a generalized wing volume at $\alpha = 0°$, $\beta = 0°$ and $M_\infty = 0.179$. In the figures, top views are provided of the top-, mid- and bottom plane shown in Figure 3.5(b)

In Figure 3.12 it is seen that when the flow approaches the sting, the angle of attack is increased. Just behind the sting, downflow is measured. When the value of $\frac{\Delta q}{q_\infty}$ is studied on these planes the deceleration of the flow in front of the sting due to a blocking effect of the sting is clear. Due to the sting profile, the flow is accelerated at the sting side. These effects decrease with increasing distance from the sting.

From the results of the panel code- and Euler (2^{nd} order central discretization) calculations, these far-field parameters are also determined at the same points. Their values are compared to the measured values in Figure 3.13 where the differences are plotted at the bottom plane (Figure 3.5(b)) displaying the largest differences as this plane is closest to the model sting.

It is observed that (summarized in Table 3.4):

1. The panel code is unable to determine the values of the far-field effects to within the accuracy bandwidth of the 5-hole probe (Table 3.3) according to Figure 3.13(a). Near the wake of the sting, the value of $\Delta\alpha$ (compared to measured values) is over-estimated by approximately 0.50 [deg]. In this same region the value of $\frac{\Delta q}{q_\infty}$ is overestimated by approximately 0.015. The discrepancy near the wake region is attributed to shortcomings in the modeling of the sting wake (discussed in Chapter 4). Near the nose of the sting, values of $\Delta\alpha$ and $\frac{\Delta q}{q_\infty}$ are over- and underestimated with approximately 0.15 [deg] and 0.005 respectively. It is therefore concluded that the internal cavity and slit affect the pressure distribution around the sting. This presumption is proven by the results of the Euler calculation,

2. The Euler calculation is also unable to predict the far-field parameters to within 5-hole probe accuracy according to Figure 3.13(b). It does however perform better compared to the panel code calculations: it is seen in the results that the value of $\Delta\alpha$ is over-estimated with approximately 0.15 [deg] near the wake region of the sting. The value of $\frac{\Delta q}{q_\infty}$ is over-estimated by 0.015 in this region. In front of the sting, these values are smaller than the 5-hole probe accuracy

As expected the Euler calculation performs better than the panel code calculation in determining the value of the far-field model sting interference in the wing volume.

Considering the measurement and calculation of model sting near-field and far-field effects, the following can be concluded: without knowing the specific details of a possibly complex interference flow field, it is not justified (from the viewpoint of accuracy) to determine model sting near-field and far-field effects using methods at low levels of complexity and intrinsic accuracy. Significant calculation offsets (out of the bounds of experimental accuracy as visualized in Figures 3.11 and 3.13) are caused by unknown characteristics of the interference flow field. These offsets are attributed to:

1. The action of the cavity and slit (compare e.g. the calculated results of panel code and Euler code calculations in Figure 3.11),

2. Additional effects of vorticity,

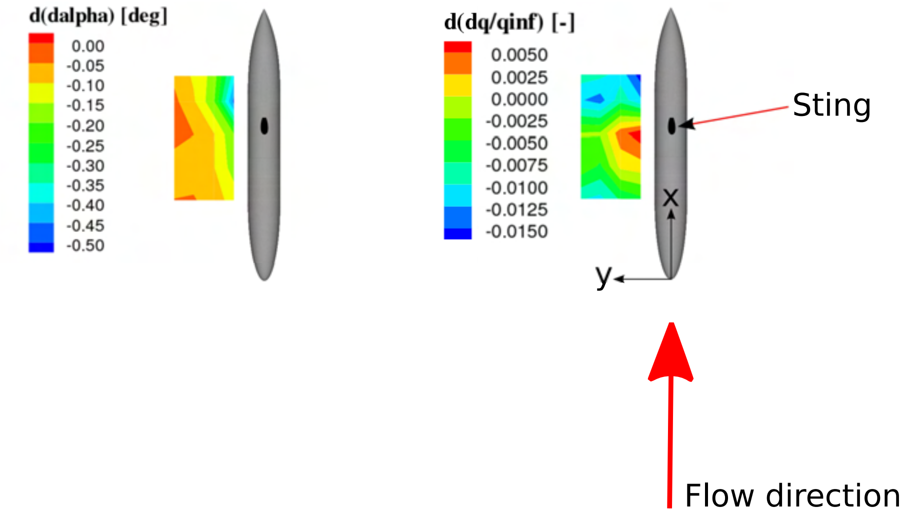

(a)

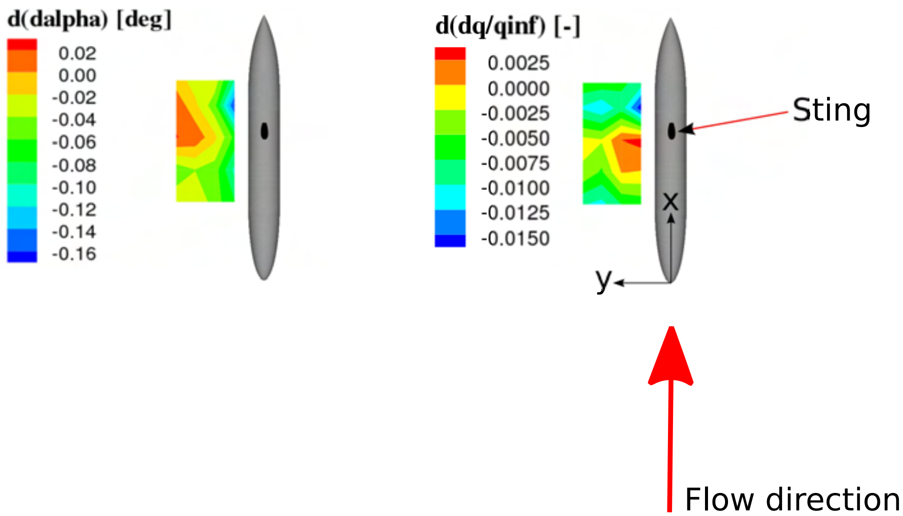

(b)

Figure 3.13: Differences (measured value - calculated value) of calculated and measured far-field effects at the bottom plane shown in Figure 3.5(b) (a) Comparison of panel code results and measurements (b) Comparison of Euler code results and measurements. $\alpha = 0°$, $\beta = 0°$ and $M_\infty = 0.179$

3. Additional effects of viscosity.

Table 3.4: Maximum absolute differences between panel code (PC) and Euler code (EC) calculations with experimental results on model sting far-field effects. The experimental accuracy (Exp.) is also indicated

	PC near wake	**PC near nose**	**Exp.**
$\Delta\left(\Delta\alpha\right)$ [deg]	0.50	0.15	0.10
$\Delta\left(\frac{\Delta q}{q_\infty}\right)$ [-]	0.015	0.005	0.006
	EC near wake	**EC near nose**	**Exp.**
$\Delta\left(\Delta\alpha\right)$ [deg]	0.15	0.10	0.10
$\Delta\left(\frac{\Delta q}{q_\infty}\right)$ [-]	0.015	0.003	0.006

An in depth understanding of the limitations of these numerical methods (panel code, Euler) as shown in Figures 3.11 and 3.13 can only be developed when the interference flow field itself is understood: interference contributions should be defined both qualitatively and quantitatively. To this end Navier-Stokes calculations are carried out. This is the subject of the next chapter.

3.5 Summary

In this chapter an introduction on the complex physics of the frequently studied “juncture flow” is given as the model sting interference flow field can be expected to show distinct similarities with its flow topology. Based on differences between the typical juncture flow configuration and the configuration of interest (a model sting penetrating an aircraft fuselage carrying an internal balance) it is concluded that a new study on the sting disturbances is inevitable. Besides the need to create an experimental and numerical data base for the tuning of calculations and validation of numerical techniques, the following question needs to be answered:

“Is it justified (from the viewpoint of accuracy) to determine model sting near-field and far-field effects using methods at low levels of complexity and intrinsic accuracy without knowing the specific details of a possibly complex interference flow field?”

This question aims at identifying low-cost computational methods for the determination of model sting interference implementable in the expert system once labeled as “good enough” (meaning to within accuracy requirements). Measurements and calculations on model sting near-field and far-field effects are presented in order to answer this question. Comparing their results it is concluded that it is not justified to implement these type of calculations (such as panel code- and Euler calculations) for determining model sting disturbances to within measurement accuracy. Significant calculation offsets (out of the bounds of experimental accuracy) are caused by unknown characteristics of the interference flow field. This flow field is thought to be governed by the action of the balance cavity and slit, and additional effects of vorticity and viscosity. An in depth understanding of the limitations of these numerical methods (panel code, Euler) can only be developed when the interference flow field itself is understood both qualitatively and quantitatively. To this end Navier-Stokes calculations are carried out. This is the subject of the next chapter.

Chapter 4

In Depth Research Into Model Sting Near-Field Effects

In this chapter the following questions are answered:

1. Are Navier-Stokes calculations suitable for resolving the near-field interference of the model sting both qualitatively and quantitatively to within accuracy requirements (based on measurement accuracy)?

2. From the viewpoint of accuracy and effort, what are the most desirable methods for determining sting interference?

3. Can this knowledge be extrapolated to a wide variety of support setups (and be used for the treatment of connected support parts)?

In this chapter the setup and analysis of Navier-Stokes calculations are presented. These calculations provide a qualitative image of the interference flow field that complies with measurements. Quantitatively however, the calculations are not able to determine the values of near-field interference with the right trends and within typical measurement accuracy. Based on gained flow field knowledge various numerical and experimental methods for determining support interference of various support setups are classified. It is concluded that the two classification parameters "accuracy" and "effort" oppose each other. This opposition might be cleared by designing a custom-made model (that is both accurate and requires a low amount of implementation effort) for calculating model support interference, implementable in an expert system.

4.1 Introduction

In Chapter 3 it is concluded that the interference flow field of model sting and fuselage is affected by the action of the balance cavity and slit, and additional effects of vorticity and viscosity. The quantitative and qualitative extent of their action can be evaluated when the interference flow field is properly resolved. To this end, Navier-Stokes calculations are carried out. The setup and analysis of these calculations are presented in this chapter.

Calculations on a fuselage-sting combination including internal balance cavity and slit at two angles of attack (0° and 8°) are performed in order to clarify the near-field flow of model sting and fuselage. To this end calculations are compared to the results of various measurements. When the interference flow field is resolved (both qualitatively and quantitatively), the performance of both exploratory calculations (presented in Chapter 3) and Navier-Stokes calculations are discussed revealing their restrictions. These restrictions enable the generalization of applicability of numerical and experimental methods to multiple sting placements and the treatment of the remaining support parts. Finally the advantages of designing a fast and accurate custom-made model for calculating model support interference are discussed.

4.2 Setting up Navier-Stokes calculations

In this section, the setup of the Navier-Stokes calculations is discussed. First, the computational domain is explained. Next, the choice on a turbulence model is treated. Finally the choice between steady or unsteady calculations is discussed.

4.2.1 The computational domain

The test section of the Low Turbulence Tunnel (LTT) defines the boundaries of the computational domain. In this domain, the model sting and fuselage including the balance cavity and slit are modeled. Figure 4.1 represents the geometry of the computational domain.

Calculations are performed with "full domains" and with "half domains" by including a longitudinal symmetry plane in the domain (for the purpose of studying the importance of unsteady flow phenomena on the fuselage). The boundary conditions are set such that a wind tunnel experiment is simulated: mass-flow inlet and pressure outlet boundary conditions (as advised in [72]) are set in order to safeguard calculation convergence and create comparable boundary conditions to an actual wind tunnel experiment (the variation of total pressure over the inlet plane matches typical 5-hole probe accuracy shown in Table 3.3). In order to reduce the number of computational nodes, boundary layers at the tunnel walls are not discretized. To maintain simulation stability the tunnel walls are modeled as symmetry planes. The fuselage, slit, cavity and sting are given the no-slip boundary condition. Their boundary layer is discretized.

The unstructured mesh consisting of hexahedral cells (defined by Hexpress) is refined in the boundary layers, wakes, regions where elevated vorticity is expected, regions of high geometrical curvature and regions where flow separation is expected to occur. In the experiments the boundary layers on the fuselage and on the sting are tripped from laminar to turbulent. For the CFD calculations this implies that turbulent boundary layers must be discretized on the surfaces of interest. The discretization of the boundary layer depends on the method used for modeling the turbulence.

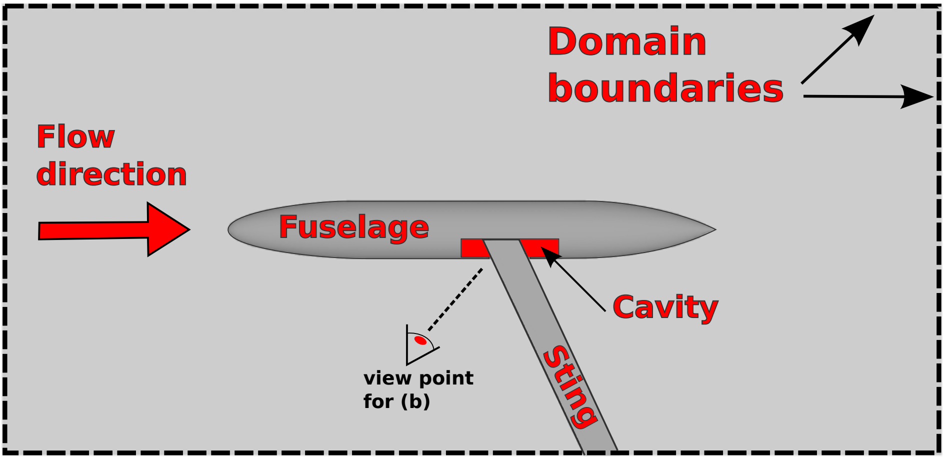

(a)

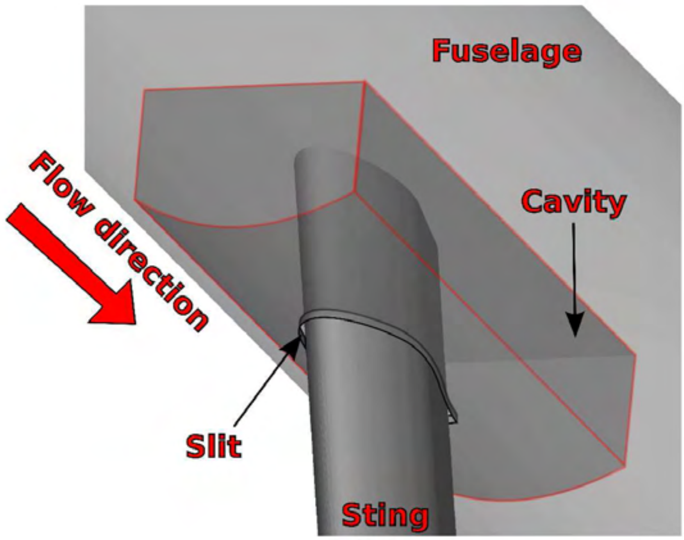

(b)

Figure 4.1: The numerical domain of the Navier-Stokes calculations (a) A longitudinal cross-section showing the test section boundaries (b) A close-up of the entrance of the model sting into the fuselage. Slit and cavity are clearly seen

4.2.2 Turbulence models

According to Nieuwstadt [73], multiple methods are available to simulate the behavior of turbulent flow around arbitrary bodies:

- Direct Numerical Simulation (DNS): these time-dependent solutions of the Navier-Stokes equations resolve the physics all the way down to the smallest scales of the motions. For high Reynolds-number turbulent flows these solutions are unlikely to be attainable for some time to come [72]. These methods are too expensive from a computational point of view to be applied and are therefore not considered here,

- Large Eddy Simulations (LES) provide an alternative approach in which large eddies are explicitly resolved while the effect of small eddies is modeled in a time-dependent simulation using the filtered Navier-Stokes equations. The principle of LES is that by modeling less of the turbulence (and resolving more), the error introduced by turbulence modeling is reduced. According to Simpson [63], Deng et al. [74], Rodi [75] and Constantinescu et al. [58], LES is the most promising numerical method for the determination of juncture flow characteristics (both qualitatively and quantitatively). LES for high Reynolds number flows requires a significant amount of computational resources caused by the need to accurately resolve the energy-containing turbulent eddies. This is especially the case in near-wall regions where the scales to be resolved become smaller. The need for accurate spatial and temporal discretization make this method computationally expensive. LES is not considered in this thesis,

- Reynolds averaging (also called ensemble averaging): the Reynolds-averaged Navier-Stokes (or RaNS) equations govern the transport of the averaged flow quantities [72]. The complete range of turbulence scales is modeled by closure models. This approach therefore greatly reduces the required computational resources compared to DNS or LES. Modeling the turbulence is accomplished by using either the Boussinesq approach or the Reynolds Stress Model (RSM). In the Boussinesq approach the Reynolds stresses are directly related to the value of the turbulent viscosity. Additional transport equations leading to the calculation of this viscosity close the model. Typical Boussinesq closure models are the Spalart-Allmaras model, the κ-ϵ model and the κ-ω model. In the RSM approach the Reynolds stresses are explicitly defined to the expense of a larger set of closure equations.

From the above mentioned techniques to resolve turbulent flow Reynolds averaging deserves the preference from the viewpoint of reducing computational expenses. Based on considerations regarding the computational expenses of applying the RSM (7 additional equations to be solved in 3D instead of maximum 2 using the Boussinesq approach) and the superiority class of the RSM method (highly swirling flows and stress-driven secondary flows), a Boussinesq approach is chosen in order to model the turbulent flow characteristics for the current study.

For performing a RaNS calculation, three closure models are selected that prove to be the most promising for the calculation of flows with juncture flow characteristics (section 3.1) according to [72]:

1. Spalart-Allmaras: this model is designed specifically for aerospace applications involving wall-bounded flows and has been shown to give reasonable results for boundary layers subjected to adverse pressure gradients,

2. The Realizable κ-ϵ model: this model provides superior performance over the other κ-ϵ model versions (the standard- and RNG κ-ϵ models) for separated flows and flows with complex secondary flow features. The term realizable implies that the model satisfies certain mathematical constraints on the Reynolds stresses more consistent with the physics of turbulent flows (compared to other models). Neither the standard κ-ϵ model nor the RNG κ-ϵ model is realizable. The Realizable κ-ϵ model is likely to provide superior performance for flows involving rotation, boundary layers under strong adverse pressure gradients, separation, and recirculation,

3. The Shear-Stress Transport (SST) κ-ω model: this model contains features that make it more accurate and reliable for a wider class of flows as e.g. adverse pressure gradient flows, airfoils and transonic shock waves than the standard κ-ω model. It combines the standard κ-ω model in the near-wall region with the freestream independence of the κ-ϵ model in the far-field and can therefore be considered a hybrid model.

According to Devenport et al. [43], Jones et al. [48] and Paciorri et al. [49] κ-ϵ models generally perform poorly in capturing juncture flow characteristics. This is caused by the fact that the anisotropy of turbulence is not resolved in the regions of interest. According to Jones et al. [48], the Spalart-Allmaras and SST κ-ω model show similar performance in quite decently capturing these characteristics. Apsley et al. [46] demonstrates however the poor performance of the SST κ-ω model in calculating juncture flow phenomena.

The above mentioned studies all concentrate on the performance of turbulence models with respect to the calculation of typical juncture flow characteristics as discussed in section 3.1. The performance of the models is expressed in the ability to capture typical juncture flow phenomena qualitatively and quantitatively such as horseshoe vortex strength and position, position of separation lines and strength of the interference shear stresses. These results are difficult to extrapolate to the current configuration that will prove to show very different characteristics than the frequently studied juncture flow (as concluded from Chapter 3).

The flow solver used for the RaNS calculations is FLUENT. Based on [72] some of its turbulence model performance indicators are given in Table 4.1. From this table it is clear that the Realizable κ-ϵ model deserves the preference from the viewpoint of calculating a flow pattern involving adverse pressure gradients, separated flow and secondary flow features (such as vortices). Whether or not this model indeed outperforms the Spalart-Allmaras- and SST κ-ω model is evaluated for a typical test case.

Table 4.1: Flow solver (FLUENT) turbulence model performance indicators

	Adv. press. gradient	Separated flow	Secondary flow feat.
Spalart-Allmaras	+		
SST κ-ω	+		
Realizable κ-ϵ	+	+	+

In this test case a part of the numerical domain considered in the final calculations is used: the fuselage is modeled as a flat plate. Cavity and slit are also modeled. Part of the model sting is included. The dimensions of the domain are chosen such that a boundary layer comparable to the final calculations will form on the plate in front of the sting and that the most prominent flow phenomena aft of the sting on the plate (like recirculation) are resolved (the unstructured mesh consisting of hexahedral cells is refined in the boundary layers, wakes, regions where elevated vorticity is expected, regions of high geometrical curvature and regions where flow separation is expected to occur). The domain has a spanwise and vertical extent of 2 sting chords. The layout of the computational domain is given in Figure 4.2.

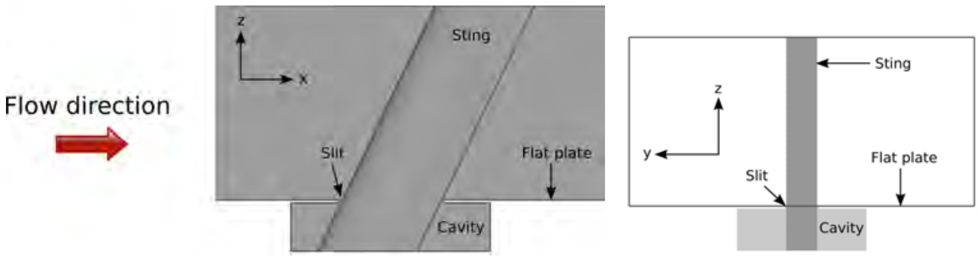

(a) (b)

Figure 4.2: Side view (a) and front view (b) of the computational domain used for the validation of turbulence models

For this test case, three turbulence models are applied: the Spalart-Allmaras, SST κ-ω and Realizable κ-ϵ models. Besides choices on computational domain and turbulence model, the accompanying near-wall treatment is of utmost importance. Modeling of the near-wall flow behavior significantly influences the accuracy of numerical solutions [72]. This is understandable because walls are the main source of mean vorticity and turbulence. It is in this region that the solution variables display large gradients and the momentum and other scalar transports occur most vigorously.

For the above mentioned turbulence models, the enhanced wall treatment seems the most appropriate choice. To achieve the goal of implementing a near-wall modeling that possesses the accuracy of the standard two-layer approach[1] for fine near-wall meshes

[1] in this approach, the whole domain is subdivided into a viscosity-affected region and a fully-turbulent region

and that, at the same time, will not significantly reduce accuracy for wall-function meshes, the two-layer model can be combined with enhanced wall functions. Enhanced wall functions formulate the law-of-the wall as a single wall law for the entire wall region. This is achieved by blending linear (laminar) and logarithmic (turbulent) laws-of-the-wall [72].

In FLUENT only enhanced wall functions are available for the Spalart-Allmaras- and SST κ-ω model provided a suitable mesh is chosen with $y^+ \leq 4$ to 5 for the first node in the boundary layer. For the Realizable κ-ϵ model where the complete enhanced wall treatment is implemented, similar constraints hold for the mesh.

Mesh independent results of above mentioned calculations are compared to experimental results on the setup shown in Figure 3.3.

Referring back to Table 4.1, the adverse pressure gradient on the flat plate center line in front of the sting is evaluated and compared to measurements described in section 4.3.2. The results are shown in Figure 4.3(a).

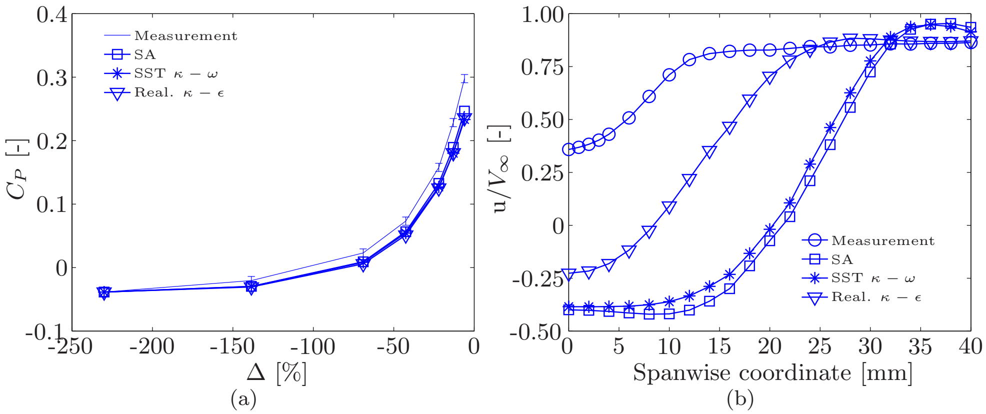

Figure 4.3: Assessment of turbulence model performance (a) Calculating the adverse pressure gradient on the flat plate in front of the sting on the sting center line. The Δ indicates the distance to the sting gap leading edge in percentage of the sting chord (b) Predicting the sting wake mean streamwise velocity component

It is seen in Figure 4.3(a) that the pressure coefficient increases when the distance to the model sting leading edge decreases. The calculated pressure coefficients match the experimental values closely (however not to within the accuracy bandwidth). For this test case the performance of the turbulence models is similar. This is in agreement with the findings in Table 4.1.

The performance with respect to resolving flow separation and secondary flow features can be assessed by:

1. Comparing experimental and numerical values of the sting wake mean streamwise velocity component. Experimentally, a hot-wire is used to probe the sting wake. The position of the spanwise rake is shown in Figure 4.4. It is positioned 5 [mm] from the surface of the flat plate 36 [mm] downstream the sting gap trailing edge,

2. Comparing experimental and numerical results on streamline visualizations at the sting.

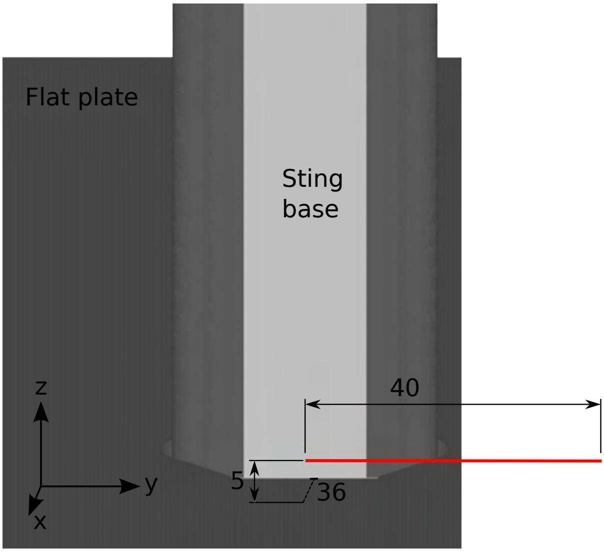

Figure 4.4: Position of the spanwise rake (shown in the computational domain) used to assess the sting wake mean streamwise velocity component. Dimensions are in [mm]

Figure 4.3(b) shows the results of the wake rake. It is seen that all numerical methods have difficulties in capturing the wake velocity profile. The fact that the velocity profile as measured near a cylindrical surface (the fuselage) is compared to the calculated profile near a flat plate complicates the comparison. The main profile shape is however not thought to be seriously affected by this. This shape is best captured by the Realizable κ-ϵ model. Calculated recirculation regions downstream the sting are larger than shown by the measurements (causing the negative values in the figure). This is typical for eddy-viscosity based turbulence models as is discussed in section 4.3.2.

An example of a comparison on the streamline visualization is given in Figure 4.5. From this figure it becomes clear that the Spalart-Allmaras (and also SST κ-ω) closure models perform poorly in predicting the streamlines in the near-field of model sting and fuselage when compared to experimental results. The Realizable κ-ϵ model outperforms the latter two by showing a distinct resemblance with the measurements.

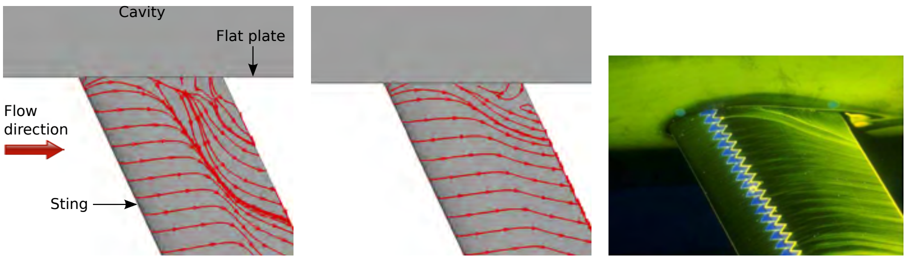

(a) (b) (c)

Figure 4.5: A comparison of the flow topology at the sting side as calculated by (a) The Spalart-Allmaras closure model (similar results are found for the SST κ-ω model) (b) The Realizable κ-ϵ model and compared to (c) Oil flow visualizations on the setup as shown in Figure 3.3. In the calculations and measurements, $\alpha = \beta = 0°$ and $M_\infty = 0.179$

Based on these results, the Realizable κ-ϵ model demonstrates to be the most suitable model for the configuration under consideration. Therefore this model is chosen to perform the final CFD calculations.

4.2.3 Steady vs. unsteady calculations

Besides the choice of a turbulence model it must be decided whether steady or unsteady calculations are performed. Performing unsteady calculations on the domain shown in Figure 4.1 using the Realizable κ-ϵ model reveals unsteady phenomena in the flow and their quantitative effect on the fuselage forces. It is shown in this section that performing steady calculations is allowable for the final calculations thereby saving time and computational effort considerably.

Measuring unsteady phenomena

Unsteady phenomena in the sting near-field are measured using a single-wire hot wire probe and the setup shown in Figure 3.3 at $\alpha = \beta = 0°$ and $M_\infty = 0.179$. The measurement rake is shown in Figure 4.4. Time series are recorded using this hot wire with a sample frequency of 10 [kHz] or a Nyquist frequency of 5 [kHz]. Measured time series are subjected to a Fourier analysis in order to identify the dominant frequencies in the power spectrum. A typical result of this analysis is shown in Figure 4.6. The measurement point is at 50% of the rake indicated in Figure 4.4 (at 20% of a sting chord spanwise from the center line of the fuselage).

In Figure 4.6 two dominant frequencies are recognized: approximately 700 and 1750 [Hz]. The first frequency is believed to originate from the unsteady vortex shedding from the sting trailing edge. Assuming that the Strouhal number of the sting is approximated initially by a value of 0.2 (as found for a cylinder), the trailing edge shedding frequency based on the trailing edge thickness of the sting is 726 [Hz], a value very close to the measurement result. The second frequency that is found with the hot

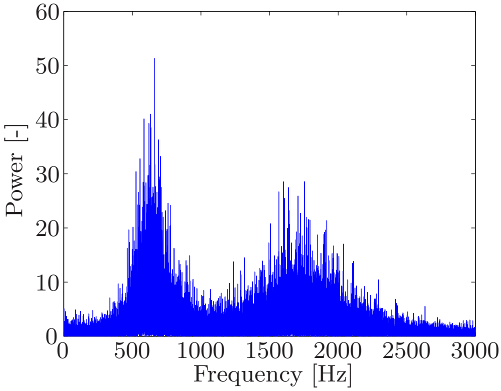

Figure 4.6: The frequency-power spectrum of the time signal measured with a single-wire hot wire in the sting wake (halfway the rake shown in Figure 4.4) at $\alpha = \beta = 0°$ and $M_\infty = 0.179$

wire is more interesting. Results from the hot wire measurements indicate that its contribution in the power spectrum reaches a maximum somewhere between 20% and 40% of the sting chord from the sting center line (between the mid point and the right most point of the rake shown in Figure 4.4). This result indicates the contribution of unsteady vorticity shed from the sting- or fuselage side (the cavity Helmholtz frequency is found to be somewhat lower than 100 [Hz] and is therefore not thought to be related to the measured frequency of 1750 [Hz]). This phenomenon is discussed later on.

With this information, an unsteady calculation using the domain presented in Figure 4.1 and applying the Realizable κ-ϵ model is performed. The time step is chosen such that both frequencies can be resolved.

Calculating unsteady phenomena

During the numerical simulation, time series of the lift and drag on both the fuselage and the sting are recorded. These signals are analyzed by a Fourier analysis. For the fuselage two governing frequencies are found. The first frequency (702 [Hz]) complies with the sting vortex shedding frequency (measured = 700 [Hz]). A second frequency of approximately 1400 [Hz] is found dominating the power spectrum of the fuselage lift. This frequency is recognized as the disturbance of unsteady vorticity shed from the sting- or fuselage side (measured = 1750 [Hz]). When however the maximum amplitude of this oscillation in lift is studied it is seen that it does not exceed a value of approximately 1 [count]. Both modes are not seen to affect the fuselage drag. It can be concluded that in the calculations the fuselage is quantitatively not significantly affected by unsteady phenomena.

When the same analysis is carried out for the unsteady lift and drag of the model sting it is seen that these are dominated by the sting vortex shedding with a frequency of 702 [Hz] recognized in the power spectrum implying a sting Strouhal number equaling 0.19.

An instantaneous snapshot of vorticity shed from the model sting is given in Figure 4.7.

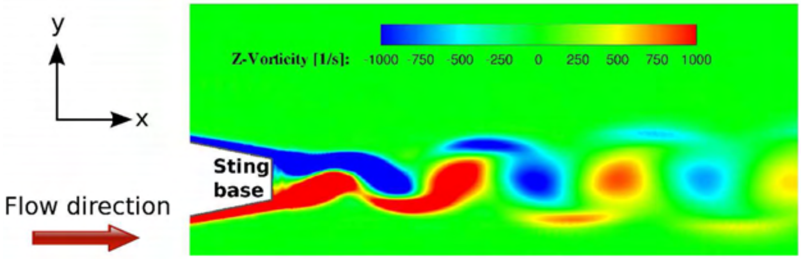

Figure 4.7: Instantaneous in plane vorticity at $\alpha = \beta = 0°$ and $M_\infty = 0.179$. The plane shown is a cross-sectional cut of the sting approximately 1 sting chord from the fuselage

The quantitative extent of the unsteadiness on the fuselage is negligible. This is the reason that it is chosen to implement the steady RaNS equations for the final CFD calculations.

4.2.4 Flow solver settings

The governing equations describing the flow are the 3-dimensional Steady Reynolds averaged Navier-Stokes equations supplemented by equations describing the turbulence (according to the Realizable κ-ϵ model) and the energy equation. These equations (with a second order discretization of the convective and diffusive terms) are solved by a pressure-based solver. The pressure-based solver uses a solution algorithm where the governing equations are solved sequentially. The governing equations are non-linear and coupled. This is why a solution loop must be carried out iteratively to obtain a converged numerical solution. The segregated algorithm is memory-efficient since the discretized equations need only be stored in the memory one at a time. The problem is solved implicitly: for a given variable, the unknown value in each cell is computed using a relation that includes both existing and unknown values from neighboring cells (taken from [72]). The main quantities defining the flow properties are summarized in Table 4.2.

Table 4.2: Reference quantities describing the flow properties implemented in the CFD calculations

Medium	Ideal Gas
M_{ref}	0.179
p_{ref}	101325 [Pa]
T_{ref}	288.15 [K]
ν_{ref}	$1.7894 \cdot 10^{-5}$ [kg/m·s]
$T_{u_{ref}}$	2.5 [%]

Results of the Navier-Stokes calculations are used for mainly four purposes:

1. To study the near-field interference flow field of the model sting and fuselage qualitatively,
2. To extract and quantify the various disturbances that govern the near-field effect (in order to quantify disturbances, Δ-calculations are carried out),
3. To assess compliance of these calculated effects with balance measurements and with other numerical methods (such as panel code- and Euler calculations).

Results of the calculations are discussed in the following sections.

4.3 Results of the Navier-Stokes calculations

Validation of the calculations is performed by comparison to experimental results. In the following sections the calculation featuring the tunnel test section, fuselage, cavity, slit and sting at $\alpha = \beta = 0°$ is compared to oil flow visualization results, results of static pressure measurements and results of total pressure measurements for this purpose. From this comparison the interference flow field is analyzed qualitatively. Using this information, a subdivision of model sting near-field effects is proposed. These effects are quantified. Results of the calculation at $\alpha = 8°$ and $\beta = 0°$ are summarized. Finally, the total near-field disturbances are compared to balance measurements in order to answer the question: "Is a Navier-Stokes calculation a satisfying method to calculate model sting near-field interference both qualitatively and quantitatively?"

4.3.1 Comparison to results of oil flow visualization

Experimental oil flow visualization is applied at the model shown in Figure 3.3 at $\alpha = \beta = 0°$ and $M_\infty = 0.179$ to obtain information on the fuselage- and sting surface streamlines. Comparison to streamlines calculated from the numerical results as a means of calculation validation and flow analysis is given in this section.

Streamlines at the sting nose

When the flow approaches the model sting on the fuselage, the 2D boundary layer transforms into a skewed 3D boundary layer (as was shown in Figure 3.1(a)). This is caused by the presence of the sting causing an increase in the pressure in the flow field in front of it leading to an adverse pressure gradient. In the case of classic juncture flow, the flow finally separates in front of the support leading to the well known horseshoe vortex wrapped around the sting. In this case, the separation in front of the support does not set in. This is due to the pressure difference between the flow just outside the cavity and inside the cavity. The flow is sucked into the cavity and this effect that can be seen as a relieving effect prevents flow separation (even though the ratio of boundary layer thickness to slit width is as high as 2!). This situation is shown in Figure 4.8(b). It is clearly seen in the figure that the flow enters the cavity and hence is prevented to separate in front of the support.

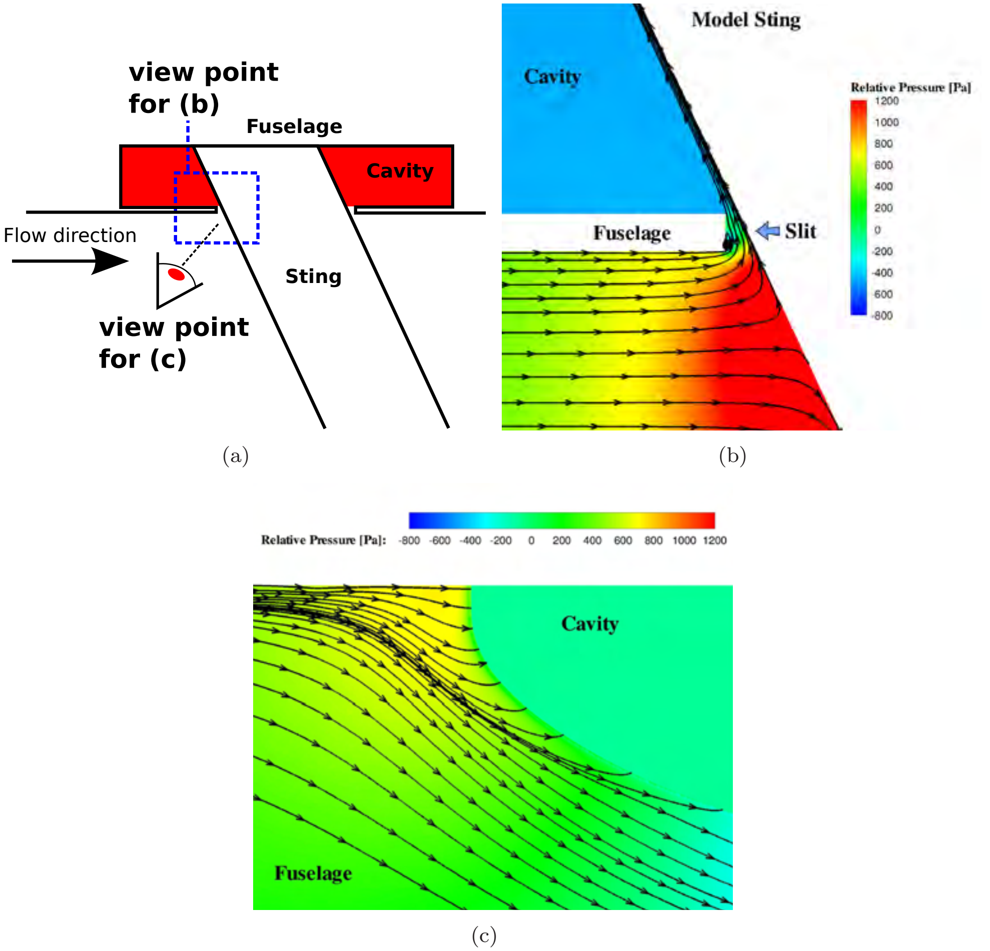

Figure 4.8: (a) Picture showing the view points for (b) and (c). The picture is a longitudinal cross-section of the fuselage (b) Streamlines in front of the support (on the model heart line) showing the relieving effect of the cavity on the adverse pressure gradient (c) A 2D picture of the streamlines around the sting gap on the fuselage (the sting is not included in the picture). Pressures are relative to a freestream reference pressure

Figure 4.8(c) shows the local surface streamlines on the fuselage around the support entry gap. No signs of separation are visible. The relieving effect is recognized in the pressure distribution as well.

Streamlines at the support side

Alongside the support (when traveling in downstream direction) the flow is accelerated due to the support shape. This creates a low pressure area on the support and a carry-over of this pressure to the fuselage. This low pressure is responsible for a re-entry of flow in the freestream from the cavity. The flow leaving the cavity is the cause of the originating of a vortex which from now on shall be called the “slit vortex”. This slit vortex (visualized in Figure 4.9(a)) is convected downstream and influences the flow in the interaction area of sting, slit and fuselage. The vortex creates a low pressure area on the fuselage and support, downstream of the maximum thickness of the support (as is seen in Figure 4.9(b)). On the fuselage, the flow is sheared towards the gap leading to a thin stagnation strip (and even local backflow) close to the gap.

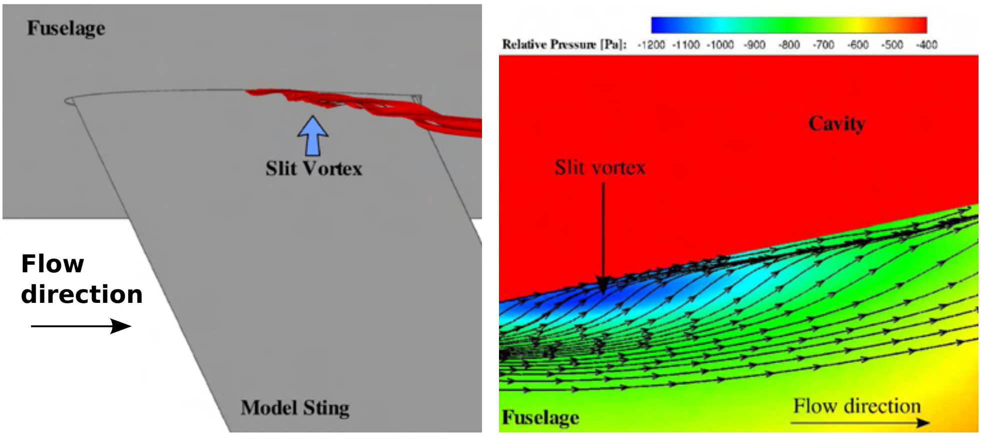

(a) (b)

Figure 4.9: (a) A 3D image of the fuselage and support revealing the existence of the slit vortex (b) The streamlines on the fuselage besides the gap showing the influence of the slit vortex. The viewpoint is similar to the viewpoint in Figure 4.8(c). The effect of the vortex on the pressure is also discernible. Pressures are relative to a freestream reference pressure

On the support, the local pressure drop leads to additional fluid exiting the cavity and joining the slit vortex. It is believed that the slit vortex keeps growing in strength and magnitude thereby increasing the turbulent kinetic energy in the interaction area. Cross-sectional planes at 40, 50, 60 and 90% of the sting chord (as illustrated in Figure 4.10) illustrate this in Figures 4.11(a), (b), (c) and (d). In these figures, cross-sections of the fuselage are shown that reveal the originating of the slit vortex. Due to a combined influence of cavity outflow and the slit vortex cross flow is induced on the support side close to the juncture. This cross flow leads to local separation of the boundary layer on the sting as is seen in Figure 4.12.

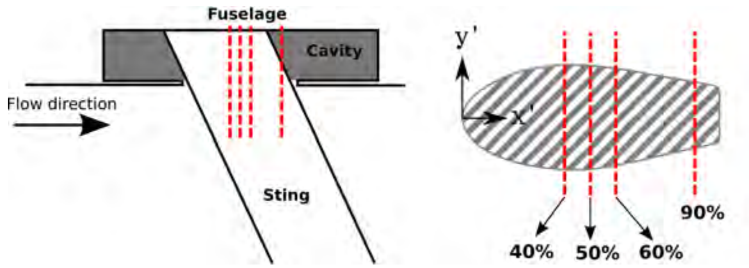

Figure 4.10: Position of fuselage cross-sectional planes used to demonstrate the growth of the slit vortex as shown in Figure 4.11

Streamlines at the fuselage backbody

At the back of the sting the flow separates. A periodic vortex shedding (the shedding is not resolved in the steady calculations) is induced with a shedding frequency of approximately 700 [Hz] determined by the Strouhal number of the support equaling 0.19 (according to section 4.2.3). The vortices that are shed form a turbulent wake behind the support. Close to the fuselage, this wake structure is affected by the separated region at the sting side and the slit vortex. This area is also disturbed by fluid exiting the cavity through the slit trailing edge thereby complicating the wake structure even more.

Sting trailing edge separation induces local separation at the fuselage aft of the sting expressed in a recirculation zone shown in Figure 4.13. This separated region closes fast. This is related to the entry location of the sting in the fuselage: the sting is inserted into the cylindrical part of the fuselage and therefore the separation is not located in an adverse pressure gradient that would discourage reattachment of the boundary layer. Because the slit vortex transports high momentum fluid into the recirculation area it facilitates a fast closure of the recirculation. It is thought that because of this wake-energizing function, the slit vortex seems to lose part of its strength. Recirculation closure results in a stagnation point. Aft of this stagnation point, a boundary layer starts to build up again on the backbody.

The fact that in the direct near-field of the support (close to the fuselage) the support wake is governed by a combination of base vortex shedding, a separated region from the sting side and the influence of the slit vortex gives the wake a unique structure. The temporal structure of the wake is not resolved. The steady wake effect on the fuselage streamline pattern is seen in Figure 4.13.

The flow behavior extracted from these numerical results is compared to the results of experimental oil flow visualizations. A typical result from experiments is given in

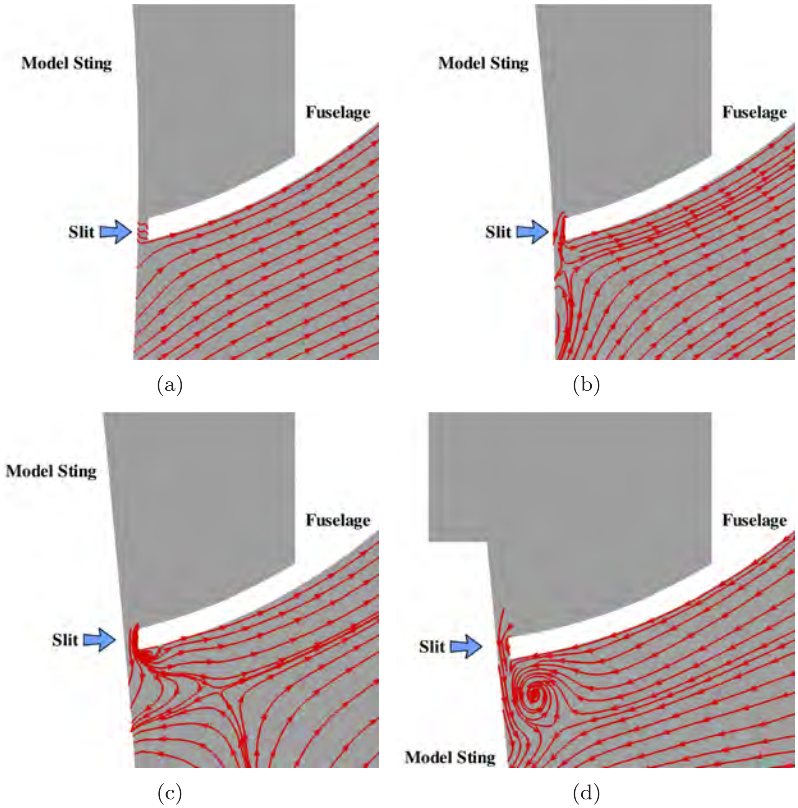

Figure 4.11: (a) The originating of the slit vortex: stagnation in the slit at 40% of the support chord (b) Exiting of fluid from the cavity at 50% of the support chord (c) The origin of the slit vortex at 60% of the support chord (d) Development (growth) of the slit vortex at 90% of the support chord. Pictures are cross-sections of the fuselage and support as shown in Figure 4.10

Figure 4.14(a).

From Figure 4.14(a) it is seen that the flow on the fuselage indeed does not separate in front of the support. The area in front of and around the support on the fuselage showing a dark band indicates regions of increased wall shear stresses. These regions exist because of the suction (acceleration) of the fluid into the cavity (reflected by Figure 4.8(c)). Figure 4.14(b) shows the streamline pattern at the fuselage and support side. The dark band around the support on the fuselage indicates that increased shear is present in this region as well. This is related to the velocity increase of the flow in the intersection caused by the shape of the support. It can also be seen that a little more downstream, this band starts to fill up again. Close to the slit, oil is accumulating. This is caused by the action of the slit vortex, transporting the oil towards the slit. The separated region at the support caused by cross flow induced by the slit vortex and the fluid exiting the cavity is also visible in the results. Aft of the support on the

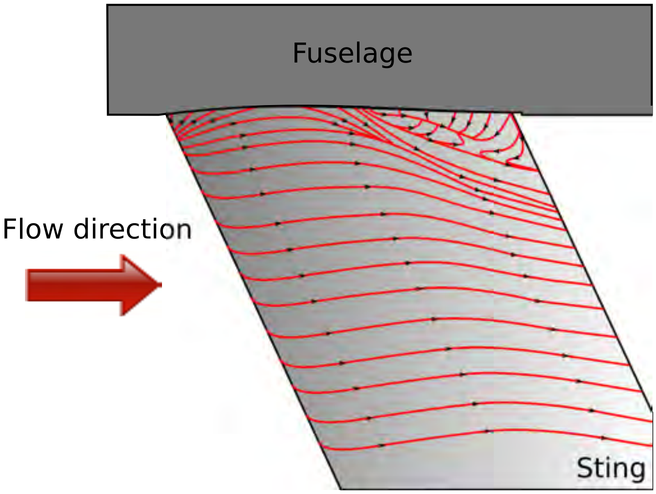

Figure 4.12: Streamlines at the support. The separated region caused by cross flow due to the influence of the slit vortex and fluid exiting the balance cavity is recognized

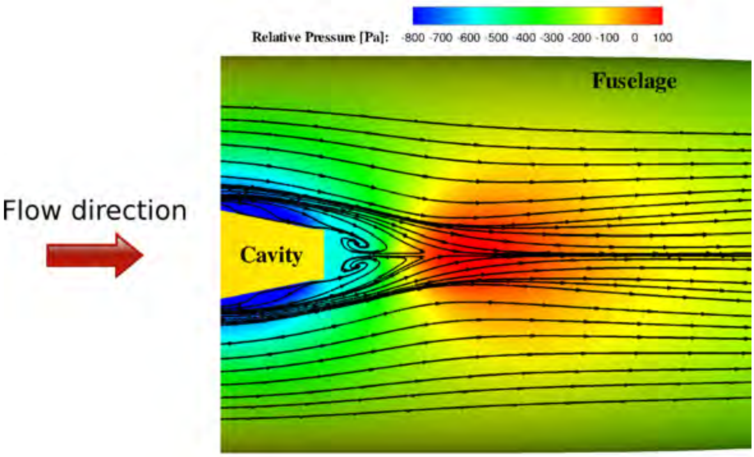

Figure 4.13: The recirculation area on the fuselage and the influence of the support wake on the fuselage. The viewpoint is as in Figure 4.8(c). Pressures are relative to a freestream reference pressure

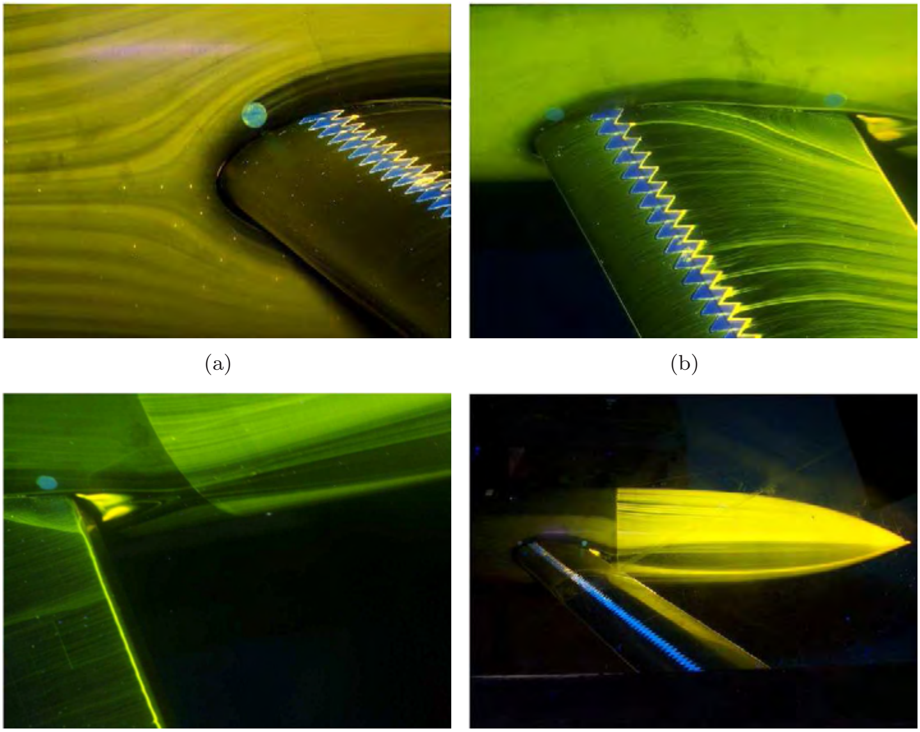

(a) (b) (c) (d)

Figure 4.14: Results of experimental oil flow visualizations showing (a) The streamline pattern near the support leading edge on the fuselage (b) The streamline pattern at the fuselage and support side (c) The streamline pattern at the fuselage afterbody and support side/back (d) The streamline pattern at the fuselage afterbody

fuselage it is seen that base vortices form (recirculation). These are also distinguished in the numerical results. On the afterbody of the fuselage it is seen that the fuselage is affected by the wake of the support. The wake signature on the fuselage shows distinct similarities with the numerical results.

4.3.2 Comparison to pressure measurements

Static- and total pressures are measured on the fuselage and aft of the model sting respectively. The static pressures are measured with pressure orifices. The total pressure is measured by a total pressure probe.

Measurements with pressure orifices

Static pressure measurements on the fuselage are carried out at multiple angles of attack and freestream velocities. The pressure orifices are positioned on the cylindrical part and at the afterbody of the fuselage. Figure 4.15 gives an overview of the pressure orifices at the model.

The pressure orifices with a diameter of 0.4 [mm] are connected to electronic pressure scanners with a range of 1, 5 and 10 [Psi]. This implies a varying accuracy for the pressure orifices on the model. A comparison between calculated and measured values of the pressure coefficients is given in Figure 4.17. The order of points is plotted according to the traverses indicated in Figure 4.16. In the figure, the accuracy bandwidth of the measurements is also plotted.

When Figure 4.17(a) is considered, the following is seen: the first pressure peak in the graph (orifice number 1 to 7) agrees with the adverse pressure gradient found when traversing on the symmetry line of the fuselage towards the support. The calculated maximum pressure coefficient is smaller than the measured pressure coefficient (outside the experimental accuracy bandwidth). This might be due to a couple of reasons. One of the reasons is that the slit width in the experiments might differ slightly from the modeled slit width in the calculations (by typically 0.5 [mm]). This affects the relieving effect of the slit on the fuselage boundary layer. A smaller slit width will lead to a smaller relieving effect and thus a larger value of the adverse pressure gradient in front of the support. In the limit where the slit width goes to zero, the flow separates on the fuselage. Secondly it might also be that the RaNS calculation is not able to resolve the "correct" value of the pressure gradient. The ability of various turbulence models to calculate this gradient is assessed in Table 4.1 and Figure 4.3(a). The difference between measurement and calculation might be caused by the essential inability of eddy-viscosity models to simulate anisotropic turbulence.

The difference between experiment and calculation is local and expressed in a change of shape of the local fuselage velocity boundary layer as shown in Appendix C where the experimental boundary layer seems to be less full as it is more affected by the adverse pressure gradient.

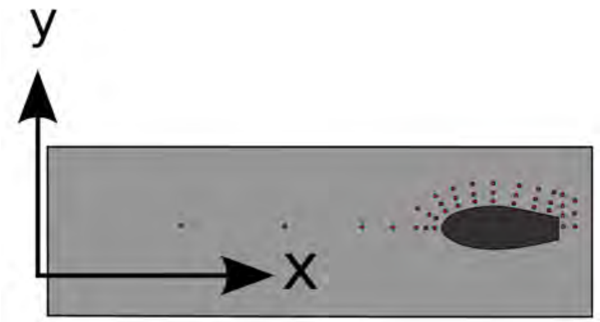

(a)

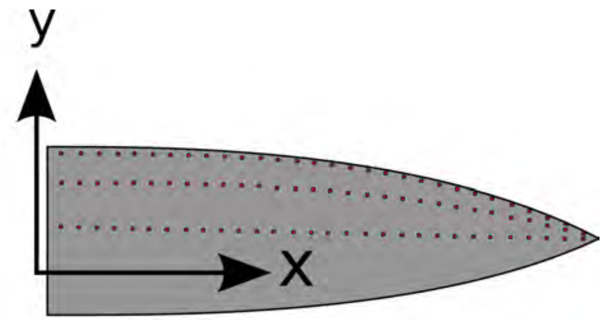

(b)

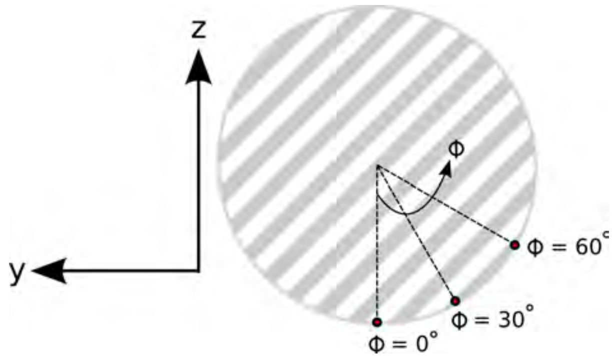

(c)

Figure 4.15: The placement of pressure orifices on the fuselage. The orifices are indicated by red dots (a) Orifices on the cylindrical part (b) Orifices on the backbody (c) A lateral cross-section of the fuselage indicating the position of the orifices at the backbody

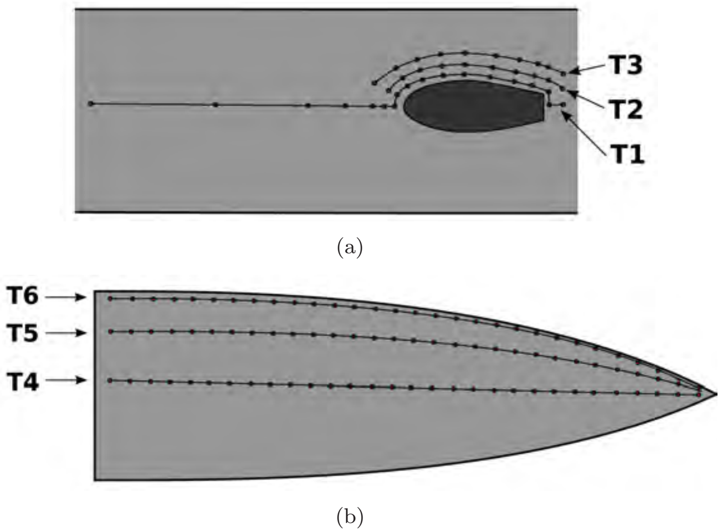

Figure 4.16: The order of orifices used in the plots of Figure 4.17 indicated by streamwise traverses T1 to T6 on (a) the cylindrical section of the fuselage (b) the afterbody of the fuselage

Referring back to Figure 4.17(a) it is seen that aft of the pressure peak the pressure coefficient drops to negative values shown by pressure orifices 8-13. The carry-over of a low pressure area of the support onto the fuselage caused by the shape of the support (accelerating the flow locally) is clearly seen. At pressure holes 14 and 15, the effect of the slit vortex becomes discernible: the vortex decreases the pressure locally. The calculated influence of the slit vortex is more pronounced than shown by experiments.

Aft of the support (orifices 16, 17 and 18) a small bump in the pressure distribution is seen. This bump is caused by the recirculation area on the fuselage. The calculated influence of this recirculation on the pressure of the fuselage is smaller than measured. This implies that the base vortices at the back of the support are stronger than calculations reveal (the difference equals approximately 3 times the experimental accuracy bandwidth). According to Simpson [63] this is an essential shortcoming of eddy-viscosity based turbulence models. The inability to correctly resolve anisotropic turbulence is a reason for the poor calculation of recirculation regions. The first traverse (T1) alongside the support ends with pressure orifice number 18. T2 and T3 show that with increasing distance from the model sting the pressure peaks decline in magnitude and the effect of the recirculation area becomes less pronounced.

Figure 4.17(b) shows the measured and calculated pressure distribution on the afterbody of the fuselage. The pressure coefficient close to the support is relatively moderate. This is caused by the boundary layer recovering from separation. Downstream the boundary layer recovery is noticeable as a decrease in pressure and more downstream the pressure starts to rise again due to the shape of the afterbody. Con-

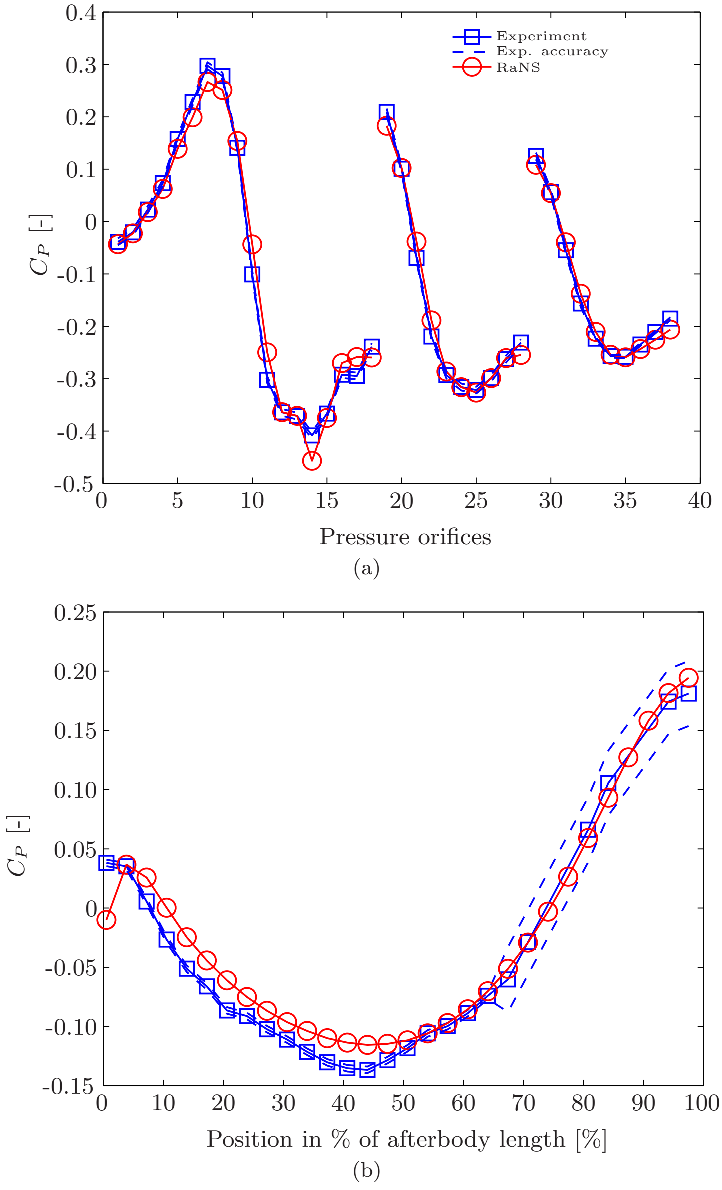

Figure 4.17: Comparison of calculated and measured pressure distributions on the fuselage at $\alpha = 0°$, $\beta = 0°$ and $M_\infty = 0.179$ (a) From left to right traverses T1, T2 and T3 as indicated in Figure 4.16(a) are shown (b) Traverse T4 shown in Figure 4.16(b)

sidering the pressures at 30° and 60° from the center line of the fuselage (T5 and T6 in Figure 4.16(c)), they show a similar behavior. Comparing numerical and experimental values it is seen that close to the support the calculated pressure coefficient is considerably lower than measured. This is caused by the calculated recirculation area that is slightly larger than recognized in the experimental results. At the afterbody (between 5 and 65% of the afterbody length) the numerical results yield a higher value of the pressure coefficients than the experimental results. In this region the numerical model fails to predict the support wake influence on the fuselage properly. As expected this deficiency decreases when the distance to the support is increased.

Measurements with a total pressure probe

A total pressure probe (schematized in Figure 4.18) with an outer diameter of 1 [mm] and an inner diameter of 0.6 [mm] is used to traverse the sting wake. The probe is connected to an electronic pressure scanner with a range of 1 [Psi]. A traverse is carried out at approximately 1/3 of a sting chord downstream of the sting trailing edge (Figure 4.19(a)). The traverse is set up such that at the center line of the traverse (located at the sting center line) the probe just touches the fuselage. An example of the measured total pressure profile is given in Figure 4.19(b).

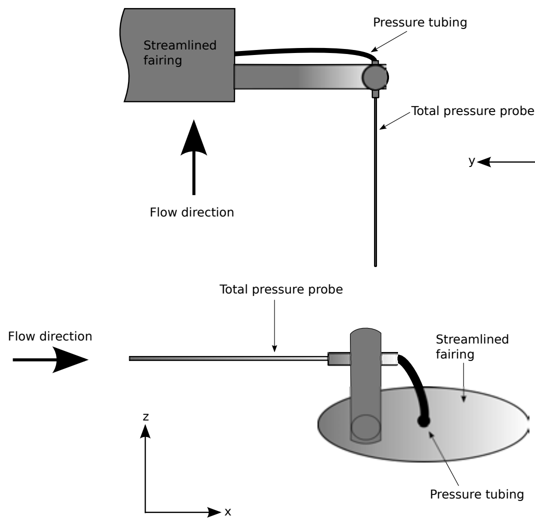

Figure 4.18: A schematic of the setup used to probe the sting wake

The profile measured at 1/3 sting chord downstream the sting trailing edge shows an expected decrease in total pressure in the sting wake. The spanwise extension of the sting wake is approximately 15% of the sting chord at this position. Looking more closely at the profile, the shoulders of this distribution show an inconspicuous bump. Moving the traverse closer to the sting trailing edge (to approximately 1/50 sting chord downstream of the sting trailing edge) this bump translates into a substantial dip in total pressure. This dip is correlated to what is presented in Figure 4.6: it was noticed

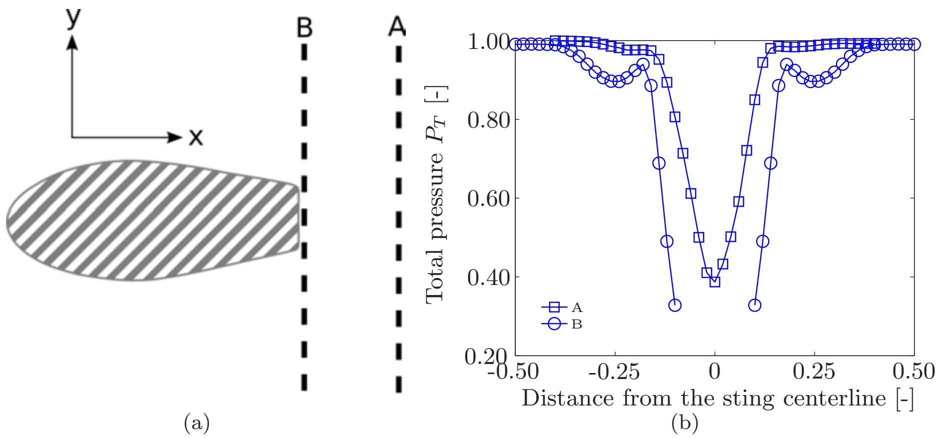

Figure 4.19: Non-dimensionalized measured total pressure profiles in the sting wake (b) The spanwise traverses are carried out at 1/3 chord (A) and 1/50 chord (B) removed from the sting trailing edge in downstream direction as shown in (a). The spanwise position is non-dimensionalized with the sting chord. The total pressure is non-dimensionalized with its freestream value. Effects of the probe sensitivity to the flow direction are not corrected for in the results

that besides the sting vortex shedding another dominating frequency (approximately 1750 [Hz]) is found in the power spectrum somewhere between 20% and 40% of the sting chord from the sting center line. This event is thought to represent the action of the slit vortex. Its presence at approximately 25% of the sting chord from the model center line is found as a local decrease in total pressure. It is remarkable that in roughly 30% of a sting chord downstream the sting trailing edge these vortices seem to have lost their strength. This is also seen in the calculations where aft of this point the slit vortex is no longer distinguished. As mentioned before it is thought that the slit vortex has an energizing function in the retarded flow region aft of the sting near the fuselage thereby facilitating a fast recirculation closure. This seems to be confirmed by this measurement. This would mean that more downstream the effects of the slit vortex have degraded. From a practical point of view this would be beneficial. Considering wind tunnel configurations including tail planes the slit vortex could affect the flow over these planes thereby complicating the correction of the interference considerably. For $\alpha = \beta = 0°$ this concern is however not justified.

In the last sections results of a Navier-Stokes calculation are used to study the near-field of model sting and fuselage. It is found that the near-field is dominated by complex flow phenomena: the boundary layer relieving effect in front of the support on the fuselage pressure, the birth and growth of the slit vortex and the complex wake structure that is governed by local separation at the sting side, the slit vortex and sting base vortex shedding. It is concluded that the Navier-Stokes calculation is able to predict the measured flow phenomena qualitatively to a satisfying extent. The question remains however whether or not its prediction is good enough in order to serve as a tool for calculating model sting disturbances to a satisfying quantitative extent. In order to judge on the quantitative prediction capabilities of this solver for the configuration under consideration the contributions that determine the interference quantitatively are identified.

4.3.3 A subdivision of model sting near-field disturbances

A method that allows a systematic quantitative assessment of the contributions of model sting near-field effects necessitates a subdivision of the disturbances in effects that can be studied separately. A study on these effects is facilitated by a division of the fuselage into 4 main regions as shown in Figure 4.20: regions A, B, B1, C and D. The definition of regions A to D is as follows:

- Region A: from the model nose to the sting gap leading edge,
- Region B: from the sting gap leading edge to the trailing edge of the sting gap,
- Region B1: the cavity and slit,
- Region C: from the sting gap trailing edge to just aft of the recirculation area on the fuselage,
- Region D: from just aft of the recirculation area to the trailing edge of the fuselage.

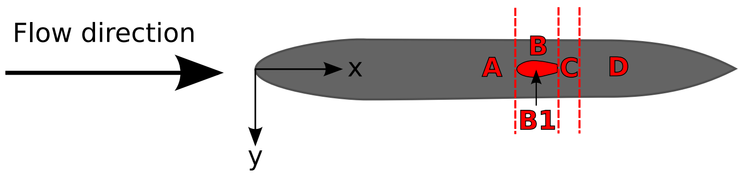

Figure 4.20: A graphical representation of the division of the model fuselage in regions A, B, B1, C and D

Using the proposed division, the near-field effects can be classified according:

1. A pressure distribution carry-over from the support to the fuselage. The fuselage pressure distribution is contaminated by the presence of the support. Examples of this effect are the adverse pressure gradient upstream the nose of the support on the fuselage and the carry-over of a low pressure area of the support (due to the acceleration of the flow at the support side) on the fuselage. This effect is from now on called the **carry-over effect**. This effect is mainly found in two regions designated as region A and region B (Figure 4.20),

2. Disturbances caused by the presence of the model cavity and slit separating the model support and fuselage at the support entry location:

- A momentum exchange between the freestream and the fluid inside the cavity (through the slit) leading to disturbances in the values of the longitudinal and lateral coefficients of the fuselage: the **cavity momentum effect**. This effect is studied in the slit and internal cavity and is expressed in a pressure disturbance (region B1),
- The effects of a complex flow pattern at the slit leading to the contamination of the region around the support: the **slit contamination effect**. This effect consists of a pressure disturbance and a disturbance in the shear stress distribution that mainly play a role in region B. An example of this effect is the disturbance induced by the slit vortex.

3. Disturbances in front of, around and aft of the model support on the fuselage due to viscous phenomena, the **viscous effect**:

    - Fuselage boundary layer skewing in front of the support (from a 2D to a 3D boundary layer as shown in Figure 3.1(a)) and shear effects besides the support on the fuselage. These are the effects on the shear stresses in regions A and B,
    - The recirculation area on the fuselage aft of the support. This is a viscous phenomenon caused by flow separation at the sting trailing edge. It affects the local pressure distribution and the shear stress distribution. The area of interest is referred to as region C,
    - The influence of the model support wake on the fuselage aft of the recirculation. This is a viscous phenomenon that affects the pressure distribution and the shear stress distribution in region D. Another effect is the recovery effect of the fuselage boundary layer downstream the recirculation area. This effect depends on the wake influence of the support and is therefore not treated separately but included in the wake effect.

Results of the Navier-Stokes calculations are used to quantify the importance of each above mentioned disturbance.

4.3.4 Evaluating disturbance contributions

In this section, the aforementioned contributions to model sting near-field effects are studied locally in regions A, B, B1, C and D. This is possible by a Δ-calculation on the integrated values of pressures and shear-stresses at the fuselage. The results (for $\alpha = \beta = 0$ [deg]) are discussed in the following sections.

The carry-over effect

This effect is obtained by subtracting the integrated values of the static pressure over the fuselage parts A and B in lift- and drag direction for the case excluding the internal cavity, slit and model support (where only the wind tunnel test section and closed fuselage are modeled) from the case including these parts at $\alpha = \beta = 0°$ and $M_\infty =$

Table 4.3: The carry-over effect in regions A and B at $\alpha = \beta = 0°$ and $M_\infty = 0.179$

Region	ΔC_L [%]	ΔC_D [%]
A	78	100
B	22	0
Total	100	100

0.179 (a Δ-calculation on the integrated value of the static pressure). The results indicate the carry-over effects in lift- and drag direction (ΔC_L, ΔC_D) as shown in Table 4.3.

In Table 4.3 it is seen that for the lift-coefficient 78% of the carry-over effect is determined in region A and 22% in region B. In region A, the lift increases caused by the increase in pressure due to by the presence of the support. In region B, the lift decreases. This is caused by the projected under-pressure of the support (due to the support shape) on the fuselage causing the local pressure on the fuselage to drop. For the drag-coefficient, the carry-over effect is determined by the contribution in region A because in region B, the fuselage normals have no component in streamwise direction (the angle of attack is 0°). In region A, the aforementioned pressure increase creates an increase in drag (which is logical considering the orientation of the normals on the fore body).

When these numbers are translated to a discrete magnitude in counts (using the reference area mentioned in Table 3.2) it is seen that the carry-over effect in regions A and B has a significant impact on the lift-coefficient (order of magnitude = 10 and 3 [counts] respectively). These effects are still moderate because of the relieving effect of the slit on the pressure peaks of the fuselage. The disturbance of the drag-coefficient in region A is in the order of 3 [counts].

The cavity momentum effect

This effect is evaluated by a Δ-calculation on the integrated value of the static pressure in the cavity and slit. For this test condition only the drag of the model is affected. The effect is caused by a pressure disturbance in region B1.

The intake of high momentum fluid is not governed by viscous processes because the flow does not separate in front of the support where the momentum exchange is initiated. This means that for a broad range of angles of attack and sideslip, much faster methods become available for calculating the cavity momentum effect. In addition, multiple Euler calculations on the same geometry are carried out in order to state more on the magnitude of this effect. It is calculated that the effects on lift and side force are negligible (negligible implies one order of magnitude smaller than typical balance accuracy shown in Table 3.2). The result for the drag-coefficient is shown in Figure 4.21.

The effect on the drag-coefficient is small as seen in Figure 4.21. Compared to the RaNS calculation, the Euler calculation shows an effect on the drag-coefficient that is

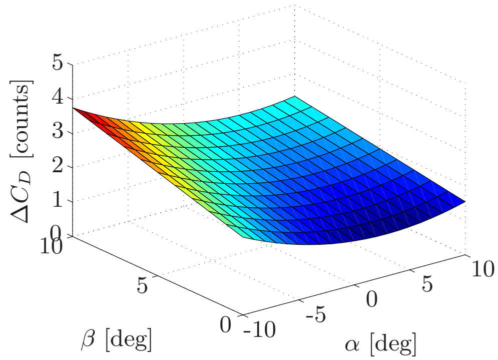

Figure 4.21: The cavity momentum effect calculated by an Euler code showing the disturbances in drag-coefficient at $M_\infty = 0.179$

approximately 3 [counts] smaller than calculated by the Navier-Stokes code, a satisfying agreement as it equals typical balance accuracy shown in Table 3.2.

The slit contamination effect

In order to study this effect Δ-calculations on the integrated value of the static pressure and shear stresses are performed in region B where the slit vortex influences the flow. These calculations reveal the slit contamination effect on the lift- and drag-coefficients of the fuselage. The results are shown in Table 4.4.

Table 4.4: The slit contamination effect for region B at $\alpha = \beta = 0°$ and $M_\infty = 0.179$

Type of disturbance	ΔC_L %	ΔC_D %
Inviscid	100	0
Viscous	0	100
Total	100	100

From Table 4.4 it is seen that the lift interference in region B is determined by pressure disturbances (of magnitude O(6) [counts]). The viscous disturbance is found to be negligible. For the drag of region B, the interference is governed by disturbances in the shear stress field. The magnitude of this contribution is however negligible at this angle of attack.

The viscous effect

These disturbances are found by a Δ-calculation on the integrated values of shear stresses in regions A, B, C and D and integrated values of the static pressures in regions C and D. Table 4.5 gives the values of these disturbances.

In Table 4.5 it is seen that the largest viscous disturbance on the lift-coefficient is found in region A. This is probably caused by the disturbance of the incoming 2D boundary

Table 4.5: The viscous effect for regions A, B, C and D at $\alpha = \beta = 0°$ and $M_\infty = 0.179$

Region and type of disturbance	ΔC_L %	ΔC_D %
A: Δ(shear stress)	72	59
B: Δ(shear stress)	0	22
C: Δ(shear stress)	14	7
D: Δ(shear stress)	14	12
C: Δ(pressure)	34	0
D: Δ(pressure)	66	100
Total Δ(shear stress)	100	100
Total Δ(pressure)	100	100

layer in front of the model support (schematized in Figure 3.1(a)). Regarding the absolute values, this effect is negligible. It can thus be concluded that the lift-coefficient is not influenced by viscous processes from the viscous effect. This also proofs to be the case for the drag-coefficient.

When the pressure disturbances of the viscous effect on the lift- and drag-coefficients are studied in regions C and D it seems that in these regions the recirculation and the wake influence are noticeable on the fuselage as they have maximum disturbances on the lift-coefficient of 3 and 6 [counts] respectively. In region C, the lift decreases. This is due to the action of the base vortices causing the local pressure to drop. In region D, the pressure increase on the fuselage causes the lift to increase. This pressure increase is caused by the effects of the support wake on the fuselage and the recovering boundary layer. This is only very local for the current sting placement as pressure measurements have indicated (up to approximately 30% of the afterbody length invariant of the angle of attack). For the drag-coefficient, the only noticeable disturbance is located in region D with a magnitude of 2 [counts]. The pressure increase causes the local drag to decrease. This is understandable considering the afterbody normal orientation.

Intermediate conclusions

When the results of the Navier-Stokes calculation as presented in the last sections are summarized, some conclusions can be drawn about the disturbances determining the near-field effects for this configuration:

1. The carry-over effect delivers a significant contribution to the model sting near-field disturbance,

2. The cavity momentum effect is negligible,

3. The slit contamination effect is pronounced as a significant change of pressure on the fuselage caused by the slit vortex. Viscous disturbances created by this vortex are negligible,

4. The viscous effect causes significant pressure changes in the recirculation area on the fuselage and at the backbody of the fuselage. Shear stress disturbances are negligible.

Besides simulations at an angle of attack and angle of sideslip of 0°, simulations are also performed at $\alpha = 8°$ and $\beta = 0°$ at the same freestream speed. These calculations are validated in a similar way as shown in the last sections. Some conclusions can be drawn for these calculations:

1. Qualitatively, the interference flow field does not change compared to the calculation at $\alpha = 0°$ and $\beta = 0°$,
2. Quantitatively, the differences with the measurements increase. These differences are found in regions of complex physics (just in front of the model sting on the fuselage and aft of the model sting on the fuselage). An analysis of this difference follows in section 4.4,
3. When studying the separate disturbance contributions it is found that the magnitude of the pressure- and shear stress disturbances is invariant with angle of attack in regions A, B and B1. It is seen that the disturbance ability of the model sting increases with angle of attack due to an increased bluntness of the model sting. However due to the relieving effect of cavity and slit only the backbody of the fuselage is seen to be affected by this. This translates into a higher value of the viscous effect mainly noticed in region D (where the disturbance becomes twice as high).

The Navier-Stokes calculations provide a substantial amount of information used to clarify the near-field of model sting and fuselage. A picture that summarizes the most prominent disturbances is shown in Figure 4.22.

The CFD results agree with experimental data on a qualitative basis. Therefore it can be concluded that this type of Navier-Stokes calculation is indeed suitable for calculating the model sting near-field interference qualitatively for this configuration. This however does not provide enough information regarding the applicability of these calculations to calculate model sting interference in general. For that purpose more validation is needed on the quantitative prediction capabilities. To this end, results of the Navier-Stokes calculations are compared to balance measurements as presented in Chapter 3.

4.3.5 Comparison to balance measurements

The quantitative prediction capabilities of the RaNS calculations are assessed by performing Δ-calculations on the total forces on the fuselage at $\alpha_\infty = 0°$ and 8°. The results of this exercise are compared to results of balance measurements discussed in Chapter 3. The comparison is given in Figure 4.23.

It is seen in Figure 4.23 that the calculated disturbances are of the same order of magnitude as shown by the balance measurements, but the Navier-Stokes solver is not able to calculate the disturbances with the right trends and within the experimental accuracy bandwidth. Aforementioned disturbance contributions are apparently under- or overestimated by the RaNS calculation. In order to find the source of this quantitative mismatch, regions A to D (Figure 4.20) need to be re-examined.

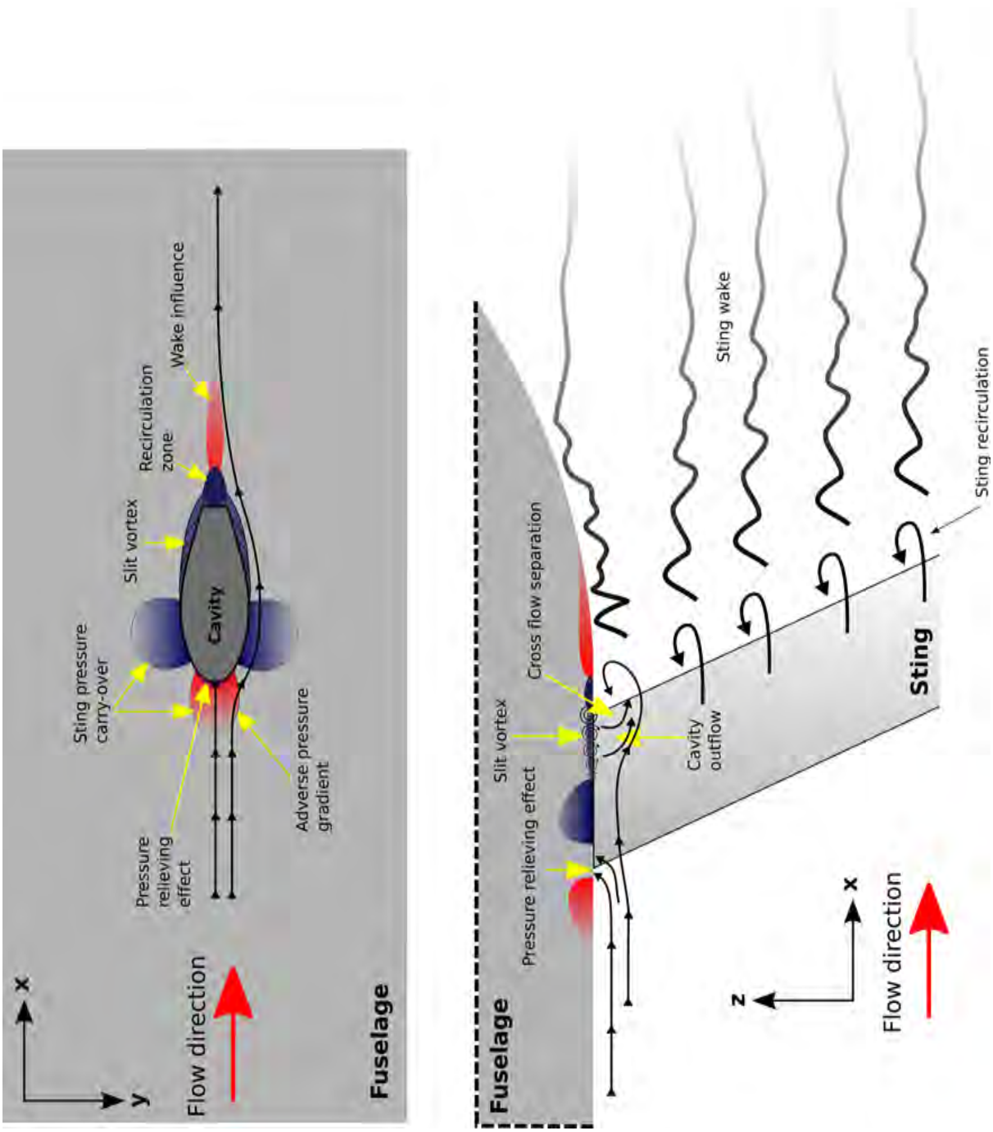

Figure 4.22: Two views of the fuselage showing the most prominent near-field interference characteristics (schematized)

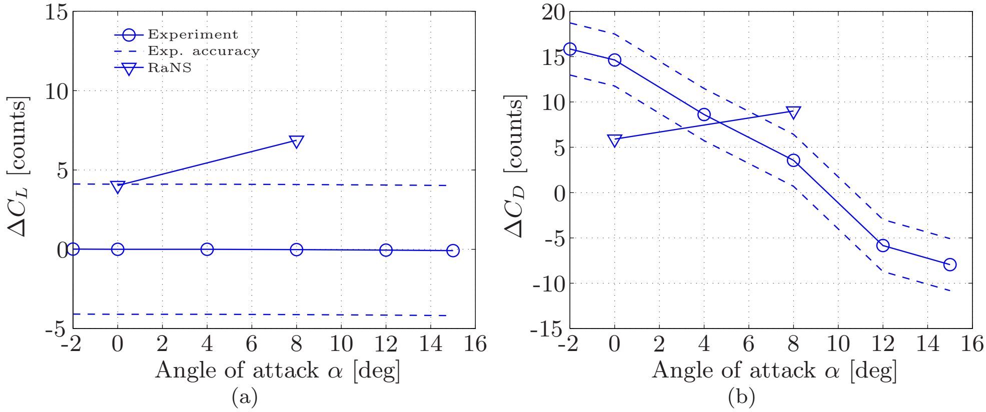

Figure 4.23: Measured and calculated model sting near-field effects on the (a) Lift-coefficient (b) Drag-coefficient on the fuselage at $\beta = 0°$ and $M_\infty = 0.179$ in the LTT of TUD

In region A, it is found that the local pressure increases due to the presence of the model sting. When the angle of attack is increased this contribution increases the lift and drag. For regions B and C, the opposite is true. The sting disturbance provides net under-pressures in these regions. When increasing the angle of attack, these under-pressures generate forces in the negative lift- and drag directions. On the backbody in region D, over-pressures are generated. These over-pressures (that increase with angle of attack) manifest in regions with a small curvature of the fuselage (at most 3°). This means that when the angle of attack is increased, positive contributions are generated for the increase in lift and drag. When the total picture of the measured drag interference (Figure 4.23(b)) is inspected, it is seen that the trends are of declining type: the measured drag interference decreases with angle of attack. Considering the contributions just mentioned, the following seems obvious: the Navier-Stokes solver is likely to underestimate the values of the pressure disturbance Δp in regions B and C and/or overestimate the values of Δp in region D. This believe is strengthened when inspecting Figures 4.24(a) and (b).

Based on Figure 4.24, the following is concluded:

1. From Figure 4.24(a) it is seen that indeed in region B and C (orifices 16 and 17) the calculated pressure disturbances are generally underestimated,

2. On the backbody of the fuselage (Figures 4.24(b)) the calculated pressure disturbances are indeed too high,

3. When Figure 4.24(a) is studied, it is clear that the pressure peak in region A and thus the positive contributions to the lift and drag are underestimated by the RaNS calculation. Considering the trend of the drag-coefficient measured by

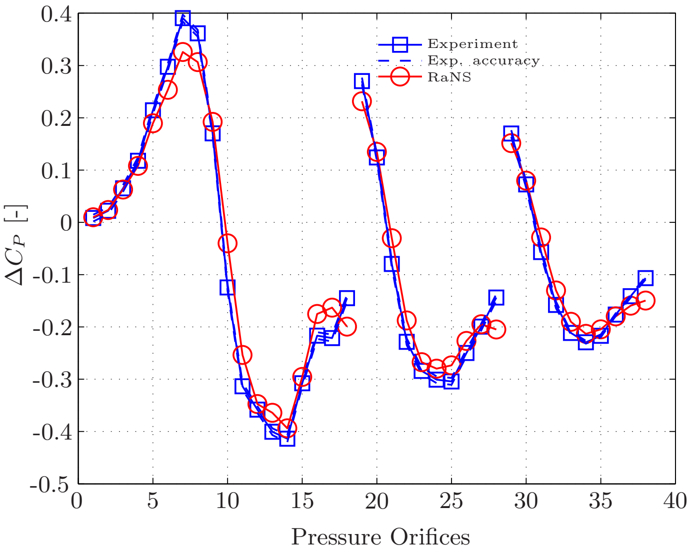

(a)

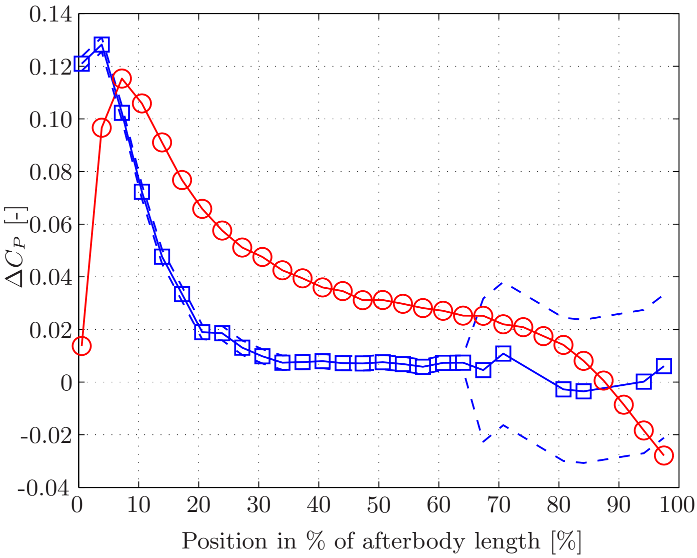

(b)

Figure 4.24: Comparison of measured and calculated pressure disturbance distributions on the fuselage at $\alpha = 8°$, $\beta = 0°$ and $M_\infty = 0.179$ (a) Pressure disturbances around the model sting (T1, T2 and T3 in Figure 4.16(a)) (b) Pressure disturbances on the tail section center line of the fuselage (T4 in Figure 4.16(b))

the balance, underestimation of pressure disturbances in regions B and C and overestimation in region D therefore become even more obvious.

It can be concluded that this RaNS calculation encounters difficulties in accurately predicting the quantitative pressure disturbances in regions A, B, C and D. This is not surprising considering the complex flow phenomena in these regions (the relieving effect, the slit vortex, recirculation and the sting wake influence). These Navier-Stokes calculations provide a qualitative image of the interference flow field that complies with measurements. Quantitatively however, the calculations are not able to determine the values of the near-field interference with the right trends and within measurement (balance) accuracy.

Multiple calculation techniques have been applied to calculate the near-field effects such as panel code calculations and Euler calculations (Chapter 3) and Navier-Stokes calculations. Now that the near-field flow topology is clarified, a more decisive answer can be given for each method on how well they perform qualitatively and quantitatively in determining model sting near-field effects. This provides an overview of the restrictions of these methods for calculating the model sting near-field effects for this configuration. This information is extrapolated to other support setups.

4.4 Model sting near-field calculations reviewed

An analysis of the competence of panel code-, Euler code- and Navier-Stokes calculations in determining the near-field model sting effects is best performed by comparing the pressure disturbance distribution calculated by all of these methods to experimental values at $\alpha = 8°$, $\beta = 0°$ and $M_\infty = 0.179$ as the differences between the methods are pronounced at these conditions. A comparison of the pressure disturbances as measured and calculated is given in Figure 4.25.

First, consider the ability of the numerical methods to resolve the adverse pressure gradient (orifices 1 to 7 in Figure 4.25(a)).

4.4.1 Resolving the adverse pressure gradient

Considering the performance of the applied numerical methods in resolving the adverse pressure gradient, the following is concluded:

1. The panel code overestimates the adverse pressure gradient and the resulting peak value of the pressure disturbance on the fuselage close to the sting (at the fuselage center line). This seems to be caused by the fact that the slit separating the sting and fuselage is not modeled. This implies that the relieving effect on the fuselage pressure is not resolved,

2. Both pressure gradient and peak value are estimated accurately by the Euler calculation where this relieving effect is included. This is also a clear sign of the fact that no significant viscous phenomena (like separation) occur in this region,

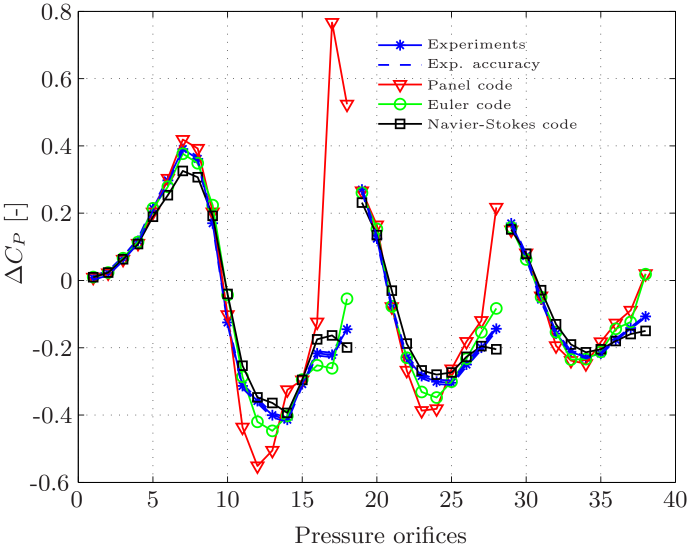

(a)

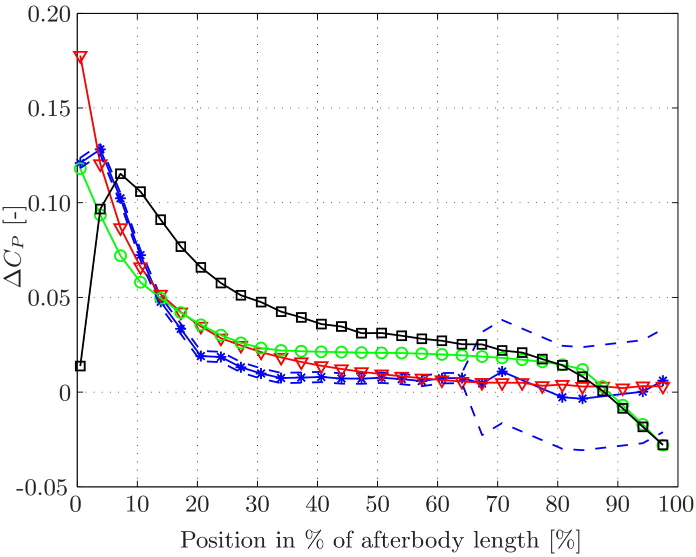

(b)

Figure 4.25: Comparison of measured and calculated (all the numerical techniques applied) pressure disturbance distributions on the fuselage at $\alpha = 8°$, $\beta = 0°$ and $M_\infty = 0.179$ (a) Pressure disturbances around the model sting (T1, T2 and T3 in Figure 4.16(a)) (b) Pressure disturbances on the tail section center line of the fuselage (T4 in Figure 4.16(b))

3. The Navier-Stokes calculation is unable to predict the gradient and peak value of the pressure disturbance on the fuselage in front of the sting accurately, both estimations are considerably lower. Considering that the relieving effect is once again included in the calculation, this offset is thought to be caused by the inability of the turbulence model to cope with adverse pressure gradients[1]. It seems that in the effort to model the viscous behavior using a carefully chosen turbulence model, this modeling afflicts more damage to the results than when the boundary layer would not be modeled at all (compared to the results of the Euler calculations). The essential inability of eddy-viscosity turbulence models to simulate anisotropic turbulence is thought to constrain the accuracy in this region.

4.4.2 Resolving the sting side pressure disturbances

Consider the agreement at pressure orifices 12, 13 and 14 just aft of the thickest point of the model sting: the pressure drop on the fuselage (by a carry-over of the pressure drop at the sting side) is resolved by the calculations. The differences between the measurements and calculations is most probably related to the properties of the calculated sting wake[2].

It should be kept in mind that the local pressure distribution around the sting is affected by the flow separating at the sting trailing edge. When the calculated sting wake is for example too thick or the wake strength is overestimated, the pressure at the sting side is overestimated. This leads to an underestimation of the negative pressure disturbances from the sting side on the fuselage. Overestimation of the wake strength is seen in the results of the Navier-Stokes calculation. When the Euler results are reviewed, the opposite seems to establish. The calculated "wake" is small leading to small positive pressure disturbances at the sting side and leading to larger negative pressure disturbances from the sting onto the fuselage. For the panel code calculation the wake strength is overestimated. In this case however the discrepancy is likely to be caused by a lack of pressure relieve from the cavity leading to an overestimation of the disturbance of the sting side onto the fuselage.

[1] It might be argued that this offset is caused by the difference between the measured and calculated boundary layer thickness: when boundary layer measurements on the fuselage are compared to results of the Navier-Stokes calculations, it seems that the value of δ_{99} is overestimated with approximately 25% by the Navier-Stokes solver, approximately half a sting chord in front of the slit leading edge on the fuselage center line. The value of the displacement thickness is also overestimated with the same order of magnitude. It could be argued that the effective streamlines calculated by the Navier-Stokes code therefore maintain a larger distance to the fuselage than in reality. This implies that when the streamlines arrive at the slit leading edge, they are separated by a larger distance to the leading edge of the sting (remember that the sting is swept backwards). This causes the gradient of the pressure disturbance and thus also the pressure disturbance in the boundary layer to be smaller. The difference in boundary layer displacement thickness (O(0.3) [mm]) seems to be caused by the fact that in the measurements, the boundary layer on the fuselage is tripped at 20% of the fuselage length from the nose whereas in the Navier-Stokes calculations, the boundary layer is turbulent from the nose on. Combined panel code/boundary layer calculations on a plain fuselage assess this difference. The difference in displacement thickness indeed proves to be 0.3 [mm]. The difference between boundary layer measurements and Navier-Stokes results is thus attributed to the transition location. The difference in boundary layer displacement thickness seems however too small to result in the above-mentioned pressure disturbance deficiency near the sting nose

[2] Regarding the Navier-Stokes results it might be argued that this difference is caused by erroneous boundary layer calculations caused by the transition location: the calculated boundary layer at the

4.4.3 Resolving wake characteristics

Panel code wake prediction

The wake influence is reflected by pressure orifices 16, 17 and 18. The panel code pressure disturbances show a poor comparison with measurements. This is understandable because in the panel code discretization, the wake is defined with uniform spanwise properties (an averaged velocity of 10% of the freestream value, based on results of a hot-wire measurement in the sting wake). The result is that the positive pressure disturbance by the wake is overestimated near pressure orifice 16. Because no recirculation region on the fuselage is calculated by the panel code, the pressure disturbance predictions are poor near pressure orifices 17 and 18 (the decrease in pressure caused by base vorticity is not resolved).

Euler wake prediction

Comparing the Euler results to the measurements, it seems at first somewhat strange, but the trends of the disturbances are in agreement with the measurement. The results of the Euler calculations presented in Figure 4.25 are governed by its numerical discretization. In this discretization the convective fluxes are approximated by a second order central scheme.

Consider the convection of the local streamwise velocity component u in streamwise direction. According to the central scheme, this term is approximated by:

$$\frac{\partial u}{\partial x} \approx \frac{\partial u}{\partial x} + C_2 \frac{\partial^2 u}{\partial x^2} + C_4 \frac{\partial^4 u}{\partial x^4} \tag{4.1}$$

In Equation 4.1 the second and third term on the right hand side are seen as artificial dissipation. The constants C_2 and C_4 are proportional to Δx^2 and Δx^4 respectively. This implies that when the mesh size decreases, the amount of artificial dissipation also decreases (in the limit where Δx goes to zero, the amount of artificial dissipation diminishes). When the flow at the sting side approaches the trailing edge of the sting it tries to "bend" around the trailing edge and create a stagnation point at the center of the sting trailing edge. When the trailing edge is sharp however (meaning that the angle between sting side at the trailing edge and sting base approaches 90°) this creates

sting side is too thick because during the calculations it is turbulent from the nose of the sting. During the measurements, the sting is tripped at 25% of the chord. In the calculations, this leads to a de-cambering of the model sting profile by overestimation of the boundary layer displacement thickness. The effect is a lower-than-measured pressure drop at the sting maximum thickness location. The pressure carry-over effect on the fuselage is therefore smaller in magnitude as seen in the figure. This seems to be confirmed when the results of the Euler calculation are reviewed. In that case, no boundary layer is calculated at all leading to a pressure drop that is too large. The panel code calculation shows a result that could be expected. The pressure drop on the fuselage is too large because no de-cambering effect of the sting is calculated as is the case with the Euler calculation. On top of this, no slit is discretized in the calculations. No relieving effect of the low pressure area on the fuselage by fluid from the cavity (in contrast to what is seen when analyzing measurements and the Euler- and Navier-Stokes results) is calculated. The de-cambering effect of an overestimated boundary layer displacement thickness on the pressure disturbances is quantified by applying a 2D viscous sting profile calculation using the freeware code *XFOIL* by Drela [76]. The results however indicate a negligible effect velocity gradients causing terms as $\frac{\partial^2 u}{\partial x^2}$ to go to infinity. Even with a very small mesh size at the sting trailing edge, this leads to a substantial amount of artificial dissipation according to Equation 4.1. These dissipation terms act as “numerical viscosity”. The dissipation does not only stabilize the calculation but also creates a flow pattern simulating separation at the sting trailing edge, recirculation of the flow aft of the trailing edge and an “Euler-wake” induced by the model sting.

This leads to a better agreement between calculations and measurements than if a stagnation point at the sting trailing edge would be introduced. The phenomena calculated are however not with a completely physical background and dependent on the amount of dissipation (partly governed by the coefficients of the Jameson dissipation scheme). This results in the fact that at pressure orifices 16, 17 and 18, the trends are similar to the measured trends, but the absolute values are off. When performing similar Euler calculations with this type of scheme it is recommendable to include a sharp trailing edge and minimize the amount of dissipation in the sting wake (by covering the sting trailing edge with typically 20 cells in spanwise direction and choosing a second order scheme for the discretization of the convective fluxes).

Navier-Stokes wake prediction

Studying the results of the Navier-Stokes calculation, the following becomes clear: at pressure orifice 16, the pressure disturbance is more positive than measured. When traversing from pressure orifice 16 to 17, it is seen that the pressure disturbance decreases somewhat in magnitude (whereas the measurements show a local increase in disturbance). At current it is thought that this is due to the fact that in the calculations, the flow through the slit trailing edge has some effect on the local pressure that is overestimated by the Navier-Stokes calculation, decreasing the local pressure disturbance caused by base vorticity. Furthermore according to Simpson [63] this reveals an essential inability of eddy viscosity closure models to simulate anisotropic turbulence, expressed in a poor calculation of the recirculation strength. Traversing to pressure orifice 18 the pressure disturbance increases again caused by the action of base vorticity. Compared to the measurements it is seen that this effect is more pronounced. Currently it is thought that this is due to the calculation of a recirculation area larger than shown by measurements.

Figure 4.25(a) shows that the trends of the pressure disturbances as discussed are consistent when moving away from the sting.

4.4.4 Backbody disturbances

Finally, the measured and calculated pressure disturbances at the backbody center line of the fuselage (T4 in Figure 4.16(b)) are considered.

Panel code backbody disturbance prediction

Referring to Figure 4.25(b), it is seen that the panel code indeed over-predicts the wake influence close to the sting. The calculated disturbances monotonically decrease to zero when the distance from the sting trailing edge is increased. The physical meaning of this curve is questionable because no viscous phenomena such as recirculation and boundary layer recovery are calculated on the fuselage behind the sting.

Euler backbody disturbance prediction

When the Euler results are compared to measurements it seems that the initial pressure disturbance at the backbody agrees well. The peak in the pressure disturbance that follows from the measurements is not resolved. A reason for this is that although a stagnation point is present on the fuselage aft of the artificial recirculation, this point is located closer to the sting trailing edge (the calculated "recirculation area" is smaller) and therefore not captured in this graph. The pressure disturbance is again seen to monotonically decrease to zero. Compared to measurements, the pressure disturbance is overestimated (wake closure is not properly simulated) but not to an extent equal as shown by the Navier-Stokes results.

Navier-Stokes backbody disturbance prediction

The Navier-Stokes calculation results in a behavior of the pressure disturbances that is similar to the measurements (at least the trend). It is seen that the positive pressure disturbance is at first rising (boundary layer recovery aft of the recirculation zone) to a maximum value. The starting point of the curve indicates that the calculated recirculation area is indeed larger than shown by measurements. Comparing the positions of maximum disturbance (this is the point from where a boundary layer starts to build up again) it is seen that the calculated recirculation area is approximately 25% larger than shown by measurements. Overall the pressure disturbances calculated by the Navier-Stokes code are larger than measured. This means that in reality, the sting wake fills up much faster than shown by the numerical results. This is typically caused by an erroneous calculation of turbulent flow properties by the turbulence model (like entrainment). It again seems that in the effort to model viscous behavior using a turbulence model, the modeling afflicts more damage to the results than not modeling the phenomena at all. The trends as shown in this figure are consistent when moving away from the sting center line.

Above-mentioned findings are summarized in Table 4.6.

From this analysis it is concluded that when the sting is positioned in an area causing small viscous disturbances, performing an Euler calculation seems a decent choice for calculating the disturbances from the viewpoint of accuracy and computational expenses. For these configurations it seems that in the effort to model viscous turbulent behavior by applying a turbulence model, this modeling might afflict more damage to the results than when these effects are not modeled at all (by increasing the amount of modeling, the total modeling error also increases). This only holds because the viscous disturbances are negligible (section 4.3.4). When however a configuration would be chosen that is prone to large viscous disturbances (discussed in section 4.5.1), applying a viscous analysis becomes inevitable. In that case the Navier-Stokes results will resemble the measurements better than e.g. Euler results. This however does not mean that the Navier-Stokes results are perceived as *accurate enough*. Because the panel code calculations are not able to cope with the modeling of cavity and slit (from a numerical point of view) that prove to be important for calculating the model sting disturbances (Table 4.6), panel code calculations are expected to perform poorly in calculating the model support disturbances of any configuration where internal balances are included.

Table 4.6: The ability of various numerical methods to capture dominant near-field model sting disturbances: the adverse pressure gradient in front of the sting on the fuselage, the projected disturbances from the sting side, near-wake disturbances and the disturbances at the fuselage backbody (B.B.). This ability is expressed by means of + and − signs where −− indicates a very poor ability and ++ indicates a very high ability

	∇P	**Sting Side Dist.**	**Near-Wake Dist.**	**B.B. Dist.**
Panel code	−− [1]	−− [1]	−− [2]	−− [3]
Euler code	+ [4]	− [5]	+ [6]	+ [7]
N.S. code	− [8]	− [9]	− [8]	− [10]

4.5 Desirable methods for determining model support interference

Various experimental and numerical techniques have been demonstrated for a study on the disturbances of the model sting. These techniques are used to clarify the disturbance flow field but also to validate several approaches for the determination of the interference. This is however carried out for a single sting placement with respect to the fuselage. In this section the available information is generalized to a much wider class of model sting placements. The knowledge is also extended to the treatment of the remaining support parts (such as e.g. a horizontal sting, torpedo, sword etc.).

4.5.1 Desirability of methods to determine model sting interference

To generalize on the desirability of methods for determining model sting interference, typical model sting placements should be defined. Figure 4.26 divides the fuselage in four typical regions where a sting placement is imaginable: regions R1, R2a, R2b and R3. Region R2b includes the constant cross-sectional part of the fuselage downstream of the mean aerodynamic center of the main wing. The study on model sting disturbances presented in the last chapters is carried out with the model sting in this region.

[1] Pressure relieving effect is not included because cavity and slit are not modeled
[2] Unable to model proper wake structure (recirculation area is not resolved)
[3] Overestimated by poor wake definition
[4] No significant viscous phenomena dominate this region
[5] Wake strength is underestimated
[6] Trend is governed by artificial viscosity
[7] Disturbances overestimated by lack of wake closure
[8] Related to the inability of eddy viscosity closure models to resolve anisotropy
[9] Wake strength is overestimated
[10] Sting wake filling is too slow

R2a comprises the constant cross-sectional part of the fuselage upstream the main wing mean aerodynamic chord. Region R3 includes the concave part of the fuselage at the fuselage tail. Because generally speaking this concave shape is only present at the ventral side of the fuselage the dorsal aft part is assigned to region R2b. Finally region R1 includes the nose of the aircraft.

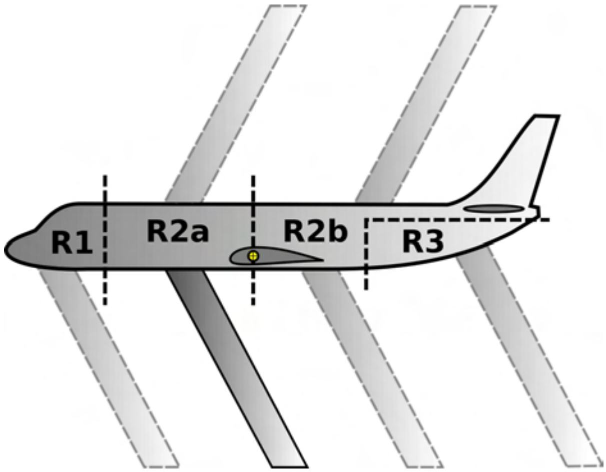

Figure 4.26: Four regions (R1, R2a, R2b and R3) of a typical wind tunnel model fuselage used for classification of the sting entry location. As a reference point, the mean aerodynamic center of the wing is defined as the separation between regions R2a and R2b. Typical ventral and dorsal sting setups are indicated

Based on the knowledge of model sting disturbances and the potential of experimental and numerical methods used to determine the interference for a sting placement in region R2b, the desirability of applying these methods to determine the sting interference for all other regions (R1, R2a, R3) is explored. Desirability is here expressed in a number of ways amongst which are **accuracy** and **effort**.

In reality, desirability is governed by a combination of the above-mentioned. Considering accuracy, the absolute accuracy in determining model sting disturbances is considered. For the interpretation of effort a distinction should be made between numerical methods and experimental methods. In the case of numerical methods modeling- and computational effort are valuable indicators. In the case of experimental methods effort is related to the amount of preparation and tunnel time. Both indicators for effort can be translated to costs. This translation is dependent on the company providing with the service (calculation or measurement) and therefore this translation is not considered here.

Accuracy

Based on the viewpoint of accuracy the desirability of applying several numerical and experimental methods for the determination of model sting interference is evaluated for a sting placement in regions R1, R2a, R2b and R3. The result of this exercise is given in Table 4.7.

In Table 4.7 the accuracy of various correction methods is given for typical sting placements (shown in Figure 4.26) for determining near-field and far-field disturbances. These results are characteristic for the juncture flow case including a cavity and slit. Unfortunately no additional literature reference is available. In this table, a mutual ranking is setup between methods with different ranges of applicability. Typically:

- For panel code calculations, -10° $\leq \alpha, \beta \leq$ 10°,
- For Euler calculations, -10° $\leq \alpha, \beta \leq$ 10°,
- For Navier-Stokes calculations, -20° $\leq \alpha, \beta \leq$ 20°,
- For measurements, -20° $\leq \alpha, \beta \leq$ 20°.

Table 4.7: The accuracy of various numerical and experimental methods in determining near-field and far-field effects of a typical model sting (shown in Figure 3.3) on a model containing an internal balance for all the sting placements indicated in Figure 4.26. This accuracy is expressed by means of + and − signs where −− indicates a very poor accuracy and +++ indicates a very high accuracy

Sting pos.	**Dist.**	**Panel c.**	**Euler c.**	**N.S. c.**	**Probe m.**	**Bal. Δ-m.**
R1	near-field	−−	+	−		++
R1	far-field	−−	+	−	++	+++
R2a	near-field	−−	+	−		++
R2a	far-field	−−	+	−	++	+++
R2b	near-field	−− [1]	+ [2]	− [3]		++ [4]
R2b	far-field	−− [5]	+ [6]	−	++ [7]	+++
R3	near-field	−−	−	+ [8]		++
R3	far-field	−−	−	+	++	+++

[1] See section 4.4 and Figure 3.11
[2] See section 4.4 and Figure 3.11
[3] See section 4.4 and Figure 4.23
[4] See Table 1.2 but also Eckert [18] for typical accuracy levels
[5] See section 3.4.2
[6] See section 3.4.2
[7] See section 3.2.4 but also Treaster et al. [77] for typical accuracy levels
[8] See Figure 4.28

The mutual ranking shown in Table 4.7 is only valid when the constraints of the methods in determining model sting interference (discussed in e.g. section 4.4) are not caused by crossing their ranges of applicability. Therefore, for -10° $\leq \alpha, \beta \leq$ 10°, Table 4.7 can be used completely. Outside of this range the integrity of the mutual ranking can only be guaranteed for the Navier-Stokes calculations and measurements.

Consider first the disturbances of a model sting placed in region R2b (the reference case). Regarding the near-field disturbances, the ranking of the numerical methods shown in Table 4.7 agrees with the results of Table 4.6 and is reflected by Figure 4.27. The ranking is based on both numerical and experimental results. The experimental method that outperforms the calculations is the balance Δ-measurement. Typical balance Δ-measurement accuracy levels are tabulated in Table 1.2.

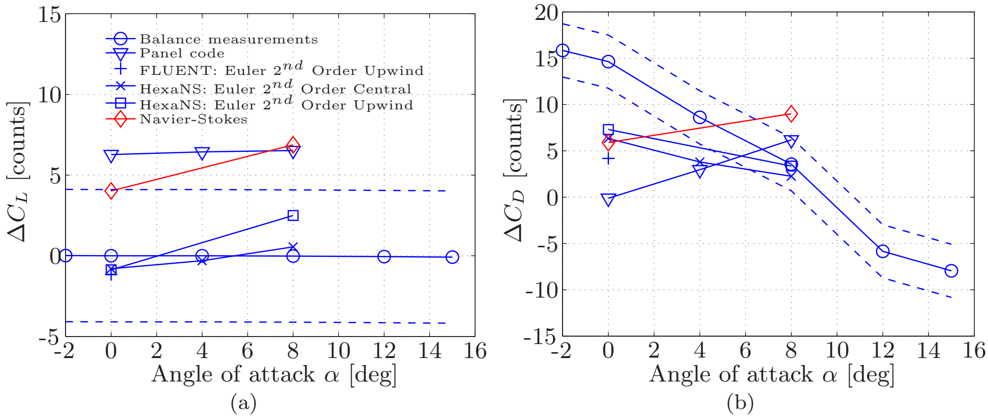

Figure 4.27: Comparison of experimental and numerical values of model sting near-field effects on (a) The lift-coefficient (b) The drag-coefficient of the fuselage of the setup shown in Figure 3.3

When it comes down to choosing a method to calculate the far-field model sting disturbances it is seen in Table 4.7 that the same ranking is applicable as for the near-field disturbances. Considering the model sting, its disturbances at for instance the lifting surfaces of an aircraft configuration partly depend on the disturbances manifesting in the near-field of sting and fuselage protrusion: when significant near-field effects are found, the far-field effects are influenced by these. Concluding: the success of the calculation of model sting far-field effects is partly dependent on the success of the model sting near-field effects (used in the derivation of the ranking of the Navier-Stokes calculations). This explains the ranking found in Table 4.7. The findings are in agreement to what is presented on the calculation of far-field effects by a panel code and Euler code in section 3.4.2. An experimental method that is preferable to performing an Euler calculation is the probe measurement. The measurement of the model sting far-field effects using a probe is described in section 3.4.2 using a 5-hole probe with characteristics as described in section 3.2.4 but also typically as described by Treaster et al [77]. Considering the accuracy of typical probe surveys, these are no match for balance Δ-measurements.

Consider a shift of the model sting to region R2a. Based on numerical- and experimental results of the sting placement in region R2b, a new ranking of methods is derived. Because the surface properties of the fuselage in region R2a and R2b are similar in terms of local curvature and thus in terms of local pressure gradients it is expected that the near-field effects manifesting in region R2b and R2a are similar both qualitatively and quantitatively. For the determination of the near-field effects this implies that a similar ranking can be applied as found for region R2b whereas even the absolute values of the accuracy of the mentioned numerical methods are not expected to change significantly. Also for the determination of the far-field effects, a similar ranking is maintained as for an R2b placement of the model sting. The absolute values of the accuracy of the numerical methods is however thought to change. This is caused by the position of the wing with respect to the model sting: as explained in section 3.4.2 discrepancies in the discretization of the sting wake increase the error in the prediction of the sting disturbances. When the sting is positioned in front of the mean aerodynamic center of the wing, the wing suffers from a prediction of the far-field effect with a lower accuracy than if the wing would be positioned upstream the model sting caused by the proximity of the mean aerodynamic center to the sting wake. The larger the distance between sting base and wing mean aerodynamic center, the smaller this effect becomes. Although the absolute values of the accuracy of the numerical methods is affected by this to a measurable extent, the mutual ranking is thought to be the same as for an R2b placement of the sting.

Moving the model sting even more upstream results in an R1 placement. In this region there are mainly two factors that might influence the topology of the interference flow:

1. The properties of the incoming boundary layer (that proves to be laminar unless tripped),
2. The nature of the pressure gradient (favorable).

It is expected (based on preliminary results of a Navier-Stokes calculation of a model sting protruding region R1) that both qualitatively and quantitatively a similar disturbance pattern manifests as given for an R2a placement[1]. This leads to a similar ranking of methods in order to determine the model sting near-field effects. The absolute accuracy of the methods is expected to coincide as well. Considering the position of the sting with respect to the mean aerodynamic center of the main wing, similar ranking and absolute levels of accuracy for the methods to determine the far-field effects as in region R2a are expected.

[1]The boundary layer emanating from the stagnation point on the fuselage nose is likely to be laminar (especially considering the favorable pressure gradient in the outer region caused by the shape of the fuselage nose). It is hereby assumed that the boundary layer is not tripped right away on the nose by artificial means (such as surface roughness) or a high turbulence level in the wind tunnel. The laminar boundary layer is fragile at this point and therefore susceptible to disturbances in the flow. It is however expected that the flow topology around the sting nose and sting side on the

Disturbances by viscous phenomena on the model fuselage caused by the model sting are found predominantly aft of the sting in regions C and D indicated in Figure 4.20. These phenomena are confirmed by both pressure measurements and oil flow visualization on the fuselage but also qualitatively by the Navier-Stokes calculations (as mentioned in section 4.3.5 the quantitative disturbance contributions are under- or overestimated leading to the trends shown in Figure 4.27. The numerical error is reflected by a disturbance of the balance between the various disturbance contributions). When strong recirculation regions exist on the fuselage and the boundary layer is discouraged to recover by the presence of some adverse pressure gradient, the viscous disturbances are expected to increase significantly. Adverse pressure gradients are mainly found at the backbody of typical fuselages such as in region R3.

Placing the model sting in region R3 large viscous disturbances are generated on the fuselage leading to the necessity of a Navier-Stokes analysis. This is shown by a Navier-Stokes calculation ($\alpha = \beta = 0$ [deg] and $M_\infty = 0.179$) on the axi-symmetrical fuselage shown in Figure 4.20 with the leading edge of the sting entering the fuselage at 87% of its length from the nose. The sting is located at the backbody in an adverse pressure gradient caused by the shape of the fuselage tail. This confirmation calculation yielded the result that compared to the sting placement at the cylindrical part of the fuselage, the interference on the fuselage lift-coefficient increases with a factor 2 and the interference on the drag-coefficient by a factor 7. This last result is confirmed by Veldhuis [12] in a similar experiment. It is seen that the flow at the backbody shows extensive areas of separated flow. In these areas, fuselage boundary layer reattachment is discouraged by the afterbody pressure gradient. A comparison of calculated streamlines at the backbody and illustrated results of the oil flow experiment described by Veldhuis is given in Figure 4.28.

For this sting placement it is thought that Euler calculations no longer provide appropriate qualitative and quantitative assessments of the near-field disturbances (panel code calculations are out of the question because of the lack of ability to model the internal balance cavity and slit but also the absence of viscosity in the calculations and the difficulty in modeling the sting wake). Navier-Stokes calculations and balance Δ-measurements are in this situation seen as the only applicable methods to determine the near-field interference. Modeling viscosity and calculating turbulence by applying a turbulence model is more profitable compared to the case of an R1, R2a or R2b placement of the sting where the modeling error overrules the disturbance of interest.

fuselage is similar as described in section 4.3.1. Because the boundary layer on the fuselage is still developing the incoming thickness is much smaller than in the case of an R2b placement. This makes it more sensitive to the relieving effect by the slit (the boundary layer thickness to slit width ratio decreases). On top of this, the adverse pressure gradient caused by the presence of the model sting is partly relieved by the shape of the fuselage nose. These considerations lead to the assumption that the laminar boundary layer in front of the sting does not separate but is relieved by the cavity and slit leading to the flow topology as described in section 4.3.1. This assumption is confirmed by initial results of a Navier-Stokes calculation of a model sting protruding region R1. The local boundary layer on the fuselage transits to turbulent. This transition is promoted by the turbulent sting boundary layer but also by secondary flow features such as the slit vortex. Aft of the sting on the fuselage, the recirculation area closes fast. The separated turbulent boundary layer is not only influenced by the effects of the slit vortex but also by a favorable pressure gradient (caused by the placement of the model sting) encouraging the recirculation closure and growth of a new boundary layer

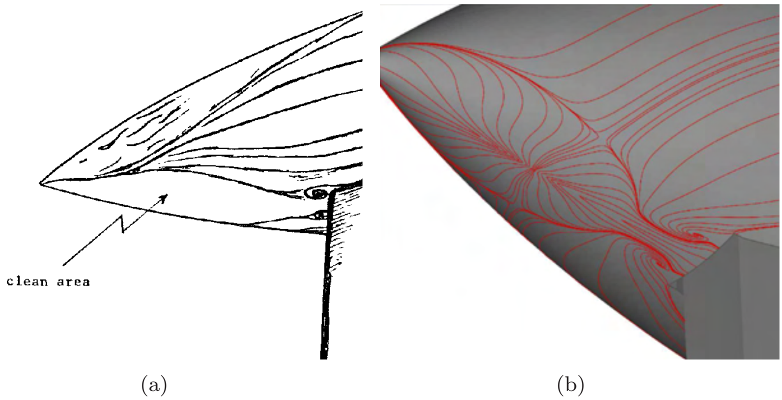

Figure 4.28: Comparison of measured (a) and calculated (b) streamlines on the backbody of an axi-symmetrical fuselage with the same geometry at $\alpha = \beta = 0$ [deg]. The model sting penetrates the fuselage boundary layer in an adverse pressure gradient. Experimental results are taken from Veldhuis [12]

This however does not mean that for the intended purpose a Navier-Stokes calculation provides an answer that is accurate enough. To this end balance Δ-measurements can be performed in order to obtain optimal accuracy (Table 1.2). These considerations are reflected by Table 4.7. Because of the increase in magnitude of the near-field effects for an R3 sting placement, the far-field effects are defined to a much larger extent by the near-field phenomena than for any other sting placement. This also implies that the success of calculating the far-field effects is thought to depend for a significant part on the success in calculating the near-field effects. This explains the ranking of methods to determine the far-field effects for an R3 placement given in Table 4.7.

Effort

As mentioned at the beginning of this section there is another criterion to express the level of desirability of a method to determine model sting near-field and far-field effects: effort. For the assessment of numerical methods, modeling- and computational effort are taken into consideration. For experimental methods effort is related to the amount of preparation and tunnel time. Just as for the accuracy, the desirability of implementing various numerical and experimental methods to determine model sting interference from the viewpoint of invested effort can be expressed. The result is given in Table 4.8. In the table more minus signs indicates that more effort should be invested in order to implement the method. More plus signs therefore reflect a more desirable scenario.

In Table 4.8 no distinction is made between the various sting placements in assessing the effort of the various methods. Various sting placements are not seen to affect the mutual ranking of the methods shown in the table, although shifting the sting entry location might increase or decrease the effort of a particular method: when a Navier-Stokes determination of the interference is implemented with the sting in region R1,

Table 4.8: The desirability of implementing various numerical and experimental methods to determine the near-field and far-field effects of a typical model sting (shown in Figure 3.3) on a model containing an internal balance from the viewpoint of effort for all the sting placements indicated in Figure 4.26. This desirability is expressed by means of + and − signs where −− indicates a very low desirability and +++ indicates a very high desirability

Sting pos.	**Dist.**	**Panel c.**	**Euler c.**	**N.S. c.**	**Probe m.**	**Bal. Δ-m.**
All	near-field	+	++	−−		−
All	far-field	++	+++	−−	−	+

more modeling- and computational effort is necessary than in the case of an R3 placement. This is because the complete wake trace of the sting over the fuselage should be resolved implying a larger amount of computational cells due to refinement in- and near the wake.

First, consider the ranking of the determination of the near-field effects. The lowest ranking is given to a Navier-Stokes calculation because:

1. For every freestream condition (α, β and M_∞) two calculations should be performed for a Δ-determination of the interference,

2. Because of the need to model the wind tunnel walls (reflected by Carlin et al. [10]) the geometry and computational mesh should be redefined for every calculation,

3. Navier-Stokes calculations require quite some computational effort depending on the mesh size, turbulence treatment, discretization and number of calculation steps etc.

The determination of a complete interference polar of a given aircraft configuration where the α, β plane is discretized by 16 points (4 angles of attack at 4 sideslip angles) at given Mach number would necessitate at least 32 Navier-Stokes calculations. This would require a tremendous effort lasting months.

One ranking higher the balance Δ-measurement is found. The effort of performing these measurements depends on the adjust-ability of the model and dummy support in the wind tunnel. Generally speaking measuring a comparable interference polar as just mentioned would require an effort typically in the order of weeks. If the model contains an internal balance, the model should be suspended by an alternative means whereas the dummy sting should be inserted into the internal balance cavity but remains detached from the model. A typical example of such a measurement is given in section 3.2. Similar setups require consideration of performing the measurement in a practical way (how to take care of the repositioning of the dummy sting during the measurements for example). The preparation of these tests however also requires quite some effort considering the design and manufacturing of the dummy setup.

Next, consider the panel code calculation. Like the Navier-Stokes calculations interference polars can be determined by Δ-calculations. The aforementioned 32 calculations however would typically be performed in the order of a day. The amount of computational effort is far less than required for a Navier-Stokes calculation. One of the great disadvantages of the panel calculation however is the extensive amount of required modeling. Besides geometrically modeling the wind tunnel, model fuselage and model sting and meshing these surfaces, a lot of effort needs to be invested in setting up the appropriate boundary conditions such as the definition of the sting wake: properties and trajectory are related to the paneling of the wind tunnel model fuselage and sting but also on its predefined characteristics (such as wake strength) that often needs tuning using experimental results. All together the amount of effort for the determination of sting interference using a panel code would typically imply weeks.

Finally considering the Euler calculations, the computational effort classifies somewhere in between the panel code calculation and Navier-Stokes calculation. 32 calculations can typically be performed in the order of weeks. This is because no boundary layers are discretized in the calculations (implying smaller computational meshes) and fewer equations should be solved compared to a Navier-Stokes analysis. The modeling of the geometry takes the same amount of time as for the panel code calculation and Navier-Stokes calculation. Discretizing the continuum and setting boundary conditions however requires far less effort than for panel code calculations or Navier-Stokes calculations. This ranks this method as the most desirable method for the calculation of sting near-field interference.

Considering the determination of the far-field effects it is seen that a similar ranking is applied. There is however one method added to the list: probe measurements. For probe measurements, similar considerations as for balance Δ-measurements hold. However probe measurements take a lot more effort: for every measurement point volumes need to be probed for a spatial representation of the disturbances (an example of such a measurement is given in section 3.2). Due to this significant increase in effort the probe measurements is classified in between the Navier-Stokes calculations and balance Δ-measurements.

Conclusions: determining sting interference

Generally speaking, whenever possible from a practical point of view, the model sting should be positioned such that the manifesting disturbances are “correctable”. By correctable it is meant that the disturbances are of such magnitude that the “signal-to-noise ratio” (or uncorrected measurement to disturbance ratio) allows to retrieve the undisturbed signal with ample accuracy (comparable to balance accuracy). This implies that a support setup is desirable with small model support disturbances and a correction method that is accurate enough to correct for these. Based on considerations defining Tables 4.7 and 4.8 it is advisable to place the model sting (if possible) in region R2b as far away as possible from the wing (e.g. using a dorsal sting for a low-wing configuration and a ventral sting for a high wing configuration). This minimizes the total amount of sting interference and enables a numerical analysis using a relatively fast and accurate Euler calculation valid for moderate ranges of angle of attack and angle of sideslip (typically -10°$\leq\alpha,\beta\leq$10°). Including Euler calculations as part of the strategy for future corrections is a sensible option although their accuracy does not fall to within typical balance accuracy. Although when compared to Navier-Stokes calculations the run-time of an Euler calculation is an order of magnitude smaller, the time spent defining the computational domain is still significant. Because it is of importance that the wind tunnel walls are modeled in these calculations every test arrangement of the model in the wind tunnel necessitates a remodeling of the domain and at least two calculations in order to determine the interference by the Δ-method. Applying advanced CFD techniques to solve for sting interference therefore remains time-consuming.

4.5.2 Extrapolation to connected support parts

Now that the experimental and numerical treatment of model sting interference is discussed it is time to recapitulate. In Chapter 2 a break down of the support structure was proposed enabling the treatment of the separate parts spanning the support. Up to now the disturbances of a typical model sting are studied. Can this knowledge be generalized such as to cover the treatment of the complete support for typical sting mounted setups? The answer to this question is not straightforward because of the wide variety in support structures. As an example, three typical support structures are given in Figure 4.29.

In Figure 4.29 various sting support setups are shown from relatively simple setups where only sting-shaped structures are distinguished (Figure 4.29(a)) to a more complex structure involving a larger variety in support part shapes (Figure 4.29(b)) to a very complex support structure (Figure 4.29(c)). Typical setups are evaluated for treatment of their disturbances from the viewpoints of accuracy and effort in the following sections.

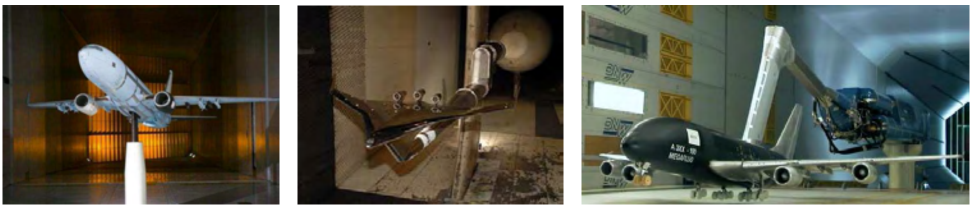

(a) (b) (c)

Figure 4.29: Three typical sting support structures showing the variety in setups. Courtesy of Boeing (a and b) and DNW (c)

Assessment from the viewpoint of accuracy

Generalizing what method is most desirable from the viewpoint of accuracy for determining the disturbances of such support structures is difficult and depends on the geometry. This is because the geometry is indicative for the nature of the disturbance.

The support structures attached to the model sting cause far-field disturbances. These manifest in changes in angle of attack, angle of sideslip and dynamic pressure at the lifting surfaces and a buoyancy force on the aircraft fuselage. It is believed that when the support structure consists of simple (referring to the geometrical definition), streamlined parts that do not show complex flow behavior (like extensive areas of separated flow), the numerical methods presented in Table 4.7 provide comparable accuracy for the calculation of the far-field effects by a Δ-calculation. This would for instance hold for the support structures shown in Figures 4.29(a) and (b) at moderate angles of attack and sideslip (typically -10°$\leq\alpha,\beta\leq$10°). Similar accuracy is also provided by the probe Δ-measurement however the range of applicability is much larger than for the numerical methods (angles of attack and sideslip are included to values where large amounts of separation of the support structure are present)[1]. Performing balance Δ-measurements as a means of determining the far-field effects is still seen as the most accurate method (with the largest range of applicability). In that case the model must be suspended by alternative means (e.g. an external balance system).

Considering typical support structures as shown in Figure 4.29(c) it is seen that such setups include complex geometry and non-streamlined parts causing extensive areas of separated flow. For these type of setups it is expected that the probe measurements and balance Δ-measurements provide the most accurate value of the far-field disturbance (the latter giving the most accurate value). Considering the numerical techniques, it is expected that a panel code does not provide a reliable answer because of the complexity in modeling the separated areas. The Navier-Stokes calculation should have the potential to calculate such flow behavior however for such complicated flows the modeling error caused by the choice of a turbulence model might become significant. It is expected that for this reason the Euler calculation does not perform much worse (or maybe even better) than a Navier-Stokes calculation.

Assessment from the viewpoint of effort

When the issue of effort is addressed what should be kept in mind is the following: when for multiple angles of attack and sideslip the setup of the far-field support does not change (such as in Figure 4.29(a)) the far-field disturbances might be resolved by a few calculations. Comparing the modeling- and computational effort to the effort of performing measurements, calculations become attractive (the type of calculation depending on the exact support geometry). However as is the case with the support geometry in Figure 4.29(c), some support structures consist of parts whose mutual orientation and orientation with respect to the wind tunnel walls change at every angle of attack and sideslip. This necessitates a remodeling of the setup at a new angle of attack and angle of sideslip at the expense of a much larger effort. The desirability of calculations from the viewpoint of effort is then lower but compared to the effort of measurements might be still preferable as long as no Navier-Stokes calculations are to be performed.

[1] When it is assumed that the wind tunnel model does not directly influence the flow around the support, it can be left out of the calculation and probe measurement. The far-field disturbances are then seen as the disturbances of the empty test section flow by the support structure of interest. Care must be taken because end effects of support parts must be minimized according to Luijendijk [8]

Considering the desirability of the determination of disturbance effects of the complete model support the following can be concluded: methods that demand the least effort in determining model support interference are usually not the most accurate methods and vice versa.

From the viewpoint of designing an expert system, this last conclusion is not very attractive. Being able to offer clients an accurate method for the determination of support interference implies offering them a method that requires a lot of implementation effort usually inferring high costs. The cheaper methods on the other hand are most probably less accurate. The question that therefore arises is: "Is there a way to combine all knowledge (both experimental and numerical) on support interference found so far to create a method that requires a very low amount of effort (both modeling as computational effort) and is very accurate (at least as accurate as balance Δ-measurements) for the calculation of model support interference?"

Considering the available methods a custom-made model should be designed. This model should calculate the model support near-field and far-field effects fast thereby incorporating the disturbance factors that are of primary interest in calculating the interference with the right trends and magnitude. It should typically combine the computational advantages of a panel code calculation with the typical accuracy of a balance Δ-measurement. Typical implications of such a model are given in the next section.

4.6 Towards a custom-made model for the determination of model support disturbances

At the beginning of the study on model support interference it is chosen to study the disturbances of the model sting separately from the disturbances of the rest of the support structure. During the research, various numerical and experimental work is performed to determine the disturbance behavior of the model sting. This knowledge might be used to develop a routine for the calculation of the disturbances of the complete support. Typical requirements on such a model are:

1. Calculations should be fast (order of minutes),
2. Calculations should be accurate (show the same trends as e.g. the balance Δ-measurements and 5-hole probe measurements to within measurement accuracy).

When it is decided to model the support disturbances, only the most prominent disturbance factors (of quantitative extent) should be incorporated. For the model sting this implies modeling the relieving effect on the fuselage pressure distribution in front of the model sting nose, the carry-over effect, the pressure disturbance of the slit contamination effect and the pressure disturbances of the viscous effects (caused by the recirculation area and the sting wake). Left out of the modeling are the cavity momentum effect and the contributions of the viscous stresses to the interference. This has the important implication that the range of applicability of such a model is limited (aft placements of the sting can not be accounted for). It is assumed that when the quality of the calculated near-field effects is high, the quality of the calculated far-field effects is also high. The disturbance effects of the support can typically be evaluated by modeling both support and disturbances as a distribution of sources, sinks, doublets and vortices (elementary solutions to the Laplace equation). In order to explore the potential of such a model a simplified 2D case for the evaluation of the sting near-field effects is setup and tested, revealing typical advantages and disadvantages. This is the subject of the next chapter.

4.7 Summary

In this chapter, the setup and analysis of Navier-Stokes calculations are presented. These clarify the near-field flow of model sting and fuselage and identify the disturbances governing the near-field of the model sting. Calculations provide a qualitative image of the interference flow field that complies with measurements. Quantitatively however, the calculations discussed are not able to determine the values of near-field interference with the right trends and within typical measurement (balance) accuracy.

Based on gained knowledge of the flow field all numerical methods applied (panel code-, Euler- and Navier-Stokes calculations) are assessed on how well they perform qualitatively and quantitatively in determining model sting near-field effects and why. This provides an overview of the restrictions of these methods for the calculation of model sting near-field effects for the configuration under study.

Based on this information various numerical and experimental methods for determining support interference of various setups are classified. It is concluded that the two classification parameters “accuracy” and “effort” oppose each other. This opposition might be cleared by designing a custom-made model (that is both accurate and requires a low amount of implementation effort) for calculating model support interference, implementable in the expert system. Such a model should calculate the disturbance effects fast (by incorporating only the disturbance factors of primary quantitative interest) with the right trends and magnitude. It should typically combine the computational advantages of a panel code calculation with the typical accuracy of a balance Δ-measurement. In order to test the potential of such a model, a simplified 2D case is setup and tested for the calculation of model sting near-field effects revealing typical disadvantages. This is discussed in the next chapter.

Chapter 5

The Design of a Custom-Made Model for Calculating Model Support Disturbances

In this chapter the following question is answered: "Are custom-made models for the determination of support interference a feasible addition to an expert system?" This chapter presents a test case example of a custom-made model developed by the author for the determination of model support interference. This model should combine all knowledge (both experimental and numerical) on support interference by incorporating the disturbance factors that are of primary interest in calculating the interference with the right trends and magnitude. It should require a low amount of effort (both modeling- and computational effort) and be accurate (at least as accurate as balance Δ-measurements) for allocation in an expert system. Typical custom-made models prove to be unsuitable for implementation in the expert system. They reveal that high accuracy, low implementation effort and wide applicability can currently not be simultaneously satisfied by whatever method to determine model support interference. This necessitates a more elaborate definition of the expert system's requirements on speed and accuracy.

5.1 Introduction

In the previous chapter, knowledge on accuracy and effort for implementing experimental and numerical methods for the determination of support interference is generalized for a wide class of sting mounted support structures. It is concluded that methods that demand the least effort in determining model support interference are usually not the most accurate methods and vice versa. From the viewpoint of designing an expert system this conclusion seems not very attractive.

Developing a method for the calculation of model support interference that requires a low amount of effort (both modeling- and computational effort) and is accurate (at least as accurate as balance Δ-measurements) might be accomplished by combining experimental and numerical knowledge in a custom-made model. This model should calculate model support near-field and far-field effects fast thereby incorporating the disturbances that are of quantitative primary interest in calculating the interference with the right trends and magnitude. In order to explore the potential of such models a simplified 2D case for the evaluation of sting near-field effects is setup and tested, revealing typical disadvantages of these models. It will be concluded that custom-made models are not feasible for further development and allocation in an expert system. These conclusions provide a more elaborate definition of the expert system's requirements on speed and accuracy.

5.2 Requirements on a custom-made model

Each numerical model that is applied in order to calculate model sting near-field effects has its own limitations. Some limitations are highlighted when the results are validated using experimental results. These are the limitations on the accuracy of the methods. Other limitations concern the practical implementation of such methods in for example an expert system. In such cases speed (concerning both modeling of the case but also the calculation time) becomes of importance. A custom-made model should omit these limitations by posing the following requirements:

1. Modeling effort is kept to a minimum,

2. Calculations should be fast,

3. Calculations should be accurate.

The terms "fast" and "accurate" deserve quantification. The fastest calculation yet considered (when strictly calculation times are considered) is the panel code calculation. Calculation times comprise order of minutes. Competing with this standard it is safe to state that the order of magnitude of the calculation time of the custom-made model must fall within the order of minutes. Considering the modeling effort, the custom-made model will have to be much faster than the panel code (typically in the order of hours). This requirement enables an allocation in an expert system and allows it to be used in a flexible way in various stages of a "wind tunnel measurement cycle" (to be explained in section 5.8). Considering the accuracy requirement, "accurate" typically implies to within balance Δ-measurement accuracy (typical values of which are given in Table 1.2). This is the same standard that is used for the validation of all the numerical methods in Chapter 4.

A custom-made model that is able of calculating the values of the interference to within these requirements would beat the existing competitors (both numerical and experimental) for the determination of support interference and provide a tool that is implementable in an expert system.

5.3 Modeling considerations

To maintain the advantages of speed, a custom-made model must incorporate the disturbance factors that are of primary interest in calculating the interference with the right trends and magnitude. For determining the far-field effects this would imply modeling the support structure using elementary solutions to the Laplace equation. Treatment of the near-field effects of the model sting is the main customizing element. When modeling these only the most prominent disturbance elements (determining the interference quantitatively) should be incorporated thereby minimizing the modeling effort. Examples of such elements are:

1. The relieving effect of the slit on the fuselage pressure distribution,
2. The carry-over effect,
3. The pressure contribution of the slit contamination effect,
4. The pressure contributions of the viscous effect (in the recirculation zone and at the fuselage backbody),
5. The contributions of viscous stresses for the treatment of aft placements of the model sting.

It is assumed that when the accuracy of the calculated near-field effects is high enough, the accuracy of the calculated far-field effects is also high enough.

A customized 3D panel code modeling the fuselage and support is considered suitable for calculating the disturbances. A panel code-based method enables a fast calculation of the interference effects. Modeling effort is kept to a minimum by including only the necessary elements for simulating the quantitative effects of support interference. Typical examples of such elements include panel normal velocities (to simulate the slit relieving effect on the fuselage pressure distribution) and 3D elementary solution elements of the Laplace equation positioned close to the sting-fuselage intersection. The latter can be used to simulate the effects of the slit vortex, the recirculation zone and the effect of the sting wake on the fuselage using 3D source/sink-lines, doublet-lines and vortex-lines.

The strength of the sources/sinks, doublets and vortices solely describing the geometry of the fuselage and support is determined by the flow tangency condition as for any regular panel code. In a custom-made model however, these also depend on the value of what is referred to as “the tuning variables”. Typical tuning variables include panel normal velocity and distribution indicators (to simulate the relieving effect) and additional source/sink/doublet and vortex strengths to simulate above-mentioned characteristic disturbances. Not only are these tuning variables inter-related, but also depend on freestream conditions and geometric relations such as:

1. Angle of attack α,
2. Angle of sideslip β,

3. Properties of the incoming boundary layer (or, position of the model sting),
4. Sting profile,
5. Size of the slit.

The various dependencies of the tuning variables (inter-relations and the dependencies on above mentioned factors) are unknown. This makes tuning a difficult and cumbersome task. A question that therefore arises is: "How sensitive are the calculated interference effects of a custom-made model to an erroneous estimation of these tuning variables?" If sensitive, one might pose the question whether or not it is sensible to develop such a model with so many uncertainties. The following section will answer this question by presenting results of a simplified model.

5.4 Example: a simplified model

In order to study the sensitivity of the solution (the interference of a model support) to uncertainties in the values of the tuning parameters, a simplified 2D model is programmed. In this model, the 2D near-field interference flow field of an ellipsoid-shaped cross sectional sting intersecting a flat plate is calculated (Figure 5.1(a)). Because no slit is discretized, the relieving effect in front of the sting and the effect of the slit vortex are not included. The interference phenomena that are modeled are the recirculation area aft of the sting on the flat plate and the effect of the sting wake on the flat plate. Despite the abovementioned simplifications, it is thought that the model is suitable for demonstrating the drawbacks of typical custom-made models.

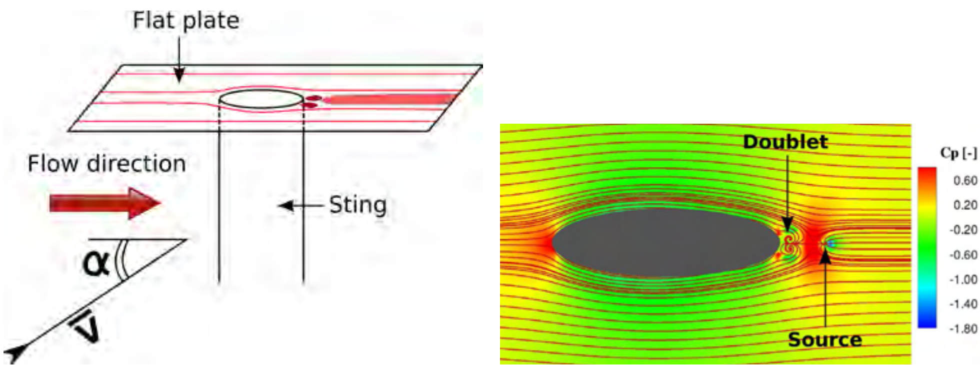

(a) (b)

Figure 5.1: (a) The outline of the test case model (b) The calculated interference flow field on the flat plate

Using elementary solutions to the Laplace equation, the resulting near-field interference flow is simulated on the flat plate. Integration of calculated pressures on the flat plate will yield the interference values in lift- and drag-direction. An example of the simulated interference flow field is given in Figure 5.1(b). In the figure two tuning variables are indicated. These are the doublet- and source strength defining the wake signature of the sting on the flat plate.

One of the tuning parameters is the doublet strength κ defining the recirculation zone on the flat plate aft of the sting (Figure 5.1(b)). This parameter is dependent on other tuning parameters, freestream conditions and geometric properties. These dependencies are however unknown. This means that errors in the determination of the doublet strength are easily made thereby influencing the solution to the near-field (and far-field) interference. The main question arising here is: "What is the effect of the variation of the doublet strength κ on the near-field interference on the flat plate?" In order to answer this question, interference polars are calculated for varying values of the doublet strength, varying up to 50% of a reference value. This reference value is determined by comparison of the calculated flow field to results of experimental oil flow visualizations. The value of the doublet strength is kept constant during the variation of angle of attack (its sensitivity is considered in section 4.3.4). Figure 5.2 shows the resulting polars for the interference on the drag-coefficient of the flat plate.

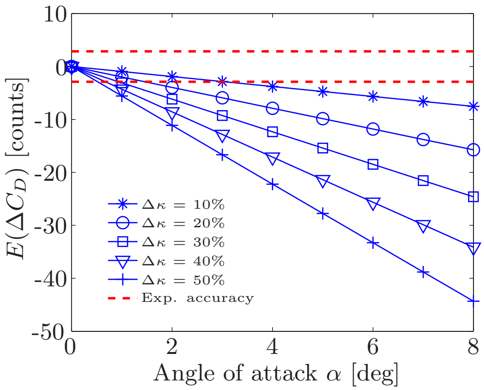

Figure 5.2: Variation in calculated sting near-field interference on the drag-coefficient of the flat plate as a result of uncertainties in the doublet strength κ defining the recirculation area

Figure 5.2 indicates that when the doublet strength κ is varied, the total error in determining the value of the drag interference grows rapidly. This implies that when an erroneous estimation of the doublet strength is given, the error introduced in the calculation of the near-field interference rapidly grows beyond the desired accuracy of the model (the balance Δ-measurement accuracy indicated in the plot). It is calculated that the doublet strength should be calculated to within 2% of the reference value in order to reduce the error to within accuracy requirements for this range in angle of attack. Considering the number of dependencies that introduce uncertainties in the determination of the doublet strength, this requirement is unrealistic.

5.5 Design of a custom-made model concluded

It is concluded that due to the lack of knowledge on the dependencies of the tuning variables defining a custom-made model, the quality of the calculated corrections is not guaranteed. Additional problematic issues are also to be addressed: in this model, it is assumed that for the considered angles of attack, the interference does not change qualitatively. However, when angles of sideslip are considered or when the configuration is changed (when e.g. the size of the slit is adapted or when the sting is positioned at the fuselage afterbody) it could be that the interference *patterns* change. This implies that the characteristics of the tuning parameters change including their inter-relations and dependencies on previously mentioned parameters thereby complicating the problem even more.

Besides the issues just addressed, there are more problematic factors. One of the problems is the inevitable intervention of an engineer in the numerical part of the model. When a new fuselage and/or support geometry are implemented, knowledge is required on 3D panel codes, elementary solutions, the program algorithm and meshing in order to guarantee a (stable) solution. Assuming that most of the engineers using this model are specialized in experimental- instead of numerical aerodynamics, this is an undesirable scenario. Of course, the model developer could make sure that such intervention by the practical engineer is minimized by taking care of the most common cases. The problem that then arises is that the range of applicability of the model will be drastically reduced (to maybe a few standard configurations) thereby exceeding the initial goal of the model: it is not desirable to spend a lot of effort in developing a model that is able of providing interference values for say 3 configurations accurately and most of all fast. In that case the justification of model employment deceases to exist.

When the disadvantages of a custom-made model are considered, it seems unattractive for further development. Even if the model would be developed (regardless of the problems encountered as described in the last paragraphs), no information on the tuning parameters is available. This information should be gathered by extensive measurement campaigns and Navier-Stokes calculations. This is however not an attractive solution from the viewpoint of time and cost.

Because a typical custom-made model is unable of determining the near-field effects of the sting with the right magnitude, the calculated far-field effects will also show inaccuracies. Considering the order of magnitude of the error made in the determination of the near-field effects (Figure 5.2), these inaccuracies might become substantial. It could be decided to bypass the custom-made modeling of physics determining the sting near-field effects in order to prevent these problems. This would however leave the user with a panel code for calculating the model support interference. Referring to Tables 4.7 and 4.8 such a model would typically fail to come up with a solution that is accurate enough and fast enough.

The custom-made model tested in the previous section is a simplified example showing its disadvantages very clearly. This simplified model is not feasible for further development. Developing more complex and complete models is therefore insensible. These are at least constrained by above-mentioned drawbacks. Typical custom-made models are non-feasible elements of an expert system.

5.6 A rule of thumb

Reviewing the results of the research presented so far, an interesting observation is made. This observation is summarized in a rule of thumb:

"High accuracy (at a minimum equal to typical balance Δ-measurement accuracy) and low implementation effort (total measurement effort or modeling effort and computational effort) of a correction method for determining model support interference are currently incompatible when a wide range of applicability (freestream conditions, setups) is desired."

Balance Δ-measurements or other experimental techniques have a high accuracy and wide range of applicability. Such methods however all imply significant effort (Table 4.8) especially for a wide operational range (angles of attack, sideslip, Mach numbers, support setups).

When a correction procedure is based on calculations it is seen that while some calculations are implemented faster than others, the accuracy generally decreases with decreasing implementation time. An illustrative example of this is the determination of model support interference by vortex-lattice codes or fast panel codes. These methods provide values of the interference within a reasonable amount of time because they typically neglect the modeling of certain physics such as viscosity, compressibility and flow-rotationality thereby decreasing the accuracy of the calculation (Figure 4.27). Besides this, some numerical methods do not allow for an accurate geometrical definition of the problem. Generally speaking, the faster the methods are implemented, the less accurate the geometrical description (compare e.g. vortex-lattice calculations to panel calculations). Inaccuracies in geometrical definitions translate to inaccuracies in the final solution (vortex-lattice calculations for example do not allow for the determination of near-field effects. In the panel code calculations these are not properly resolved because the internal cavity and slit can not be modeled). Referring again to Table 4.7, Table 4.8 and Figure 4.27 it is seen that the Euler calculation should display a high accuracy and relatively low implementation effort. The downside however is in the range of applicability which is limited for these calculations: for aft sting placements and angles of attack and sideslip larger than typically 10 [deg] the accuracy of an Euler calculation is not guaranteed.

With respect to the first paragraphs in this chapter, the main goal of developing a custom-made model for the calculation of support interference was to find a method that would be the exception to this rule of thumb. By combining the advantages of fast calculation methods and modeling interference contributions determined by measurements and calculations to achieve a high accuracy this was deemed possible. As explained in this chapter this would lead to a model with high modeling effort, limited accuracy and a low range of applicability. Therefore unfortunately such models also comply with the rule of thumb described in this section. This conclusion seems to introduce difficulties for the design of elements defining the expert system whereas this system should preferably be build on accurate and low-effort methods. There is however more to be said about accuracy and effort.

In the previous chapter labels are assigned to various experimental and numerical methods to determine model support interference from the viewpoint of accuracy and effort. In the perception of the user certain methods can be tagged as "accurate" or "fast". For implementing certain methods in the expert system the question should be posed whether or not such methods are *accurate enough* and *fast enough*. If the user is provided ample time to implement a measurement, even this measurement is fast enough for the intended purpose. If a vortex-lattice calculation gives ample information to make decisions about some test, even this vortex-lattice calculation can be accurate enough.

At this point it is of importance to carefully consider the terms *fast enough* and *accurate enough* as stated in the research objective: they need refinement.

5.7 How fast is "fast enough", and how accurate is "accurate enough"?

A way to assess the requirements *fast enough* and *accurate enough* is by looking at the expert system's operational environment. This environment comprises a low-speed wind tunnel measurement by a certain party at a wind tunnel company or institute. It is likely that expert systems are used to guide the project manager of the hosting company or institute in his dealings with both the test and the client. To illustrate this, a typical example of such a measurement is given in the next section.

5.8 Example: outsourcing a measurement

When a client decides to subcontract a company or institute for a wind tunnel measurement, the accompanying trajectory can roughly be divided in four stages from the negotiations on the practical and financial extent of the measurement to the delivery of the final data to the client. For every stage, requirements on *fast enough* and *accurate enough* are defined.

5.8.1 Stage 1: negotiations at the client

During the first stage the project manager of a wind tunnel company or institute contacts the client about the practical and financial extent of the desirable measurement. Depending on the outcome of the negotiations the client will decide whether or not the measurement will take place at the facility offered by the project manager. Because the accuracy of the measurement is dependent on the quality of wind tunnel support corrections, the project manager will have to be able to give at least a first indication on the interference using an application in the expert system.

This application should typically be able to indicate the trends and order of magnitude of the interference. This information enables an evaluation of the effects of support placements in combination with model setup and test conditions on the values of the interference and allows the client to orientate on desirable and attainable test scenarios. Provided that the project manager has time for preparing the meeting, *fast enough* typically implies within a day. Both trends in the estimated interference patterns as the order of magnitude must be calculated correctly by the expert system application thereby indicating the extent of *accurate enough*.

5.8.2 Stage 2: test preparation phase

When the client agrees with a certain test setup based on this information, the project manager will have weeks or months in advance of the wind tunnel tests. In that time, the project manager receives detailed information about the wind tunnel model to test. Expert system applications must identify methods for determining the interference. The time scale associated with the determination of the interference is typically weeks or months. The question how accurate the determination must be is answered by looking at the client's requirements on the accuracy of the test (usually based on a desirable balance between accuracy and costs).

5.8.3 Stage 3: performing the measurements

During the actual measurements the data can be corrected by an expert system application on-line for the interference effects determined in stage 2. Fast enough typically implies within seconds. Depending on the storage format of the corrections and measured data, mathematical operations are likely to be performed on the corrections (such as interpolation sequences). Numerical errors caused by these operations should typically be an order of magnitude smaller than the accuracy of the determined corrections.

5.8.4 Stage 4: post test corrections

It might be decided to bypass on-line corrections and to post-process the measured data after the actual test is performed. If the corrections have already been determined during stage 2 the required application accuracy is comparable to the stage 3 level. Fast enough however might imply a level comparable to the stage 2 requirement and typically depends on how fast the client desires the final data to be delivered.

It might also be that after the test, corrections are still not determined. In that case application requirements on fast enough and accurate enough resemble the stage 2 levels. An illustrative and realistic scenario might also be that the corrections have already been determined during stage 2 but the measurements in stage 3 indicate that a different correction methodology should be chosen such as not to cross the correction borders of applicability. For instance choosing a correction method that guarantees a specified accuracy level with the restriction that the amount of separated flow of the model is limited. Finding out during the test that this amount is out of the bounds might lead to the conclusion that in order to guarantee the prescribed level of accuracy, a different method should be chosen to correct the measurements.

By illustrating four distinct stages that define a typical commercial wind tunnel measurement, expert system element requirements on "fast enough" and "accurate enough" are identified. The stages together with the accompanying requirements on speed and accuracy are summarized in Table 5.1.

Table 5.1: Expert system application requirements on speed and accuracy for the determination of wind tunnel (wall- and) support interference according to four stages defining a typical commercial wind tunnel measurement

Stage	**Fast enough**	**Accurately enough**
Stage 1	O(hours)	Trends and O(magnitude) agree
Stage 2	O(weeks/months)	Determined by client
Stage 3	O(seconds)	$\ll$ Accuracy of correction method
Stage 4*	Determined by client	$\ll$ Accuracy of correction method
Stage 4**	O(weeks/months)	Determined by client

* corr. determined

** corr. not determined

The expert system should be able to provide applications satisfying the requirements on speed and accuracy given in Table 5.1. Typical applications as expert system elements define a feasible structure of the expert system and are defined in the next chapter.

5.9 Summary

In this chapter an example of a custom-made model for the determination of wind tunnel support interference is presented. This model should combine all knowledge (both experimental and numerical) on support interference by incorporating the disturbance factors that are of primary interest in calculating the interference with the right trends and magnitude. It should require a low amount of effort (both modeling- and computational effort) and be accurate (at least as accurate as balance Δ-measurements) for allocation in an expert system. A simplified 2D case reveals typical disadvantages of such models: due to the lack of knowledge on the dependencies of the tuning variables, the quality of the calculated corrections is not guaranteed. Additional problematic issues such as qualitative interference changes (when α, β or the configuration is changed) and inevitable intervention of an engineer in the numerical part of the model are addressed. Solving for these disadvantages implies an inevitable reduction in the operational applicability range of the model. Typical custom-made models are non-feasible elements of the expert system. They do however reveal that high accuracy, low implementation effort and wide applicability can currently not be simultaneously satisfied by whatever method to determine model support interference. This necessitates a more elaborate definition on requirements on speed and accuracy of the expert system's elements. It is shown that a feasible expert system might consist of applications with given accuracy and speed assisting in four stages defining a typical commercial wind tunnel measurement. Typical applications as expert system elements define a feasible structure of the expert system and are defined in the following chapter.

Part II

Identifying Typical Expert System Elements

Chapter 6

The Expert System's Application Structure

In this chapter, a feasible structure of the expert system in terms of its applications (or, elements) is discussed. Typical applications developed by the author are explained in more detail.

6.1 Introduction

In the previous chapter, 4 operational stages are identified that are typical for a commercial wind tunnel measurement. These stages form the basis of the expert system's structure as the system should provide applications assisting in every stage. The applications are subject to the requirements on speed and accuracy coupled to these stages (summarized in Table 5.1).

In this chapter, a feasible application-based structure is discussed in more detail after summarizing the requirements on the expert system. Typical applications are studied more thoroughly. It is shown that the proposed structure fulfills the expert system's requirements.

6.2 Expert system's requirements

The expert system for support interference should be able to perform the following tasks:

1. Advise on the test setup,
2. Advise on correction methods,
3. Calculate the interference fast enough and accurate enough,
4. Calculate the interference pre-test and on-line,

5. Correct for the interference on-line and off-line,

6. Allow easy plug-in of modules dealing with the problem of wall interference.

Additional requirements relate to the use of the system. These requirements must be met if the expert system is to be used by engineers that are not considered experts in the field of low-speed wind tunnel wall- and support interference:

- The expert system must be programmed in such a way as to meet computer platform standards,

- The expert system must be user friendly,

- The user interface to the direct user (the engineer) and the indirect user (client) must be professional.

In the following sections an application-based structure of the expert system (that is subject to above mentioned requirements) is proposed and discussed. Certain applications are discussed in detail.

6.3 The application-based structure of the expert system

A schematic of the expert system's structure is given in Figure 6.1.

In Figure 6.1, the main tasks of the expert system, necessary input, output and operational stages where these tasks are requested are indicated. These tasks can be performed by applications (expert system specific elements). Therefore, Figure 6.1 basically reveals the application-based structure of the expert system.

In order to discuss this structure, consider a client request for a wind tunnel measurement. Generally speaking, this implies a sequence of events according to the stages shown in the figure:

- During the first stage (client negotiations), the task of the expert system is to provide an estimation of the support interference within hours whereas trends and order of magnitude of the result should be correct. As input for this task, the project engineer can typically use initial data from the client and/or make use of its data-base to describe the test to be performed (define the wind tunnel model, test parameters, sting placement etc.). The interference estimate is typically performed by an application (developed by the author) as discussed in section 6.4). This application enables a study on the effects of sting type and placement on the order of magnitude and trends of support interference for various test conditions. Advice on the test setup is also an important tasks of this application,

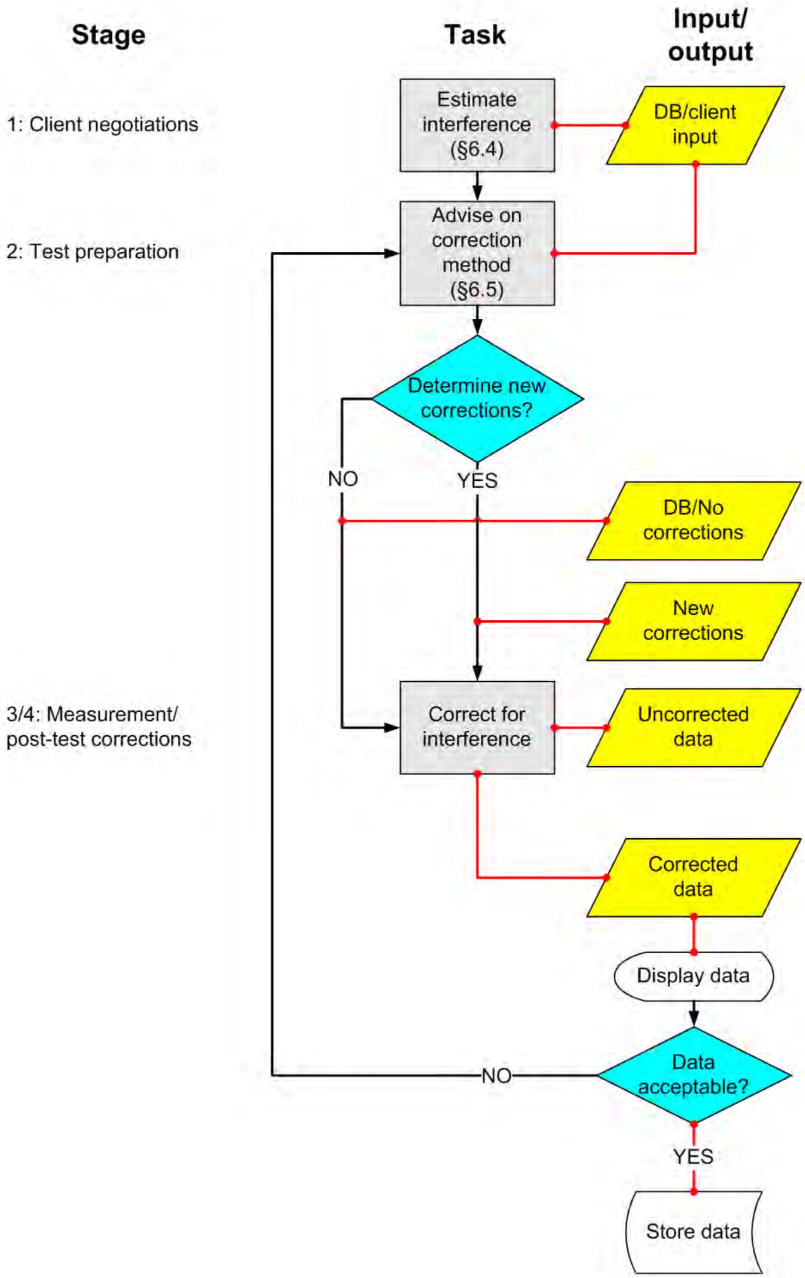

Figure 6.1: The proposed expert system's application-based structure

- During the second stage (test preparation), the client is more closely involved in choosing a method to correct for the effects of support interference. This choice is based on a desirable balance between accuracy and costs. The task of the expert system is to assist in the choice on a correction method representing that particular balance for a given test. As input, similar information as during the previous stage is good enough as a rough description of the test is needed. The expert system's advisory application for this task (developed by the author) is described in section 6.5. The expert system confronts the user with the question whether or not new corrections need to be determined (based on measurements and/or calculations). When it is decided that new corrections need to be determined, the advice is used by the project engineer to initiate certain measurements/calculations in house and/or outsourced. For this action (out of bounds of the expert system) detailed test information is necessary. The determination may take weeks or months and the accuracy is determined by the client specifications. It could also be decided not to determine new corrections. Besides the fact that this might be a direct client wish, it is also possible that existing corrections are good enough (determined for another similar test or as determined by the interference estimation application during stage 1). Besides the expert system's advisory application, an additional method for the determination of support interference during this stage (developed by the author) is introduced in this chapter: VOLAER (VOrtex-LAttice/EuleR),

- During the third/fourth stage (measurements/post-test corrections) the main task of the expert system is to correct for interference. As input, uncorrected measurement data and corrections must be provided (the corrections may even be provided by on the spot determination, both on-line and off-line!). The corrections can be performed during the measurement (on-line, the measurement data is delivered by the wind tunnel data acquisition software) and after the measurement (off-line, the measurement data can be imported from a file). Support interference corrections are applied to the measurements in this stage subject to requirements on speed and accuracy given in Table 5.1 (an application is developed by the author and will be introduced in this chapter. It combines uncorrected wind tunnel measurements with vortex-lattice calculations to correct for all the disturbances of wind tunnel walls and support, both on-line and off-line: MVL (Measurement/Vortex-Lattice)). The expert system application for this task must perform conversion- and interpolation techniques on both measurement- and correction data. Displaying the corrected data poses the question whether or not the data is acceptable, meaning to within client specifications. When this is the case, the data can be stored and the cycle is completed. When however it is decided that the corrected data is not to the satisfaction of the client, the task of the expert system will be to propose a new correction method and repeat the correction cycle again just as long as is required to meet the client specifications (note, this may take months when is decided that new corrections should be determined).

Because the tasks of the expert system are carried out by modular applications, similar applications can be added for the assessment of wall interference.

Typical applications offered in each stage of the trajectory by the expert system are explained in more detail in the following sections. They are focused on the problem of dealing with model support interference in the LLF of DNW. Typical applications can however be easily generalized to other wind tunnels. It is shown that these applications fulfill the expert system's requirements.

6.4 Stage 1 application: Evaluation of Support Interference (ESI) Module

To fulfill the task of estimating the interference during the client negotiations (stage 1), an application is developed by the author for the evaluation of support interference (from now on, the ESI module). An impression of the structure of this application is given in Figure 6.2.

This application should determine correct trends and order of magnitude of the support interference typically within hours (this enables the engineer to prepare a meeting using this application but also to perform on the spot calculations. Involvement of the client might create an increased level of confidence in the quality of the corrections).

As can be seen in Figure 6.2 using the application starts by defining the input. Typical input that is needed for this application includes:

1. Model parameters: these describe the wind tunnel model geometry. Geometrical definitions describing the fuselage as well as the lifting surfaces (including the definition of the lifting surface configuration such as flap deflection) are necessary,

2. Test parameters: these parameters define the test conditions as angles of attack, angles of sideslip and Mach number,

3. Initial sting placement: based on both experience and test characteristics the engineer must be able to define an initial placement. When measurements are performed including a tail, the engineer knows for example that a ventral sting placement is preferable to a dorsal placement in order to decrease the interference on the tail caused by the sting wake. The initial sting placement is given with a pre-defined margin. It can be specified for instance that the interference of the support should be evaluated with the sting at position x with a margin of y percent of the fuselage length to the front and back of this initial placement. This enables the evaluation of trends of support interference with respect to sting placement later on in the process,

4. Requirements on interference: it occurs that clients wish to minimize the interference on a particular aerodynamic coefficient. When for instance the drag-coefficient of a certain test is of primary interest, the interference on this coefficient should be minimized such as to increase the accuracy of the final corrected coefficient.

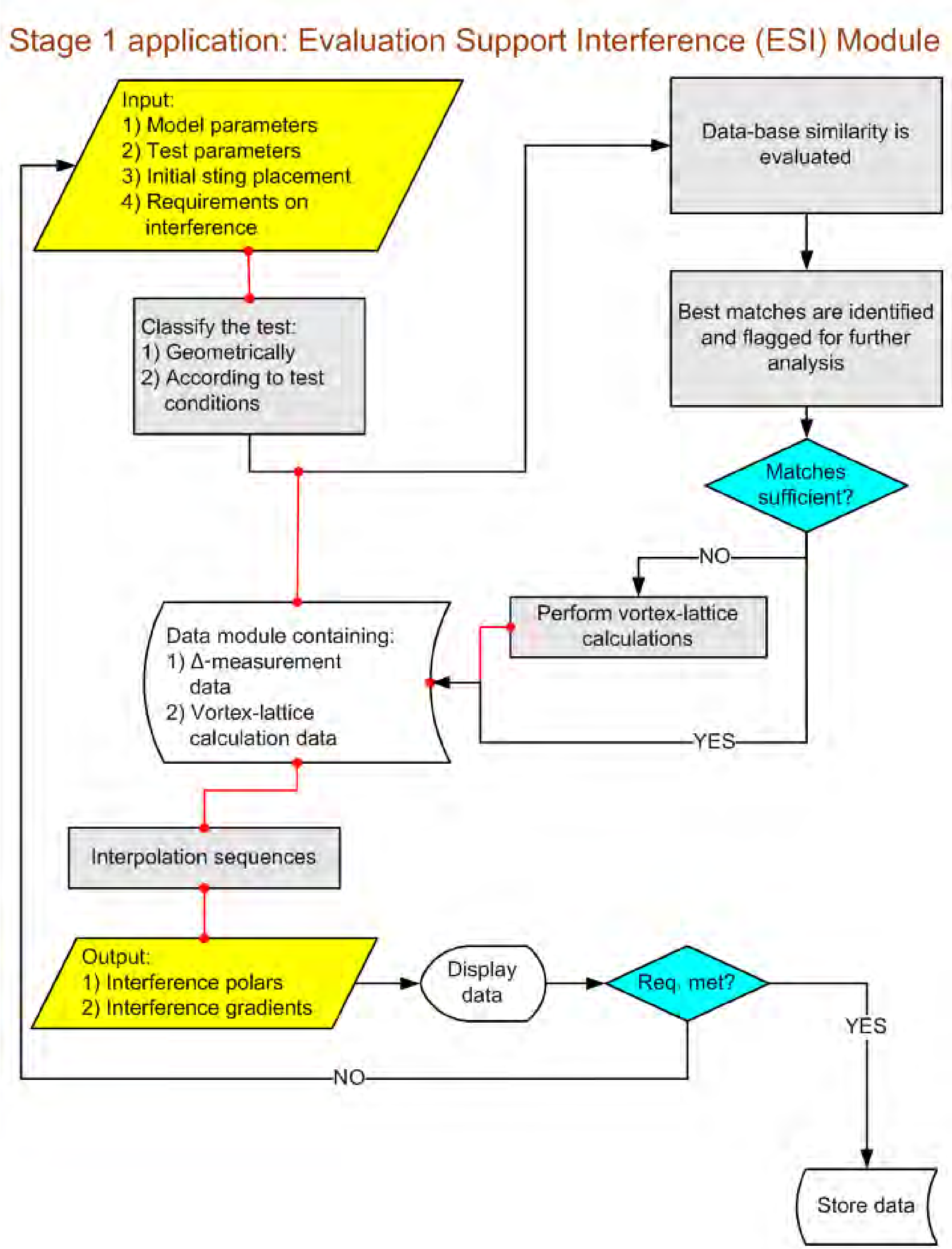

Figure 6.2: The structure of the ESI module

The above mentioned input is used to classify the test. This classification is performed both on a geometrical basis of the test (model geometry characteristics, sting characteristics and placement) and according to test conditions. The reason for this is that the classification parameters can then be easily compared to data contained in a data module: it is assumed that the company or institute employing this application possesses a certain amount of experimental/numerical correction data determined for previously performed tests. These data are related to a test configuration by means of the same classification parameters as for the test of interest. It is assumed that when the classification of tests “coincides” (or shows a close match), their corrections will display a strong correlation in both order of magnitude and trend. This is the basis for the determination of support interference of the new test.

Using the available data in the data module the data-base similarity is evaluated: it is calculated what cases are *best* used for evaluating the support disturbances of the new configuration with predefined margin in sting placement. For instance, when the test to be performed is characterized by a model sting placement between 30% and 50% of the fuselage length (measured from the model nose) the application starts to look for configurations with model sting placements between 30% and 50% of the fuselage length showing the highest possible agreement of remaining classification parameters. To identify “best matches”, the application should contain a list of classification parameters including their impact on support interference. This could be realized by an extensive sensitivity analysis. Due to the limited amount of experimental data, the application considered here includes equal impact (or, weighing) factors. The best matches are identified and flagged for further analysis. This analysis implies performing interpolations in order to determine the order of magnitude and trends of the support interference of the configuration of interest.

It is possible that the extent of the data module is such that the amount of matches is not sufficient to determine the interference. It might also be that the agreement of the remaining classification parameters is not satisfying. For instance, consider that only two matches are found for a sting placement between 30% and 50% of the fuselage length measured from the model nose. Even if the remaining classification parameters show perfect agreement with the test case, only a linear interpolation can be applied on the values of support interference to evaluate the effect of sting (and thus support) placement. In such cases the data module must be extended. This can be done by performing calculations (assuming that the accuracy of these calculations is good enough for the intended purpose).

Considering the requirements on speed of this application, calculations demanding high modeling- and computational effort are undesirable. It is shown that calculations based on a vortex-lattice representation of the test can be performed (to be discussed in the next section). Calculations have typical run times in the order of a minute. When such a calculation is performed, the output is used to extend the data module. The data-base similarity is once again evaluated and the cycle is repeated until it is found that ample cases are present to guarantee a sufficient set of matches. Both numerical and experimental results are in that case used to complement each other in determining an estimation of the interference.

Additional future experimentally and numerically determined interference corrections can be added to this data module thereby extending its range of applicability. It is of importance that the data in the module has a well defined accuracy. Therefore it is recommended to use Δ-measurements for this purpose and a validated calculation technique such as a vortex-lattice calculation. Adding all sorts of correction data determined by various methods is possible (if the data format is suitable) however it complicates a reliable evaluation of the accuracy of the result of the ESI application.

The output of ESI is twofold:

1. Display interference polars. These polars illustrate the effects of support interference on the values of the aerodynamic coefficients for various angles of attack (the first version of this application will be concerned with angle of attack polars only) within the margin of indicated sting placements,

2. Display support interference as a function of model support placement parameters (horizontal distance of the sting to the mean aerodynamic center of the wing for example). This information illustrates the interference gradients caused by the choice of sting-fuselage protrusion location for a specified angle of attack. These gradients give the engineer the ability to advise on the sting placement. Consider for example the sting-fuselage arrangement given in Figure 6.3. In this figure typical output of this application is shown. It is seen that the interference of the model support can be reduced by increasing the distance of the support to the wing. Based on this output the client requirements are re-evaluated. If the requirements are satisfied the data can be stored. It might also be that the requirements are not met, for instance when the resulting graphs do not show a minimum in the interference. When the client desires a minimum interference on the drag-coefficient it could be decided to reposition the sting and restart the iteration process.

The advisory function in ESI is two-fold:

1. Various advice is included in the knowledge base of the application. This advice is based on what is found in the study on model sting interference. As an example: when the engineer desires a ventral model sting placement at the backbody of the aircraft fuselage, a caution window is triggered stating that this causes the model sting near-field effects to increase significantly (discussed in section 4.5.1 and shown in Figure 4.28). It is then advised to reconsider the chosen sting placement,

2. The second type of advisory function of this application is more interactive. Based on the output the engineer is able to give advice regarding the placement of the model sting. This advice is based on an evaluation of the interference gradients as a function of model sting placement parameters.

Considering the requirements on the expert system it can be concluded that this application is able to advise on the test setup (both actively and passively by means of

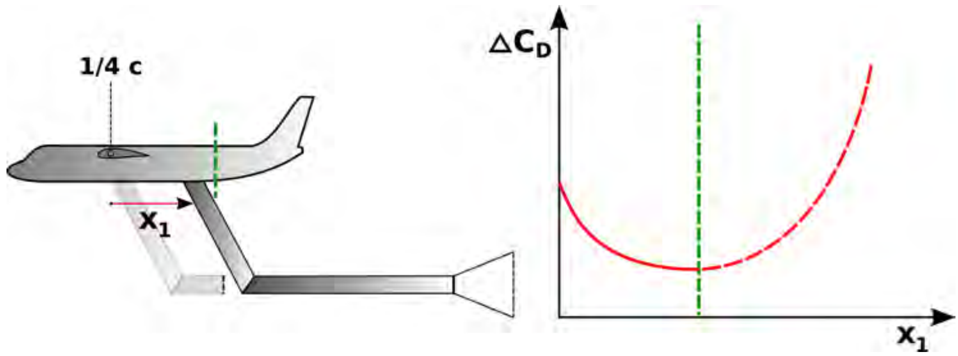

Figure 6.3: An example of a typical sting-fuselage arrangement with the results of the support interference on the drag-coefficient as a function of horizontal distance between model sting and quarter-chord location of the main wing as calculated by ESI. The green dashed line indicates the limit of assessment of the numerical part of ESI as aft of this region large viscous disturbances manifest

interpretable output) and it is able to calculate the interference in a pre-test stadium. A similar type of application for the problem of wind tunnel wall interference could be developed as well. The question remains however whether or not this application is able to calculate the interference fast enough and accurate enough in order to fulfill the expert system's task during the client negotiation stage (stage 1). This question is answered by evaluating some typical results of a first version of ESI.

Typical results of the ESI module
An ESI test case is presented showing its value in determining support interference on the lift-coefficient and pitching moment-coefficient of an aircraft configuration. The effects of repositioning the model sting, tail installation and wing configuration on the interference are demonstrated.

The support configuration considered is a ventral sting setup in the LLF of DNW (the closed-wall 8 x 6 [m] test section). The wind tunnel model under consideration is representative for a new design and concerns a typical high-wing aircraft configuration including tail. A three-view of this configuration is shown in Figure 6.4. More detailed information is given in Table 6.1.

The configuration specified in Figure 6.4 and Table 6.1 is attached to the torpedo and sword of the LLF support (also schematized in Figure 2.1) by means of a model sting/horizontal sting combination shown in Figure 6.5.

Referring back to Figure 6.2, ESI requires the following input:

- Model parameters: these are summarized in Figure 6.4 and Table 6.1. At first instance, the model without tail is considered,

- Test parameters: the test parameters of the test case are as follows:

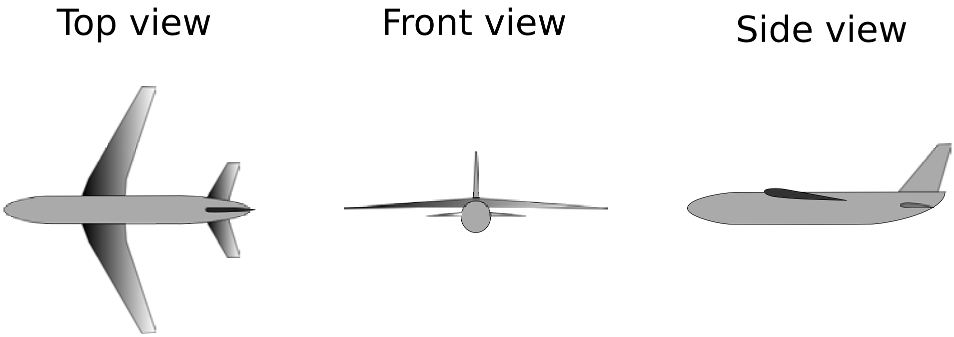

Figure 6.4: A 3-view of the aircraft configuration considered for a test case in the ESI module

Table 6.1: Detailed characteristics of the aircraft configuration shown in Figure 6.4 for the fuselage, wings, horizontal tailplanes (HTP) and vertical tailplane (VTP)

Parameter	**Value**
Fuselage length	4.00 [m]
Fuselage width	0.45 [m]
Fuselage height	0.50 [m]
Wing reference area	1.89 [m^2]
Wing span	4.00 [m]
Mean aerodynamic chord	0.52 [m]
Wing root chord	0.60 [m]
Wing dihedral	-3.0°
Inner wing sweep	20°
Outer wing sweep	30°
Inner wing taper ratio	0.80
Outer wing taper ratio	0.35
Wing flap deflection	0°
HTP root chord	0.40 [m]
HTP dihedral	-3°
HTP sweep	30°
HTP taper ratio	0.50
HTP elevator deflection	0°
VTP root chord	0.60 [m]
VTP sweep	40°
VTP taper ratio	0.30
VTP rudder deflection	0°

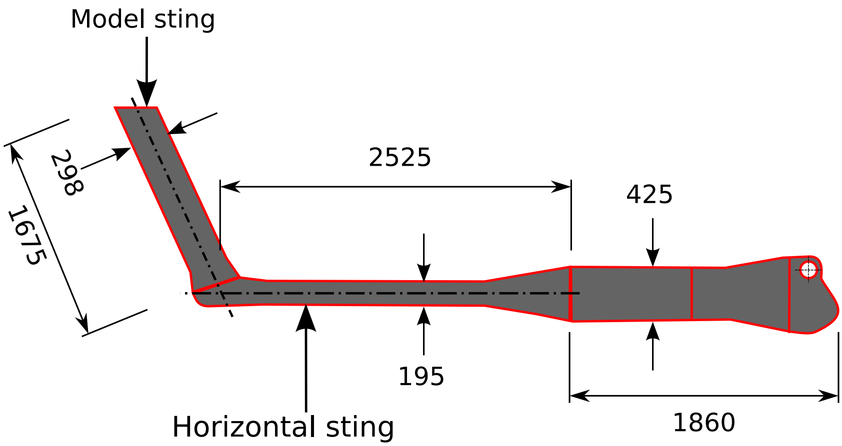

Figure 6.5: A schematic of the model sting/horizontal sting combination to suspend the test case configuration of Figure 6.4 in the LLF of DNW. Dimensions are in [mm]

$\alpha = 0$ [deg],
$\beta = 0$ [deg],
$V_\infty = 70$ [m/s].

- Initial sting placement: ventral sting placements are considered between 25% and 60% of the fuselage length from the nose of the model. Because of practical reasons, the lower limit for the sting placement is set at 25% of the fuselage length from the model nose (the internal balance can for instance not be fitted in the fuselage upstream of this point),

- Requirements on interference: a typical requirement stated by a client is to minimize the support interference on the aircraft lift-coefficient and pitching moment-coefficient when accurate polars of the configuration are of interest.

Using this input, the test under consideration is classified both geometrically and according to test conditions by ESI. Classification parameters include:

- Model configuration: tail-off, no flap deflection,

- Characteristic distance from the sting leading edge at the fuselage protrusion to the wing's m.a.c., both horizontally and vertically (non-dimensionalized by the fuselage maximum length and height respectively): i_1 and i_2[1],

- Model sting placement: ventral,

- Reference velocity V_∞.

[1]Positive i_1 and i_2 imply that the sting leading edge is aft- and above the wing's m.a.c. respectively. Negative signs imply an upstream/underneath placement

Shown in Figure 6.2, the values of the classification parameters are compared to those in a data-base containing experimental and numerical interference data. For this configuration, ESI indicates that there are no matches that can be used for an interference estimate. This is caused by the lack of experimental data (2 configurations that have a low degree of geometrical similarity) and numerical data (no data whatsoever) in the data-base currently available for the first version of ESI.

To this end, additional calculations are necessary for this model configuration that cover the complete range of -8.75% $\leq i_1 \leq$ 26.25% (with i_2 = -100%): vortex-lattice based calculations are initiated. In these calculations, the following features are modeled:

1. The wind tunnel walls using lifting surfaces without camber. According to Carlin et al. [10] and Sons [78], wind tunnel walls are of importance for capturing the right order of magnitude and trends of support interference,

2. The support structure: model sting, horizontal sting, torpedo and sword are modeled by means of slender body theory (the accuracy of this approach is assessed by Sons [78]),

3. The aircraft configuration modeled by means of lifting surfaces (the fuselage is not modeled).

This type of representation by a vortex-lattice code shows constraints as described by Sons [78]. The main constraints can be summarized as:

- The implementation of wind tunnel walls necessitates a rotation of all bodies in the wind tunnel when non-zero angles of attack are simulated. This is not implemented in the first version. Currently, only the situation where $\alpha = \beta =$ 0 [deg] can be simulated. For the considered model support however, this does not seem a problem: because the interference gradients (with angle of attack) are small (see e.g. Figure A.2) the situation at $\alpha = \beta = 0$ [deg] will give a correct indication of the order of magnitude of the interference,

- Model sting near-field effects are not included in the calculation. When the model sting placement is carefully chosen (this is part of the advice function of ESI), these near-field effects are small (for an indication, see Figure 4.27),

- Viscosity is not modeled.

Because no fuselage is modeled, the buoyancy of the model support on the drag-coefficient seems to be excluded from the calculation. Model specific control points describing the fuselage can however be included in the calculation. In these points the values of $\frac{\Delta q}{q_\infty}$ are evaluated. Combined with the fuselage geometry (cross-sectional area) at these control points, the buoyancy can thus still be evaluated. Explained in Sons [78] however, the interference on the drag-coefficient is not predicted satisfactorily (and hence not considered further in this test case).

The vortex-lattice routine performs Δ-calculations to determine the support disturbances. After performing several calculations with the sting at various locations (or, values of i_1) the results are stored in the data-base for future use. The number of data module matches (described in Figure 6.2) is now enough to determine the effect of horizontal sting position on the support disturbances on the lift-coefficient and pitching moment-coefficient by means of interpolation. Results are plotted in Figure 6.6 for i_2 = -100%. For comparison, results of a mid-wing (i_2 = -50%) and a low-wing (i_2 = 0%) configuration are also shown.

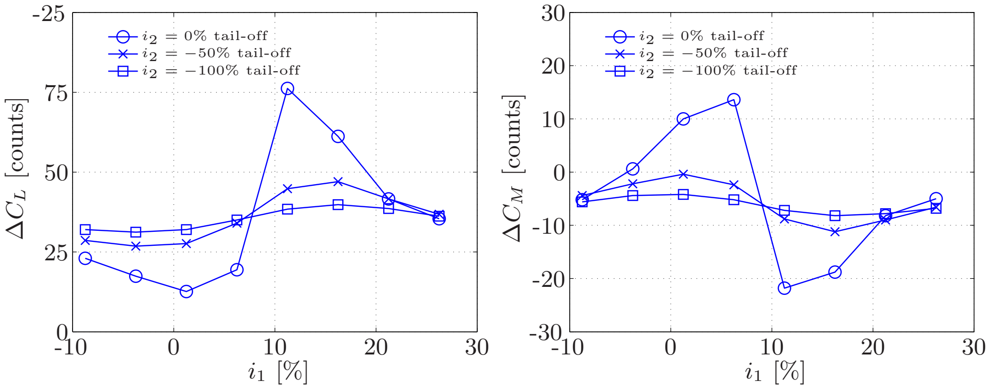

(a) (b)

Figure 6.6: ESI results revealing the effect of horizontal sting placement on the interference on the (a) Lift-coefficient (b) Pitching moment-coefficient of the configuration shown in Figure 6.4 (without tail). Results are for $\alpha = \beta = 0$ [deg], $V_\infty = 70$ [m/s]. For comparison, results of a mid-wing (i_2 = -50%) and a low-wing (i_2 = 0%) configuration are also shown

In Figure 6.6 the following becomes obvious for all values of i_2 (most clearly shown for $i_2 = 0\%$ when the sting is closest to the model wing):

- for -8.75 $\leq i_1 \leq$ 1.25%: it is seen that the lift-disturbance initially shows a decreasing trend, resulting in an increasing pitching moment. It is likely that these lift-disturbances manifest at the rear of the wing and are caused by the action of the horizontal sting and torpedo,
- for 1.25 $< i_1 \leq$ 16.25%: in this area, the uplift of the model sting becomes apparent as the value of ΔC_M shows a distinct fluctuation. This uplift is seen to sequentially increase- and decrease the pitching moment as the sting is traversed along the wing,
- for $i_1 >$ 16.25%: with a decreasing uplift, the pitch-down moment on the wing decreases. Because the support parts are removed further away from the model wing, disturbances on the lift and pitching moment are seen to monotonically decrease,

- It is seen that when the model sting and wing are further apart, these trends are maintained and the order of magnitude of the disturbances decreases as expected.

For these configurations, the tail installation effect is also determined. Results showing the change in support disturbance as a result of the tail installation are given in Figure 6.7.

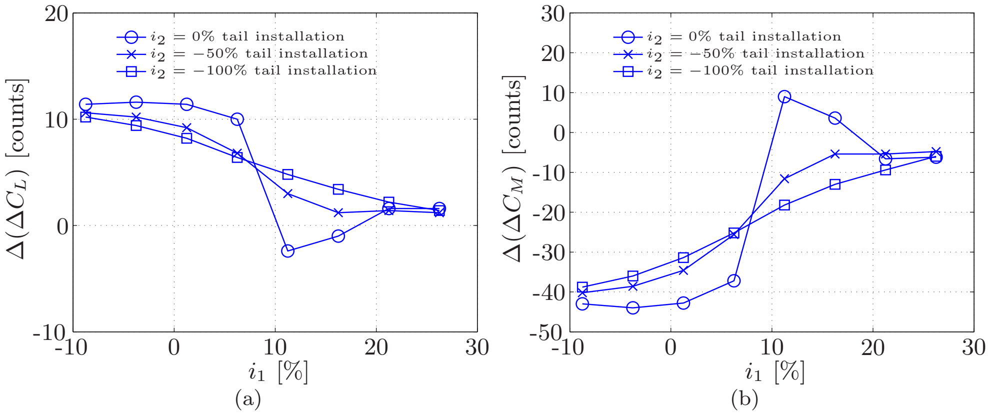

Figure 6.7: ESI results revealing the additional interference caused by tail installation on the (a) Lift-coefficient (b) Pitching moment-coefficient of the configuration shown in Figure 6.4. Results are for $\alpha = \beta = 0$ [deg], $V_\infty = 70$ [m/s]. For comparison, results of a mid-wing (i_2 = -50%) and a low-wing (i_2 = 0%) configuration are also shown

From Figure 6.7, the following becomes clear:

- The horizontal sting and torpedo create an uplift at the tail, resulting in a model pitch down disturbance. The reason that this effect is mainly attributed to the horizontal tail and torpedo is twofold:

  1. At the domain borders, the additional interference is approximately equal for all values of i_2: no direct influence of the model sting is observed. It is concluded for this configuration that the displacement effect of the horizontal sting and torpedo is much larger than the displacement effect of the model sting,
  2. Values of $\Delta(\Delta C_L)$ show a monotonically decreasing trend with i_1 resulting in a monotonically decreasing value of $\Delta(\Delta C_M)$.

- An extremity is seen in the case when $i_2 = 0$: in that case the tail is significantly affected when the model sting is underneath the wing. The support interference on the tail is reflected by the wing-tail interaction,

- It is seen that when the model sting and wing are further apart, these trends are maintained and the order of magnitude of the disturbances decreases as expected.

It is shown from these figures, that ESI can provide very valuable information on model support interference. With respect to the test-case configuration (i_2 = -100%): it becomes clear that the client requirements (minimizing the interference on both lift- and pitching moment-coefficient) can be met by either shifting the model sting more upstream than shown in the figures or more downstream (no minima are identified in the interference graphs). More upstream is not possible because of the constraints on the placement of the internal balance. This leaves with the only option of an even more downstream placement. Re-evaluating this test case with an even more downstream position of the model sting however triggers an advice function. The module advises not to place the sting more downstream because it will be positioned at the backbody of this configuration where adverse pressure gradients on the fuselage might cause very high values of interference as explained in section 4.5.1. This means that the optimum position of sting placement has been found: at 60% of the fuselage length from the model nose ($i_1 = 26.25\%$). Having met the client requirements, the interference polars are stored in ESI.

Although still in an early developmental stage, ESI's characteristics on speed and accuracy can be assessed. A typical test case as presented in this section has an execution time of approximately 1 hour. According to Table 5.1, this expert system application is therefore fast enough for the intended purpose (to be used at client negotiations). Assessing the accuracy of ESI is complicated because of the limited amount of experimental data available in this early developmental stage (this is also one of the main conclusions stated in Sons [78]). The trends as shown in Figures 6.6 and 6.7 are encouraging as they reflect behavior that is to be expected considering the configuration under study. Comparing the results to measured interference patterns shown in Eckert [18] (for similar support setups, sting placements and the same test section) it is seen that both signs and order of magnitude (absolute differences are attributed to variations in model geometry) coincides. Considering the prediction of the interference on the drag-coefficient with ESI, the user must rely on interpolation of experimental results that should be available in the data-base. It can be concluded that results of ESI look promising but need thorough validation by available experimental data.

This expert application is suitable for implementation during stage 1 (client negotiations) of a typical commercial wind tunnel test. Evaluating ESI from the viewpoint of expert system requirements the following can be noticed: this application results in advice on the test setup while evaluating the interference fast enough and accurate enough. Although at first instance it focuses on the problem of support interference, a similar application for the treatment of wall interference is easily implemented.

6.5 Stage 2 application: the Advice on Support Interference Determination (ASID) module

Client involvement during the test preparation phase (stage 2) is expressed in defining the balance between accuracy and costs for selecting a method to correct for the effects of support interference. The task of the expert system (according to Figure 6.1) is to provide the user a trade-off table which is used to give advice on the correction method taking this balance into account. This trade-off table includes a list of implementable correction methods including their operational range of applicability, accuracy and costs.

For this task, the author has developed the Advice on Support Interference Determination (ASID) module for the support structure in the LLF of DNW. A similar application for the treatment of wall interference is also possible (but not yet developed). The structure of ASID is given in Figure 6.8.

The core of this application is based on an extensive analysis of the ability of various experimental and numerical methods in determining model sting near-field and far-field interference. The results are generalized to a wide range of sting placements (as has resulted in Table 4.7) and for the complete model support used in the LLF. Methods that are analyzed include:

- Panel code calculations,
- Euler calculations,
- Navier-Stokes calculations,
- 5-hole probe measurements,
- Balance Δ-measurements.

Besides hardware characteristics (e.g. balance accuracy) the results in the trade-off table depend on the geometry and configuration of the wind tunnel model, the support setup and the location of sting protrusion in the fuselage of the model. The first part of the advice module is concerned with the definition of the wind tunnel model geometry and configuration in terms of its lifting surfaces. This description is necessary in order to calculate some basic inviscid aerodynamic properties of the wind tunnel model at zero degrees angle of attack and sideslip (lift, drag, lift slope and drag slope) by using a vortex-lattice code. The contribution of the fuselage to the aerodynamic characteristics of the configuration (the drag-coefficient) can be included if an estimate of this parameter is available.

The next part of the advice module concentrates on the support characteristics. The question that is posed by the module is whether or not the model sting is positioned such that its wake interferes directly with any lifting surface. This has consequences for which correction techniques are recommended including their accuracy. It is for instance known that the accuracy of an Euler-based calculation on the sting interference in angle of attack reduces near the wake area (this is discussed in Chapter 3). The accuracy of correction methods also depends on the location of the model sting protrusion in the fuselage as discussed in Chapter 4 and shown in Table 4.7. The nature of the disturbances changes when a different protrusion location of the model sting is chosen. This has consequences for the correction methods and their accuracy for such

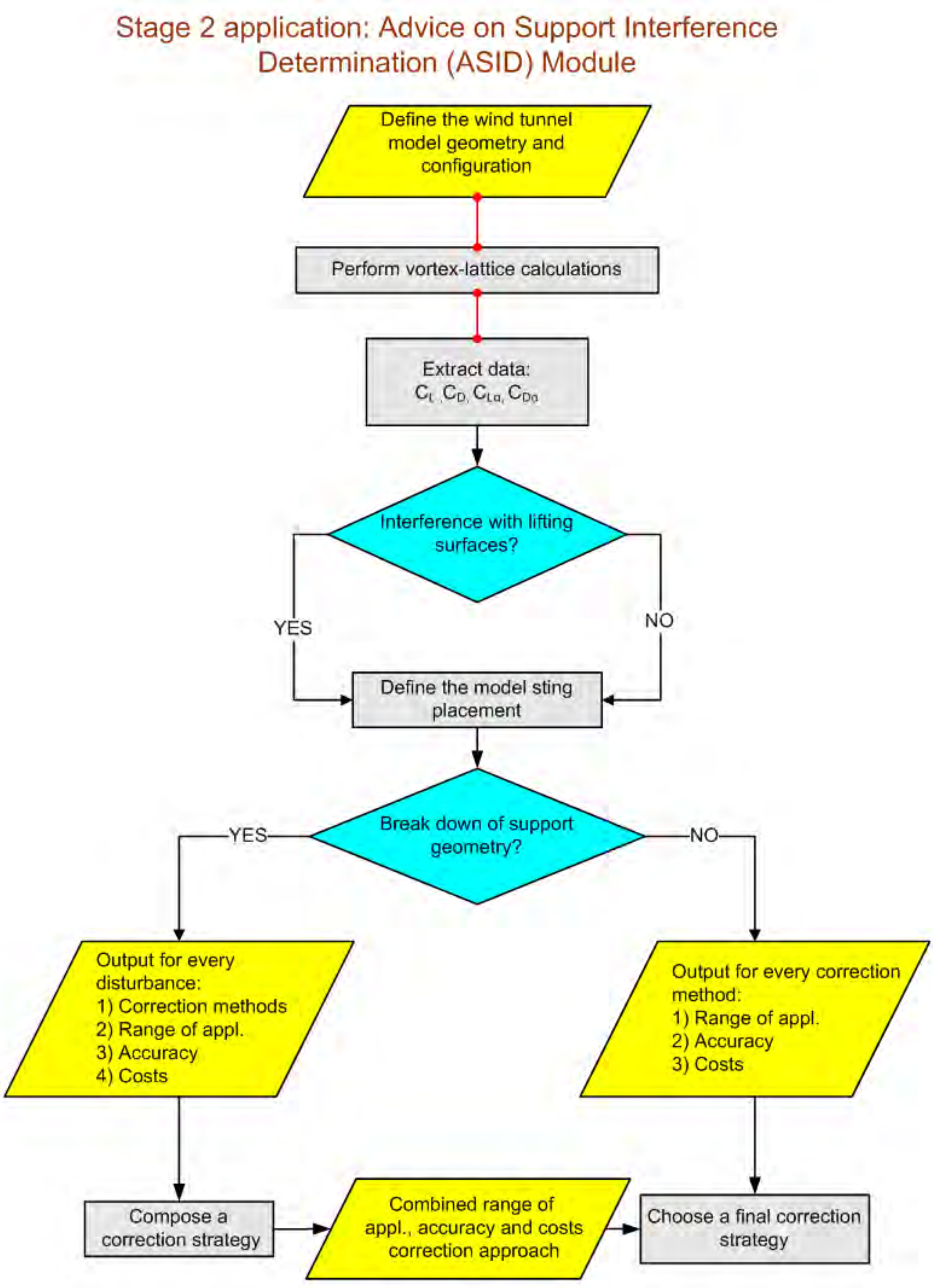

Figure 6.8: The structure of the Advice on Support Interference Determination (ASID) module

a sting placement. Depending on the exact support structure geometry, the placement of the model sting will also provide information on the proximity of the remaining support parts to the model.

Next, the user is provided the question whether or not the support geometry should be broken down to separate members for individual treatment. If not, the results in the trade-off table are concentrated on methods that are able to calculate or measure the total interference of the complete support structure as a whole. If so, the results are concentrated on methods to correct for the near-field and far-field effects of the separate support members.

No support geometry break down
In case no support geometry break down is desirable ASID provides an overview informing the user about recommended correction methods, their range of applicability (in terms of angle of attack and angle of sideslip ranges), their accuracy at zero degrees angle of attack and sideslip (seen as an indication of the order of magnitude of the accuracy) and related costs. The accuracy is given in terms of the longitudinal aerodynamic coefficients. It is determined using the characteristics of the model as calculated by the vortex-lattice code. When it is for instance known that the accuracy of a certain method in determining $\overline{\Delta\alpha}$ is X [deg], the accuracy of the method in determining the interference on the lift-coefficient is proportional to $\frac{\partial C_L}{\partial \alpha} X$.

An example of typical ASID output is given in Figure 6.9.

```
*****************************************************************************************
* Correction Method | AOA range [deg] | AOS range [deg] | Accuracy           | Costs [Euro] *
*---------------------------------------------------------------------------------------*
* Dummy measurement    -5 < AOA < 15     -25 < AOS < 25    dCL = +/- 0.008       25.000      *
*                                                          dCD = +/- 0.0010                  *
* Method B             -5 < AOA < 10     -10 < AOS < 10    dCL = +/- 0.015        5.000      *
*                                                          dCD = +/- 0.0050                  *
* Method C             -5 < AOA <  5     - 5 < AOS <  5    dCL = +/- 0.050        1.000      *
*                                                          dCD = +/- 0.0100                  *
*****************************************************************************************
```

Figure 6.9: ASID output in case of no support geometry break down. The costs are purely fictional and for illustration purposes only

Based on the results shown in Figure 6.9, the engineer and client should have enough information for a trade-off on correction methods given the desired balance between accuracy and costs resulting in a choice on the final correction strategy.

Choosing for a support geometry break down
It can also be decided to break down the support geometry for individual treatment of the support parts. This provides the client with more alternatives for the determination of the interference. The output is divided into implementable methods for the separate disturbance classes: for the model sting near-field and far-field disturbances, different methods are listed including their range of applicability, accuracy and costs. The same is given for the far-field effects of the remaining support parts. Typical output is given in Figure 6.10.

```
*****************************************************************************************************************************************
* Disturbance Effect      | Correction method        | AOA range [deg] | AOS range [deg] | Accuracy                      | Costs [Euro]      *
*---------------------------------------------------------------------------------------------------------------------------------------*
* Model sting near-field       Euler calculations      -5 < AOA < 10     -10 < AOS < 10    dCL = +/- 0.005               10.000            *
*                                                                                          dCD = +/- 0.0005                                *
* Model sting far-field     1) Probe measurements      -5 < AOA < 15     -25 < AOS < 25    dCL = +/- 0.008               50.000            *
*                                                                                          dCD = +/- 0.0010                                *
*                           2) Panel calculations      -5 < AOA < 10           AOS = 0     dCL = +/- 0.025                5.000            *
*                                                                                          dCD = +/- 0.0030                                *
*                           3) Euler calculations      -5 < AOA < 10     -10 < AOS < 10    dCL = +/- 0.010               10.000            *
*                                                                                          dCD = +/- 0.0015                                *
* Remaining parts far-field 1) Probe measurements      -5 < AOA < 15     -25 < AOS < 25    dCL = +/- 0.008               75.000            *
*                                                                                          dCD = +/- 0.0010                                *
*                           2) Panel calculations      -5 < AOA < 10           AOS = 0     dCL = +/- 0.035               15.000            *
*                                                                                          dCD = +/- 0.0040                                *
*                           3) Euler calculations      -5 < AOA < 10     -10 < AOS < 10    dCL = +/- 0.008               20.000            *
*                                                                                          dCD = +/- 0.0010                                *
*                           4) N.S. calculations       -5 < AOA < 15     -25 < AOS < 25    dCL = +/- 0.015              150.000            *
*                                                                                          dCD = +/- 0.0020                                *
*****************************************************************************************************************************************
```

Figure 6.10: ASID output in case of a support geometry break down. The costs are purely fictional and for illustration purposes only

Based on a typical table as shown in Figure 6.10 the user is requested to compose a custom correction package by choosing correction methods for the near-field and far-field disturbances of the model sting and remaining support parts. Based on this input the total range of applicability, accuracy and costs of the correction package are calculated. If not satisfying, the user will have to trade-off a different composition of the correction package until the final correction strategy is satisfying from the viewpoint of accuracy and costs.

Evaluating ASID from the viewpoint of expert system requirements the following can be noticed: this application results in advice on correction methods. Although at first instance it focuses on the problem of support interference, a similar application for the treatment of wall interference is easily implemented.

Besides ASID, an additional method that can be used during stage 2 of a typical commercial wind tunnel measurement is presented in this thesis: VOLAER (VOrtex-LAttice/EuleR). This is a method that combines the best performance of both Euler calculations and vortex-lattice calculations for the determination of support interference. The method is therefore called a hybrid method (it is composed of multiple approaches). VOLAER exhibits its own characteristics on accuracy and speed allowing for its allocation in the expert system. This method and its characteristics are discussed in the following chapter where hybrid methods are treated.

6.6 Expert system applications for stage 3 and 4

Expert system applications to be used during measurements (stage 3) and post-test corrections (stage 4) are introduced in this section.

The purpose of applications in these stages is to correct for the interference on one hand (in an on-line or off-line sense) but also to determine the corrections on the spot (on-line or off-line):

- In the first case (merely correction) uncorrected measurement data and corrections are combined in the correction process. This data is delivered to an expert system application on-line or by data files that are also used for the off-line correction. Before these corrections are applied to the measurement results, both uncorrected measurements and corrections need to be interpolated to the same numerical grid. It is clear that the exact characteristics of such correction processes depend on hardware and software characteristics of the company or institute employing the expert system. The corrections fed into the expert system will have a specified format (e.g. $\Delta\alpha$ or ΔC_L) corresponding to a customized correction strategy (e.g. $C_{L_{corr}} = C_{L_{uncorr}} - \Delta C_L$ or $\alpha_{corr} = \alpha_{uncorr} - \Delta\alpha$). This poses a compatibility constraint between the stage 2 application output and the stage 3 or 4 application input. Typical applications will not be further considered,

- In the second case an application should determine the interference on the spot (both on-line and off-line): an application is developed that combines uncorrected wind tunnel measurements with vortex-lattice calculations to correct for all the disturbances of wind tunnel walls and support, both on-line and off-line. This hybrid method is called MVL (Measurement/Vortex-Lattice). Like VOLAER this method is thoroughly discussed in the following chapter where hybrid methods are treated.

The above mentioned application (MVL) closes the set of expert system requirements (calculate- and correct for the interference on-line and off-line fast- and accurate enough) mentioned in section 6.2. MVL exhibits its own characteristics on accuracy and speed allowing for its allocation in the expert system. The method and its characteristics are discussed in the following chapter.

6.7 Additional expert system requirements

6.7.1 Easy addition of wall interference assessment modules

Considering the expert system applications these are mainly focused on the main topic in this thesis: low-speed wind tunnel support interference. In Chapter 1 it is mentioned that besides support interference, wall interference is also a significant disturbance that should be accounted for when results of wind tunnel tests are corrected to "free flow" values. Considering the fact that wind tunnel wall interference can be expressed in the same characteristic variables as the problem of support interference ($\Delta\alpha$, $\Delta\beta$, $\frac{\Delta q}{q_\infty}$ or simply ΔC_i), its inclusion in the expert system is only apparent. Because the proposed expert system structure resembles an application frame holder, including additional modules for the treatment of wall interference is facilitated: an advisory module for determining the most suitable method to correct for wall interference (implementable in the test preparation phase) can be setup in a similar way as for the problem of support interference. Because of the interrelationship between wall- and support interference, the current applications might also be expanded to include the treatment of wall interference: modeling of the wind tunnel walls in ESI has opened the door to extracting wind tunnel wall interference as well in an early stage 1 (client negotiations). MVL (stage 3/4) already includes the calculation of wind tunnel wall interference, although not separately from support interference as will be clear in the next chapter.

Meet computer platform standards

Compatibility of the expert system (or basically of its expert applications) with a predefined platform must be guaranteed to ensure easy distribution amongst the users. To this end it would be safe to delegate the administration of the expert system to a software expert. This expert would carry the responsibility of including future expert applications, ensuring compatibility and monitoring the distribution of (updated) versions of the expert system amongst its users.

A user friendly system with professional interfaces

It is noted in section 1.4 that the success of an expert system depends on the successive communication between system and user(s). This can be achieved by user friendly, professional interfaces. The expert applications that are currently developed obey to this requirement: ESI is setup with a user friendly, visual interface. This graphics-based program clarifies the user what input is necessary and what steps should be taken to arrive at the desired output. The output is structured in such a way as to provide ample information to both engineer and client. ASID contains a very high information density based on the research on model support interference presented in this thesis. This information is however structured and interpreted by asking the user only a few clear questions. MVL (discussed on the next chapter) is an example of an expert system application that hardly needs user intervention and interface. All the expertise is in the methodology behind the program (the theory). User intervention is however required when the method is implemented in the data-acquisition system of the wind tunnel.

6.8 Summary

In this chapter, a feasible application-based structure of the expert system is discussed in more detail after summarizing its requirements. Typical applications are studied in more detail. It is shown that the proposed structure fulfills the expert system's requirements. Two newly developed hybrid methods for the determination of wall- and support interference are introduced: VOLAER (VOrtex-LAttice/EuleR) implementable during stage 2 (test preparation) and MVL (Measurement/Vortex-Lattice) implementable during stages 3 and 4 (measurements/post-test corrections) of a typical commercial wind tunnel measurement. The principle and evaluation of characteristics of these methods is demonstrated in the next chapter on hybrid methods.

Chapter 7

Hybrid Methods for Determining Wall- and Support Interference

This chapter presents two newly developed hybrid methods for the determination of wall- and support interference: VOLAER and MVL. These methods can be implemented during a typical commercial wind tunnel measurement. They are given the label "hybrid" because they combine results of two standard methods (experimental and/or numerical) for the determination of interference. In this way the most favorable characteristics of these standard methods are combined. VOLAER and MVL are explained in this chapter and their potential is demonstrated by test cases. They prove to be valuable elements for an expert system.

7.1 Introduction

Standard methods to determine wall- and support interference typically implement one numerical or experimental technique. As shown in Chapters 2 and 3, typical methods such as panel code-, Euler-, Navier-Stokes calculations but also 5-hole probe measurements are constrained in their range of applicability. By combining such methods in a clever way, new interference determination methods arise with wider ranges of applicability because their most favorable characteristics are utilized. These smart combinations are called hybrid methods and are the subject of this chapter.

In this chapter, two hybrid methods are introduced (developed by the author):

1. VOLAER (VOrtex-LAttice/EuleR): this method combines vortex-lattice calculations and Euler calculations for the determination of support interference (both near-field and far-field),

2. MVL (Measurement/Vortex-Lattice): this method combines uncorrected wind tunnel measurements with vortex-lattice calculations to correct for all the disturbances of wind tunnel walls and support.

In the following sections, VOLAER and MVL are explained and their potential is demonstrated by test cases. This enables the evaluation of their characteristics in terms of speed and accuracy.

7.2 VOrtex-LAttice/EuleR method: VOLAER

In this section VOLAER is demonstrated and evaluated. It is shown that this method provides valuable information on support interference. For this hybrid method, the calculation of support interference is divided in two parts:

1. The calculation of model sting near-field effects and far-field effects (buoyancy) on the fuselage and evaluation of values of disturbance parameters at the lifting surfaces. These effects are calculated by an Euler Δ-calculation,
2. The evaluation of the characteristics of the lifting surfaces by a vortex-lattice calculation. This enables the determination of the far-field disturbances on the lifting surfaces.

Successive recombination of results of both parts yields the final correction for support interference.

VOLAER is a method that uses numerical methods only. As explained in detail in Chapter 4, Euler methods are (from the viewpoint of both accuracy and implementation effort) preferable over e.g. panel calculations and Navier-Stokes calculations (when the sting is not placed in region R3 according to Figure 4.26). This method therefore seems the most suitable for determination of the disturbances. A fast and fairly accurate method for the determination of the lifting surface characteristics is a vortex-lattice calculation. Including this method in VOLAER enables fast parametric studies of wing configurations (e.g. flap settings) on the values of far-field effects.

The division of the interference calculation in the above mentioned parts necessitates a particular formulation of support interference. This formulation is treated next.

7.2.1 A general formulation of support interference

When the total disturbance of a support on a model in a low-speed wind tunnel is evaluated, it can be written as:

$$\Delta C_i = \Delta C_{i_{n.f.}} + \sum_{i=1}^{N} \Delta C_{i_{f.f.}} + \Delta C_{i_{f.f._{Buoyancy}}}. \tag{7.1}$$

In Equation 7.1 the total disturbance of the model support is divided into a near-field (n.f.) disturbance of the model sting on the fuselage, a summation of far-field (f.f.) disturbances of the complete support over all N lifting surfaces and a buoyancy force on the fuselage. Summing the terms of Equation 7.1 leads to the support interference effect for one freestream condition. The far-field disturbances on the lifting surfaces can be written out. The result is given in Equation set 7.2.

$$
\begin{aligned}
\Delta C_{D_{f.f.}} &= \frac{\partial C_D}{\partial \alpha}\overline{\Delta\alpha} - C_L \sin\overline{\Delta\alpha} + \frac{\partial C_D}{\partial \beta}\overline{\Delta\beta} + C_Y \sin\overline{\Delta\beta} + C_D \frac{\overline{\Delta q}}{q_\infty}, \\
\Delta C_{Y_{f.f.}} &= \frac{\partial C_Y}{\partial \alpha}\overline{\Delta\alpha} + \frac{\partial C_Y}{\partial \beta}\overline{\Delta\beta} - C_D \sin\overline{\Delta\beta} + C_Y \frac{\overline{\Delta q}}{q_\infty}, \\
\Delta C_{L_{f.f.}} &= \frac{\partial C_L}{\partial \alpha}\overline{\Delta\alpha} + C_D \sin\overline{\Delta\alpha} + \frac{\partial C_L}{\partial \beta}\overline{\Delta\beta} + C_L \frac{\overline{\Delta q}}{q_\infty}, \\
\Delta C_{l_{f.f.}} &= \frac{\partial C_l}{\partial \alpha}\overline{\Delta\alpha} + \frac{\partial C_l}{\partial \beta}\overline{\Delta\beta} + C_l \frac{\overline{\Delta q}}{q_\infty}, \\
\Delta C_{m_{f.f.}} &= \frac{\partial C_m}{\partial \alpha}\overline{\Delta\alpha} + \frac{\partial C_m}{\partial \beta}\overline{\Delta\beta} + C_m \frac{\overline{\Delta q}}{q_\infty}, \\
\Delta C_{n_{f.f.}} &= \frac{\partial C_n}{\partial \alpha}\overline{\Delta\alpha} + \frac{\partial C_n}{\partial \beta}\overline{\Delta\beta} + C_n \frac{\overline{\Delta q}}{q_\infty}.
\end{aligned}
\tag{7.2}
$$

In Equation set 7.2 the far-field disturbances are calculated by combining values of the undisturbed aerodynamic coefficients (C_L, C_D, etc.), their aerodynamic derivatives to the angle of attack and sideslip and finally spanwise chord-averaged (to the m.a.c.) disturbance parameters as presented in Appendix A:

- Averaged angle of attack disturbances $\left(\overline{\Delta\alpha}\right)$ at the $\frac{3}{4}$ chord position of the lifting surfaces,
- Averaged angle of sideslip disturbances $\left(\overline{\Delta\beta}\right)$ at the $\frac{3}{4}$ chord position of the lifting surfaces,
- Averaged dynamic pressure disturbances $\left(\frac{\overline{\Delta q}}{q_\infty}\right)$ at the $\frac{1}{4}$ chord position of the lifting surfaces.

Moments in Equation set 7.2 are evaluated at the quarter chord point of the main wing.

The buoyancy term specified in Equation 7.1 is approximated by:

$$
\Delta C_D = \sum_{i=1}^{M} \left(\frac{Vol_i}{S_{Ref}}\right) \left(\frac{\left(\frac{\Delta q}{q_\infty}\right)_i}{dx_i}\right) \cos\alpha \cos\beta \tag{7.3}
$$

In Equation 7.3, the fuselage is divided into M parts (by cross-sectional cuts) whereas an analysis of the pressure gradient over these parts (with volume Vol_i) leads to the buoyancy on the fuselage.

The challenge is to determine all unknown values in Equation sets 7.1, 7.2 and 7.3 in order to calculate the value of the support disturbance on a certain configuration at given freestream conditions. For the hybrid technique presented, two methods are implemented to collect all the missing terms:

1. Euler Δ-calculations: these calculations model the complete wind tunnel test section, support structure and wind tunnel model fuselage. No lifting surfaces are discretized. The reason behind this is that the interference of the lifting surfaces on the support structure can not be calculated. This only accounts for situations where the support structure is not in the wake of the lifting surfaces close to their trailing edge. Such situations are usually prevented because they result in high interference values. Two Euler calculations should be performed: one calculation including the support structure and one calculation excluding the support structure. The interference terms that can be derived from this Δ-calculation are:
   - The near-field effects of the model sting on the fuselage,
   - The buoyancy due to the support structure on the fuselage (Equation 7.3),
   - The spatial distribution of $\Delta\alpha$, $\Delta\beta$ and $\frac{\Delta q}{q_\infty}$ leading to their spanwise chord-averaged values.
2. Vortex-lattice calculations: these calculations are performed on the configuration of the lifting surfaces (no fuselage is modeled). From these calculations, the values of the undisturbed aerodynamic coefficients and their derivatives are calculated. The value of the drag-coefficient is not very accurately determined because the parasitic drag is not evaluated (only the induced drag). Within the linear lift-region where flow separation is minimal this problem can be solved by adding an estimated constant value for the parasitic drag (thereby neglecting its gradient compared to the induced drag).

When the values of the unknowns are evaluated by Euler calculations and vortex-lattice calculations, they are recombined to form the values of near-field and far-field disturbances of the model support. The total interference is then calculated according to Equation 7.1. A schematic of the principle of VOLAER is shown in Figure 7.1.

Besides the fact that this method leads to the total interference on the configuration of interest, the spatial distribution of the disturbances over the configuration can be analyzed providing valuable information of disturbances in regions of interest. This is demonstrated by a test case. This test case is presented after discussing the typical range of applicability of this method in the next section.

7.2.2 Range of applicability of VOLAER

The applicability of this hybrid method lies within the domain bounded by the most stringent applicability restrictions of the two numerical methods. Considering vortex-lattice calculations one of the restrictions is that the flow around the configuration of interest (the wind tunnel model) should be steady. This poses restrictions on the applicable angle of attack and sideslip. Because this method is not able to resolve viscous effects (like boundary layer separation) the range of applicability in terms of angle of attack and angle of sideslip (consider separated flow from the fuselage) is to within the linear lift regime, typically -10 $\leq \alpha,\beta \leq$ 10 [deg]. In vortex-lattice calculations it is assumed that the lifting surfaces that are modeled can be approximated

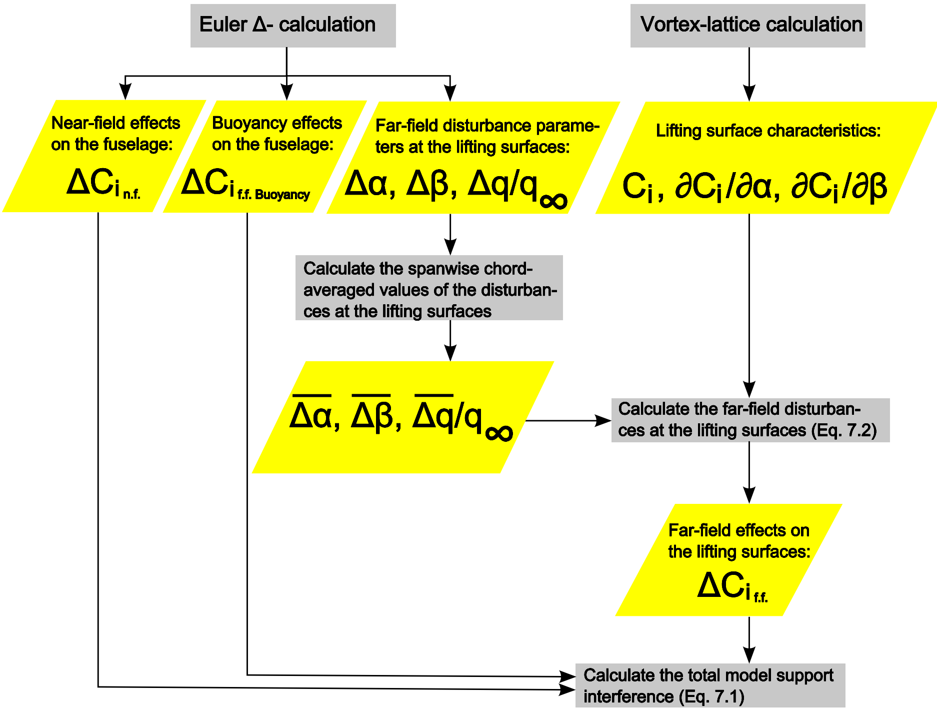

Figure 7.1: The principle of VOLAER. For every new freestream condition, the calculations in this figure should be repeated

by thin airfoil theory according to Drela et al. [79]. The influence of airfoil thickness on the aerodynamic characteristics is not captured in such calculations. According to Anderson [80] this restricts its use to airfoils with a maximum thickness-to-chord ratio of 0.12. On top of this it is assumed that the wake trailing from the lifting surfaces runs parallel to the wind tunnel longitudinal axis: wake relaxation is not simulated. This implies that situations with large wake deflections should be avoided (e.g. caused by high lift). Last, thrust effects on the aerodynamics of the lifting surfaces are not included implying that engine power effects on support interference can not be evaluated.

Considering the Euler calculations, similar limitations hold: although unsteady flow can be triggered around the fuselage and support, a steady state solution of the disturbances is implemented in Equations 7.1, 7.2 and 7.3. When convergence problems arise during a steady calculation caused by unsteady phenomena, an unsteady calculation should be performed. Time-averaged disturbances are then implemented in order to determine the support interference. Because Euler calculations neglect the modeling of viscosity, situations where large viscous disturbances arise should be avoided. This can be done by taking the following into consideration:

1. By paying attention to the model sting placement. It is explained in section 4.5.1 that the accuracy of an Euler calculation in determining model sting interference depends on a successful choice of the sting protrusion location that minimizes the viscous disturbances. This is accomplished by ensuring that the model sting is not placed in regions that are characterized by adverse pressure gradients on the fuselage. Placements where the sting wake interferes with the lifting surfaces should also be avoided. These are scenarios that are usually avoided in reality. Therefore they form no uncomfortable restriction,

2. By ensuring that the angle of attack and angle of sideslip of the model remains limited (typically within $-10 \leq \alpha,\beta \leq 10$ [deg]). This ensures a trustworthy calculated pressure distribution at both fuselage and sting and accompanying interference profile.

Even within these limits substantial separation can be introduced at remaining support parts depending on the complexity of the support geometry. Calculation convergence is usually compromised by such factors. Sometimes these problems can be solved by simplifying modeling assumptions. An example is to simplify the support geometry to represent the most important geometrical characteristics responsible for the bulk of the total disturbance. Regions that contain large amounts of separated flow can be modeled as “solid regions” (that extend downstream to the domain boundaries) thereby improving the convergence rate of the calculation while accounting for the correct levels of support blockage and buoyancy.

Other numerical methods often including such simplifying modeling assumptions are the panel code calculation (consider the wake modeling) or even simpler methods that rely on distributed singularities (slender body theory for example) as typically found in e.g. the AGARDograph 336 [5]. Such methods however do not capture the near-field effects properly. It will be shown in this chapter that at angles of sideslip these near-field effects become much more pronounced than at zero sideslip, caused by the action of the cavity and slit. Panel codes are therefore (Table 4.7) not a sensible option as they prove to predict the near-field effect erroneously. Other methods based on distributed singularities do not resolve the near-field effects and are often not able to simulate support structures at sideslip angles (consider e.g. slender body theory). Performing Euler calculations is therefore the most sensible option.

Summarizing on the applicability of the VOLAER method dictated by the common restrictions of vortex-lattice- and Euler calculations:

1. Steady flow is assumed at the lifting surfaces,
2. The lifting surfaces can be approximated by thin airfoil theory (typically $t/c \leq 0.12$),
3. Large wake deflections (caused by high lift) should be avoided (control surface/flap deflections typically ≤ 20 [deg]),
4. Effects of viscosity can be neglected:
   - Typically $-10 \leq \alpha,\beta \leq 10$ [deg],
   - The model sting is not located in regions of adverse pressure gradients on the fuselage and the interference of the sting wake with lifting surfaces is avoided.
5. Thrust effects on support interference are not included.

Abiding by these restrictions, a test case is setup to demonstrate the usefulness of VOLAER. This case is discussed next.

7.2.3 Test case: applying VOLAER

In this test case the model support interference on a typical aircraft configuration resembling the ALVAST model fuselage and wings (described by Brodersen [65]) is determined. Because this model does not contain a tail, a tail geometrically resembling the Airbus A319 tail is discretized. To demonstrate a general application of VOLAER this model is put at an angle of attack and angle of sideslip of 8 [deg]. It is supported by the very complex model support of the Large Low-speed Facility of DNW in their 8 x 6 [m^2] closed test section. The model is mounted by a dorsal sting and contains an internal balance. It is subject to an incoming flow with a Mach number of 0.20 (resembling a Reynolds number of 1.5 million based on the mean aerodynamic chord). A picture of the geometrical setup is given in Figure 7.2. In this picture the wind tunnel walls are removed for clarity.

In the following sections, it will be shown how the Euler- and vortex-lattice calculations are set up. The results of the calculated near-field and far-field effects are presented. This will lead to the final value of support interference at given freestream conditions. Because of the very limited availability of experimental data, only parts of this test case can be validated experimentally. The test case will however clearly reveal the usefulness of the hybrid method.

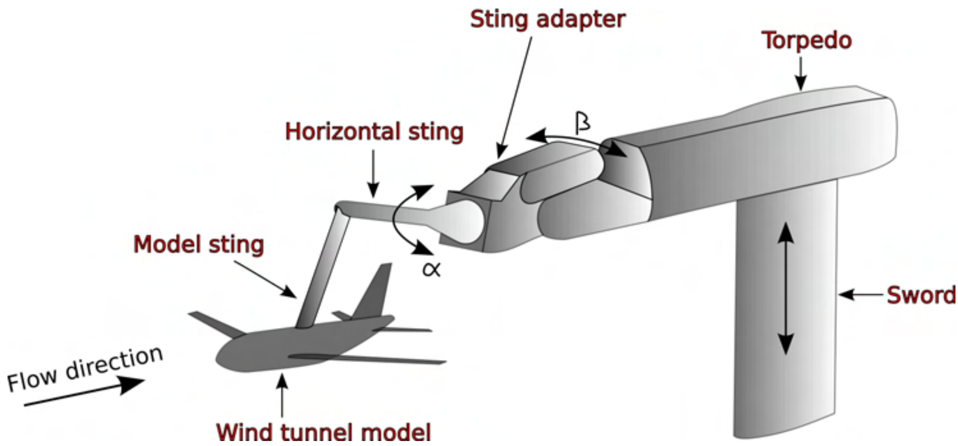

Figure 7.2: A geometrical description of the VOLAER study case: a typical aircraft configuration resembling the ALVAST model with A319-like tail. The model is attached to the dorsal model support of the Large Low-speed Facility at DNW and positioned at angle of attack and sideslip of 8 [deg]. In the figure, the degrees of freedom of the support structure are indicated

7.2.4 Setting up the Euler calculations

An Euler Δ-calculation is performed: one calculation includes the model fuselage, internal cavity (normally accommodating the internal balance), the slit separating the sting and fuselage at the sting protrusion location, the complete model support and the wind tunnel test section. The second calculation includes the model fuselage and test section. In the latter case, the fuselage is closed by a "filling cap" (as implemented in Chapter 3). A Δ-calculation on the fuselage forces and moments provides the near-field effects and buoyancy. A Δ-calculation on the flow angles and dynamic pressure (α, β and q) at the lifting surfaces' $\frac{3}{4}$ and $\frac{1}{4}$ chord lines respectively provides the terms $\Delta\alpha\left(\overline{x}\right)$, $\Delta\beta\left(\overline{x}\right)$ and $\frac{\Delta q}{q_\infty}\left(\overline{x}\right)$. These terms are used to calculate the far-field effects on the lifting surfaces according to Equation set 7.2.

The numerical domain is bounded by the 8 x 6 $[m^2]$ closed test section. The model support structure is simplified such as to catch the most significant characteristics of the setup while not jeopardizing the convergence of the calculation. Wind tunnel walls, model support and fuselage are given flow tangency boundary conditions. From the viewpoint of reducing the amount of cells in the unstructured computational grid by Hexpress (approximately 13 million for this calculation) it is chosen not to extend the wind tunnel too far upstream and downstream. Instead, mass flow inlet and pressure outlet boundary conditions are chosen to represent the boundary conditions appropriately (explained in section 3.3.2). In this domain the steady Euler equations are solved by the flow solver FLUENT using a pressure-based implicit solver. The convective fluxes of pressure, density, momentum and energy are discretized with second order schemes.

7.2.5 Setting up the vortex-lattice calculations

The freeware vortex-lattice code “Athena Vortex-Lattice” or *AVL* by Drela ([79] and [81]) is used to model the lifting surfaces: wings, horizontal tailplanes and vertical tailplane are discretized. Flaps and control surfaces (ailerons, elevators and rudder) are included. AVL allows the calculation of the aerodynamic properties of lifting surfaces including sweep, dihedral and taper. Lifting surfaces are discretized by specifying the camber line of its airfoils. This makes AVL a suitable program for the intended use.

AVL provides the capability to model slender bodies such as fuselages using source and doublet filaments according to slender body theory described by Drela et al. [79]. However a note of caution is placed for this implementation due to limited experience with such modeling. Therefore it is chosen not to model the fuselage. Because normally the fuselage experiences a signature of the lift- and induced drag distribution from the lifting surfaces by a carry-over effect, it is decided to stretch the lifting surface definition to the model centerline. This improves the quality of the prediction of the aerodynamic characteristics of the lifting surfaces close to the fuselage. Figure 7.3 shows the configuration of the study case implemented by AVL.

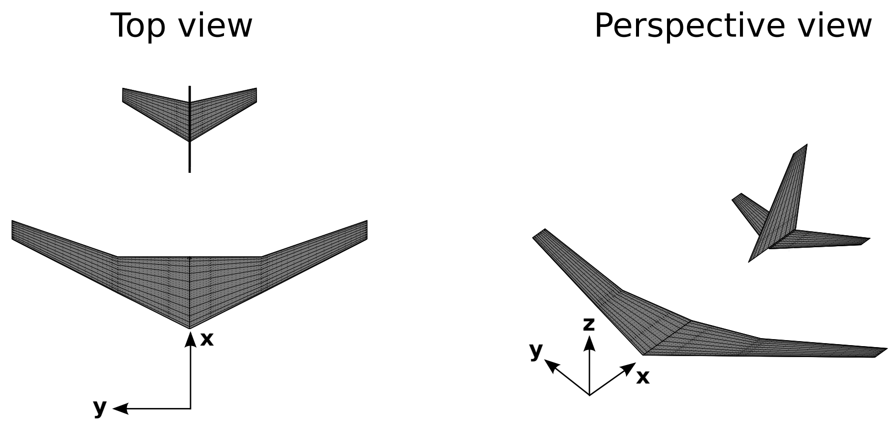

Figure 7.3: Top view and perspective view of lifting surfaces of the VOLAER study case model used in the vortex-lattice calculations

The geometrical description of the wings and tailplanes is translated by AVL to a numerical discretization by the placement of a number of horseshoe vortices on the lifting surfaces to model the circulation. More on vortex-lattice codes is given in section 7.3.4. In order to calculate the aerodynamic coefficients and their derivatives with respect to α and β with the highest accuracy possible, the maximum number of horseshoe vortices is used for the numerical discretization of the lifting surfaces. The density of vortices is increased at places where steep gradients in the lift distribution are expected (e.g. at control surface hinges).

The values of the aerodynamic coefficients are found by performing a calculation at (α,β) = (8,8) [deg]. The values of aerodynamic derivatives are found by performing multiple calculations in the direct vicinity of (α,β) = (8,8) [deg] and determining the trend lines through these points.

7.2.6 Results of a typical VOLAER calculation

In the following sections, results of Euler calculations and vortex-lattice calculations leading to the disturbance terms given in Equation 7.1 are presented.

Calculating near-field and buoyancy effects

Values of support near-field interference are found by an Euler Δ-calculation on the fuselage forces and moments. This calculation includes the far-field buoyancy effect on the drag-coefficient given in Equation 7.3. These disturbance effects together with model reference values for the wing area, mean aerodynamic chord and span (used for non-dimensionalization purposes) are given in Table 7.1. The moment reference point is taken at the wing quarter-chord location. In the table, the calculated force coefficients are compared to:

- An indication of the values at (α, β) = (8,0) [deg]. These experimental results are taken from Chapter 3 where balance measurements on sting near-field interference are presented. These results are thought to be representative for comparison as a similar fuselage shape is used with a similar sting placement (region R2b according to Figure 4.26). The additional buoyancy term of the complete support is taken from experimental results of DNW on a similar fuselage with the same support setup (based on Eckert et al. [37]),
- Determined in a similar way are indicative experimental values at (α, β) = (0,0) [deg] to assess the effect of sideslip angles and angles of attack on the interference.

Unfortunately, no reference experimental material for (α, β) = (8,8) [deg] is available. Because there was no certainty on the values of the moment arms in all experimental reference material, a fair comparison on moment coefficients is left out of the consideration.

When Table 7.1 is studied, the following can be concluded: the angle of sideslip has a pronounced effect on the interference on the lift- and drag-coefficients. When the interference on the side force-coefficient C_Y is considered, it is seen that at a sideslip angle the fuselage has the tendency to move to the port side. This is triggered by an asymmetrical pressure disturbance on the fuselage. The resulting interference is significant. Although the rolling moment- and yawing moment are not greatly affected by the near-field disturbances at this sideslip angle, the pitching moment is significantly affected. It is seen in the table that the drop in fuselage lift and the increase in drag induces a nose-up pitching moment about the moment reference point. Relating this increase in pitching moment to the drop in lift results in an average moment arm of 0.3 [m]. This arm is approximately equal to the distance from the wing quarter-chord

Table 7.1: Combined result of near-field effects and far-field buoyancy effect of the model support shown in Figure 7.2 on the mounted fuselage at (α,β) = (8,8) [deg] and M_∞ = 0.20. Reference experimental values at α, β = (8,0) [deg] and α, β = (0,0) [deg] are also given

Parameter	α, β = **[8,8] [deg]**	α, β = **[8,0] [deg]**	α, β = **[0,0] [deg]**
ΔC_D	54	25	50
ΔC_Y	-42	0	0
ΔC_L	-36	0	0
ΔC_l	0	-	-
ΔC_m	12	-	-
ΔC_n	-7	-	-

Parameter	**Value**
S_{ref}	1.738 m^2
c_{ref}	0.391 m
b_{ref}	3.989 m

location to the nose of the sting where approximately 80% of the sting carry-over effect takes place (as found in section 4.3.4).

At non-zero angles of sideslip, the near-field interference is significantly larger than at zero degrees. It is shown later on that the near-field effects have the same order of magnitude as the far-field effects and can certainly not be neglected. This poses the question whether or not introducing non-zero angles of sideslip changes the model sting near-field effects in a qualitative way. This is indeed the case: an indication of the near-field flow at non-zero sideslip angles is provided in Figure 7.4.

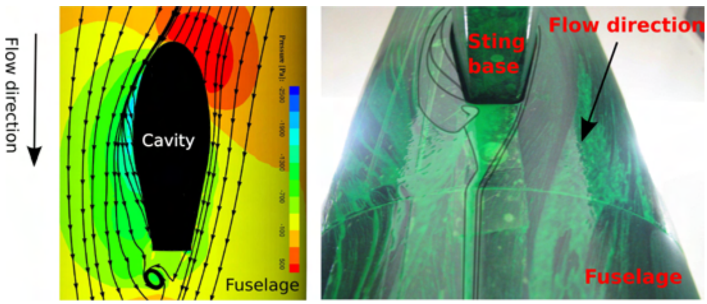

Figure 7.4: Near-field support effects of the arrangement shown in Figure 7.2 revealing the pressure distribution and streamlines on the fuselage. Configuration: (α,β) = (8,8) [deg], M_∞ = 0.20. The viewpoint is on top of the fuselage looking directly at the balance cavity (for clarity the sting is not visualized). Pressures are given relative to a freestream reference pressure of 0 [Pa]. This image is compared to the result of an experimental oil flow visualization on a similar sting/fuselage configuration. For clarity, some streamlines are highlighted

In this figure the pressure distribution and streamline behavior on the fuselage is shown at the protrusion location of the model sting. It is compared to a result of an experimental oil flow visualization on a similar sting/fuselage configuration. Keeping in mind that no actual viscous flow is simulated (however the streamline pattern seems to match the oil flow visualizations), some highlights of the flow pattern are distinguished:

- A carry-over of sting stagnation pressure onto the fuselage,
- A carry-over of a low pressure area of the sting leeward side (portside) onto the fuselage,
- The effect of vortex formation on the leeward side of the sting near the slit,
- An asymmetric recirculation zone aft of the sting,
- An asymmetric sting wake trace on the fuselage.

In the streamline pattern and pressure distribution, the asymmetry of the flow with respect to the fuselage centerline is clearly discernible. Pressure differences between the windward side (starboard) and leeward side (portside) of the model sting are responsible for the interference on C_Y of the fuselage as indicated in Table 7.1. One of the more interesting phenomena is the asymmetry in the formation of vortical structures near the slit. In [11] it is recognized that the slit vortex is caused by separation of fluid exiting the model balance cavity. This fluid is sucked out of the cavity by an underpressure that is caused by acceleration of the flow at the sting side by the sting profile. Considering Figure 7.4 it is seen that vortex traces on the fuselage are only identifiable at the leeward side of the sting. This is caused by the fact that the pressure at the leeward side of the sting reaches very low values (caused by a combined action of angle of sideslip and sting profile) thereby sucking out the fluid from the balance cavity. By the action of numerical dissipation the flow separates from the fuselage leading to a vortical structure near the slit. At the windward side however, such pressure differences are not reached (this is the “stagnation side” of the sting) disabling formation of such vortical structures. Figure 7.5 shows streamline patterns on the fuselage and sting at the windward and leeward side. The picture gives a clear indication of the flow asymmetry.

Asymmetry in the vortex pattern is confirmed when cross-sections of the fuselage are considered. In Figure 7.6 two lateral cross-sections of the fuselage are seen. In Figure 7.6(b) the cross-section is taken at the stagnation point on the sting. It is seen that at the windward side, fluid is forced into the cavity by the high pressure at the stagnation point. At the leeward side, an equilibrium has established between the fluid in the cavity and the freestream leading to a local zero net flow through the slit. Figure 7.6(c) is a cross-section at approximately 50% of the sting chord. In this picture it is seen that at the windward side, no vortex formation is recognized (the pressure at this side of the sting is too high). At the leeward side however, a clear vortical structure is visible. The cause of the existence of the vortex is seen in the low pressure area at the top of the picture. This low pressure area has also manifested more upstream at the slit (this is a straight cross-section of a back swept sting) thereby sucking out fluid of the balance cavity hence giving rise to the vortex.

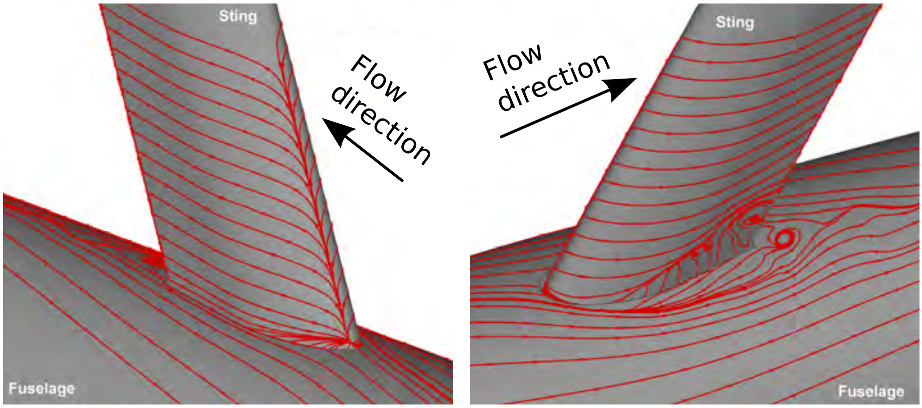

(a) (b)

Figure 7.5: Near-field support effects of the arrangement shown in Figure 7.2 revealing streamline patterns at the model fuselage and sting at the (a) Windward side (b) Leeward side of the model sting. Configuration: $(\alpha,\beta) = (8{,}8)$ [deg], $M_\infty = 0.20$

The angle of sideslip has a significant effect on the near-field disturbances, both qualitatively and quantitatively. The effects shown in the figures are in line with what would be expected based on results of Navier-Stokes calculations presented in Chapter 4 but also typical experimental results shown in e.g. Figure 7.4. In Chapter 5 it is mentioned that the design of a custom-made model for calculating support interference could be jeopardized by interference flow fields that change qualitatively (and therefore quantitatively) under the influence of e.g. angles of sideslip. Based on the results of this section this concern is justified.

Calculating far-field disturbances

The disturbance parameters $\Delta\alpha$, $\Delta\beta$ and $\frac{\Delta q}{q_\infty}$ are evaluated at the lifting surfaces' $\frac{3}{4}$ and $\frac{1}{4}$ chord lines respectively by a Δ-calculation on the values of α, β and q that are given by:

$$\begin{aligned} \alpha &= \arctan\left(\frac{w}{u}\right), \\ \beta &= -\arctan\left(\frac{v}{u}\right), \\ q &= \frac{\rho\left(u^2+v^2+w^2\right)}{2}. \end{aligned} \tag{7.4}$$

In Equation set 7.4, the values of the velocity components in x, y and z direction (u, v and w) and the density ρ are local values. The Δ-calculation leads to a spatial distribution of the disturbances in angle of attack, angle of sideslip and dynamic pressure along the lifting surfaces' $\frac{3}{4}$ and $\frac{1}{4}$ chord lines respectively. A typical example of the spatial

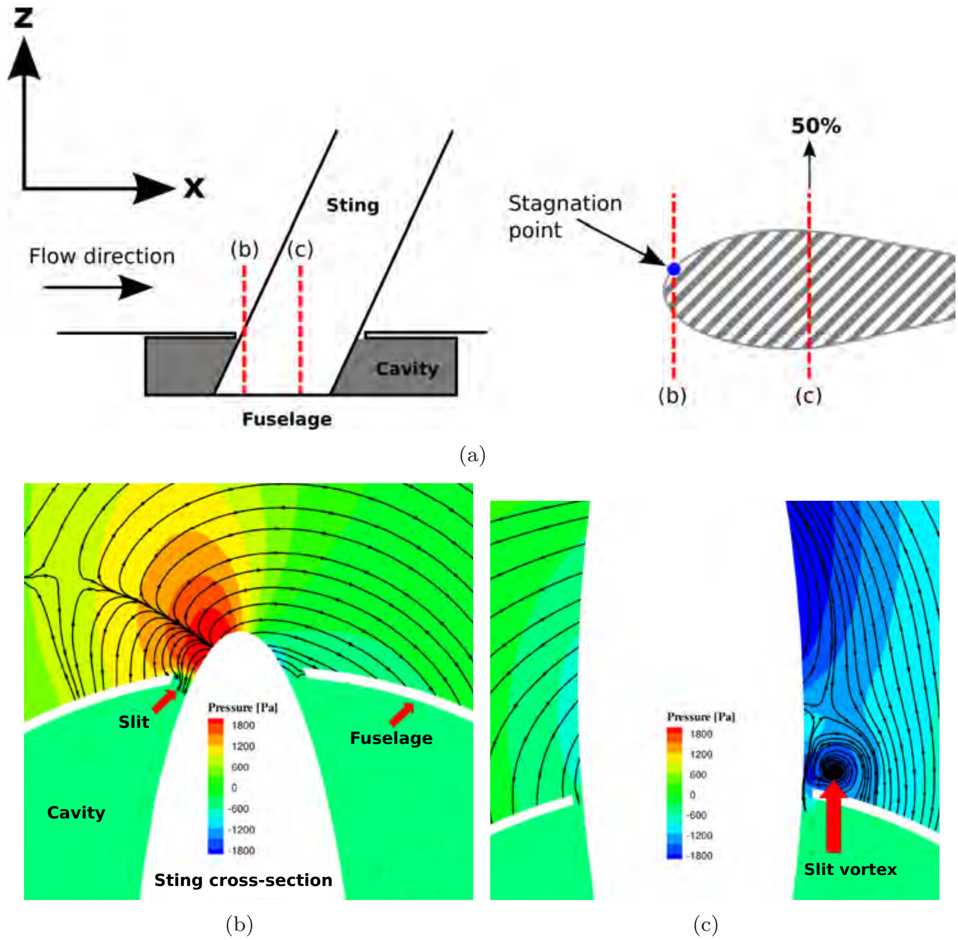

Figure 7.6: Near-field support effects of the arrangement shown in Figure 7.2 revealing pressure distribution and streamline patterns at fuselage and sting lateral cross-sections. In (a), the cross-sections shown in (b) and (c) are indicated. Configuration: $(\alpha,\beta) = (8,8)$ [deg], $M_\infty = 0.20$. Pressures are given relative to a freestream reference pressure of 0 [Pa]

distribution of the disturbance parameters is given in Figure 7.7 for the starboard wing and starboard horizontal tailplane where the disturbances are largest. The coordinate plotted on the horizontal axis is non-dimensionalized by the half span along the $\frac{3}{4}$ or $\frac{1}{4}$ chord line.

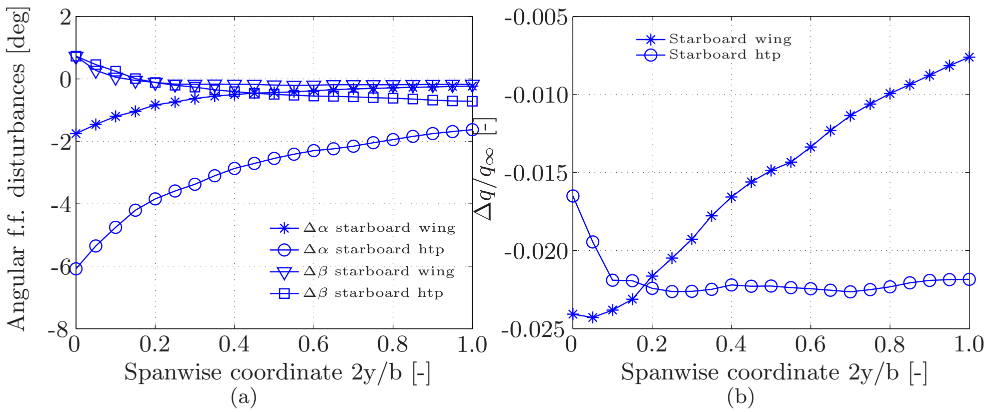

Figure 7.7: Far-field disturbance parameters at the starboard (windward) wing and starboard (windward) horizontal tailplane of the configuration shown in Figure 7.2 at $(\alpha,\beta) = (8,8)$ [deg], $M_\infty = 0.20$ (a) The values of $\Delta\alpha$ and $\Delta\beta$ at the $\frac{3}{4}$ chord line of the lifting surfaces (b) The values of $\frac{\Delta q}{q_\infty}$ at the $\frac{1}{4}$ chord line of the lifting surfaces

From Figure 7.7 it becomes clear that valuable information (besides the value of the near-field effects) can be extracted from the Euler calculations: the spatial structure of the far-field disturbances. It is seen in the Figure 7.7(a) that the disturbances in α and β decrease monotonically in spanwise direction for both wing and tailplane, a result that can be expected when traversing further away from the support. Especially the disturbances in angle of attack show significant values for this case. The disturbance in α is negative. For the wing this is mainly caused by the effects of a downwash caused by the dorsal model sting. For the horizontal tailplane, the additional downwash effects of the horizontal sting become clear as the disturbance grows in magnitude. It is also seen in the figure that the disturbances in β have a complicated signature: close to the fuselage, the disturbance reverses sign. The complex near-field effects of the model sting are thought to be the main cause of this. Figure 7.7(b) reveals the blockage effect of the model support. It becomes clear that this effect is particularly concerning near the horizontal tailplane, closest to the support parts that are thought to induce a significant blockage (the sting adapter and torpedo shown in Figure 7.2).

Typical distributions shown in Figure 7.7 can be integrated along the span of the lifting surfaces. This leads to average disturbance values of the parameters: $\overline{\Delta\alpha}$, $\overline{\Delta\beta}$ and $\overline{\frac{\Delta q}{q_\infty}}$. Integration of the disturbance parameters is performed according to guidelines described in Luijendijk [8]. For an elliptical distribution of circulation and chord:

$$\begin{aligned}
\overline{\Delta\alpha} &= \frac{4}{\pi}\int_0^1 \sqrt{\left(1-(\eta)^2\right)}\Delta\alpha\,(\eta)\,d\eta,\\
\overline{\Delta\beta} &= \frac{4}{\pi}\int_0^1 \sqrt{\left(1-(\eta)^2\right)}\Delta\beta\,(\eta)\,d\eta,\\
\frac{\overline{\Delta q}}{q_\infty} &= \frac{4}{\pi}\int_0^1 \sqrt{\left(1-(\eta)^2\right)}\frac{\Delta q\,(\eta)}{q_\infty}d\eta.
\end{aligned} \tag{7.5}$$

In Equation set 7.5 (η) provides the spanwise coordinate along the $\frac{3}{4}$ (for $\Delta\alpha$ and $\Delta\beta$) or $\frac{1}{4}$ chord line (for $\frac{\Delta q}{q_\infty}$) of the lifting surfaces from the root to the tip. The spanwise averaged values are evaluated for the wings, horizontal tailplanes and vertical tailplane. The results are shown in Table 7.2.

Table 7.2: Values of spanwise averaged far-field disturbance parameters of the lifting surfaces of the configuration shown in Figure 7.2 at (α,β) = (8,8) [deg] and $M_\infty = 0.20$

Surface	$\overline{\boldsymbol{\Delta}\alpha}$**[deg]**	$\overline{\boldsymbol{\Delta}\beta}$**[deg]**	$\overline{\boldsymbol{\Delta}\mathbf{q}}/q_\infty[-]$
Port wing (leeward side)	0.13	0.03	0.0130
Port htp (leeward side)	2.24	0.00	-0.0062
Vtp	-0.91	-3.08	-0.0334
Starboard htp (windward side)	-3.01	-0.30	-0.0214
Starboard wing (windward side)	-0.64	-0.11	-0.0166

Applying these spanwise averaged values, the far-field disturbances given by Equation set 7.2 can be evaluated for all the lifting surfaces provided that the aerodynamic coefficients of the lifting surfaces and their derivatives with respect to angle of attack and sideslip are evaluated by a vortex-lattice calculation.

Two main flaws are highlighted in this approach towards the calculation of far-field effects:

1. The aerodynamic characteristics of the lifting surfaces are determined using an inviscid vortex-lattice technique. Effects of viscosity on the aerodynamic characteristics (consider e.g. parasitic drag) are neglected,

2. The values of the disturbance parameters of the lifting surfaces are spanwise averaged. According to Luijendijk [8] this averaging is only valid when the distribution of the circulation is elliptic.

VOLAER becomes more accurate if an estimate of the parasitic drag is given for the lifting surfaces. Including only the induced drag is however thought to represent the appropriate order of magnitude and trends of the far-field effects. Considering the second drawback: in real life, lifting surface configurations with exact elliptic circulation distributions are rare. The lifting surfaces used in the study case do not have this property, especially not when flaps and/or control surfaces are deflected. The spanwise averaged disturbances calculated using Equation set 7.5 are combined with integrated characteristics of the lifting surfaces (such as e.g. lift) for calculation of the far-field effects in Equation set 7.2. The effect of local disturbance peaks combined with gradients in local aerodynamic characteristics (e.g. circulation increments at flap hinge locations) are smoothed. Another disadvantage of this method is that it does not provide a spanwise distribution of the disturbances (e.g. $dc_l(\eta)$) but merely with a net value for each lifting surface.

Reconsidering the calculation of far-field disturbances at the lifting surfaces, the problem posed in Equation set 7.2 is reformulated without the restrictions of spanwise averaging. For instance, for the disturbance on the drag-coefficient:

$$\begin{aligned}\Delta c_d(\eta) =& \frac{\partial c_d}{\partial \alpha}(\eta)\,\Delta\alpha(\eta) - c_l(\eta)\sin\Delta\alpha(\eta) + \frac{\partial c_d}{\partial \beta}(\eta)\,\Delta\beta(\eta) + \\ & c_y(\eta)\sin\Delta\beta(\eta) + c_d(\eta)\frac{\Delta q(\eta)}{q_\infty}, \\ \Delta C_D =& \frac{b}{S}\int_0^1 \Delta c_d(\eta)\, c(\eta)\, d\eta.\end{aligned} \tag{7.6}$$

This evaluation is applicable for all types of chord- and circulation distributions. Besides this advantage it also provides information on the disturbances in terms of Δc_i locally. This approach is evaluated in the study case and compared to the approach of spanwise averaged disturbances. It is concluded that the differences can become significant (outside typical balance accuracy), as shown by the disturbances on the drag-coefficient and pitching moment-coefficient in Table 7.3.

Table 7.3: Far-field support disturbances of the configuration shown in Figure 7.2 at (α,β) = (8,8) [deg] and $M_\infty = 0.20$ calculated by the "local approach" given in Equation set 7.6 and by using the spanwise disturbance averages according to Equation set 7.5

F.F. interference	Local approach [counts]	Spanwise averaged [counts]
ΔC_D	45	94
ΔC_Y	27	28
ΔC_L	-22	-25
ΔC_l	-14	-16
ΔC_m	32	54
ΔC_n	10	11

Considering its advantages over the local approach, the approach outlined by Equation set 7.6 is adopted and used for the presentation of results for the study case.

Flap- and elevator setting effects on far-field interference

The aerodynamic characteristics of lifting surfaces depend on the surface configuration. When flap- and/or control surface deflections are implemented, these characteristics change. It is assumed that changing the lifting surface configuration does not affect the value of the near-field effects (and far-field disturbance parameters). If affected, this would imply that the disturbance ability of the model support changes due to a change in "inflow conditions". This is possible if the support structure is in- or very close to the wake of the lifting surfaces. Such support setups are not desirable because of their resulting high values of support interference; they are therefore not considered in this thesis. The implication of this assumption is that only one Euler Δ-calculation needs to be carried out in order to assess the effect of multiple surface configurations (at a particular value of α, β and Mach number) on far-field interference.

In this section typical influences of the lifting surface configuration on far-field effects are treated. Values of far-field interference between a "clean" configuration (no flap- and control surface deflections) and for the case where flaps and elevators of the study case are deflected by 20° are compared. Implementing the far-field effect formulation given in Equation set 7.6 results in the graphs presented in Figure 7.8.

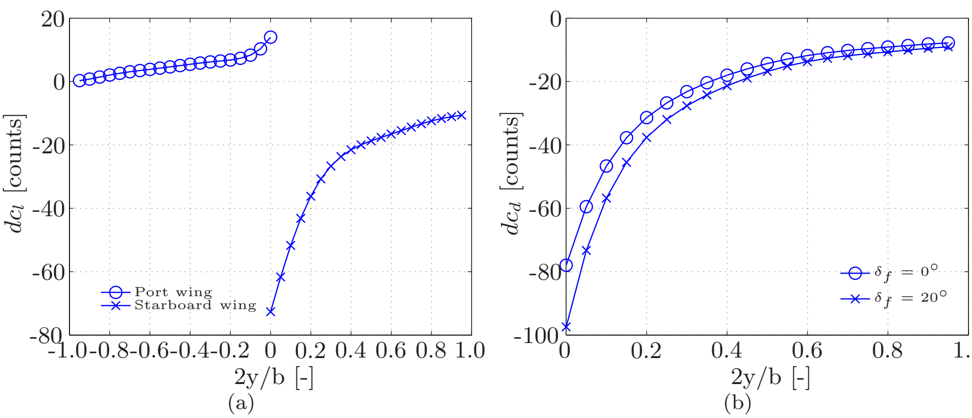

Figure 7.8: Local spanwise disturbances of the model support shown in Figure 7.2 on the wind tunnel model at $(\alpha,\beta) = (8,8)$ [deg] and $M_\infty = 0.20$ (a) Disturbances on the lift-coefficient for both port- and starboard wing. The configuration of the wings is clean (no flap deflection) (b) Disturbances on the drag-coefficient of the starboard wing. In this figure the effect of a flap deflection of 20° is shown

It is seen in Figure 7.8(a) that a completely different local disturbance pattern arises at the port- and starboard wings. The disturbances on the port wing are smaller in magnitude and of opposite sign compared to the disturbances on the starboard wing. This is caused by the complex model support geometry (reflected by Figure 7.2) creating a non-apparent angle of attack disturbance. The effects of flap deflection are not included in the figure. The reason for this is found in the formulation of Δc_l:

$$\Delta c_l(\eta) = \frac{\partial c_l}{\partial \alpha}(\eta)\,\Delta\alpha(\eta) + c_d(\eta)\sin\Delta\alpha(\eta) + \frac{\partial c_l}{\partial \beta}(\eta)\,\Delta\beta(\eta) + c_l(\eta)\,\frac{\Delta q(\eta)}{q_\infty} \qquad (7.7)$$

The leading, most significant term in Equation 7.7 is $\frac{\partial c_l}{\partial \alpha}(\eta)\,\Delta\alpha(\eta)$. A flap deflection of the wing does not affect the value of $\frac{\partial c_l}{\partial \alpha}(\eta)$. The terms including c_l and c_d are significantly affected by a flap deflection. For this model support configuration however their net contribution to Equation 7.7 is negligible. This is caused by the magnitude of the terms $\sin\Delta\alpha$ and $\frac{\Delta q}{q_\infty}$ (orders of magnitude of these terms are 0.01). The terms including c_l and c_d are expected to become more significant for higher values of the angle of attack or control surface/flap deflections (high lift). These conditions however fall outside the range of applicability of VOLAER.

Referring to Figure 7.8(b) it is seen that the support disturbances on the (induced) drag-coefficient are significantly affected by the flap setting of the wings. This is mainly caused by a change in the value of $\frac{\partial C_D}{\partial \alpha}$. Rewriting this term leads to:

$$\frac{\partial C_D}{\partial \alpha} \propto \frac{\partial}{\partial \alpha}\left(\frac{{C_L}^2}{\pi A e}\right) = \frac{2C_L}{\pi A e}\frac{\partial C_L}{\partial \alpha} \qquad (7.8)$$

It is seen in Equation 7.8 that deflected flaps causing an increase in the value of C_L cause the drag-slope to increases as well (as mentioned before, the value of $\frac{\partial C_L}{\partial \alpha}$ does not change).

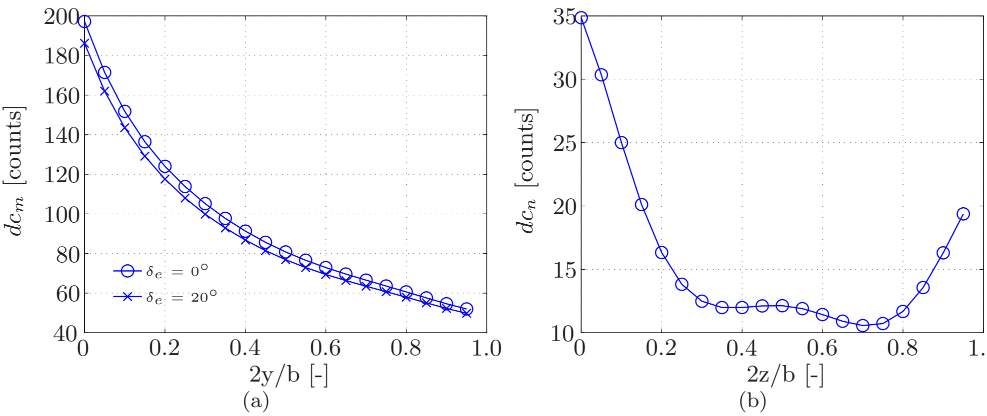

Figure 7.9: Local spanwise disturbances of the model support in Figure 7.2 on the wind tunnel model at $(\alpha,\beta) = (8,8)$ [deg] and $M_\infty = 0.20$. (a) Disturbances on the pitching moment-coefficient of the starboard horizontal tailplane. The effect of elevator deflection is visualized (b) Disturbances on the yaw moment-coefficient of the vertical tailplane

Figure 7.9 displays two more disturbance distributions of this test case. Figure 7.9(a) shows the spanwise distribution of the disturbance on the pitching moment-coefficient of the starboard horizontal tailplane with and without elevator deflections (20°). It is seen in the figure that a smooth disturbance pattern is found. This is mainly caused by the distribution of the disturbance in angle of attack at this tailplane shown in Figure 7.7(a). Due to negative values of $\Delta\alpha$ at the starboard horizontal tailplane, the local lift of the tailplane decreases. This causes a pitch-up effect as seen in Figure 7.9(a). The distribution of the angle of sideslip disturbance at the vertical tailplane is more complicated, caused by the complex non-symmetrical support arrangement. This distribution is seen to affect the values of the tailplane side force-coefficient C_Y and yaw moment-coefficient C_n significantly. The spatial distribution of dc_n is shown in Figure 7.9(b). The vertical tailplane is not seen to be affected by the flap- and elevator deflections to a significant extent.

The net support effect on the lifting surfaces is evaluated by numerical integration of the disturbance distributions by means of typical integrals given in Equation 7.6. In the study case this integration is performed by means of the trapezium rule. The far-field effects are tabulated in Table 7.4 (they are shown here for illustration purposes and are discussed in the next section).

Table 7.4: Values of support far-field interference of the setup shown in Figure 7.2. Configuration: clean with (α,β) = (8,8) [deg] and M_∞ = 0.20. Disturbances are given in counts. HTP = horizontal tailplane, VTP = vertical tailplane, SB = starboard

Parameter	Port wing	Port HTP	VTP	SB HTP	SB wing	Total
ΔC_D	3	12	63	-17	-16	45
ΔC_Y	1	1	23	1	1	27
ΔC_L	4	10	-1	-14	-21	-22
ΔC_l	-2	-1	-3	-2	-6	-14
ΔC_m	-2	-42	5	60	11	32
ΔC_n	0	1	10	1	-2	10

The resulting net values of the far-field disturbances on the lifting surfaces are the last step in determining the total model support interference according to the formulation given by Equation 7.1. The final result is presented in the next section.

Determining the final value of support interference

Combining the calculated near-field and far-field disturbances according to Equation 7.1 leads to the final value of support interference on the configuration shown in Figure 7.2 at (α,β) = (8,8) [deg] and M_∞ = 0.20. Results are presented in Table 7.5.

Studying the values in Table 7.4 and Table 7.5 some observations are made:

- The net far-field contribution to the drag-coefficient is of comparable order of magnitude as the near-field effect on the fuselage. This is mainly caused by the interference effect on the vertical tailplane,

Table 7.5: Total values of support interference of the setup shown in Figure 7.2. Configuration: clean with $(\alpha,\beta) = (8,8)$ [deg] and $M_\infty = 0.20$. Disturbances are given in counts

Parameter	Near-field effect	Far-field effect	Total
ΔC_D	54	45	99
ΔC_Y	-42	27	-15
ΔC_L	-36	-22	-58
ΔC_l	0	-14	-14
ΔC_m	12	32	44
ΔC_n	-7	10	3

- The angle of sideslip disturbance at the vertical tailplane is responsible for a disturbance on the side force-coefficient counteracting the near-field contribution of the fuselage,
- Angle of attack disturbances on the starboard wing and starboard horizontal tailplane (shown in Figure 7.7(a)) increase the disturbance effect on the lift-coefficient (counteracted by the action of the port wing and port horizontal tailplane),
- The disturbance on the rolling moment-coefficient increases under the influence of the lift drop at the starboard wing and the side force at the vertical tailplane,
- The pitch-up moment of the fuselage caused by the near-field effects is increased by the action of the far-field disturbances on the lifting surfaces (the starboard wing- and starboard tailplane are mainly responsible for this),
- The vertical tailplane is once again responsible for an increase in interference on the yaw moment-coefficient to positive values.

Figure 7.2 is thought to represent a generic example of a complex support setup responsible for the complete spectrum of model support disturbances discussed in Chapter 2 and is therefore an attractive study case. For some tests on typical aircraft configurations performed in the LLF, Δ-measurements are performed in order to determine model support interference. This seems to provide suitable validation material for VOLAER. The contrary is true however: currently such a validation can not be carried out. The reason becomes clear considering Equation set 7.6: accurate determination of the distribution of forces and moments over the lifting surfaces must be guaranteed in order to properly determine the far-field interference (providing a distinct contribution to the total interference as shown in Table 7.5). This requires knowledge on the exact lifting surface geometry (such as camber). Besides influencing local values of the force- and moment coefficients these factors also influence values such as $\frac{\partial c_d}{\partial \alpha}$ (Equation 7.8). Referring back to Equation set 7.6, uncertainties in these factors might lead to substantial errors. Consider for instance the leading terms of ΔC_D: $\frac{\partial C_D}{\partial \alpha}\overline{\Delta\alpha} + C_L \sin\overline{\Delta\alpha}$). It is evaluated for the current case that if the camber is underestimated by 2%, this results in an error of 30% in the prediction of far-field interference on the drag-coefficient. It will also affect the other interference values. For a proper validation of VOLAER, the following lifting surface properties are considered a minimum:

- Exact geometry lifting surface planform,
- Airfoil camber lines,
- Wing sweep, dihedral and twist.

For the tests classifying as suitable validation material typical information (especially on the camber line) is not available for the author from the viewpoint of confidentiality. This places the validation of VOLAER with an experimental test case currently out of the options. Future work to provide the absolute accuracy of this method is left to others.

It is shown that when VOLAER is used abiding by the boundaries on applicability as stated in section 7.2.2, it provides valuable qualitative information on the near-field and far-field effects of a complex support structure. Quantitative assessment of the method by comparison to experimental data is not treated in this thesis. More is to be said about the accuracy and speed of VOLAER. This is discussed in the following section.

7.2.7 VOLAER: characteristics on speed and accuracy

The time span of implementation of a VOLAER calculation is determined by the largest time span of both numerical methods defining VOLAER (both calculations can be decoupled and performed parallel). The associated time scale of the determination of aerodynamic characteristics using a vortex-lattice calculation is in the order of an hour. This includes the modeling, calculation and post processing of the results. The required computational effort is low. These calculations are typically ran on personal computers.

Implementing Euler calculations however requires a substantially larger effort. For every test condition (α, β and M_∞) a Δ-calculation is to be performed. Setting up a Δ-calculation (geometry modeling and meshing) typically requires a week, the exact time depending on geometry complexity and domain size (and accompanying number of computational nodes). Compared to the vortex-lattice calculation the computational effort also increases: these Δ-calculations are typically ran within a week. Depending on the amount of computational nodes covering the domain it might be decided to parallelize the computation on several CPU's. Summarizing, the implementation effort of a VOLAER calculation is determined by the Euler Δ-calculation. When it is decided to use VOLAER during stage 2 (test preparation) as a means of determining an interference polar the associated time scale will be in the order of weeks/months according to Table 5.1.

The accuracy of VOLAER is determined by both Euler- and vortex-lattice calculations. When the operational boundaries of a VOLAER calculation as outlined in section 7.2.2 are respected, the accuracy of the Euler calculation is indicated by the following:

- Considering the determination of model sting disturbances: for sting placements R1, R2a and R2b in Figure 4.26) the accuracy of the determination of model sting near-field effects is indicated by Figure 3.11. The accuracy of the determination of model-sting far-field effects is outlined in section 3.4.2,

- The accuracy in the determination of the far-field effects of the remaining support structure is discussed in section 4.5.2. It is explained that generalizing on the accuracy for determining the disturbances of various support structures is difficult and depends on the geometry because the geometry is indicative for the characteristics of the disturbances. When simplifying modeling assumptions (separated flow regions that are modeled as "solid regions" for instance) as discussed in section 7.2.2 are adopted it is believed that similar accuracy can be achieved as indicated in section 3.4.2.

Generalizing on the accuracy of a vortex-lattice calculation is difficult because the accuracy is configuration-dependent. It is known that vortex-lattice codes are able to determine the values of aerodynamic derivatives (such as $\frac{\partial C_L}{\partial \alpha}$, also written as C_{L_α}) with a satisfying accuracy: from Thomas [82] it is seen that differences in the values of C_{L_α} and C_{m_α} compared to wind tunnel measurements are smaller than 1 and 2.5 percent respectively for a low-speed analysis on an F15 fighter aircraft. Absolute values of aerodynamic coefficients are expected to show poorer agreement with measurements.

Regardless of the accuracy of both separate numerical methods, the accuracy of the combined approach is representative for the true accuracy of VOLAER. A validation of this accuracy is not treated in this thesis. Whether or not this level of accuracy proves to be acceptable for implementation in stage 2 of a typical commercial wind tunnel measurement depends on the client's vision on the desirable balance between accuracy, costs and perceived value of the calculation output.

The main characteristics of VOLAER are summarized in Table 7.6.

VOLAER concluded

Implementing VOLAER requires a substantial amount of effort (both modeling and computational effort). If the expert system is to provide an application for the **determination** of support interference on-line such methods are inappropriate from the viewpoint of accompanying time scale. On-line determination of support interference therefore excludes typical calculation techniques requiring repetitive geometrical modeling, meshing and performing calculations when the angle of attack and/or the angle of sideslip are changed.

Reviewing the VOLAER calculation it becomes clear that such calculations typically consist of two parts:

1. Calculations that allow for the extraction of the disturbances (Euler calculations, demanding a high effort),

Table 7.6: Summarized characteristics of VOLAER

Range of applicability	
Flow	Steady -10 $\leq \alpha, \beta \leq$ 10 [deg]
Lifting surface requirements	t/c $\leq$ 0.12 Control surface-/flap deflections $\leq$ 20 [deg]
Sting Placement	R1, R2a, R2b (Figure 4.26) No direct sting interference with lifting surfaces
Additional	Power effects on interference are not included
Performance	
Output	Provides near-field disturbances and spatial distributions of far-field disturbances
Effort	Determined by the Euler calculation: O(weeks/months) for a polar
Accuracy	1) Euler, near-field effects: Figure 3.11 2) Sting far-field disturbances: section 3.4.2 3) Remaining structure far-field effects: section 3.4.2 if modeling is smart 4) Vortex-lattice: $C_{L_\alpha} \approx 1\%$, $C_{m_\alpha} \approx 2.5\%$ Absolute values of C_L and $C_m \geq 1\%$ and 2.5%
Combined accuracy	Unknown

2. Calculations that provide an undisturbed reference of the model aerodynamics (vortex-lattice calculations, demanding a very low effort).

A similar approach can be adopted for on-line implementation if the component requiring the highest effort is replaced. To this end it can be replaced by uncorrected wind tunnel measurements. Uncorrected measurements contain besides information on undisturbed values of the model aerodynamics also valuable information on the disturbances. These disturbances however are caused by wind tunnel walls and model support.

An on-line wind tunnel wall- and support interference correction method is developed that combines uncorrected wind tunnel measurements with low-effort vortex-lattice calculations. This method (that can also be adopted during post-test corrections) is discussed in the following section.

7.3 Measurement/Vortex-Lattice method: MVL

In this section a new hybrid method is presented that determines wall interference, support interference and all the residual interference effects (consider the additional disturbances on the model when the support structure approaches the wind tunnel walls closely) for all types of wind tunnels and support configurations. The method is fast and reasonably accurate. It provides a formula for the calculation of the interference gradient. This gradient is based on uncorrected wind tunnel measurements and a successive calculation of the interference-free aerodynamic derivatives of the configuration of interest by fast vortex-lattice calculations. This makes it a suitable method for on-line use (stage 3 of a typical commercial wind tunnel measurement) during a wind tunnel test but it will become clear that this method is also applicable off-line during stage 4.

The following sections will demonstrate the theoretic principle of this hybrid method. It will be explained that a vortex-lattice routine correcting for viscous effects is needed to maintain the advantages of both speed and accuracy. The structure of this newly developed vortex-lattice routine is discussed. Test cases showing the application of the method will be presented and the results will be discussed. It is shown that the numerical stability of this method is guaranteed if it is used as an interpolation tool to reduce the number of Δ-measurements. Finally the characteristics on speed and accuracy are discussed justifying its value as element of an expert system.

7.3.1 Theory

General application

To explain the theory behind MVL and to demonstrate the wide applicability to other experimental environments than wind tunnel measurements, consider any test setup. The exact setup is of no importance. The purpose of this setup is to obtain the value of a certain signal C. This signal is dependent on the variable x. Unfortunately, the measurement of $C(x)$ is affected by the test setup. As a result of this, the measured signal contains a certain amount of noise, or interference from the experimental environment.

The measured, raw signal $C(x)$ is now said to consist of an undisturbed part C_{und} (clean, excluding the interference of the experimental environment) and a disturbance ΔC_{int} (interference/noise).

Consider a measurement at $x = x_1$. It can now be said that (for clarity, $C(x_1)$ is from now on written as C_1):

$$C_1 = C_{und_1} + \Delta C_{int_1}. \tag{7.9}$$

Assume that the value of the interference term (ΔC_{int_1}) is known for this first measurement point. The measurement can then be corrected for the interference according to:

$$C_{und_1} = C_1 - \Delta C_{int_1}. \tag{7.10}$$

The next measurement point is taken at x_2. At this new measurement point:

$$\begin{aligned} C_2 &= C_{und_2} + \Delta C_{int_2} \longrightarrow, \\ C_2 &= C_{und_1} + \frac{\partial C_{und_1}}{\partial x}(x_2 - x_1) + \Delta C_{int_1} + \frac{\partial \Delta C_{int_1}}{\partial x}(x_2 - x_1) + O\left(x^2\right). \end{aligned} \tag{7.11}$$

When Equation 7.9 is subtracted from Equation 7.11, the result is as follows:

$$C_2 - C_1 = \frac{\partial C_{und_1}}{\partial x}(x_2 - x_1) + \frac{\partial \Delta C_{int_1}}{\partial x}(x_2 - x_1) + O\left(x^2\right). \tag{7.12}$$

One of the assumptions that is now introduced is that the higher order terms in Equation 7.12 are ignored. This results in a linear formulation of the difference between two measurements. In the upcoming sections, linearization of this formula will be justified. The meaning of the resulting formula is schematized in Figure 7.10.

The gradient of the noise/interference can now be calculated as:

$$\frac{\partial \Delta C_{int_1}}{\partial x} = \frac{(C_2 - C_1) - \frac{\partial C_{und_1}}{\partial x}(x_2 - x_1)}{(x_2 - x_1)}. \tag{7.13}$$

The first part of the numerator in Equation 7.13 follows directly from the measurements. It is considered here that the second part of the numerator is found by other means, such as calculations. A requirement on such a calculation is that it must be fast (in order to apply this technique on-line) and also accurate. Assume that such a technique exists and that the interference gradient is evaluated by Equation 7.13. In that case, the interference at the new measurement point (x_2) can be calculated as follows:

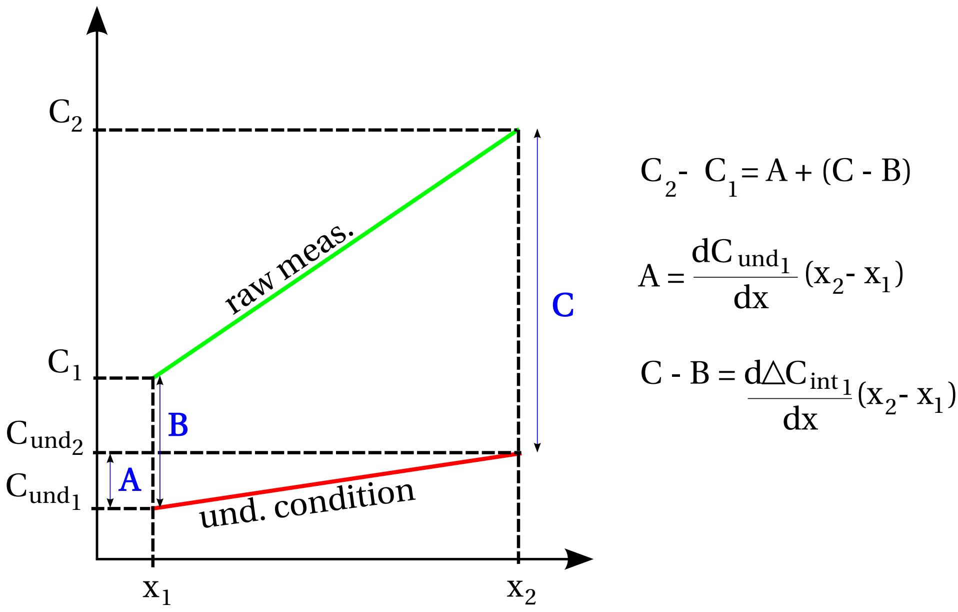

Figure 7.10: Equation 7.12 schematized: arbitrary lines are shown indicating the uncorrected (raw) measurement and the undisturbed (und.) condition

$$\Delta C_{int_2} = \Delta C_{int_1} + \frac{\partial \Delta C_{int_1}}{\partial x} (x_2 - x_1) . \tag{7.14}$$

The measurement at x_2 can be corrected right away (on-line) according to:

$$C_{und_2} = C_2 - \Delta C_{int_2} . \tag{7.15}$$

When this correction is performed, the next measurement point can be taken, and the procedure is repeated.

Wind tunnel wall- and support interference

The theory as described in the previous section is applicable to the problem of wind tunnel wall- and support interference. The following sections will concentrate on this application, named MVL.

Assume a certain wind tunnel model being attached to some support configuration in a wind tunnel. The support configuration and the wind tunnel layout are of no importance at all. A measurement can be performed using this model at a certain angle of attack $\alpha = \alpha_1$ and angle of sideslip $\beta = \beta_1$. It can now be said that:

$$C_{i_1} = C_{i_{und_1}} + \Delta C_{i_{int_1}} . \tag{7.16}$$

In Equation 7.16 the measured value of a certain parameter (it could be the lift-coefficient for example) consists of a "clean" value (with the subscript "und" for "undisturbed") and an interference part from the support structure, wind tunnel walls and residual interference (with the subscript "int" for "interference"). Furthermore assume that the value of the interference term is known for this first measurement point.

The next measurement point is taken at $\alpha = \alpha_2$ and $\beta = \beta_1$ (here for convenience only angle of attack polars are considered. The theory is also applicable to angle of sideslip polars). Following the theory described in the previous section, the gradient of the total interference on the considered model can now be calculated as:

$$\frac{\partial \Delta C_{i_{int_1}}}{\partial \alpha} = \frac{(C_{i_2} - C_{i_1}) - \frac{\partial C_{i_{und_1}}}{\partial \alpha}(\alpha_2 - \alpha_1)}{(\alpha_2 - \alpha_1)}. \tag{7.17}$$

The first part of the numerator in Equation 7.17 once again follows directly from the measurements. The second part of the numerator is found by calculations (here, the slope of the coefficient under consideration is calculated at angle of attack $\alpha = \alpha_1$ and angle of sideslip $\beta = \beta_1$). A very efficient way (from the viewpoint of the reduction of effort) of calculating this gradient is by the use of a vortex-lattice code. This method is able of calculating the necessary characteristics fast and for a variety of lifting surface configurations, angles of attack and angles of sideslip. When the gradient of the interference is calculated, the interference at this new measurement point can be determined as follows:

$$\Delta C_{i_{int_2}} = \Delta C_{i_{int_1}} + \frac{\partial \Delta C_{i_{int_1}}}{\partial \alpha}(\alpha_2 - \alpha_1). \tag{7.18}$$

And the measurement can be corrected right away (on-line) according to:

$$C_{i_{und_2}} = C_{i_2} - \Delta C_{i_{int_2}}. \tag{7.19}$$

When this correction is performed, the next measurement point can be taken, and the procedure is repeated.

It is shown that with a relatively simple method (applicable to a variety of problems involving disturbances), a setup-independent determination of wind tunnel wall- and support interference is demonstrated. Its name (MVL) shows that this hybrid method is based on both measurements and calculations as explained in this section. Advantages and disadvantages of MVL are given in the next section.

7.3.2 Advantages and disadvantages of MVL

Some advantages of the method described in the last section are:

1. No geometrical representation of the wind tunnel and support are necessary: the method is independent of the wind tunnel wall- and support configuration,

2. The method is valid for angle of attack- and angle of sideslip-polars,
3. The calculation is fast and reasonably accurate: vortex-lattice codes are known to be able to calculate the right trends and gradients of aerodynamic characteristics whereas the absolute value of the parameters may have a limited accuracy. These absolute values are however not of interest,
4. Because of the flexibility of a typical vortex-lattice code, different configurations (tail on/tail off, including elevator/rudder/flap-deflections) can be assessed,
5. This method is applicable up to the transonic flow regime ($M_\infty \approx 0.7$). Compressibility below this threshold is treated using the Prandtl-Glauert transformation,
6. Calculation and correction of the interference can be performed on-line during a measurement or off-line when the uncorrected wind tunnel data are available.

The most important disadvantages of this method are:

1. Because of the inclusion of a vortex-lattice calculation, this method is applicable to within typical restrictions as provided by such codes:
   - The method is applicable within the linear angle of attack- and angle of sideslip ranges. Typical effects such as the interference of the fuselage on the wings (at significant angles of sideslip) are not included,
   - When the disturbance parameter of interest would be the drag-coefficient, the vortex-lattice calculation will only provide the gradient of the induced drag. The parasitic drag is not included because no viscous effects are simulated by a vortex-lattice code. This disadvantage can be relieved when a numerical method is used that is able to correct for the effects of viscosity. A custom method is developed for this purpose and will be discussed in section 7.3.4.
2. As initial condition the first interference term should be known. From this term on, the residual interference pattern is calculated,
3. Because this method is based on a combination of a Δ-measurement and a numerical technique, the accuracy will never be better than the accuracy of the Δ-measurement.

7.3.3 Distinguishable error sources

Considering Equation 7.18 it becomes clear that the accuracy of the determination of the interference at a new measurement point depends on the following factors:

1. The accuracy of the determination of the interference of the previous point. When the first interference term with this method is calculated, the accuracy is determined by the accuracy of the initial condition. This implies that it is of utmost importance to choose the initial condition in terms of α and β properly. It is therefore wise to choose the initial condition at the point where the total interference is expected to be minimal and accurately known. Large errors in the initial condition are maintained throughout the complete interference polar,

2. The determination of the interference gradient. According to Equation 7.17 the accuracy in the determination of this gradient depends on:
   - The measurement accuracy (consider the first term in the numerator of Equation 7.17),
   - The accuracy of the determination of interference-free aerodynamic derivatives (by the vortex-lattice code).
3. The step size $\Delta\alpha$ or $\Delta\beta$ also affects the accuracy: when measurements are taken with smaller measurement intervals, this linear approach will more accurately predict the complete interference polar. During wind tunnel measurements, this step size is usually rather large (O(0.5-1.0) [deg]). Therefore it is recommendable when using this method to first measure a polar, spline the results (with some cubic function for instance) and interpolate the results to a fine grid (O(0.01 [deg])) as if the measurements are taken with a very small step size. The same is done for the results of the vortex-lattice calculations. This enables an analysis of the interference with a higher accuracy. It also makes including second- and higher order terms in Equation 7.12 redundant (the vortex-lattice calculation determines the accuracy to a much larger extent).

The most troublesome accuracy requirement is on the determination of the interference-free aerodynamic derivatives by a vortex-lattice code. When it is assumed that the initial condition of an interference calculation has an error of 0 ("an exact determination of the interference") the errors in the calculation of the interference for the upcoming measurement points are proportional to:

$$
\begin{aligned}
&Calculation\, 1 \rightarrow E\left(\Delta C_{i_{int_1}}\right) = 0, \\
&Calculation\, 2 \rightarrow E\left(\Delta C_{i_{int_2}}\right) \propto E\left(\Delta C_{i_{int_1}}\right) + E\left(\frac{\partial C_{i_{und_1}}}{\partial \alpha}\left(\alpha_2 - \alpha_1\right)\right), \\
&Calculation\, 3 \rightarrow E\left(\Delta C_{i_{int_3}}\right) \propto E\left(\Delta C_{i_{int_2}}\right) + E\left(\frac{\partial C_{i_{und_2}}}{\partial \alpha}\left(\alpha_3 - \alpha_2\right)\right) = \ldots \\
&E\left(\frac{\partial C_{i_{und_1}}}{\partial \alpha}\left(\alpha_2 - \alpha_1\right)\right) + E\left(\frac{\partial C_{i_{und_2}}}{\partial \alpha}\left(\alpha_3 - \alpha_2\right)\right), \\
&....
\end{aligned}
\tag{7.20}
$$

Equation set 7.20 shows that the error in the method is decreased when the interference-free aerodynamic derivatives are properly calculated. It is also seen that when the vortex-lattice code systematically over- or under-predicts the value of the interference-free aerodynamic derivatives, the error will grow during the calculation of the interference in a polar. When however the true values are scattered around the prediction by the vortex-lattice code (some values are under-estimated and other values are over-estimated) it is seen that the errors (but not the uncertainties!) have the tendency of canceling each other out. This property is hard to rely on when the interference needs to be determined with a high accuracy!

It is of importance that the calculated values of the interference-free aerodynamic derivatives by the vortex-lattice code closely approximate the true values. To increase the accuracy and the operational boundaries of MVL, applying a correction for the effects of viscosity is unavoidable. For this purpose, a custom vortex-lattice routine is developed. This routine is discussed in the next section.

7.3.4 Development of a custom vortex-lattice routine correcting for the effects of viscosity

Successively modeling the viscous gradients of the aerodynamic coefficients of a wind tunnel model is the key to the development of a custom vortex-lattice routine implementable in MVL. This routine combines 3D steady vortex-lattice calculations in the program AVL with a 2D viscous airfoil calculation in the freeware code $XFOIL$ by Drela ([83] and [76]).

The vortex-lattice routine starts by defining the lifting surfaces of interest by means of user input. At current, the first version of this program is designed to deal with the main wing only. The main wing is defined by identifying its typical sections in 3D space. The sections are defined by describing the mean camber line (by customized coordinates describing the mean camber line or the 4-digit designation of a 4-digit NACA airfoil series). Wing sections are designated a chord. Between these wing sections, linear interpolation is applied on the camber line and chord length thereby defining the wing surface. Geometric features such as sweep and dihedral are included by a proper definition of the section placements. Twist can also be included by defining a local angle of attack (between the sections, the local twist value is linearly interpolated). The presence and deflection angle of flaps can also be defined. Besides geometrical information describing the wing surface, parameters describing the freestream (such as the Mach number, angle of attack and angle of sideslip) are prescribed. All the data is written to an input file for the program AVL.

The input file is read by AVL and the geometrical description of the wing is translated to a numerical discretization by the placement of a number of horseshoe vortices on the wing surface to model the circulation. The wing is represented by a number of spanwise bound-vortex collections placed at various chord wise stations and ending in free trailing vortices extending downstream in analogy with Helmholtz's vortex theorem. Based on the boundary conditions described by the freestream parameters and the flow tangency condition (prescribed by the law of Biot-Savart) at the collocation points on the surface of the wing, the strength of the horseshoe vortices is calculated. This leads to the inviscid lifting properties of the wing at given freestream conditions. An example of a typical wing implemented in AVL is shown in Figure 7.11. The wing consists of 4 sections with a NACA 2315 profile. Features such as taper, sweep and dihedral are included. At the inboard part of the wing a flap is specified from 80% of the local chord to the trailing edge. Figure 7.11 clearly shows the trailing legs of the horseshoe vortices discretizing the wing. The wing properties are given in Table 7.7.

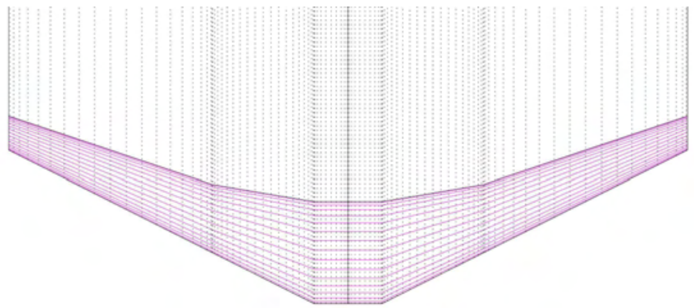

Figure 7.11: An example of a typical wing as implemented by AVL: top view

Table 7.7: Properties of the wing configuration shown in Figure 7.11

Parameter	Value
Taper inner wing	0.67 [-]
Leading edge sweep inner wing	26.6 [deg]
Dihedral inner wing	1.90 [deg]
Taper outer wing	0.50 [-]
Leading edge sweep outer wing	26.6 [deg]
Dihedral outer wing	1.90 [deg]
Profile	$NACA-2315$
Reynolds Number	2.5x10^6 [-]

At given freestream conditions AVL is capable of calculating the inviscid aerodynamic characteristics of the prescribed wing. Of particular interest is the spanwise distribution of induced angle of attack. This value can be visualized by a Trefftz-plane plot as given by Figure 7.12.

The spanwise distribution of the induced angle of attack is used in order to calculate the effective angle of attack of the sections describing the wing as follows:

$$\alpha_{eff} = \alpha_{\infty} - \alpha_{ind} + \alpha_{twist}. \tag{7.21}$$

In Equation 7.21 the effective angle of attack is calculated by adding the freestream angle of attack α_{∞}, the induced angle of attack α_{ind} and on the local twist of the section α_{twist}. Consider the case for a particular value of α_{∞}. For this freestream angle of attack the spanwise distribution of effective angle of attack is evaluated. For every section 2D XFOIL calculations are performed, both inviscid and viscous (at the local Reynolds number). The calculations are performed for a wide range of angles of attack spanning a complete angle of attack polar. This leads to viscous and inviscid

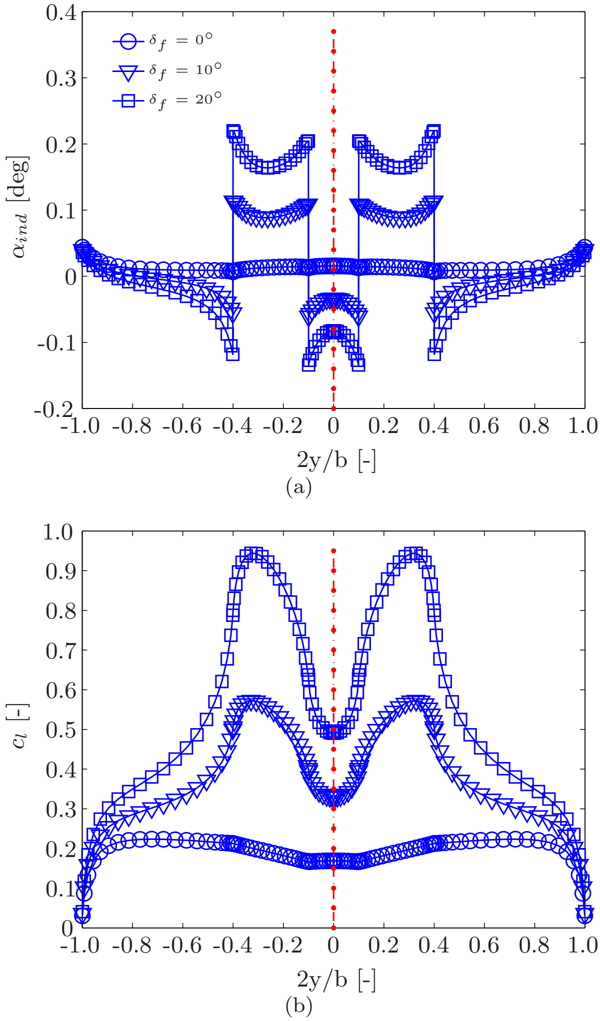

Figure 7.12: A Trefftz-plane plot of the spanwise distribution of (a) Induced angle of attack α_{ind} (b) Local lift-coefficient c_l for the discretized wing shown in Figure 7.11 at $\alpha_\infty = 0°$, $\beta_\infty = 0°$ and $V_\infty = 60$ [m/s] showing the effect of various flap settings

polars for every section. The calculated value of the effective angle of attack of every section is then used to find the inviscid and viscous 2D lift-coefficient for every section spanning the wing by piecewise cubic Hermite interpolation. The difference between 2D inviscid- and viscous lift of a particular wing section at α_{eff} can be defined as dc_l. This difference is caused by the effects of viscosity. It can be translated to a shift in local angle of attack from the inviscid polar to the viscous polar as follows:

$$d\alpha_{section} = \frac{dc_l}{\frac{\partial c_l}{\partial \alpha}_{inv}}. \tag{7.22}$$

In Equation 7.22 it is seen that the inviscid lift-slope is used in order to calculate the shift in angle of attack that is necessary to correct the 2D inviscid lift for the effects of viscosity. The inviscid lift-slope is used here because the viscous lift-slope will reach values of zero at higher angles of attack (at profile stall conditions) thereby introducing singularities in Equation 7.22.

The implication of the above is the following: if at a certain angle of attack α_∞ the induced angles of attack are calculated by an inviscid calculation (in AVL), the XFOIL results will enable the determination of a correction in angle of attack for all the sections to transform the 2D inviscid lift-coefficient to 2D viscous lift-coefficients of the sections. This shift in local angle of attack can be super-imposed on the local section twist of the airfoil as a means of a local viscosity correction. This enables a new AVL calculation with a "morphed" wing. The output of this calculation provides a lift distribution that is corrected for the local effects of viscosity.

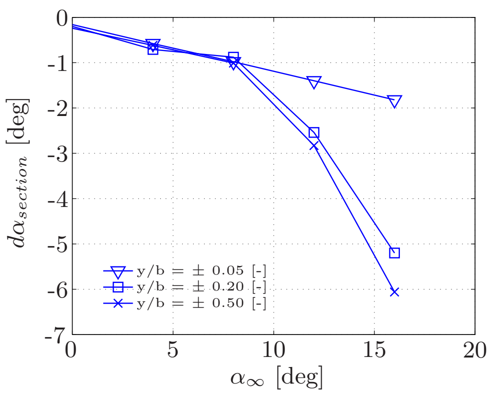

Figure 7.13: Angle of attack dependency of the twist corrections at various wing stations of the wing shown in Figure 7.11 to correct locally for the effects of viscosity. It is seen that the viscosity correction becomes more important towards the outer wing

For every angle of attack α_∞ a new spanwise twist correction is necessary (because changing the freestream angle of attack changes the spanwise distribution of α_{ind}). This also means that in order to calculate a lift polar that is corrected for viscous effects (consisting of N angles of attack), N further corrected AVL calculations are run implementing N new twist distributions over the wing. Figure 7.13 shows the twist correction at various angles of attack for the sections spanning the wing shown in Figure 7.11. It is seen that for some sections defining the wing the twist correction is significant (the viscosity correction becomes more important towards the outer wing). Implementing this twist leads to the calculation of a new lift distribution over the wing as given in Figure 7.14 where the inviscid and "viscous" lift distributions in the Trefftz plane are shown. Integrating this new lift distribution over the wing at a given value of α_∞ provides the value of the corrected lift-coefficient. Comparing the viscous and inviscid lift curves given in Figure 7.15(a) it is seen that the viscous curve indeed shows non-linear behavior at high angles of attack indicating stall behavior.

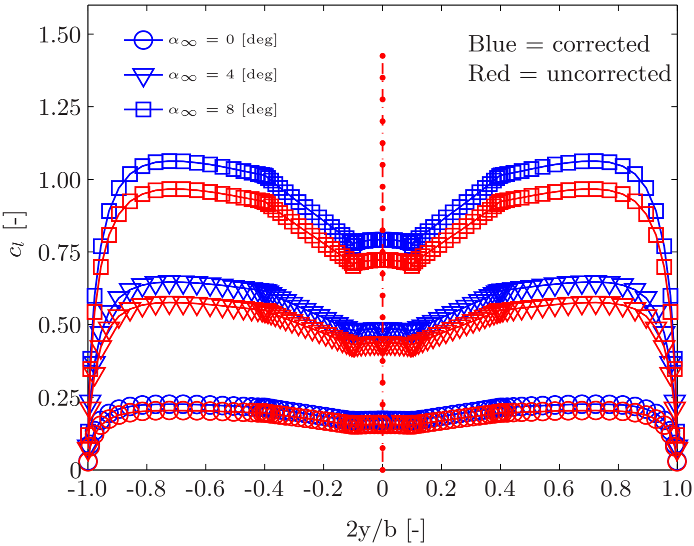

Figure 7.14: Trefftz plane plot of the inviscid and "viscous" (or, corrected for the effects of viscosity) lift distributions over the wing shown in Figure 7.11 at various angles of attack. In the figure, the symmetry line of the configuration is indicated

With the new corrected spanwise lift distribution calculated by AVL, a corrected induced drag distribution is also calculated. The complete drag of the wing is however determined by adding the integrated value of the induced drag to the integrated value of the parasitic drag. The calculation of the spanwise distribution of the parasitic drag is performed as follows: using the corrected calculation of the induced angles of attack, the effective angle of attack of the sections spanning the wing are re-calculated. Using the two-dimensional XFOIL results, the sectional value of the profile drag is found by interpolation using this value of α_{eff}. The spanwise positions on the wing in between the sections are then evaluated by linear interpolation of the profile drag of the sections. Once the spanwise distributions of induced drag and parasitic drag are calculated, the complete drag of the configuration follows by integration of the drag over the wing. An

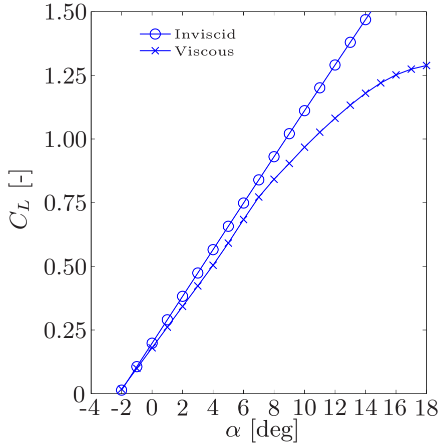

(a)

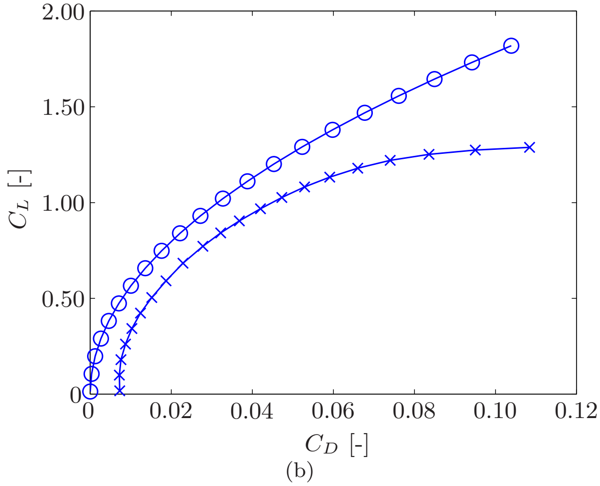

(b)

Figure 7.15: Inviscid and viscous polars of the wing shown in Figure 7.11 (a) Lift polars (b) Drag polars

example of a resulting drag polar compared to the uncorrected inviscid result is given in Figure 7.15(b).

7.3.5 A demonstration of MVL using the new vortex-lattice routine

To demonstrate the validity of MVL to correct for wall- and support interference, a test case is setup. This test case concerns the measurement of a finite wing in a wind tunnel. In the wind tunnel, this wing is disturbed by the presence of wind tunnel walls and model support members. Corrected aerodynamic polars of such a measurement (the corrections are determined by the methods as described in the AGARDograph 336 [5]) will be regarded as "unaffected/undisturbed". The characteristics of the test case wing are given in Table 7.8. A geometrical description is also provided in Figure 7.16.

Table 7.8: Wing properties of the MVL test case

Parameter	Value
Wing Span	1.28 [m]
Mean Aerodynamic Chord	0.24 [m]
Wing Taper Ratio	1.00 [-]
Wing Sweep	0.00 [deg]
Wing Dihedral	0.00 [deg]
Profile	$NACA - 64_2\,(A)\,015$
Reynolds Number	1.0x10^6 [-]

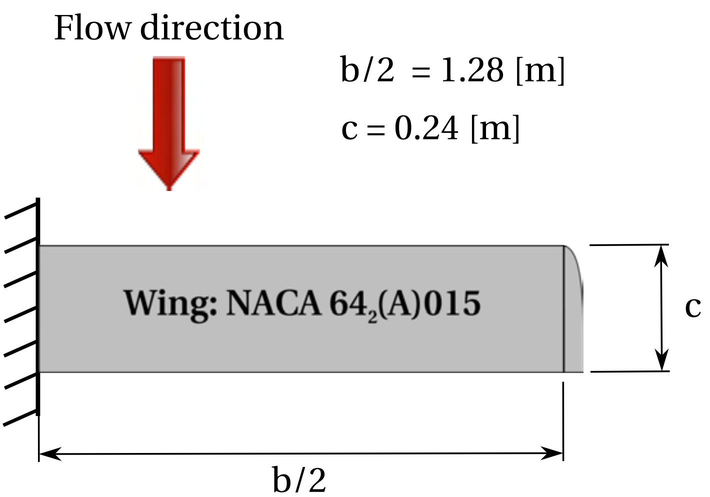

Figure 7.16: Geometry of the MVL test case

To demonstrate the wide applicability of MVL, the unaffected/undisturbed aerodynamic characteristics of the wing shown in Figure 7.16 is contaminated by a random error simulating any wall- and support interference pattern for any wind tunnel using any support structure for the wing. In this test case a random error for both the unaffected value of lift- and drag-coefficients is generated by a random number generator. This random error is added to the clean measurements to generate "uncorrected data". MVL will use this uncorrected data in order to back-calculate the value of the interference on both lift- and drag-coefficients. These back-calculated values can be compared to the analytical solution of the interference.

In using MVL, an approximation of the aerodynamic derivatives of interest is calculated by the new vortex-lattice routine. The results of this exercise are given in Figure 7.17 (from here on α is used instead of α_∞). In the figure, the calculated characteristics for a regular inviscid implementation of the wing in AVL are also given as well as the results of an implementation in a Navier-Stokes solver.

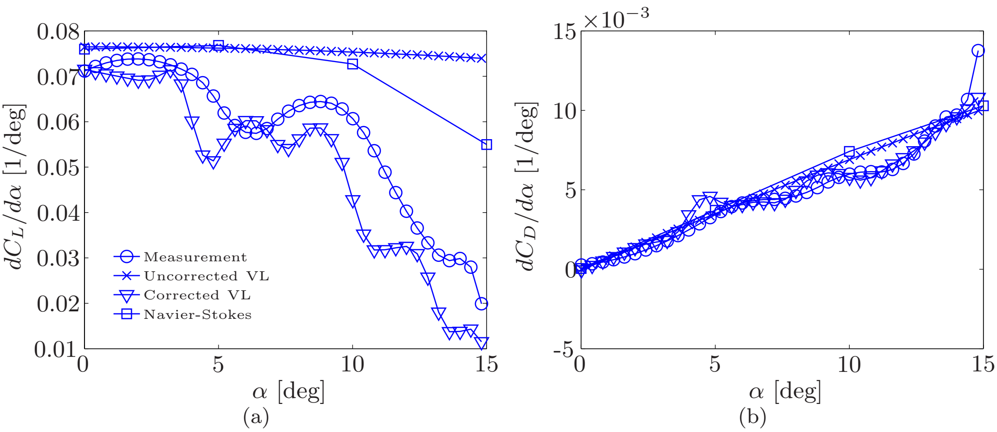

Figure 7.17: Measured and calculated values of the aerodynamic derivatives of the wing shown in Figure 7.16 (a) The lift-coefficient (b) The drag-coefficient. Distinction is made between using MVL with an inviscid vortex-lattice code (uncorrected VL) and with a vortex-lattice code that corrects for the effects of viscosity (corrected VL)

It is seen in Figure 7.17(a) that applying the new vortex-lattice routine greatly improves the determination of the lift-slope compared to the inviscid result. Considering typical results from a Navier-Stokes calculation it is seen that such calculations do not necessarily provide a better answer. Figure 7.17(b) shows not much difference between inviscid- and viscous results of the vortex-lattice calculations, an indication that for the considered angles of attack the drag-slope is not much affected by viscosity. The Navier-Stokes results verify this. The aerodynamic derivatives calculated by the vortex-lattice codes are used in order to back-calculate the values of the interference according to Equations 7.17 and 7.18 using the uncorrected data. The results of this exercise are given in Figure 7.18.

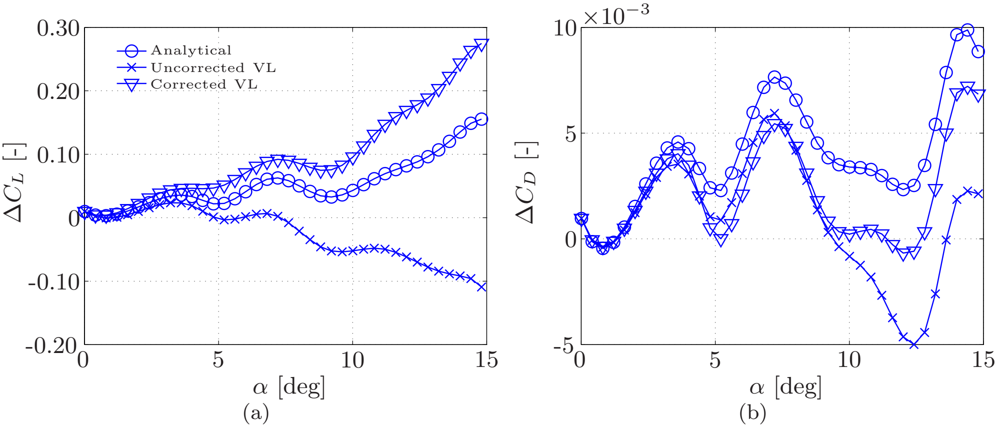

Figure 7.18: Analytical and calculated (by MVL) values of interference on the (a) Lift-coefficient (b) Drag-coefficient

It is seen in Figure 7.18 that the interference as described by the random number generator is reproduced fairly accurately by applying the new vortex-lattice routine in MVL: both trend and order of magnitude are predicted properly (however not to within typical balance accuracy given for instance in Table 1.2). It is seen that for increasing angle of attack the error of the method in determining the lift-interference increases. This is due to the fact that from $\alpha = 7$ [deg] onwards a systematic under prediction of the lift-slope is calculated as is seen in Figure 7.17(a). According to Equation set 7.20, this leads to an accumulation of the error that can be written as:

$$Calculation\, N \rightarrow E\left(\Delta C_{i_{int_N}}\right) \propto \sum_{i=1}^{N-1} E\left(\frac{\partial C_{i_{und_i}}}{\partial \alpha}\right)(\alpha_{i+1} - \alpha_i)\,. \tag{7.23}$$

Applying a regular inviscid vortex-lattice code in MVL results in a larger error for the determination of lift-interference. Error divergence is apparent caused by a systematic over prediction of the lift-slope, resulting in the error divergence seen in Figure 7.18. Because the slope of the drag-coefficient for both numerical methods show a fair agreement (pointed out earlier), the back-calculated value of the drag-interference also shows an agreement with the pre-generated pattern.

From these results it is seen that the more accurate the prediction of the aerodynamic derivatives becomes, the more accurate the interference pattern is determined. Although the vortex-lattice code correcting for the effects of viscosity shows a great improvement over its inviscid variant when considering the final interference pattern (especially at higher angles of attack) possible error divergence seems a great disadvantage of MVL. Error divergence excludes MVL to be used safely with initial intended purpose for the prediction of wind tunnel wall- and support interference. By including more (instead of only one) boundary conditions in MVL this error divergence can be controlled. This however necessitates its use in a somewhat different way: a tool for the reduction of Δ-measurements. This is discussed in the next section.

7.3.6 A predictor-corrector formulation of MVL

General

Consider a Δ-measurement campaign on the configuration studied in the last section (the test case). An image of the support corrections can be constructed by performing Δ-measurements with a typical spacing of approximately 1 [deg] in α and β. Performing such measurements may lead to high operational costs. MVL may prove to be of value for the reduction of the amount of Δ-measurements thereby reducing the total operational costs of a wind tunnel measurement.

The intended purpose of MVL is to interpolate the interference patterns between two measurement points. At these points the total interference (wall- and support interference) should be known and serve as the boundary conditions of the interpolation. In this way the regular Δ-measurement spacing (in angle of attack and/or angle of sideslip) can be increased by almost a factor 10 thereby decreasing the amount of necessary measurement points and reducing operational costs. The problem of error divergence is then accounted for by constraining the solution by means of boundary conditions. The gain that can be achieved for an angle of attack polar and an angle of sideslip polar is likely to be different and depends on the flexibility of the support. In this section the gain is demonstrated for an angle of attack polar. The key to this particular application of MVL is to damp its calculated (and possibly diverging) interference profile with a damping function to avoid error divergence. This damping function is constructed using the boundary conditions attained by Δ-measurements.

Consider two simplified interference profiles (on any aerodynamic coefficient) as shown in Figure 7.19. One profile with the subscript “meas” is determined using mainly experimental techniques (Δ-measurements for the support interference and an experimental, numerical or empirical method for the wall interference). The other profile with the subscript “calc” is determined using MVL with as initial condition an experimental value at α_0. This is the reason that at α_0 the interference values coincide. It is seen that the error using MVL increases with increasing angle of attack (error divergence). The calculated polar can be seen as a “predictor” step in MVL. Consider now that a second experimental interference value (in addition to the initial boundary condition) is available. In that case a damping function can be defined using solely the boundary conditions such that both interference profiles almost collapse. This is seen as a “corrector” step in using MVL. A distinction between two damping functions is made: multiplication- and translational damping functions. These are explained in the following section.

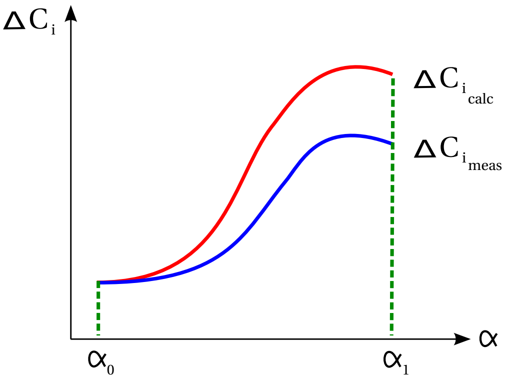

Figure 7.19: Two simplified interference profiles as measured ("meas") and as calculated ("calc") using MVL clearly showing error divergence

Multiplication damping functions

Consider a calculated interference profile using MVL based on an initial boundary condition at α_0. This calculated profile may or may not show error divergence (this is unknown to the user in advance). Consider that an additional boundary condition at α_1 is available. In that case a damping function $D(\alpha)$ can be constructed such that (referring to Figure 7.19):

$$\Delta C_{i_{calc}}(\alpha) D(\alpha) \approx \Delta C_{i_{meas}}(\alpha) . \tag{7.24}$$

Equation 7.24 clarifies why this damping function is referred to as a multiplication damping function: it aims at damping the error by multiplying the calculated solution by some predefined damping function. The boundary conditions on this damping function are given by:

$$\begin{aligned} D(\alpha_0) &= 1, \\ D(\alpha_1) &= \frac{\Delta C_{i_{meas}}(\alpha_1)}{\Delta C_{i_{calc}}(\alpha_1)}. \end{aligned} \tag{7.25}$$

This completes the definition of the linear multiplication damping function that is now defined as:

$$D(\alpha) = 1 + \left(\frac{\alpha - \alpha_0}{\alpha_1 - \alpha_0}\right)\left(\frac{\Delta C_{i_{meas}}(\alpha_1)}{\Delta C_{i_{calc}}(\alpha_1)} - 1\right). \tag{7.26}$$

From a practical point of view, applying the damping function is performed according to the following steps:

1. Using 1 initial condition of the interference at α_0, calculate the interference profile between α_0 and α_1 by using MVL including a (viscous) vortex-lattice routine,

2. Evaluate the multiplication damping function according to Equation 7.26 and a second boundary condition at α_1,
3. Multiply the interference profile determined by MVL with the damping function according to Equation 7.24 to obtain the damped interference solution between α_0 and α_1.

This concept is applied to the test case presented in section 7.3.5. A random interference profile representative for typical interference is generated and added to the clean wing data. Damped and undamped MVL solutions can be compared to the analytical solution. An example is shown in Figure 7.20.

From Figure 7.20 it is clear that the damped MVL solutions are in much closer agreement with the analytical solution of the interference than the undamped solutions. It is also seen that the damped solution implemented by a viscous (corrected) vortex-lattice routine outperforms the regular inviscid variant. This is more closely observed in Figure 7.21 revealing the errors made in the final MVL solutions by the choice of the vortex-lattice routine.

From Figure 7.21 it is clearly seen that the viscous vortex-lattice routine outperforms the inviscid variant as part of MVL used as an interpolation tool. On a given interpolation interval this implies that the more accurate the prediction by the vortex-lattice code becomes, the more accurate the final (damped) solution of the calculated interference will be. When a specified accuracy level is required this also implies that the interpolation interval can be extended when implementing a more accurate vortex-lattice routine (leading to a total reduction in the number of experimental boundary conditions) without crossing the specified accuracy level. Referring back to Equation 7.26 it is seen that a linear implementation is given for the damping function. Second order damping functions of the type $C1\alpha^2 + C2$ and $C1\alpha^2 + C2\alpha + C3$ where C1, C2 and C3 are constants are also implemented. These however do not lead to substantial improvements in accuracy.

Typical damped solutions with comparable accuracy as shown in Figure 7.20 are generated for random interference patterns as long as the value of the damping function is constrained:

$$D(\alpha) \leq 1. \tag{7.27}$$

It is found that when the value of the damping function becomes larger than 1, the numerical solution is not damped but blown up. This leads to erroneous solutions. An example of such an event is given in Figure 7.22.

It is seen in Figure 7.22(a) that the damping function generated by MVL including an inviscid vortex-lattice code does not exceed the value of 1. As a result the predicted interference profile (shown in Figure 7.22(b)) approaches the analytical value. It is seen that the damping function of the MVL calculation including the viscous vortex-lattice routine exceeds values of 1. As a result the numerical values in between the

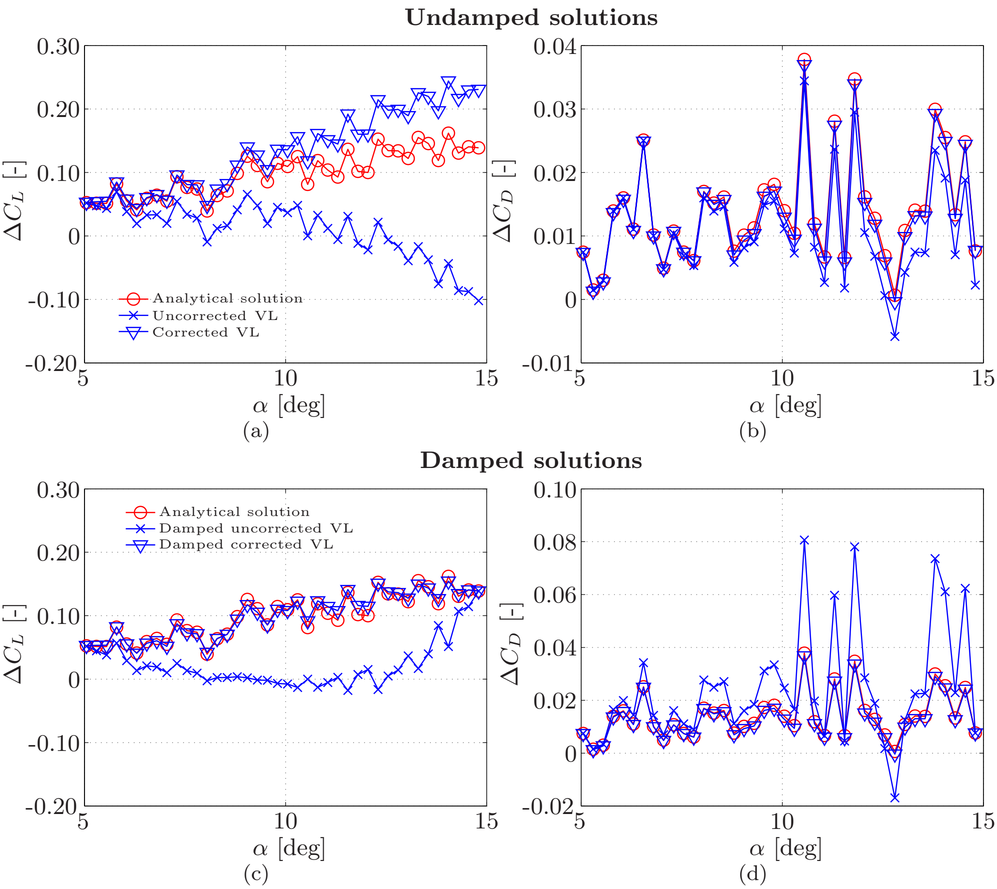

Figure 7.20: An example of using MVL as an interpolation tool to predict the total interference on the wing shown in Figure 7.16 between 5 and 15 degrees angle of attack. (a) and (b): Undamped MVL solutions for the interference on the lift- and drag-coefficient including a regular (uncorrected) vortex-lattice routine and a viscous (corrected) vortex-lattice routine. (c) and (d): Damped (multiplication-damping) MVL solutions for the interference on the lift- and drag-coefficient

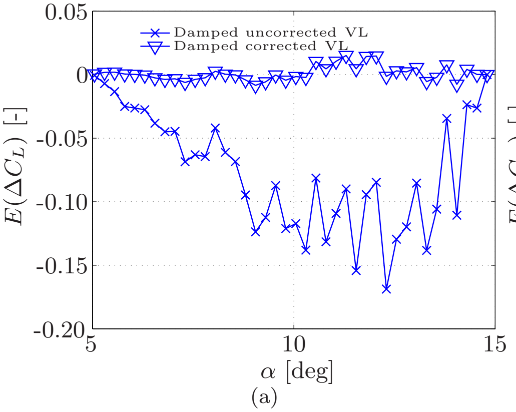

Figure 7.21: Error indication of MVL as an interpolation tool to predict the total interference on the lift-coefficient (a) and drag-coefficient (b) of the wing shown in Figure 7.16 between 5 and 15 degrees angle of attack. In the graphs the errors of damped (multiplication damping) MVL solutions including a regular (uncorrected) vortex-lattice routine and a viscous (corrected) vortex-lattice routine are shown

boundaries of the interpolation interval are blown up by this as is seen in the result of Figure 7.22(b). This reveals a typical disadvantage of the multiplication damping function: consider that the absolute experimental and numerical values at α_1 are 0.005 and 0.001, or 5 and 1 lift count respectively. From an absolute point of view this difference is small. When a multiplication damping function would be constructed however the damping value at α_1 would become 5 thereby blowing up the numerical solution in between α_0 and α_1. Considering the interference on the drag-coefficient it is seen in Figure 7.22(c) that the MVL result including a viscous vortex-lattice calculation does not exceed a value of 1 in contrast to the results including a regular inviscid vortex-lattice implementation. The consequences are visible in Figure 7.22(d) where it is seen that between α_0 and α_1 the numerical results of the latter are blown up.

As is shown in this section, MVL can be used as an interpolation tool in order to reduce the amount of necessary Δ-measurements and hence operational costs. This however necessitates a damping function that damps out the error of MVL in the complete interpolation interval. Multiplication damping is not suitable for this purpose as it tends to blow up the numerical solution once the damping function exceeds a value of 1. Another type of damping function is evaluated that omits this disadvantage. It is called a translational damping function.

Translational damping functions

Consider a particular wing configuration such as the test case wing shown in Figure 7.16. Consider that the clean (not affected by any interference) lift-slope of this wing is known and that in the linear lift regime (from e.g. $\alpha = 0$ to 10 [deg]) this lift

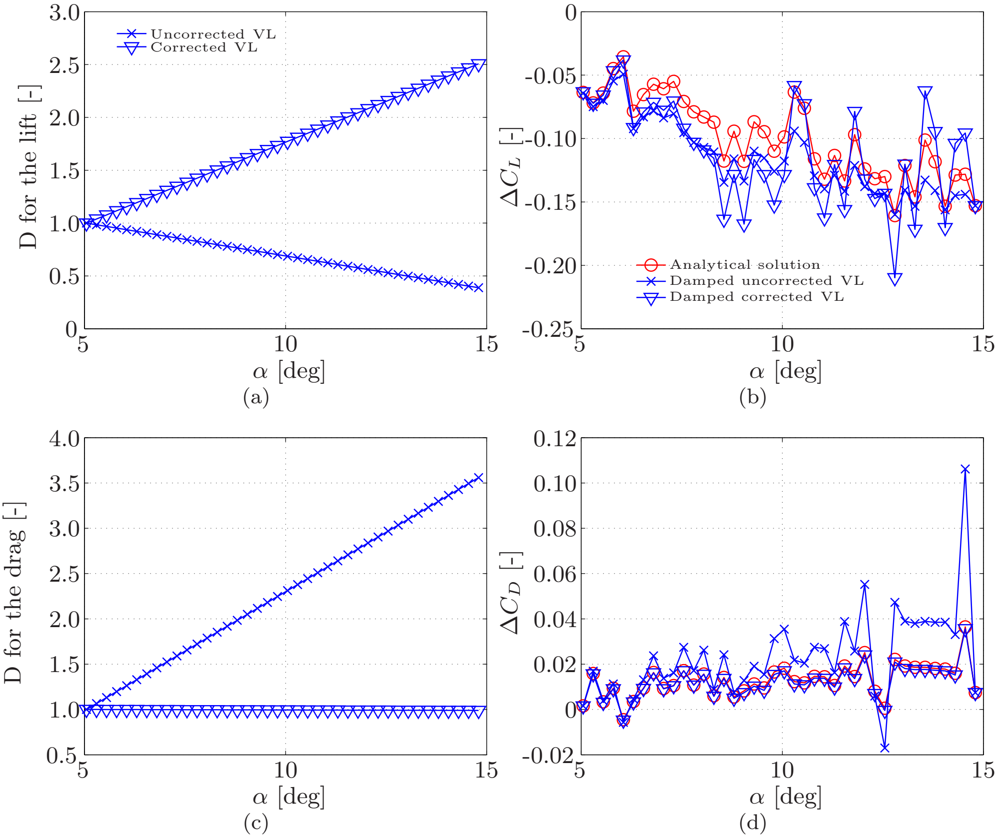

Figure 7.22: Damping functions ((a) and (c)) and resulting damped solutions ((b) and (d)) for predicting a random interference profile on the lift- and drag-coefficients of the wing shown in Figure 7.16 between 5 and 15 degrees angle of attack. Damping functions for the MVL solutions including an inviscid (uncorrected)- and viscous (corrected) vortex-lattice calculation are shown

slope equals a value of $\left(\frac{\partial C_L}{\partial \alpha}\right)_M$ where the subscript "M" stands for "Measurement". The same parameter obtained with a vortex-lattice code is called $\left(\frac{\partial C_L}{\partial \alpha}\right)_C$ where the subscript "C" denotes "Calculation". Define the difference between the two as Δ. According to Equation 7.23, the error buildup in the MVL calculation is proportional to:

$$Calculation\, N \rightarrow E\left(\Delta C_{i_{int_N}}\right) \propto \Delta \sum_{i=1}^{N-1} \left(\alpha_{i+1} - \alpha_i\right). \tag{7.28}$$

It is seen from Equation 7.28 that a linear error buildup will manifest in the MVL results when a constant over- or under-prediction of the aerodynamic derivatives is calculated by the vortex-lattice code. This is the source of inspiration of a linear translational damping function, a function that damps out the error by adding a linear damping term to the solution of MVL.

Consider a calculated interference profile using MVL based on an initial boundary condition at α_0. This calculated profile may or may not show error divergence. Consider that an additional boundary condition at α_1 is available. In that case a damping function $D(\alpha)$ can be constructed such that (referring to Figure 7.19):

$$\Delta C_{i_{calc}}(\alpha) + D(\alpha) \approx \Delta C_{i_{meas}}(\alpha). \tag{7.29}$$

The boundary conditions on this damping function are given by:

$$\begin{aligned} &D(\alpha_0) = 0, \\ &D(\alpha_1) = \Delta C_{i_{meas}}(\alpha_1) - \Delta C_{i_{calc}}(\alpha_1). \end{aligned} \tag{7.30}$$

This completes the definition of the linear translational damping function that is now defined as:

$$D(\alpha) = \left(\frac{\alpha - \alpha_0}{\alpha_1 - \alpha_0}\right)\left(\Delta C_{i_{meas}}(\alpha_1) - \Delta C_{i_{calc}}(\alpha_1)\right). \tag{7.31}$$

The damping function given in Equation 7.31 is evaluated. The results are given in Figure 7.23.

Figure 7.23 clearly shows that using the translational damping function is a much safer choice than using the multiplication damping function in a sense that it does not have the tendency to blow up the numerical solution. Considering Figure 7.23 it once again becomes clear that the interpolation becomes more accurate when the accuracy in the prediction of the vortex-lattice code increases.

Because it seems impossible to generalize on the shapes of interference profiles (this depends on the model geometry, wind tunnel geometry, support geometry and flow properties) different types of interference profile shapes are tested for predictability by MVL as interpolation tool. The following shapes are tested:

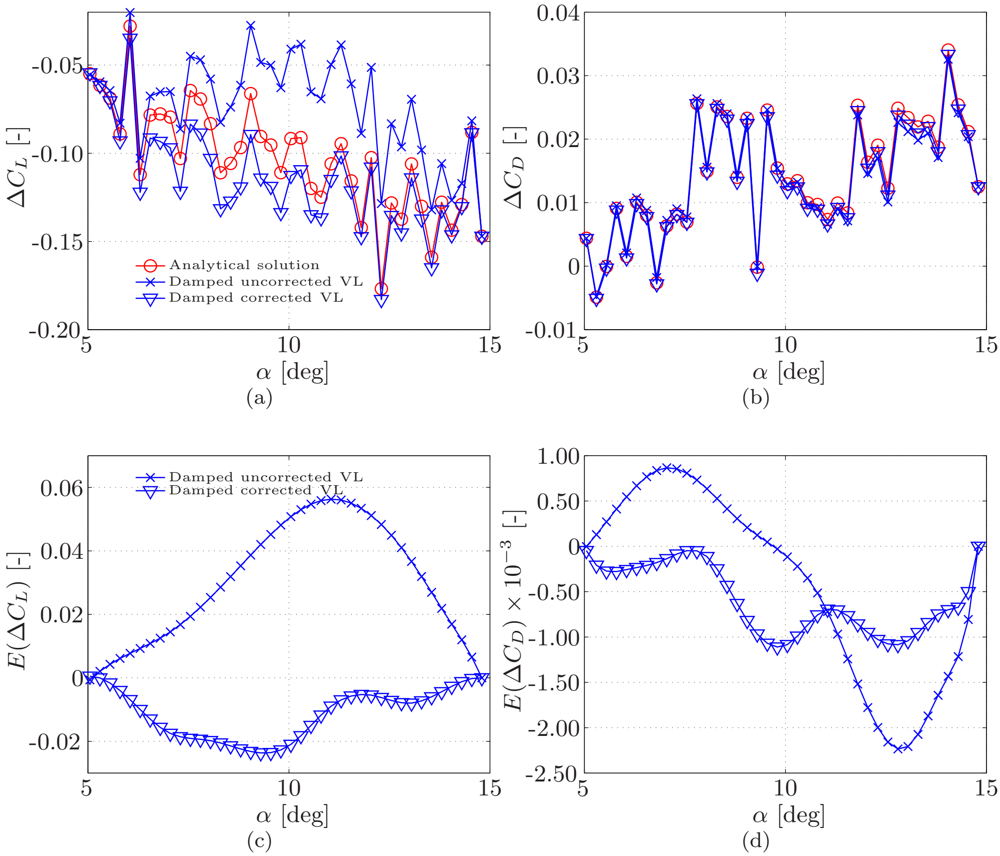

Figure 7.23: Translational damped solutions to a random wall- and support interference profile on the lift-coefficient (a) and drag-coefficient (b) of the wing shown in Figure 7.16 between 5 and 15 degrees angle of attack. The interference is determined by MVL as an interpolation tool including uncorrected (inviscid) and corrected (viscous) vortex-lattice routines. Respective errors are indicated in (c) and (d)

1. Linear profiles,
2. Second order profiles,
3. Third order profiles,
4. Sine-shaped profiles,
5. Combinations of the aforementioned.

For these interference profiles the damped solutions (using translational damping) and their comparison to the analytical solution is evaluated. The results are shown below in Figures 7.24 to 7.28.

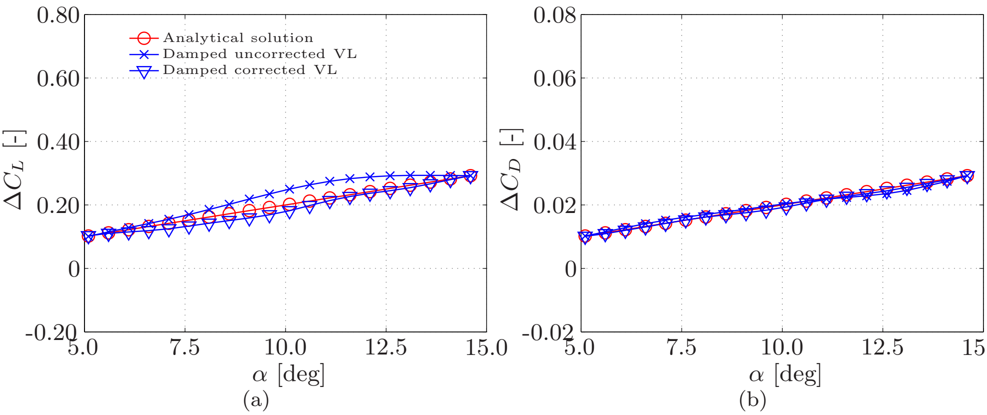

Figure 7.24: The interpolated interference profile on the wing shown in Figure 7.16 between 5 and 15 degrees angle of attack as determined by MVL including translational damping. Results of applying an uncorrected (inviscid) and corrected (viscous) vortex-lattice routine are shown for calculating the interference on the (a) Lift-coefficient (b) Drag-coefficient. The disturbance profile has a linear character

It is seen that the concept of translational damping functions works for a wide variety of interference profiles. For these profiles, the accuracy is typically 20 lift counts and 10 drag counts (these are maximum errors found in the interpolation interval). This accuracy can be increased when:

1. For the same interpolation interval a better approximation of the aerodynamic derivatives is calculated. This implies the development of a more accurate vortex-lattice code,
2. Using the same vortex-lattice code, the interpolation intervals can be decreased (or, equivalently, for a given range in angle of attack and/or angle of sideslip the number of boundary conditions must be increased).

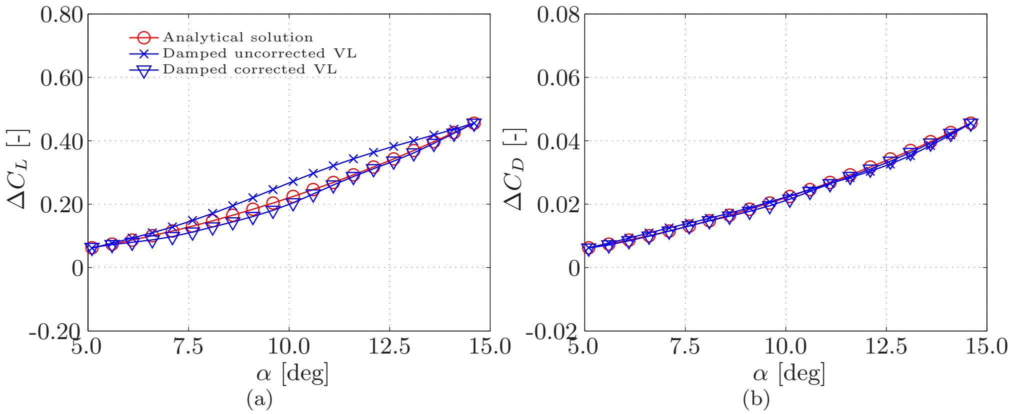

Figure 7.25: Same as Figure 7.24 for a disturbance profile with a quadratic character

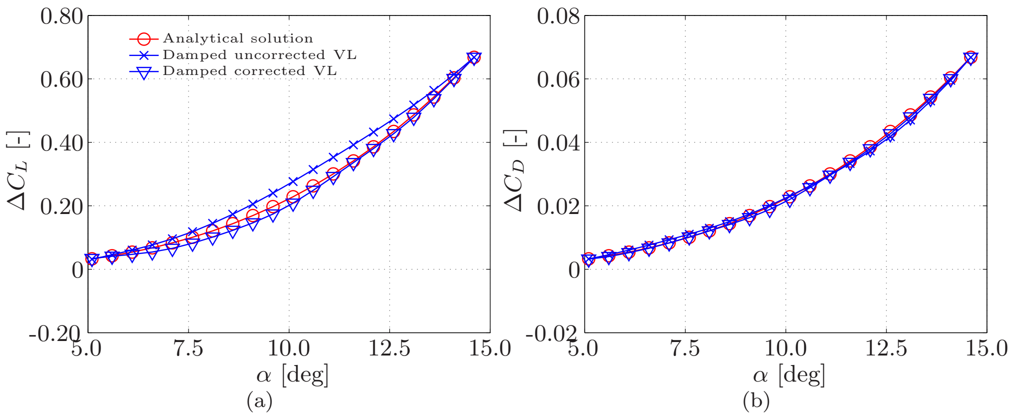

Figure 7.26: Same as Figure 7.24 for a disturbance profile with a cubic character

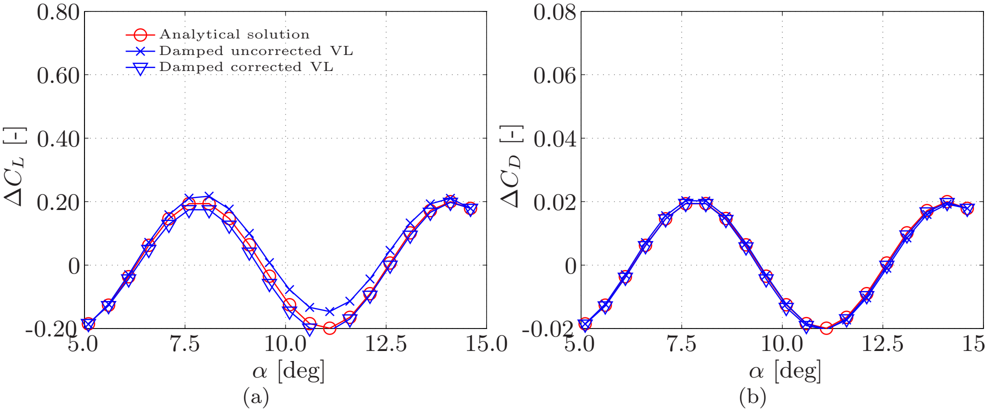

Figure 7.27: Same as Figure 7.24 for a disturbance profile with a sine character

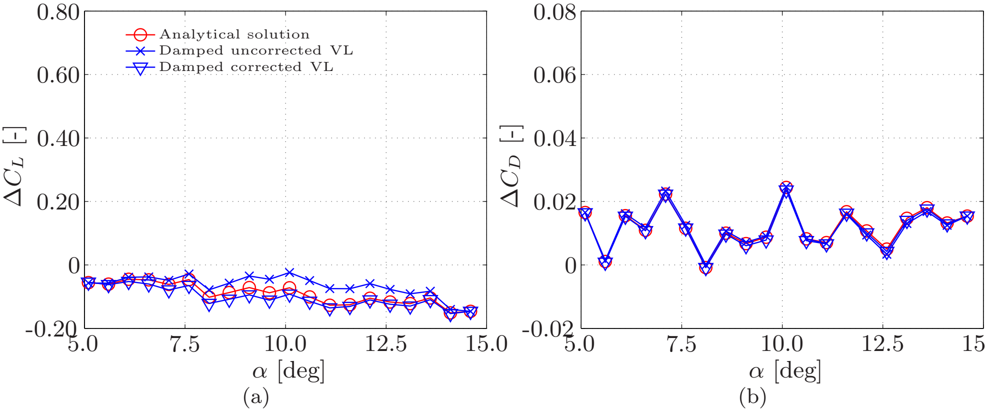

Figure 7.28: Same as Figure 7.24 for a disturbance profile with a blended character (consisting of the product of a third order polynomial and cosine function with a random fluctuation)

Considering the fact that the current interpolation interval is chosen rather large, the second option seems the most attractive. For example, reducing the interpolation intervals to 5 instead of 10 degrees reduces the error to a maximum of 10 and 5 lift- and drag counts respectively. Another reduction of the interpolation intervals by a factor 2 leads approximately to an increase of this accuracy by a factor 3 for the interference on the lift-coefficient and a factor 2 for the interference on the drag-coefficient.

The influence of the introduction of Gauss-Legendre quadrature points in the interpolation domain on the interpolation accuracy is also evaluated. In that case the boundary conditions are not enforced at the interpolation boundary points (α_0 and α_1) but at $\alpha_0 + \Delta\alpha$ and α_1 - $\Delta\alpha$) where $\Delta\alpha$ is a function of the interval size. The damping functions are however evaluated on- and applied to the complete domain ($\alpha_0 \leq \alpha \leq \alpha_1$). The increase in accuracy of the interpolation due to the introduction of these points seems negligible.

7.3.7 Real test case: F50 measurement

The value of MVL as interpolation tool is best demonstrated by a realistic test case: the measurement of the aerodynamic characteristics of the Fokker-50 (F50) aircraft in a closed-wall test section of the Low Speed Tunnel (LST) of DNW. Characteristics of the test are given in Table 7.9. The test setup is schematized in Figure 7.29.

Table 7.9: Characteristics of the F50 test case measurement

Parameter	**Value**	**Unit**
Test section shape	Rectangular	-
Test section width	3.00	[m]
Test section height	2.25	[m]
Freestream velocity	60	[m/s]
Freestream Reynolds number	$0.66{\cdot}10^6$	[-]
Model scale	1:15	[-]
Model suspension	Sting suspended	-
Force balance type	Internal balance	-

In this wind tunnel test, the model of the F50 is suspended by a sting whereas the forces and moments acting on the model are measured by means of an internal balance. Wind tunnel wall corrections for this test are determined by using typical methods described in the AGARDograph 336 [5]. Support corrections are determined by means of Δ-measurements using dummy supports. Adding the wall- and support corrections for this test gives a total correction package. MVL (in combination with a viscous vortex-lattice code) is used in order to determine this correction implementing translational damping. Results of calculations and measurements are compared. This comparison is schematized for an angle of attack polar in Figure 7.30.

It can be seen in Figure 7.30 that the results of MVL closely match the experimental results, almost completely to within balance accuracy. In the calculations, use is made

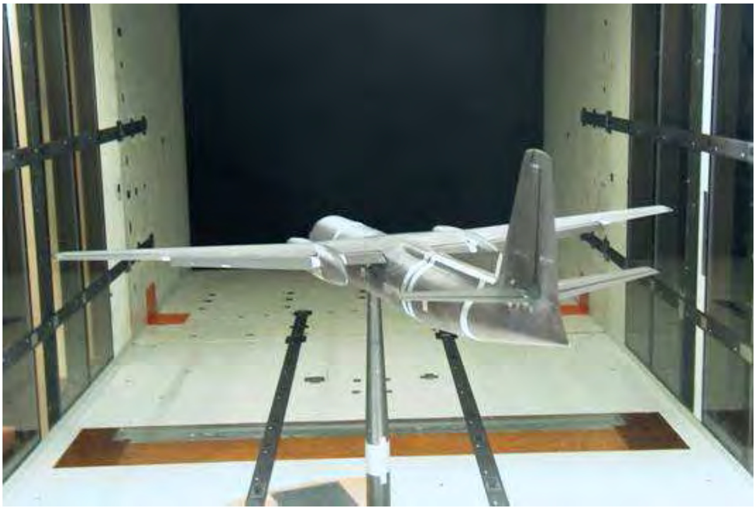

(a)

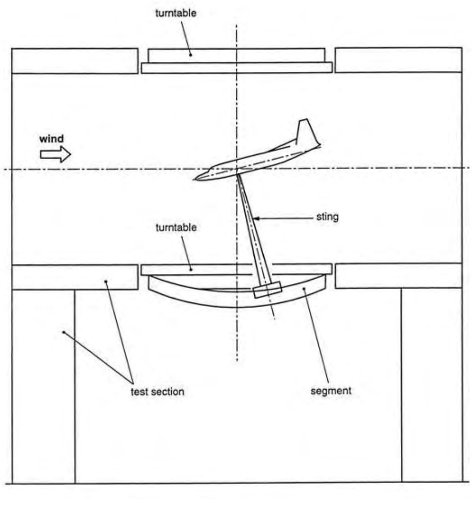

(b)

Figure 7.29: Fokker-50 (F50) aircraft in a closed-wall test section of the Low Speed Tunnel (LST) of DNW. A picture (a) and a schematic (b) of the experimental setup of the test

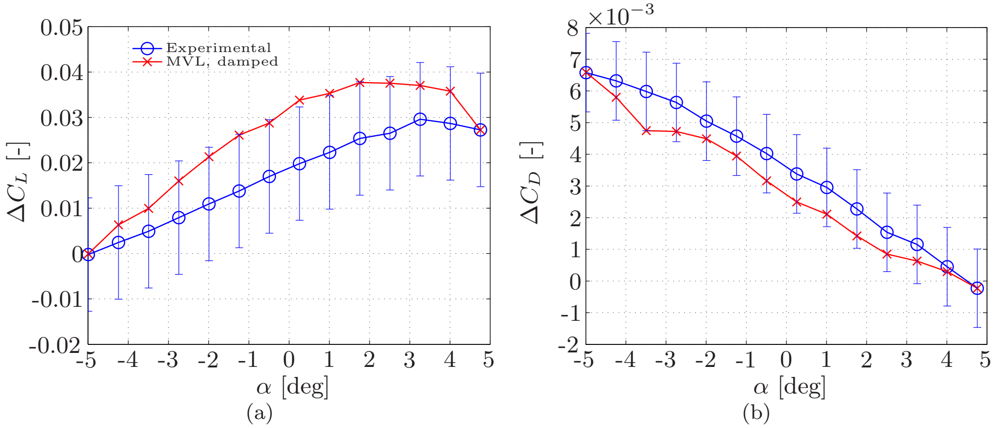

Figure 7.30: Comparison of experimental and numerical (MVL, implementing a viscous vortex-lattice routine combined with translational damping) values of wind tunnel wall- and support interference on the setup shown in Figure 7.29 (a) Interference on the lift-coefficient (b) Interference on the drag-coefficient. The experimental accuracy bandwidth is indicated in the plots

of boundary conditions at α = -5 and 5 degrees. Only two boundary conditions instead of 20 Δ-measurement points (with a spacing of 0.5 [deg]) are required for this result.

Implementing MVL, the achievable gain for an angle of attack polar and an angle of sideslip polar is likely to be different and depends on the flexibility of the support. The performance of MVL at angles of sideslip for this measurement is also assessed and presented in Figure 7.31.

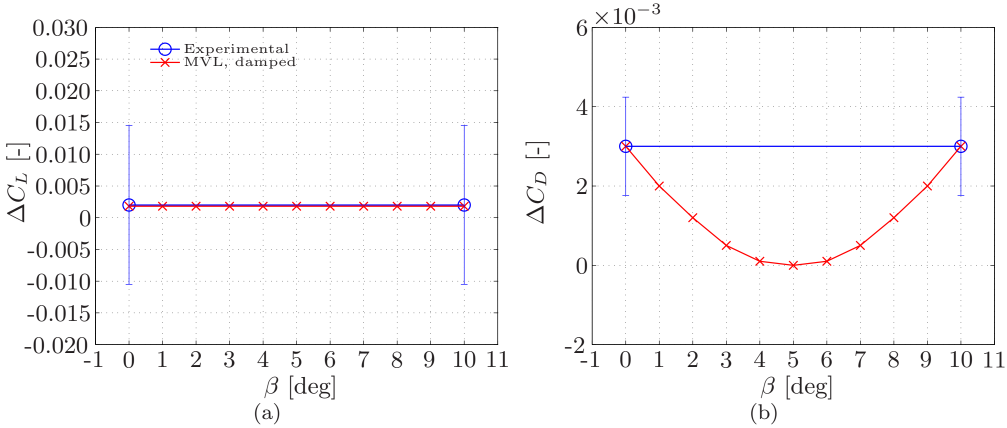

Figure 7.31: As in Figure 7.30 but now for sideslip angles

The comparison between experimental- and numerical result is complicated because the spacing of the Δ-measurements in β is 10 [deg]. Although this facilitates the boundary conditions for MVL, an accurate comparison is out of the question. It is seen that the calculated order of magnitude of the interference on the lift-coefficient and drag-coefficient coincides with the measurements. The calculated interference on the drag-coefficient shows a trend that is not understood and might be called questionable. This is attributed to the following: it is of utmost importance that the main aerodynamic characteristics of the model of interest is best represented by the vortex-lattice code. At angles of sideslip model fuselage- and engine nacelle viscous effects start to influence this aerodynamic behavior. This influence is however not modeled in the viscous vortex-lattice routine complicating the determination of the interference pattern.

This test case emphasizes that exploiting the maximum potential of MVL in an expert system implies developing a method for accurate determination of the aerodynamic derivatives of the model of interest at angles of attack and sideslip. This is left for future research.

7.3.8 MVL: characteristics on speed and accuracy

To make MVL an element of an expert system implementable during a typical commercial wind tunnel measurement cycle the following input is necessary:

1. Uncorrected wind tunnel measurements,
2. The aerodynamic derivatives calculated by a vortex-lattice code,
3. (A) Boundary condition(s).

With this input MVL can be used in an on-line fashion and an off-line fashion:

Consider the on-line fashion first: during the wind tunnel measurement, uncorrected measurement data will become available immediately upon data acquisition. Because these uncorrected results should be splined to a fine grid (e.g. $\Delta\alpha = \Delta\beta = 0.05$ [deg]) the angle of attack- or angle of sideslip polar should be completed before the correction can be carried out. Vortex-lattice calculations and determination of the boundary condition(s) are performed before the measurements. Performing the actual calculation and correction during the measurement is performed within seconds according to the requirements on speed for stage 3 ("performing the measurements") mentioned in section 5.8. The accuracy of the method depends on the number of boundary conditions and the prediction capabilities of the vortex-lattice method. For an elaborate discussion on the accuracy, the reader is referred to the previous sections.

Secondly, consider the off-line use of MVL: the availability of the uncorrected measurements is guaranteed by data files saved by the data acquisition system. According to Table 5.1 a distinction can be made between the case where all the necessary input is available for the determination of the interference and the case when only the uncorrected measurements are available (no preparations are taken at all):

- When all the necessary input for MVL is available the time associated with the correction of the measurements equals the situation where MVL is used on-line: O(seconds),
- When only uncorrected measurements are available: modeling of the wind tunnel model in a vortex-lattice code and performing the necessary calculations typically requires a budget in the order of hours. It is the collection of boundary conditions that is most time consuming and determines the speed. These must be extracted from measurements stored in a data-base or perhaps dedicated calculations. For this reason the time associated with the use of MVL agrees with a stage 2 event ("test preparation phase"). It is not excluded that the ESI (Evaluation of Support Interference) module (as presented in Chapter 6) might prove to be of value for this purpose. Experimental data complemented with calculations might be useful for estimating the boundary conditions necessary.

The main characteristics on speed and accuracy are summarized in Table 7.10.

Table 7.10: Main characteristics on speed and accuracy of MVL

MVL allocation	Performance: speed	Performance: accuracy
On-line	O(seconds)	Sections 7.3.6/7.3.7
Off-line*	O(seconds)	Sections 7.3.6/7.3.7
Off-line**	O(weeks)	Sections 7.3.6/7.3.7

* All necessary input available

** Only uncorrected measurements available

7.4 Expert system additions concluded

Consider again the rule of thumb quoted in Chapter 5:

"High accuracy (at a minimum equal to typical balance Δ-measurement accuracy) and low implementation effort (total measurement effort or modeling effort and computational effort) of a correction method for determining model support interference are currently incompatible when a wide range of applicability (freestream conditions, setups) is desired."

In the light of the applications presented in this chapter, this rule of thumb can be assessed. Consider at first instance VOLAER. Even if a calculation on a certain support structure would contain a very high accuracy, the implementation effort is substantial thereby classifying it suitable for implementation during stage 2 (test preparation phase) of a typical commercial wind tunnel measurement. On top of this, VOLAER calculations have a limited applicability as discussed in section 7.2.2 and shown in Table 7.6. Because of the implementation effort and the limited range of applicability VOLAER is not a very flexible method. Unfortunately the rule of thumb seems to be confirmed for this application.

When MVL is considered, it seems at first that a very high accuracy and wide range of applicability can be realized. However in order to reach a very high accuracy (as discussed in the previous sections), the number of boundary conditions must be increased beyond 1 in order to ensure a stable solution. In the last section it is explained that such activities are typically associated with a stage 2 activity (lasting potentially O(weeks)) whereas the appropriate boundary conditions should be determined by processing experimental data or performing numerical calculations. Although the use of ESI (Evaluation of Support Interference module) might speed up this process, the amount of implementation effort can become substantial. Once again, the rule of thumb is confirmed.

Although for the applications presented in this chapter the above stated rule of thumb seems applicable, they prove to be valuable elements of an expert system:

1. VOLAER can be used for a decent range of sting placements (R1, R2a, R2b as shown in Figure 4.26) whereas it gives valuable information on both near-field disturbances as spatial far-field distributions (Table 7.6),

2. MVL is usable for all support setups in whatever type of wind tunnel provided a vortex-lattice method is used enabling an accurate representation of the model aerodynamic derivatives (modeling effort is minimized). It is shown that the amount of dummy measurements can be seriously reduced for α-polars using MVL as an interpolation tool. The gain that can be achieved for an angle of attack polar and an angle of sideslip polar is likely to be different and depends on the flexibility of the support. The value of MVL can be optimized when the amount of Δ-measurements for β-polars can also be reduced. This however necessitates a calculation of the aerodynamic derivatives taking the model fuselage and engine nacelles into account. This is left for future research.

Characterized by restrictions on speed and accuracy these methods are appealing for offering both engineer but especially client more alternatives for the treatment of wind tunnel wall- and support interference. Referring back to the needs regarding support interference determination as presented in Chapter 1 (according to Lynch et al. [17]) the development of alternatives is the key to a future systematic approach towards the problem of support interference.

7.5 Summary

This chapter has presented two hybrid methods for the determination of wall- and support interference. These methods can be implemented during a typical commercial wind tunnel measurement. They are given the label “hybrid” because they combine results of two standard methods (experimental and/or numerical) for the determination of interference. In this way the most favorable characteristics of these standard methods are combined. The methods discussed are:

1. VOLAER (VOrtex-LAttice/EuleR): this method combines vortex-lattice calculations and Euler calculations for the determination of support interference (both near-field and far-field),

2. MVL (Measurement/Vortex-Lattice): this method combines uncorrected wind tunnel measurements with vortex-lattice calculations to correct for all the disturbances of wind tunnel walls and support.

These two methods are explained and their potential is demonstrated by test cases enabling the evaluation of characteristics in terms of speed and accuracy:

1. VOLAER can be used for a decent range of sting placements (R1, R2a, R2b) whereas it gives valuable information on both near-field disturbances and spatial far-field distributions. Typical characteristics on speed and accuracy are presented in section 7.2.7 and Table 7.6,

2. MVL proves to be particularly valuable as it predicts the interference of wind tunnel walls, support and includes secondary interference (when e.g. the support is traversed close to the wind tunnel walls). The fact that only the wind tunnel model should be modeled in a vortex-lattice code makes it much more attractive than dedicated finite-volume solvers that require remodeling of the wind tunnel, support and model once the angle of attack and/or angle of sideslip are changed.

   MVL is usable for all support setups in whatever type of wind tunnel provided a vortex-lattice method is used enabling an accurate representation of the model aerodynamic derivatives. MVL's prediction capabilities necessitate the use of multiple boundary conditions in order to guarantee a stable solution thereby categorizing it as an interpolation tool to reduce the amount of Δ-measurements. In such cases the introduction of a translational damping function is seen to provide the most accurate solution when a wide range of interference patterns is considered. The extent of the Δ-measurement reduction that can be achieved for an angle of attack polar and an angle of sideslip polar is likely to be different and depends on the flexibility of the support.

   The value of MVL can be optimized when the amount of dummy measurements for β-polars can also be reduced. This however necessitates a calculation of the aerodynamic derivatives taking the model fuselage and engine nacelles into account. This is left for future research. Typical characteristics on speed and accuracy are presented in section 7.3.8.

Unfortunately VOLAER and MVL apply to the rule of thumb stated in Chapter 5. However they prove to be of value as elements of an expert system. These methods are appealing for offering both engineer but especially client more alternatives for the treatment of wind tunnel wall- and support interference according to the future needs regarding support interference determination presented in Chapter 1 (according to Lynch et al. [17]). The development of alternatives is the key to a future systematic approach towards the problem of support interference.

At this point it is wise to take a step back and review the results of the previous chapters. Over-viewing the results presented in Chapters 1 to 7 provides a clear picture of the justification of this research and the research activities. The problem of wind tunnel support interference, the future needs towards the treatment of support interference and the introduction of the expert system as a means of meeting these future needs are touched upon. The fundamental research on the elements of the knowledge base of the expert system and the study on the structure of the system in terms of its applications (or, elements) will be revised. This will finally give an indication of whether or not the research objective as stated in section 1.5 is met. With this indication, the future prospects of the expert system can be highlighted.

Stepping back in order to revise the research as presented in this thesis is the topic of the next chapter.

Chapter 8

Future Prospects of the Expert System

8.1 Introduction

This chapter recapitulates on the research presented in this thesis. It will become clear that the research objective as stated in section 1.5 is met. Windows of opportunity for the development of the expert system by means of knowledge base expansion and the development of new expert applications/elements will be highlighted. The treatment of the problem of wind tunnel wall interference by the expert system is also touched upon. The rule of thumb as stated in section 5.6 will finally be the center of attention in a discussion on future prospects of the expert system.

8.2 Recapitulating the research results

In Chapter 1 wind tunnel support interference is identified as one of the constraints affecting the quality of wind tunnel measurements. Multiple methods (experimental, empirical or computational) to correct for support interference are pointed out. Experimental methods are often time consuming and costly. This also holds for empirical methods as they are founded on a vast number of experimental data sets. CFD is also found to be time consuming and sometimes computationally expensive. Desirable accuracy of methods to determine support interference is related to the typical Δ-measurement accuracy, depending on the performance of the force balance. Future guidelines for the treatment of support interference aim at providing engineers more alternatives. Such alternatives require however an extensive knowledge on experiments and CFD: it requires the engineer to be an expert in the field, something that is often impossible. Engineers should therefore be guided by an expert system (a computer program that represents and reasons with knowledge of some specialist subject with a view to solving problems or giving advice) in their dealings with support interference. These considerations lead to the research objective:

"To identify the necessary elements for the design of an expert system for support interference on sting mounted models carrying internal balances applicable to low-speed wind tunnels."

Identifying the necessary components of an expert system requires at first a study on the elements of its knowledge base. More intelligibility on support interference is therefore necessary. Before commencing with this research, a summary of typical support effects (Appendix A and Appendix B) demonstrates the status quo on intelligibility.

In Chapter 2 a starting point for the study on the fundamentals of low-speed model support interference on sting mounted models accommodating internal balances is given: the model sting. Focusing on the sting is justified by a support break down that facilitates the treatment of disturbances of individual support parts spanning a certain support structure. This break down should be such that the support members spanning a particular part deliver the same type of disturbance (near-field or far-field) and can be determined by the same method. A proof of concept is given by analyzing measurement results of DNW. It seems that the order of magnitude and the nature of the disturbances are not compromised when this approach is adopted provided that the amount of separate parts is kept to a minimum. This approach enables the study on the disturbances of the model sting alone, the support member protruding the fuselage. The model sting is an essential object for further study as it causes the complete spectrum of disturbances (both near-field and far-field). Besides practical advantages another advantage of studying the sting is the possibility to generalize the research results to a wider class of support structures. The sting is a crucial starting point for further research on model support interference. It allows a qualitative analysis on the nature of near-field and far-field effects but also a qualitative and quantitative validation of several methods applied to determine the interference. As a starting point "exploratory" measurements and calculations are performed on model sting interference assessing the complexity of the interference field.

In Chapter 3 an introduction on the complex physics of the frequently studied "juncture flow" is given as the model sting interference flow field can be expected to show distinct similarities with its flow topology. Based on differences between the typical juncture flow configuration and the configuration of interest (a model sting penetrating an aircraft fuselage carrying an internal balance) it is concluded that a new study on the sting disturbances is inevitable. Besides the need to create an experimental and numerical data base for the tuning of calculations and validation of numerical techniques, the following question needs to be answered:

"Is it justified (from the viewpoint of accuracy) to determine model sting near-field and far-field effects using methods at low levels of complexity and intrinsic accuracy without knowing the specific details of a possibly complex interference flow field?"

This question aims at identifying low-cost computational methods for the determination of model sting interference implementable in the expert system once labeled as "good enough" (meaning to within accuracy requirements). Measurements and calculations on model sting near-field and far-field effects are presented in order to answer this question. Comparing their results it is concluded that it is not justified to implement these type of calculations (such as panel code- and Euler calculations) for determining model sting disturbances to within measurement accuracy. Significant calculation offsets (out of the bounds of experimental accuracy) are caused by unknown characteristics of the interference flow field. This flow field is thought to be governed by the action of the balance cavity and slit, and additional effects of vorticity and viscosity. An in depth understanding of the limitations of these numerical methods (panel code, Euler) can only be developed when the interference flow field itself is understood both qualitatively and quantitatively. To this end Navier-Stokes calculations are carried out.

In Chapter 4 the setup and analysis of Navier-Stokes calculations are presented. These clarify the near-field flow of model sting and fuselage and identify the disturbances governing the near-field of the model sting. Calculations provide a qualitative image of the interference flow field that complies with measurements. Quantitatively however, the calculations discussed are not able to determine the values of near-field interference with the right trends and within typical measurement (balance) accuracy.

Based on gained knowledge of the flow field all numerical methods applied (panel code-, Euler- and Navier-Stokes calculations) are assessed on how well they perform qualitatively and quantitatively in determining model sting near-field effects and why. This provides an overview of the restrictions of these methods for the calculation of model sting near-field effects for the configuration under study.

Based on this information various numerical and experimental methods for determining support interference of various setups are classified. It is concluded that the two classification parameters "accuracy" and "effort" oppose each other. This opposition might be cleared by designing a custom-made model (that is both accurate and requires a low amount of implementation effort) for calculating model support interference, implementable in the expert system. Such a model should calculate the disturbance effects fast (by incorporating only the disturbance factors of primary quantitative interest) with the right trends and magnitude. It should typically combine the computational advantages of a panel code calculation with the typical accuracy of a balance Δ-measurement.

In Chapter 5 an example of a custom-made model for the determination of wind tunnel support interference is presented. A simplified 2D case reveals typical disadvantages of such models: due to the lack of knowledge on the dependencies of the tuning variables, the quality of the calculated corrections is not guaranteed. Additional issues such as qualitative interference changes (when α, β or the configuration is changed) and inevitable intervention of an engineer in the numerical part of the model are addressed. Solving for these issues implies an inevitable reduction in the operational applicability range of the model. Typical custom-made models are non-feasible elements of an expert system. They do however reveal that high accuracy, low implementation effort and wide applicability can currently not be simultaneously satisfied by whatever method to determine model support interference. This necessitates a more elaborate definition on requirements on speed and accuracy of the expert system's elements. It is shown that a feasible expert system might consist of applications with given accuracy and speed assisting in four stages defining a typical commercial wind tunnel measurement.

Having collected a considerable amount of intelligibility on model support interference and a more elaborate definition on requirements on speed and accuracy of expert system's elements, a closer look is taken at a feasible structure of the expert system.

In Chapter 6 a feasible application-based structure is discussed in more detail after summarizing the main requirements on the expert system. Typical applications are studied more thoroughly. It is shown that the proposed structure fulfills the expert system's requirements.

These requirements can be seen as a minimum set of criteria. The expanded knowledge base on model support interference has resulted in two basic expert applications (ESI and ASID, directly applicable for measurements in the LLF of DNW for which they are customized) and new methods (VOLAER and MVL) to approach the problem of wind tunnel wall- and support interference. These products are seen as basic elements of an expert system (generalizable to other wind tunnels). This does however not imply that the expert system is complete and directly implementable. In order to launch a first version of the expert system, the engineers should become confident with the expert applications. On top of this, it is recommendable that methods as MVL are integrated in the data acquisition system of the wind tunnel of interest and tested thoroughly. Implementation of a first version will show the typical shortcomings of the applications by exposure to the typical user. Feedback of such information might then lead to improvement of the applications or the addition of new applications.

8.3 Recapitulating the research objective

A successful survey on a feasible structure of an expert system in terms of its applications (or, elements) is performed. Several feasible applications of such a system are designed and evaluated. The applications are based on a study on low-speed wind tunnel support interference on sting mounted models with internal balances and can therefore be seen to arise from the expanded knowledge base on support interference. Based on these considerations, the research objective as stated in Chapter 1 is satisfied.

Although a feasible structure and several applications of the expert system are provided, a first version of a complete expert system would still be far from matured. There is plenty of room for development. This will be discussed in the next section.

8.4 Future expert system development

In this section, the potential of future expert system development is highlighted. Development is mainly stimulated by maintaining and expanding the knowledge base. This is possible through adding more data to the applications (experimental and/or numerical) or by developing more expert applications. These matters are discussed in the following sections.

8.4.1 Gaining more expertise

As an example, consider once again the application ESI. This application features a module containing experimental data (Δ-measurement data) and numerical data (the results of e.g. vortex-lattice calculations). In the near-future (within one or two years) this module can be expanded: additional experimental results can be included. When during the operational phase it seems that this data base does not contain enough information in order to determine an appropriate sting placement for a given configuration, new vortex-lattice calculations can be performed to fill this gap. The results of the calculations can be added to the data module. When the extent of the data module increases, statistics may point out new rules of thumb that are directly implementable and lead to the expansion of the knowledge base. Stimulated by frequent use, the application will therefore become more intelligent (or, more of an expert). The same holds for the ASID application. It is stressed that this is only possible by maintaining and updating the knowledge base.

8.4.2 Wall interference treatment

The problem of wind tunnel wall interference is coupled to support interference as assessed by Carlin et al. [10]. Determining values of support interference is performed by including the modeling of wind tunnel walls as these walls change the disturbance ability of the support under consideration. The disturbance parameters characterizing wall interference show agreement with those for support interference. This encourages the treatment of wall interference in a similar way: including one vortex-lattice calculation without modeling the wind tunnel walls enables the evaluation of some basic wall interference parameters (lift interference for instance) in ESI by a simple Δ-calculation. Besides such treatment of wind tunnel wall interference, a variety of known methods exist that enable its evaluation. It is believed that enough knowledge on the treatment of wind tunnel wall interference is available (consider for instance the AGARDograph 336 [5] and Lynch et al. [17]) to design expert applications attainable in all stages of a typical wind tunnel test. The modular framework of the expert system is suitable for this purpose.

8.4.3 Breaking the rule of thumb?

Consider once again the rule of thumb stated in section 5.6. Will it ever become possible to break this rule of thumb by expert system applications?

Regarding the experimental determination of support interference, the outlook seems grim. Wide ranges of applicability can be met with a high accuracy experimental method such as a dummy measurement. The implementation effort of such methods however pose a problem. Major improvements in implementation effort are not very likely to be introduced in the near future because a certain degree of human intervention during a wind tunnel test remains inevitable.

When a numerical treatment of support interference is considered, high accuracy and a wide range of applicability seem compatible when very advanced calculations are initiated. Programs should be able to mesh domains automatically within a reasonable amount of time (e.g. half an hour). The wide range of applicability can only be guaranteed when advanced calculations are ran without having to cope with e.g. turbulence modeling issues. This points towards solving the Navier-Stokes equations by means of a Direct Numerical Simulation (DNS). According to Nieuwstadt [73], solving for the micro- and macro scales in a turbulent flow with a steady calculation necessitates a 3-dimensional domain where the number of mesh points is proportional to $Re^{9/4}$ where Re represents the flow Reynolds number. This is the reason that such methods can only be implemented for low Reynolds number flows. A steady DNS calculation on a typical configuration shown in Figure 7.2 with Reynolds numbers of roughly 2.5 million will for the coming years be unattainable due to the lack of computer power. Computational effort will still be a problem for the years to come. On top of this, experts in the field of numerical aerodynamics would still be required to solve numerical problems (diverging solutions for example). Low effort for this type of solutions does not seem realizable for the near future.

Although measurements or calculations are not very likely to break this rule of thumb for the near future, smart combinations of the two might very well. In Chapter 7 it is explained that MVL at first instance seems to break the rule of thumb by a smart combination. For an accuracy level compared to typical balance accuracy however (and in order to ensure stability) the number of boundary conditions needs to be increased leading to high implementation effort. This problem can be solved by a more accurate vortex-lattice calculation. The development of such methods seems more within reach for the near future than the computational power for solving the Navier-Stokes equations with a DNS.

It is currently believed that the most promising method to break the rule of thumb in the near future is a well developed ESI-type application. When such applications are developed and expanded as discussed in section 8.4.1 they are very likely to provide solutions to the problem of support interference breaking the rule of thumb: high accuracy and a wide applicability depend on the number of available data sets (both experimental and numerical) that can be added to expand their data module and the growing expertise caused by expansion of their knowledge base. The implementation effort of using such models is very low (they classify as stage 1 applications). It is thought that the accuracy and range of applicability will increase asymptotically in time to typical balance accuracy and typical wind tunnel operational envelope when as much data and expertise is added to the application as possible. In the light of this viewpoint availability of new data and updating the applications are the key to breaking the rule of thumb.

8.5 Meeting the future needs?

Once again, consider the future needs towards the treatment of model support interference mentioned in section 1.3. These future needs aim at providing engineers with more alternatives in their dealings with support interference. A well developed expert system will provide guidance in these dealings in various stages of a typical measurement, on-line and off-line. Currently, the structure and typical elements of a very basic variant of such an expert system is considered in this thesis. This is a good initiative towards meeting the future needs: it is basically built on that requirement. It is believed that the future needs can be met when further development of the expert system is stimulated. Availability of new data and updating the applications is of utmost importance in this matter.

To the authors opinion, data availability can be expanded to exceed the companies thresholds and to span multiple companies and countries. An example of such an initiative is shown by the Garteur Action Group [15]. In this light, cooperation might very well be seen as the most important future need of all.

Chapter 9

Conclusions and Recommendations

9.1 Introduction

Future guidelines for the treatment of support interference aim at providing engineers more alternative approaches. Such alternatives however require an extensive knowledge on experiments and CFD. It requires the engineer to be an expert in the field, something that is often impossible. Engineers should therefore be provided with an expert system for guidance in their dealings with support interference. The application-based expert system discussed in this thesis answers to this need. It focuses on low-speed model support interference on single sting mounted models carrying an internal balance.

In this thesis the necessary components of such an expert system are identified through:

1. A study on the elements of its knowledge base (Part I of this thesis),
2. A study on a feasible structure of the system in terms of its applications or elements (Part II of this thesis).

Conclusions on both topics are discussed in the following sections. Finally, concluding remarks and future recommendations are given.

9.2 Conclusions from the study on model support interference

9.2.1 Systematic approach

A support break down facilitating the treatment of disturbances of individual support parts spanning a certain setup is a systematic method to analyze support interference. The order of magnitude and the nature of the disturbances are not compromised when this approach is adopted provided that the amount of separate parts is kept to a minimum. This approach enables the crucial study on the disturbances of the model sting that causes the complete spectrum of support disturbances. Advantages of studying the sting include the possibility to generalize the research results to a wider class of support structures, a qualitative analysis on the nature of near-field and far-field effects but also a qualitative and quantitative validation of several methods applied to determine support interference.

9.2.2 Sting interference flow field understanding

Comparing measurements (balance measurements and 5-hole probe measurements) to calculations (panel code- and Euler calculations) on model sting near-field and far-field effects shows that without knowing the specific details of a complex interference flow field, it is not justified (from the viewpoint of accuracy) to determine model sting near-field and far-field effects using methods at low levels of complexity and intrinsic accuracy. Significant calculation offsets (out of the bounds of experimental accuracy) are caused by the action of the balance cavity and slit, vorticity and viscosity. An in depth understanding of the limitations of these numerical methods (panel code, Euler) can only be developed when the interference flow field itself is understood both qualitatively and quantitatively. Navier-Stokes calculations are used for this purpose.

Navier-Stokes calculations are a useful aid in identifying the disturbances governing the near-field of the model sting. Calculations provide a qualitative image of the interference flow field that complies with measurements. The interference flow field is dominated by:

- The boundary layer relieving effect in front of the sting on the fuselage pressure distribution due to the slit separating the model sting and fuselage. This effect prevents flow separation in front of the sting and thereby prevents the formation of the well known horseshoe vortex found in classical juncture flow,
- The carry over of the sting pressure distribution onto the fuselage,
- The formation and growth of the slit vortex in the intersection area of sting and fuselage,
- The complex sting wake structure that is governed by local separation at the sting side, the slit vortex and sting base vortex shedding.

Quantitatively, the Navier-Stokes calculations are not able to determine the values of near-field interference with the right trends and within typical measurement (balance) accuracy.

Gained near-field flow knowledge is used for an assessment of numerical methods in determining model sting near-field effects qualitatively and quantitatively. The results for a sting placement in region R2b (for its definition, see Figure 9.1) are given in Table 9.1.

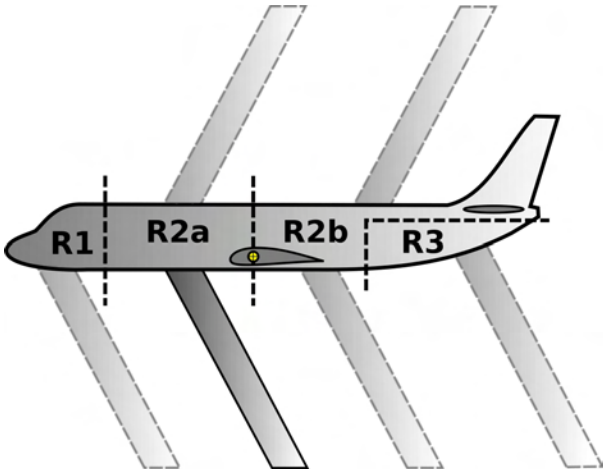

Figure 9.1: Four regions (R1, R2a, R2b and R3) of a typical wind tunnel model fuselage used for classification of the sting entry location. As a reference point, the mean aerodynamic center of the wing is defined as the separation between regions R2a and R2b. Typical ventral and dorsal sting setups are indicated

Table 9.1: The ability of various numerical methods to capture dominant near-field model sting disturbances: the adverse pressure gradient in front of the sting on the fuselage, the projected disturbances from the sting side, near-wake disturbances and the disturbances at the fuselage backbody (B.B.). This ability is expressed by means of + and − signs where −− indicates a very poor ability and ++ indicates a very high ability

	∇P	**Sting Side Dist.**	**Near-Wake Dist.**	**B.B. Dist.**
Panel code	−− [1]	−− [1]	−− [2]	−− [3]
Euler code	+ [4]	− [5]	+ [6]	+ [7]
N.S. code	− [8]	− [9]	− [8]	− [10]

[1] Pressure relieving effect is not included because cavity and slit are not modeled
[2] Unable to model proper wake structure (recirculation area is not resolved)
[3] Overestimated by poor wake definition
[4] No significant viscous phenomena dominate this region
[5] Wake strength is underestimated
[6] Trend is governed by artificial viscosity
[7] Disturbances overestimated by lack of wake closure
[8] Related to the inability of eddy viscosity closure models to resolve anisotropy
[9] Wake strength is overestimated
[10] Sting wake filling is too slow

9.2.3 Performance of numerical- and experimental methods in determining model sting disturbances

The results of Table 9.1 are generalized: the quantitative accuracy of various numerical and experimental methods in determining the near-field and far-field model sting effects on wind tunnel models at low speed is assessed for various sting placements. The results are given in Table 9.2 (refer to Figure 9.1 for a definition of sting placements).

Table 9.2: The accuracy of various numerical and experimental methods in determining near-field and far-field effects of a typical model sting on a model containing an internal balance for various sting placements. This accuracy is expressed by means of + and − signs where −− indicates a very poor accuracy and +++ indicates a very high accuracy

Sting pos.	Dist.	Panel c.	Euler c.	N.S. c.	Probe m.	Bal. Δ-m.
R1	near-field	−−	+	−		++
R1	far-field	−−	+	−	++	+++
R2a	near-field	−−	+	−		++
R2a	far-field	−−	+	−	++	+++
R2b	near-field	−−	+	−		++
R2b	far-field	−−	+	−	++	+++
R3	near-field	−−	−	+		++
R3	far-field	−−	−	+	++	+++

Above mentioned methods can also be classified according to the amount of effort they require for implementation. The results are given in Table 9.3.

Table 9.3: The desirability of implementing various numerical and experimental methods to determine the near-field and far-field effects of a typical model sting on a model containing an internal balance from the viewpoint of effort for various sting placements. This desirability is expressed by means of + and − signs where −− indicates a very low desirability and +++ indicates a very high desirability

Sting pos.	Dist.	Panel c.	Euler c.	N.S. c.	Probe m.	Bal. Δ-m.
All	near-field	+	++	−−		−
All	far-field	++	+++	−−	−	+

9.2.4 Extrapolation of results to connected support parts

The knowledge on the potential of experimental and numerical methods to determine model sting interference is generalized such as to cover the treatment of the remaining support for typical sting mounted setups. Generalizing what method is most desirable from the viewpoint of accuracy for determining the disturbances of such support structures is difficult and depends on the geometry because the geometry is indicative for the nature of the disturbance.

When the support structure consists of simple (referring to its geometrical definition), streamlined parts that do not show complex flow behavior (like extensive areas of separated flow), a comparable ranking and accuracy for the determination of far-field effects as given in Table 9.2 is maintained. For the numerical methods, this will hold for typically -10°$\leq\alpha,\beta\leq$10°. 5-hole probe measurements and balance Δ-measurements have operational boundaries outside this range (typically -25°$\leq\alpha,\beta\leq$25°).

For setups including complex geometry and non-streamlined parts (not considered in Tables 9.2 and 9.3) causing extensive areas of separated flow, the probe measurements and balance Δ-measurements provide the most accurate value of the far-field disturbances (the balance Δ-measurement giving the most accurate value). Considering the numerical techniques, a panel code does not provide a reliable answer because of the complexity in modeling the separated areas. The Navier-Stokes calculation should have the potential to calculate such flow behavior however for such complicated flows the modeling error caused by the choice of a turbulence model might become significant. It is expected that for this reason the Euler calculation does not perform much worse (or maybe even better) than a Navier-Stokes calculation.

Considering the numerical and experimental treatment of support disturbances (both near-field and far-field) of any support part it is concluded that classification parameters “accuracy” and “effort” (classifying the various methods for the determination of the interference) oppose each other: accurate methods demand a lot of implementation effort and vice versa.

9.2.5 Custom-made models for the determination of support interference

The opposition between accuracy and effort can not be solved by designing a custom-made model (that is both accurate and requires a low amount of implementation effort) for calculating model support interference. Such a model should calculate the disturbance effects fast (by incorporating only the disturbance factors of primary quantitative interest: this insight is gained by the sting interference research) with the right trends and magnitude. It should typically combine the computational advantages of a panel code calculation with the typical accuracy of a balance measurement. Typical confinements of such models are:

- Due to the lack of knowledge on the dependencies of the tuning variables (e.g. doublet strength simulating the sting-induced base-flow), the quality of the calculated corrections is not guaranteed,

- Qualitative interference changes (when α, β or the configuration is changed) result in erroneous results as the characteristics of the tuning variables change,
- Intervention of an engineer in the numerical part of the model is inevitable, a rather undesirable scenario.

Solving for these confinements implies an inevitable reduction in the applicability range of the model. Typical custom-made models are unsuitable for implementation in the expert system. They reveal the following rule of thumb:

"High accuracy (at a minimum equal to typical balance Δ-measurement accuracy) and low implementation effort (total measurement effort or modeling effort and computational effort) of a correction method for determining model support interference are currently incompatible when a wide range of applicability (freestream conditions, setups) is desired."

This rule of thumb necessitates a more elaborate definition of the expert system's requirements on speed and accuracy. This results in an expert system with an application-based structure. The applications with given accuracy and speed assist in four stages defining a typical commercial wind tunnel measurement as shown in Table 9.4:

Table 9.4: Requirements on speed and accuracy for the determination of wind tunnel (wall- and) support interference according to four stages defining a typical commercial wind tunnel measurement

Stage	Fast enough	Accurate enough
Stage 1	O(hours)	Trends and O(magnitude) agree
Stage 2	O(weeks/months)	Determined by client
Stage 3	O(seconds)	$\ll$ Accuracy of correction method
Stage 4*	Determined by client	$\ll$ Accuracy of correction method
Stage 4**	O(weeks/months)	Determined by client

* corr. determined
** corr. not determined

A feasible expert system is thus seen to provide applications satisfying the requirements on speed and accuracy given in Table 9.4.

9.3 A feasible application-based expert system structure

Having collected a considerable amount of intelligibility on model support interference and a more elaborate definition on requirements on speed and accuracy of expert system's elements, a closer look is taken at a feasible structure of the expert system. Such a structure is shown in Figure 9.2.

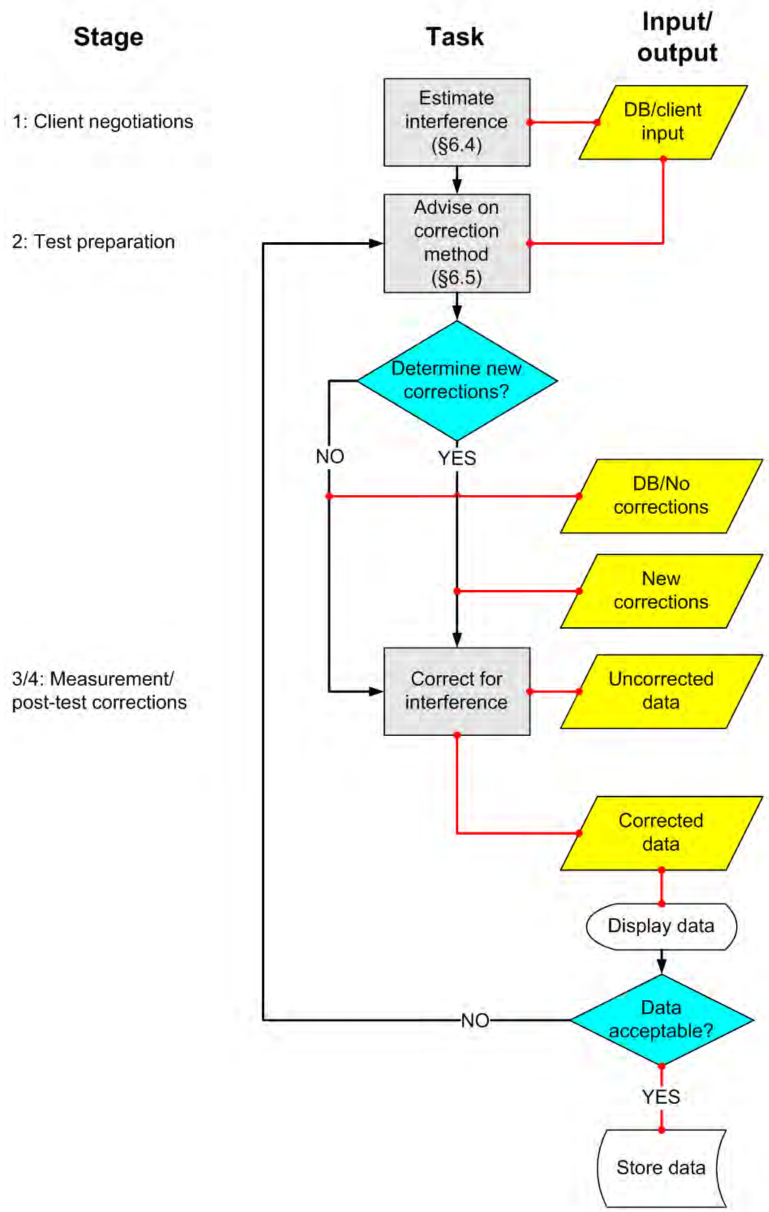

Figure 9.2: The proposed expert system's application-based structure

This expert system structure fulfills its main requirements as discussed in the following section.

9.3.1 Expert system requirements

The expert system for support interference should be able to perform the following tasks:

- Advise on the test setup: this is provided by typical modules such as the Evaluation of Support Interference (ESI, used during the client negotiations) module presented in this thesis (Chapter 6),
- Advise on correction methods: this is provided by typical modules such as the Advice on Support Interference Determination (ASID, used during the test preparation) module presented in this thesis (Chapter 6),
- Calculate the interference fast enough and accurate enough: by introducing stages defining a typical commercial wind tunnel measurement that are characterized by associated time- and accuracy scales (Table 9.4) and appointing various applications to these stages, these applications are by definition fast- and accurate enough for the intended purpose. Because accuracy is often determined by the client, the client's perception on the desirable balance between accuracy, effort and costs is of importance,
- Calculate the interference pre-test and on-line: pre-test determination is provided by typical modules as ESI. Implementation of the advice from typical ASID modules in a pre-test stadium is also seen as a pre-test determination of the interference. In addition to standard correction methods an additional hybrid pre-test calculation technique is demonstrated in this thesis (Chapter 7): VOLAER (VOrtex-LAttice/Euler). On-line and off-line determination of wall- and support interference is realized by introducing a hybrid method named MVL (Measurement/Vortex-Lattice also presented in Chapter 7):
  - VOLAER (a method combining both Vortex-Lattice and Euler calculations) can be used for a decent range of sting placements (R1, R2a, R2b) whereas it gives valuable information on both near-field disturbances and spatial far-field distributions,
  - MVL (a method combining both uncorrected wind tunnel measurements and Vortex-Lattice calculations) proves to be particularly valuable as it predicts the interference of wind tunnel walls, support and includes secondary interference (when e.g. the support is traversed close to the wind tunnel walls). The fact that only the wind tunnel model should be modeled in a vortex-lattice code makes it much more attractive than applying dedicated finite-volume solvers that require remodeling of the wind tunnel, support and model once the angle of attack and/or angle of sideslip are changed. MVL is suitable for all support setups in all types of wind tunnels provided a vortex-lattice method is used enabling an accurate representation of the model aerodynamic derivatives (preferably including the effects of viscosity). MVL's prediction capabilities necessitates the use of multiple boundary conditions (interference values) in order to guarantee a stable solution thereby categorizing it as an interpolation tool with the potential of decreasing the amount of necessary experimental balance Δ-measurements.

In such cases the introduction of a translational damping function (by means of a predictor-corrector formulation) is seen to provide the most accurate solutions when a wide range of interference patterns is considered. The gain in balance Δ-measurement reduction that can be achieved for an angle of attack polar or an angle of sideslip polar is likely to be different. The value of MVL is optimized when the amount of balance Δ-measurements for β-polars can also be reduced. This however necessitates a calculation of the aerodynamic derivatives taking the effect of the model fuselage and engine nacelles into account. This is left for future research.

- Correct for the interference on-line and off-line: the exact characteristics of the on-line and off-line correction processes depend on hardware and software characteristics of the company or institute employing an expert system. This subject is not further considered in this thesis,

- Allow easy plug-in of modules dealing with the problem of wall interference: considering the fact that wind tunnel wall interference can be expressed in the same characteristic variables as the problem of support interference its inclusion in the expert system is only apparent. Because the proposed expert system structure resembles an application frame holder, including additional modules for the treatment of wall interference is facilitated.

Additional requirements relate to the use of the system. These requirements must be met if the expert system is to be used by engineers that are not considered experts in the field of low-speed wind tunnel wall- and support interference:

- The expert system must be programmed in such a way as to meet computer platform standards: compatibility of the expert system (or basically of its expert applications) with a predefined platform must be guaranteed to ensure easy distribution amongst the users. To this end it would be safe to delegate the administration of the expert system to a software expert. This expert would carry the responsibility of including future expert applications, ensuring compatibility and monitoring the distribution of (updated) versions of the expert system amongst its users,

- The system must be user friendly with professional interfaces: the success of an expert system depends on the successive communication between system and user(s). This can be achieved by user friendly, professional interfaces. The expert applications that are currently developed obey to this requirement: ESI is setup with a user friendly, visual interface. This graphics-based program clarifies the user what input is necessary and what steps should be taken to arrive at the desired output. The output is structured in such a way as to provide ample information to both engineer and client. ASID contains a very high information density based on the research on model support interference presented in this thesis. This information is however structured and interpreted by asking the user only a few clear questions. MVL is an example of an expert system application that hardly needs user intervention and interface. All the expertise is in the methodology behind the program (the theory). User intervention is however required when the method is implemented in the data-acquisition system of the wind tunnel.

The proposed application-based structure of the expert system fulfills its requirements. These requirements can be seen as a minimum set of criteria. Typical necessary system elements are identified: the expanded knowledge base on model support interference has resulted in two basic expert applications (ESI and ASID, directly applicable for measurements in the LLF of DNW for which they are customized) and new methods (VOLAER and MVL) to approach the problem of wind tunnel wall- and support interference. These products are seen as basic elements of an expert system (generalizable to other wind tunnels). This does however not imply that the expert system design is complete and directly implementable. In order to launch a first version of the expert system, the engineers should become confident with the expert applications. On top of this, it is recommendable that methods as MVL are integrated in the data acquisition system of the wind tunnel of interest and tested thoroughly. Implementation of a first version will show the shortcomings of the applications by exposure to the typical user. Feedback of such information might then lead to improvement of the applications or the addition of new applications.

9.3.2 Future expert system development

Although a feasible structure and several applications of the expert system are provided in this thesis, a first version of a complete expert system would still be far from matured. There is plenty of room for future development. Expert system development is mainly stimulated by maintaining and expanding the knowledge base. This is possible through adding more data to the applications (experimental and/or numerical) and by developing more expert applications (for e.g. the treatment of wall interference):

- Gaining more expertise: expert system applications evolve when more experimental and/or numerical data is added to their data-modules. Statistics may point out new rules of thumb that are directly implementable and lead to the expansion of their knowledge base. Stimulated by frequent use, the application will therefore become more intelligent (or, more expert-like). This is only possible by maintaining and updating their knowledge base,

- Wall interference treatment: the disturbance parameters characterizing wall interference agree with those for support interference. This encourages the treatment of wall interference in a similar way. The modular framework of the expert system is suitable for this purpose.

9.4 Concluding remarks and recommendations

A question that arises is whether the rule of thumb stated in section 9.2.5 will ever be broken by methods that are implementable in the expert system. Although measurements or calculations are not very likely to break this rule of thumb for the near future (say within 10 to 15 years), smart combinations of the two might very well. Development of typical methods as MVL are a nice example of this. It is currently believed that the most promising method to break the rule of thumb in determining the value of model support interference is a well developed ESI module: high accuracy and a wide applicability depend on the number of available data sets (both experimental and numerical) that are added to its data module and the growing expertise caused by expansion of the knowledge base. The implementation effort of using such models is very low as it classifies as a stage 1 (client negotiations) application. It is thought that the accuracy and range of applicability will increase asymptotically in time to typical balance accuracy and typical wind tunnel operational envelope respectively when as much data and expertise is added to the module as possible.

Currently, a very basic variant of an expert system is presented in this thesis and its necessary elements are identified. This is seen as a good initiative towards meeting the future needs. It is believed that the future needs can be met when further development of this expert system is stimulated. Increasing data availability and updating the applications is of utmost importance in this matter. To the authors opinion, the data availability can be expanded to exceed the companies thresholds and to span multiple companies and countries. In this light, cooperation might very well be seen as the most important future need of all.

Appendix A

Primary Support Disturbances

A.1 Introduction

In this Appendix the author illustrates the determination of typical primary support disturbances experimentally. For this purpose, results of low-speed (free-stream Mach number of approximately $M_\infty \approx 0.20$) wind tunnel measurements on a typical four-engine turboprop aircraft in the Large Low-Speed Facility (LLF) of the German-Dutch Wind Tunnels (DNW) are used. The nature and order of magnitude of such disturbances are discussed.

A.2 A break-down of primary corrections

According to Eckert et al. [37] an elegant method for determining the primary disturbances proposes a division of the support correction into four distinctive parts:

1. A support correction for the wind tunnel model fuselage and wing, no tail (vertical tailplane and horizontal tailplane) installed, at a certain angle of attack α and zero sideslip β. This correction forms the base of the support corrections (and is from now on referred to as the *base correction*),

2. An additional correction for this configuration is carried out when the model is put at angles of sideslip (and is from now on referred to as the *basic sideslip correction*),

3. When a tail is installed on the model, a tail installation correction is added to the base support correction ($\beta = 0$ [deg]),

4. If the model with tail is at a sideslip angle, a third addition is necessary to include the sideslip disturbances at the tail.

This method is elegant because like the model during a wind tunnel test, the corrections are made modular thereby enabling their use for tests of aircraft of the same family (with a high test- and setup comparability). Although the way of attaining the various correction terms presented above varies from one support interference correction method to another (both experimental and numerical techniques can be applied), this method gives the structure of the primary support interference correction for a model at certain angle of attack and sideslip.

A.3 Determining primary disturbances

The various contributions can for instance be attained by performing Δ-measurements for all configurations under consideration (tail on/off, different wing configurations, varying Mach numbers, angles of attack, sideslip etc.). Results of measurements with various support configurations are combined to lead to the corrections of force- and moment-coefficients for the support setup of interest. Examples of such setups are given in Figure 1.5 and A.1. Figure A.1 illustrates a dummy measurement setup and a dorsal setup of a typical four-engine turboprop aircraft. The ventral and dorsal support structures contain a model sting protruding the model, attached to a horizontal sting. The horizontal sting is attached at the back to a nacelle-like structure called the torpedo. The torpedo connects to the sword, a part that penetrates the tunnel floor.

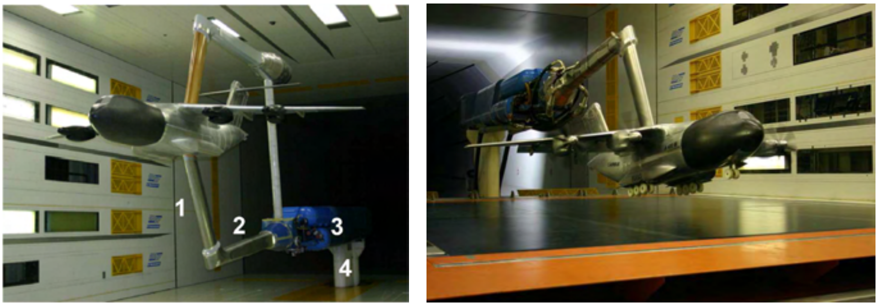

(a) (b)

Figure A.1: Setup of a low-speed measurement on a typical four-engine turboprop aircraft in the LLF of DNW showing (a) The dummy dorsal setup. The model is supported by a ventral support (penetrating the model belly) while a dummy dorsal setup (penetrating the model back) is installed. The numbers in the figure correspond to the model sting (1), the horizontal sting (2) the torpedo (3) and the sword (4) (b) A dorsal setup (courtesy of DNW)

Values of primary support disturbances can be determined for all force- and moment-coefficients in the complete domain (α,β) for all measured configurations. Rearranging these results leads to the division of primary interference into one of four above mentioned categories. Examples of primary support disturbances on the lift- and drag-coefficient C_L and C_D for both ventral and dorsal setups of the test shown in Figure A.1 as a function of angle of attack and flap setting of the wing are given in Figure A.2. The configuration considered is without tail at zero angle of sideslip (and therefore classifies as the “base correction”). The corrections for tail installation and sideslip measurements (deduced from e.g. Δ-measurements) are added to this base correction according to the modular approach.

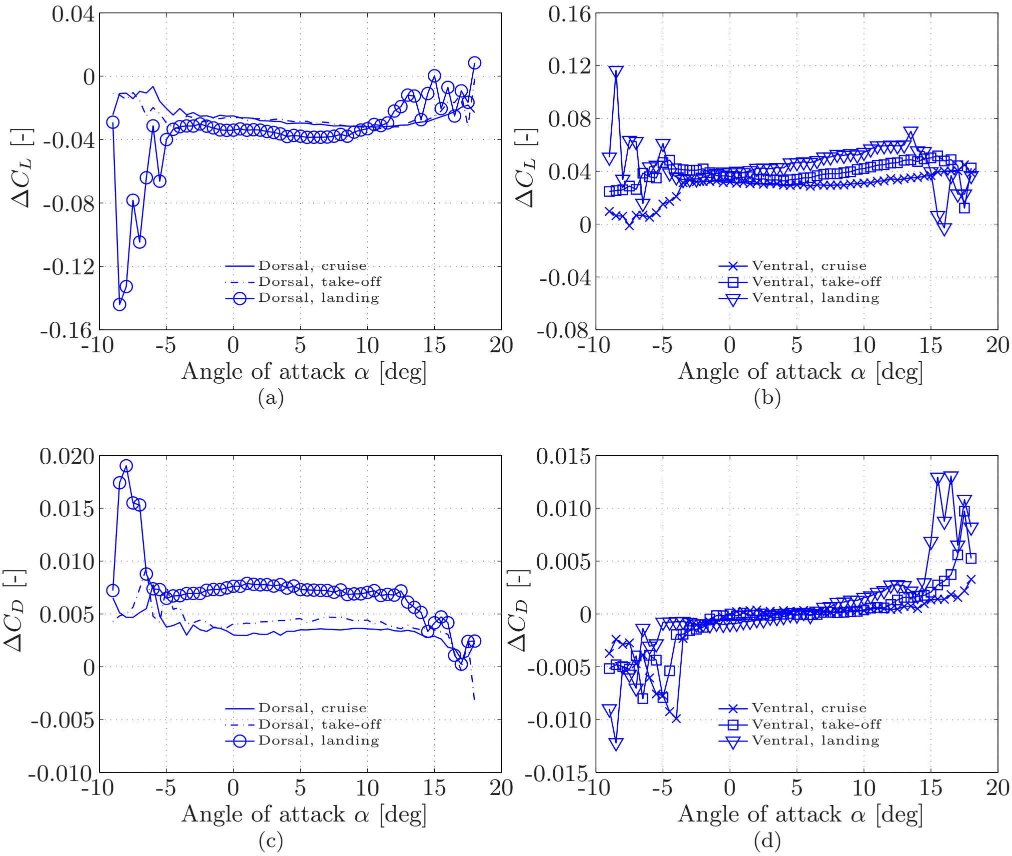

Figure A.2: Primary dorsal and ventral model support disturbances on the lift-coefficient (a,b) and drag-coefficient (c,d) of a low-speed measurement of a typical four-engine turboprop aircraft in the LLF of DNW (excluding the tail) at zero angle of sideslip. The effects of flap settings on the support disturbances are illustrated

As can be seen in Figure A.2, the effects of the dorsal and ventral sting setup are of opposite sign, which is logical considering the position of the support parts with respect to the model. Outside the angle of attack range $-4 \leq \alpha \leq 14$ [deg] the results show spurious behavior caused by flow separation at the wings of the aircraft. Considering this range it is apparent that the wing's configuration has an influence on the support interference. The larger the flap deflection, the larger the support interference. This is caused by two reasons:

1. At higher flap settings, the values of lift and drag of the aircraft configuration increase (considering a fixed value of the angle of attack). Because the support

disturbance manifests in changes in dynamic pressure at the lifting surfaces, a measure for (part of) the wing averaged (subscript w) far-field effects becomes $\overline{\Delta C_L} = \overline{\frac{\Delta q_w}{q_\infty}} \cdot \overline{C_L}$ and $\overline{\Delta C_D} = \overline{\frac{\Delta q_w}{q_\infty}} \cdot \overline{C_D}$. An increased value of lift and drag due to the flap setting is thus translated into a higher value of the support disturbance although it can be assumed that the disturbance ability of the support has not changed (it is assumed that Δq remains constant),

2. The support disturbance ability changes when the wake of the wing interferes with the support. When this happens (this scenario is likely to occur at high flap settings), this will lead to a change in interference magnitude.

A.4 Analyzing the base correction

The values of the "base correction" are of particular interest because unlike the values of the modular additions, they can be subjected to a more elaborate analysis of the nature of the interference. This is achieved by introducing an analytical model representing the base disturbance effects according to Eckert [18]. In this model the base corrections are converted to values referred to as "disturbance parameters" (Figure A.3):

- $\Delta\alpha_w$: the angle of attack disturbance at the wing three-quarter chord position (a far-field effect). This value is a wing spanwise averaged value and is caused by a combined effect of streamline curvature and lift interference,
- $\Delta q_w/q_\infty$: the disturbance of dynamic pressure at the wing quarter chord position (a far-field effect). This value is also a wing spanwise averaged value. The disturbance is caused by solid blockage and wake blockage of the support,
- C_{NT}: a disturbance in model normal direction that embodies viscous near-field effects on the fuselage,
- C_{TT}: a disturbance in model tangential direction that embodies a combination of the support buoyancy at the model and tangential viscous near-field effects. Both the concentrated loads C_{NT} and C_{TT} act at unknown distances X_T and Z_T from the model aerodynamic center.

Using these parameters, the support disturbances on the aerodynamic longitudinal coefficients are calculated as follows:

$$\begin{aligned}
\Delta C_L &= \left(\frac{\partial C_L}{\partial \alpha} + C_D\right)\Delta\alpha_w + C_L\frac{\Delta q_w}{q_\infty} + C_{NT}\cos\alpha - C_{TT}\sin\alpha, \\
\Delta C_D &= \left(\frac{\partial C_D}{\partial \alpha} - C_L\right)\Delta\alpha_w + C_D\frac{\Delta q_w}{q_\infty} + C_{NT}\sin\alpha + C_{TT}\cos\alpha, \\
\Delta C_m &= \frac{\partial C_m}{\partial \alpha}\Delta\alpha_w + C_m\frac{\Delta q_w}{q_\infty} - \frac{X_T}{\bar{c}}C_{NT} + \frac{Z_T}{\bar{c}}C_{TT}.
\end{aligned} \tag{A.1}$$

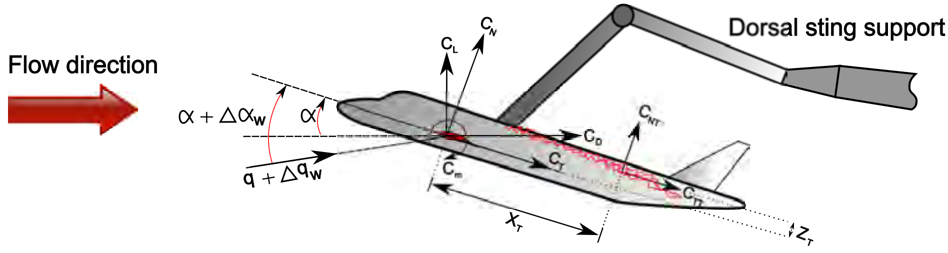

Figure A.3: A schematic of the analytical model used by DNW to analyze the base support corrections of aircraft configurations according to Eckert [18]

As input for the equations in Equation set (A.1), values resulting from the Δ-measurements on the base configuration are used. This set of equations is then solved for the disturbance parameters at every angle of attack. It is seen that the system is underdetermined: three equations involving 6 unknowns ($\Delta\alpha_w$, $\frac{\Delta q_w}{q_\infty}$, C_{NT}, C_{TT}, $\frac{X_T}{\bar{c}}$,$\frac{Z_T}{\bar{c}}$) have to be solved. To evaluate the unknowns, multiple sets of linearly independent corrections are used (correction sets for different wing configurations by varying the flap settings) and the resulting overdetermined system of equations is solved with a least-squares method. This leads to the values of the disturbance parameters as a function of angle of attack independent of the flap configuration. An advantage of this method is that the system matrix of the analytical model is robust thereby providing a non-singular, stable least-squares solution. Flow unsteadiness and measurement inaccuracy lead to a certain data scatter that is smoothed by applying quadratic or cubic polynomials to the results. This decomposition is performed for the disturbances illustrated in Figure A.2. Results are given in Figure A.4.

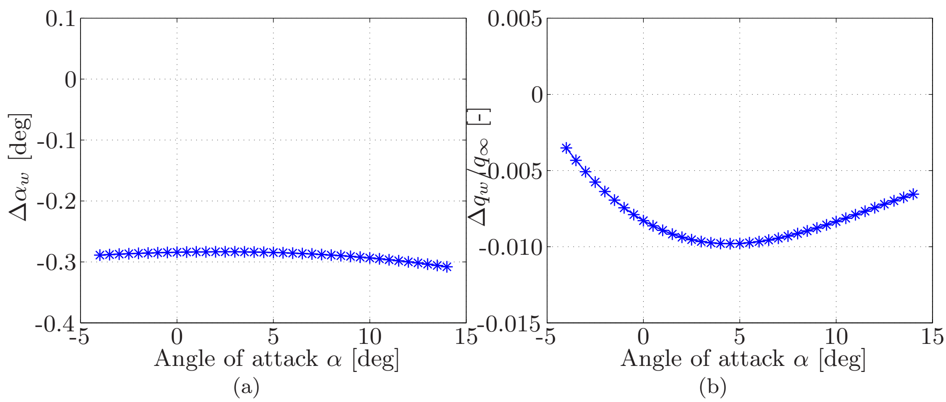

Figure A.4: The base support correction of a low-speed measurement of a typical four-engine turboprop aircraft in the LLF of DNW decomposed in (a) $\Delta\alpha_w$ (b) $\frac{\Delta q_w}{q_\infty}$. The results shown are cubic fits for the dorsal configuration

The results are splined using cubic functions. The values of these disturbance parameters can be stored as polynomials depending on angle of attack and e.g. distance from the tunnel floor. They are used to form corrections on the longitudinal coefficients of the base configuration (aircraft fuselage plus wing). Using these disturbance parameters, corrections can be carried out in multiple ways. When for instance an angle of attack polar is measured, it can be corrected right away by applying corrections to the angle of attack and dynamic pressure as follows:

$$\begin{aligned} \alpha &= \alpha + \Delta\alpha_w, \\ q_\infty &= q_\infty \left(1 + \frac{\Delta q_w}{q_\infty}\right). \end{aligned} \tag{A.2}$$

As shown in Equation set (A.2), the model is rotated and the coefficients are non-dimensionalized using the corrected value of the undisturbed dynamic pressure. An alternative way of performing the base correction is by calculating the left-side terms of Equation set (A.1) on-line. Along with the measurement of aerodynamic coefficients this requires an on-line polar slope analysis according to Eckert [18]. The values of the disturbances are then used in order to correct the aerodynamic coefficients.

On top of this base-correction, the modular corrections for tail installation and sideslip effects (extracted from e.g. Δ-measurements) are added. In that way all the force-and moment-coefficients are corrected for primary support interference.

The disturbance parameters representing the primary disturbances can also be found by performing Δ-measurements with a probe (according to Eckert [18]). This necessitates two measurements: one measurement includes the presence of the support and the other measurement excludes the support structure. In both measurements, the model is not included or only the fuselage of the model is present and supported by an additional support. The support under study can then be seen as a dummy support that can be removed. The probe is positioned in the wind tunnel with the tip at the location of interest (e.g. at various spanwise locations that discretize the wing's quarter- and three-quarter chord positions). Subtracting the values of the local angle of attack, local angle of sideslip and local dynamic pressure of the measurement excluding the support from the measurement including the support leads to the value of the disturbance parameters at given model- and flow conditions. Numerical techniques can also be applied: Δ-calculations also lead to the determination of the disturbance parameters.

A.5 Efficient use of the support corrections

The advantage of a break down of disturbance effects in the previously mentioned four categories and the analysis of the base correction are clear: it facilitates a modular approach towards support interference. The separate contributions that span the final value of support interference can be studied in order to better understand the phenomena. Besides this, support correction extrapolation to new configurations is simplified. When the values of the disturbances are stored in a data-base, aircraft configurations of the same family can be corrected using existing corrections. When a test is performed on an aircraft of the same family but with for instance an extended wing, and the support structure (including the position of the support structure relative to the aerodynamic center of the wing) is not changed, the values of the disturbance parameters $\Delta\alpha_w$ and $\frac{\Delta q_w}{q_\infty}$ can be used to correct for this new test. When a new sting mounted model is tested with a fuselage extension, the disturbance parameters are also interchangeable when the values of X_T and C_{TT} are recalculated. The latter is increased when the buoyancy increases because the back part of the model moves closer to the support structure. According to Eckert [18] this increase can be defined by measurements of the support pressure field but also by numerical calculations that model the support structure.

Appendix B

Secondary Support Disturbances

B.1 Introduction

In this Appendix the author demonstrates the experimental and numerical determination of a typical secondary support disturbance: the engine power effect. This effect is being drawn more and more into the center of attention: renewed interest in propeller propulsion on aircraft configurations combined with higher propeller loads lead to the question how the effects of the propulsion on model support disturbances should be accounted for.

The order of magnitude and characteristics of engine power effects caused by co-rotating propellers are demonstrated in the following sections. This is done by analyzing experimental data provided by DNW (concerning measurements on a typical four-engine turboprop aircraft as shown in Figure A.1) and by analyzing numerical results on a more generic model in order to clarify a possible mechanism behind engine power effects on support interference. Results show that engine power effects caused by co-rotating propellers can become substantial and necessitate a correction. The induced angle of sideslip caused by the propeller slipstream affects both the near-field and far-field effects of the model sting.

It is concluded that in future experiments care should be taken in the setup of wind tunnel tests involving model engines. The magnitude of engine power effects on support interference can be decreased by:

1. Ensuring that the engine slipstream maintains a maximum distance from the model support parts,

2. Minimize the sensitivity of the near-field and far-field disturbances to engine power effects by choosing an appropriate placement of the support parts with respect to the wind tunnel model. This is realized by choosing a placement of the sting that is removed as far from the wing as possible while still attached to the cylindrical (constant cross-sectional) part of the fuselage.

The author believes that for contra-rotating propellers the engine power effects might be insignificant. Further research should shine more light on this.

B.2 Engine power effects on support interference

When a wind tunnel model is equipped with one or more engines (propeller or jet), the aerodynamic characteristics of the model will change. The measured lift of the aircraft will increase due to locally higher dynamic pressures. Not only lift-, but also drag- and pitching moment-coefficients (think of the effect of the engine slipstream over the stabilizer) show a strong dependency on engine thrust setting. The adapted streamline pattern around the model configuration (caused by the interference of the slipstream) will also affect the aerodynamic characteristics. Besides the fact that the model aerodynamics is directly affected by the engine slipstream, the engines also affect the flow around the model support parts. When using external balances, these effects can be directly measured. This is not the case for internal balances: when the flow around the support changes, the interference of the support on the model also changes. This effect is defined as an engine power effect on the support disturbance. The effect of the engine slipstream on the support corrections is translated into a change of interference from the support onto the wind tunnel model.

B.3 Measuring engine power effects

In this section the determination of engine power effects is illustrated using results of low-speed (freestream Mach number $M_\infty \approx 0.20$) wind tunnel measurements on a typical sting-mounted four-engine turboprop aircraft in the Large Low-Speed Facility (LLF) of the German-Dutch Wind Tunnels (DNW) accommodating an internal balance (shown in Figure A.1).

The key to successively measuring engine power effects is to perform two Δ-measurement campaigns, one campaign at "power-on" (engines running) and the other campaign at "power-off" (engines not running) conditions. For both campaigns the Δ-measurements are used in order to calculate the support interference. The difference between the power-on and power-off support corrections indicates the magnitude of engine power effects on support interference. In the following sections the engine power effects on the "base" correction and the "basic sideslip" correction (discussed in Appendix A) are considered.

B.3.1 Engine power effects on the base correction

For both power-on and power-off conditions Δ-measurements are carried out on the configuration consisting of a fuselage and wing, no tail installed, at a certain angle of attack α and zero sideslip β.

Consider the power-off case first. Performing linear operations on the measurement data (by subtraction of the measurement results) leads to the values of the total support disturbance on the lift-, drag- and pitching moment-coefficients. These disturbances are converted to values of the disturbance parameters $\Delta\alpha_w$, $\Delta q_w/q_\infty$, C_{NT} and C_{TT} according to Eckert [18]. Converting the disturbances from the power-off Δ-measurement campaign to the values of the disturbance parameters is straightforward.

Problems do arise however when this same exercise is carried out for the power-on case. A difficulty with this approach is the successive subtraction of the various measurements before arriving at the disturbances on the longitudinal coefficients. Because the measurements of various configurations are performed with slightly alternating thrust levels of the engines, the aerodynamic coefficients can not be subtracted. This is caused by the high dependency of the coefficients on the thrust level of the engines. This implies that when longitudinal coefficients from two measurements are subtracted, the coefficients will have to be adjusted such that the thrust level of the measurements is equal. It could be decided to make all the measurements "thrust free", meaning that all the longitudinal coefficients are reduced to a thrust level of zero. This however would imply large corrections (in the order of the value of the measured coefficients) especially at large negative and positive angles of attack. Because during this campaign results of a dorsal- and ventral measurement are subtracted from the results of a dummy measurement setup to arrive at the ventral and dorsal support corrections respectively, it is chosen to keep the dummy measurement setup as a reference. This implies that the longitudinal coefficients of the dorsal- and ventral measurements are corrected to the thrust level of the dummy measurement setup at every angle of attack. This "thrust correction" can be performed in two different ways:

1. Using a semi-theoretically, semi-empirically determined value of $\frac{\mathrm{d}C_i}{\mathrm{d}C_T}$ where C_T is the configuration thrust-coefficient. The theory according to Eckert et al. [37] is based on the principles of super-velocity caused by a propeller in front of a wing. It is assumed that the lift of the wing is built up of a clean, no thrust value of the lift (that is representative for the actual circulation of the wing that is used to correct for the lift interference in the wall corrections) and an additional lift term that is caused by super-velocity. The corrections on the drag- and the pitching moment-coefficients are based on this super-lift as well. Corrections to the reference thrust level (C_{T_B}) are carried out as follows:

$$
\begin{aligned}
C_{L,C_{T_B}} &= C_{L,C_T}\frac{F\left(C_{T_B}\right)}{F\left(C_T\right)},\\
C_{D,C_{T_B}} &= C_{D,C_T}+\frac{C_{L,C_T}^2}{\pi\Lambda}\left(\left(\frac{F\left(C_{T_B}\right)}{F\left(C_T\right)}\right)^2-1\right),\\
C_{M,C_{T_B}} &= \left(C_{M,C_T}-C_{M,C_{T_0}}\right)\frac{F\left(C_{T_B}\right)-1}{F\left(C_T\right)-1}+C_{M,C_{T_0}},\\
F\left(C_T\right) &= 1+k\frac{D_p}{b}\sum_{i=1}^{n}\frac{c_i}{\bar{c}}\left(\sqrt{\frac{\sqrt{1+C_{T_i}}+1}{2\sqrt{1+C_{T_i}}}}\right)C_{T_i}.
\end{aligned}
\tag{B.1}
$$

In Equation set (B.1), Λ stands for the aspect ratio of the wing, k is a shape factor to compensate the formulas for the absence of the modeling of propeller swirl effects changing the local angle of attack at the wing and a nacelle volume underneath the wing, D_p is the propeller diameter, b is the wing span, $\overline{c}$ the mean aerodynamic chord and c_i the local chord at the wing part wetted by the slipstream of propeller i. For the correction of the drag-coefficient it is assumed that the viscous component of drag does not need a thrust correction and that correction of the induced drag will cover the most significant part. The constants appearing in the formulas are determined using experimental data,

2. Using experimental data to construct various cross plots in order to determine the value of $\frac{\mathrm{d}C_i}{\mathrm{d}C_T}$. Because two power settings are measured in the campaign under consideration (a low and a moderate power setting), a linear relation could be deduced.

Both methods are applied and compared by the author. Future measurements with more than two power settings might clarify whether or not the value of $\frac{\mathrm{d}C_i}{\mathrm{d}C_T}$ can indeed be considered linear. This indicates one of the great disadvantages of the second method: because standard interpolation techniques are used, two or more power settings have to be measured. Thrust corrections of both above mentioned methods are applied to the dorsal and ventral measurements (with respect to the dummy measurement base with a moderate power setting). The thrust corrections can be compared for various flap settings (cruise, take-off and landing). This comparison is visualized for the ventral setup in Figure B.1.

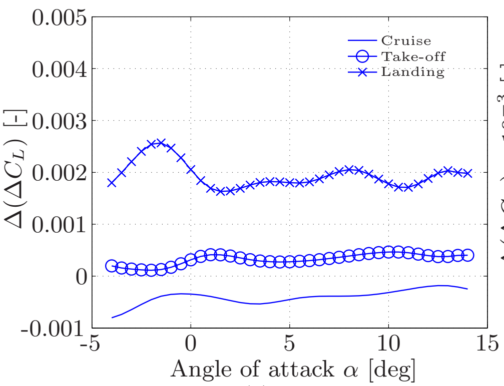

(a)

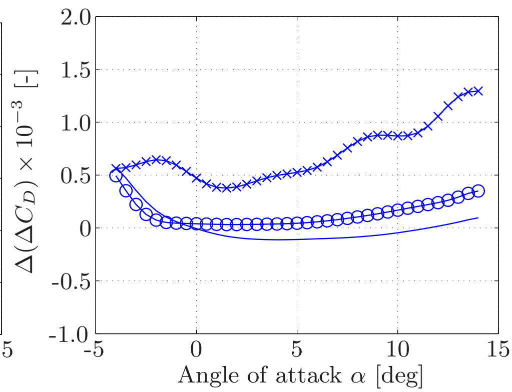

(b)

Figure B.1: Differences in thrust corrections on the longitudinal coefficients between the method proposed by Eckert et al. [37] and a linear correction method for the (a) Lift-coefficient (b) Drag-coefficient of a typical four-engine turboprop low-speed power-on test in the LLF of DNW at moderate power setting

In Figure B.1 it is seen that both methods provide thrust corrections of similar order of magnitude on the longitudinal coefficients except for the cases where the flaps are deflected at high values (landing configuration). Reasons for this might be that at these flap settings, a linear correction of the coefficients is not sufficiently accurate. Besides this, errors might be introduced using the shape factor k at high flap settings: this parameter is assigned a mean value for all flap settings to compensate for the absence of the modeling of propeller swirl effects changing the local angle of attack at the wing and a nacelle volume underneath the wing. Such effects however might be seriously affected when flaps are given large deflections. Mean values of the shape factor might therefore introduce significant errors in such cases.

When the corrections proposed by Equation set (B.1) are applied to the dorsal and ventral measurements, leveling these to the same thrust setting as the dummy measurements, linear operations are carried out on the measurements to arrive at the support corrections. These corrections are converted to the values of the disturbance parameters as given by Eckert [18]. The values of these parameters can be compared to the values of a power-off test. This leads to the order of magnitude and nature of the engine power effects on support interference. These effects are seen in Figure B.2 for the ventral setup with a moderate power setting.

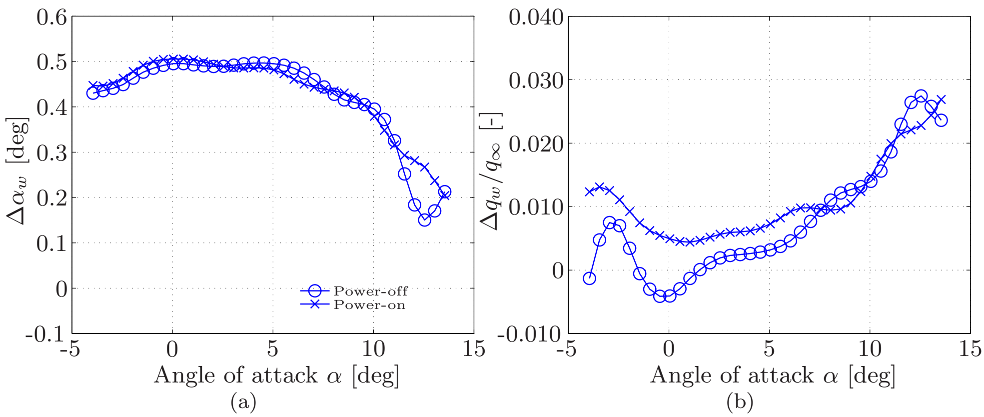

Figure B.2: Engine power effects on the values of (a) $\Delta\alpha_w$ (b) $\frac{\Delta q_w}{q_\infty}$ for the ventral setup of a low-speed measurement on a typical four-engine turboprop aircraft with a moderate power setting in the LLF of DNW

As can be seen in Figure B.2 a change in disturbance ability of the model support due to the slipstream of the propellers can become significant. The difference between the power-on and power-off disturbance parameters indicates the order of magnitude of the effect. It is seen that the trends of the support interference with angle of attack do not change. These effects are not negligible. This becomes apparent when they are compared to the requirements on data resolution mentioned by Steinle et al. [7]: in Figure B.2(a) for instance, the effect is approximately a factor 10 times the target proposed by Steinle.

B.3.2 Engine power effects on the basic sideslip correction

The magnitude of engine power effects on the basic sideslip correction is calculated by comparing the values of the corrections on the aerodynamic force- and moment coefficients between power-on and power-off conditions. For the power-on condition prior to subtraction of the measurement results of the various support setups, the results of the ventral and dorsal measurements have to be corrected to the same power setting as the dummy measurement. Typical results of engine power effects on the lift- and drag correction of a ventral setup with a take-off flap setting at a moderate thrust level are shown in Figure B.3.

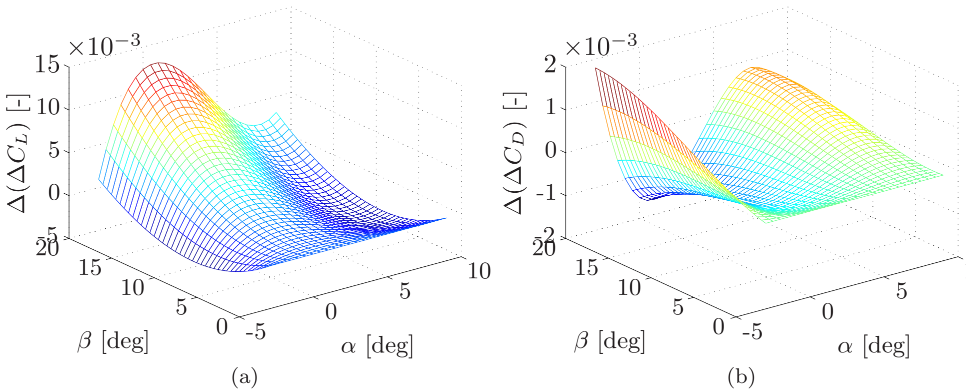

Figure B.3: Engine power effects on the basic sideslip correction. Effects on the values of the (a) Lift correction and (b) Drag correction for the ventral setup of a low-speed measurement on a typical four-engine turboprop aircraft in the LLF of DNW with a take-off flap setting at a moderate thrust level. The surfaces shown are least-square fits of the experimental results

When compared to the values of the power-off basic sideslip correction, it seems that both power-off correction and engine power effect are of the same order of magnitude. Keeping in mind the requirements on data resolution according to Table 1.1, these power effects are worth including in the correction process.

Besides being able to determine the values of engine power effects on support interference experimentally, understanding the possible mechanism that leads to these effects is of crucial importance for avoiding future situations where high undesirable power effects arise. To this purpose, CFD calculations are performed. The setup of these calculations and implementation of their results is discussed in the next section.

B.4 CFD calculations on engine power effects

Referring to Figure A.1 it is seen that from all the support parts the engine slipstream is likely to influence the model sting (support part number 1 in Figure A.1(a)) the most as it is located in the propeller slipstream's near-field. The remaining support parts are located in the far-field. Besides this, a small change in disturbance ability of the model sting will have a larger effect on the aircraft aerodynamics than caused by the other parts because the distance between the model sting and the aircraft surrounding flow field is much smaller (essentially, the model sting is located in the near-field of the aircraft and thus vice versa): according to Anderson [80] the strength of a small change in disturbance potential decreases from the source by $1/r$ where r is the distance from the source. The derived induced radial disturbance velocity component decreases proportional to $1/r^2$. This leads to the conclusion that the main characteristics of engine power effects will most probably be found when studying the model sting. For CFD purposes this implies that not the complete support structure should be modeled reducing the amount of computational expenses considerably.

B.4.1 Calculation setup

In order to assess engine power effects at one freestream condition (one angle of attack, angle of sideslip, Mach number) and at one configuration setting (for instance one engine power setting and flap setting), four calculations are performed with the commercial code $Fluent^{TM}$ [71] on a typical propeller powered aircraft configuration. These calculations are:

1. A calculation modeling: the wind tunnel, aircraft fuselage and wing, rotating propellers and model sting,
2. A calculation modeling: the wind tunnel, aircraft fuselage, wing and rotating propellers,
3. A calculation modeling: the wind tunnel, aircraft fuselage, wing and model sting,
4. A calculation modeling: the wind tunnel, aircraft fuselage and wing.

After every calculation, the forces and moments on the aircraft configuration are determined. Subtracting the results of the second from the first calculation leads to the support interference effects in power-on conditions. Subtracting the results of the fourth from the third calculation leads to the support interference effects in power-off conditions. Finally subtracting the power-off from the power-on interference effects leads to the values of the engine power effects on support interference.

The computational domain of the calculations performed is based on wind tunnel tests on model support interference presented by Horsten et al. [11]. The bounds of the computational domain coincide with the test section walls where inlet and outlet planes are extended upstream and downstream respectively such as to guarantee the integrity of the inlet and outflow boundary conditions. A picture of the considered aircraft configuration including model sting and propellers is given in Figure B.4. The aircraft fuselage and sting as the position of the sting with respect to the fuselage are the same as presented in Horsten et al. [11].

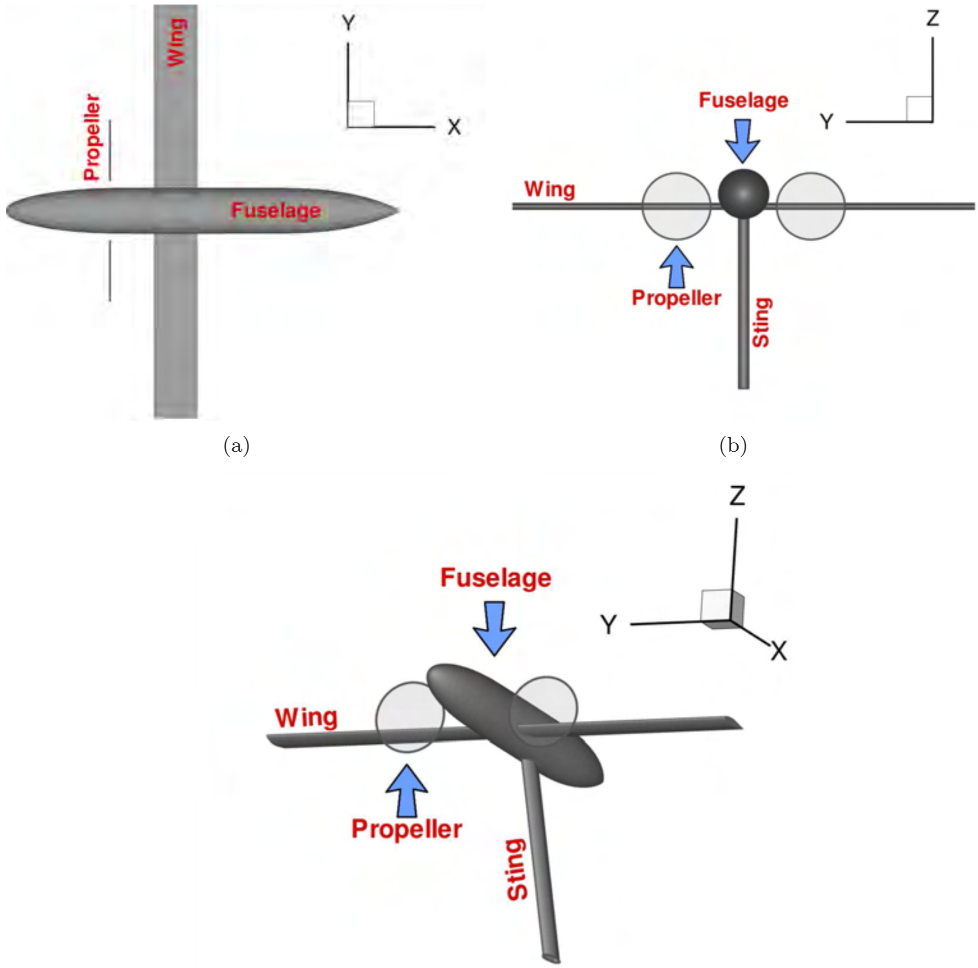

Figure B.4: A graphical representation of the aircraft configuration used to calculate engine power effects on support interference (a) Top view (b) Front view (c) 3D view

Unlike the experiment according to Horsten et al. [11], the model sting is attached to the fuselage instead of inserted into the fuselage. Internal balance cavity and slit separating the model sting and fuselage are not modeled. When the near-field effect of the model sting is studied, this would be sensible as indicated by Horsten et al. [11]. It is expected however that modeling the slit and internal cavity have no distinct influence on the *change* of disturbance ability due to the engine slipstream. The wing that is modeled is a straight wing without taper, sweep and dihedral with a NACA $64_2\,(A)\,015$ profile. Modeling of the wing is necessary because the wing has a distinct influence on the slipstream properties of the engines according to Veldhuis [84]. A deformed slipstream is likely to induce a different value of change in disturbance ability at the model sting. Two co-rotating propellers are modeled in front of the wing. Their dimensions, placement and thrust properties are typical for modern turboprop aircraft. Geometrical characteristics of the setup are given in Table B.1.

Table B.1: Geometrical properties of the setup for calculating engine power effects on support interference

Parameter	**Value**
Test section dimensions [W x H]	1.80 x 1.25 [m]
Fuselage length	1.35 [m]
Fuselage maximum thickness	0.16 [m]
Wing span	1.45 [m]
Wing mean aerodynamic chord	0.15 [m]
Wing taper ratio	1.0
Wing sweep	0.0 [deg]
Wing dihedral	0.0 [deg]
Sting chord	0.091 [m]
Propeller diameter	0.21 [m]

Besides the configuration shown in Figure B.4, another configuration is generated excluding the model sting. Because the propeller planes are modeled as actuator discs, changing the boundary conditions of these discs leads to the distinction between a power-on and a power-off case. This leads to four distinct cases mentioned earlier in this section to calculate engine power effects on support interference.

It is thought by the author that solving for the unsteady Euler equations will provide sufficient information on engine power effects. For the configuration under study the viscous disturbances caused by the model sting are not thought to be affected by the engine slipstream. To this end, inviscid meshes (no boundary layers are discretized) are generated by the commercial code $Hexpress^{TM}$ [69] consisting of triangular cells. Errors are introduced in performing Δ-calculations using different grids. Grid refinement however leads to no significant change in results. The unsteady Euler equations are solved on these meshes using a second order discretization. The settings characterizing the flow properties and propeller action are given in Table B.2.

Table B.2: Settings characterizing the flow properties and propeller action for determining engine power effects on support interference

Parameter	**Value**
Medium characterization	Incompressible ideal gas
Angle of attack α_∞	0 [deg]
Angle of sideslip β_∞	0 [deg]
Mach number M_∞	0.147
Thrust-coefficient C_T	0.29
Advance ratio J	0.94

As seen in Table B.2 it is chosen to select a high power setting in order to create a "worst case scenario". Creating a worst case scenario is also the reason that two co-rotating propellers are simulated instead of contra-rotating propellers (as would be the case for a typical configuration shown in Figure A.1). The latter is explained at the end of the next section. The thrust of the propeller discs is realized by prescribing a pressure jump over the actuator discs. The propeller swirl is prescribed such as to vary over the actuator disc from the hub to the tip with $\frac{1}{r}$ where r is the local radius of the disc having a value of 0 at the hub. The strength of the swirl is calculated according to the swirl model proposed in [68].

Unsteady calculations are performed to improve the rate of iterative convergence. The converged solutions are used to analyze the magnitude and nature of the engine power effects. The results are presented in the next sections.

B.4.2 Calculation results

Δ-calculations on the lift-, drag- and side force-coefficients of the fuselage at power-on and power-off conditions results in the support near-field disturbances. Subtracting these values leads to the value of the power effects on near-field support interference. It is found that the engine power effects on the values of the near-field lift-, drag- and side force interference are negligible for the current configuration (a generalization to more configurations is performed at the end of this section). The power effects are an order of magnitude smaller than typical balance accuracy (Table 1.2: the desirable accuracy for the side force is comparable to the lift). The same exercise is performed for lift- and drag-coefficients of the wings indicating the power effects on the far-field support interference. Once again it is found that the order of magnitude is negligible.

Because the power effects on the near-field and far-field support disturbances are net (integrated) results it is wise to postpone judgment on these effects and first take a closer look at the power effects on the disturbances locally.

Due to the slipstream induced velocity field caused by the co-rotating propellers the streamlines in front of the model support are given an induced angle of sideslip (this is illustrated by Figure B.5). The magnitude of this induced angle is of the order of $2.5°$ taken half a sting chord in front of the nose of the model sting. This is clearly seen in Figure B.6. It is seen that the propeller slipstream puts the model sting locally at an angle of sideslip. This results in a slightly alternated asymmetric local pressure distribution around the model sting (seen in Figure B.7). However clearly present, integrating this pressure change leads to a negligible net effect on both near-field and far-field effects.

A way to look at the power effects on the far-field disturbances is by studying the change in the spanwise distribution of the disturbance parameters $\Delta\alpha$ and $\frac{\Delta q}{q_\infty}$ at the wings. For the power-on and power-off cases, these values are calculated. Subtracting the values of $\Delta\alpha$ and $\frac{\Delta q}{q_\infty}$ of the power-off case from the values as found for the power-on case leads to the engine power effects on these far-field parameters. But how are the values of $\Delta\alpha$ and $\frac{\Delta q}{q_\infty}$ determined? Consider the power-off cases. For both cases (including- and

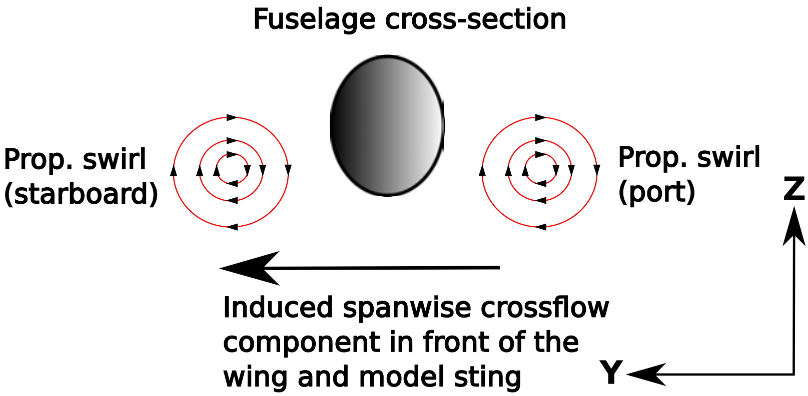

Figure B.5: Example of induced velocity field by the slipstreams of two co-rotating propellers. In the figure, the influence of the fuselage and sting is not included

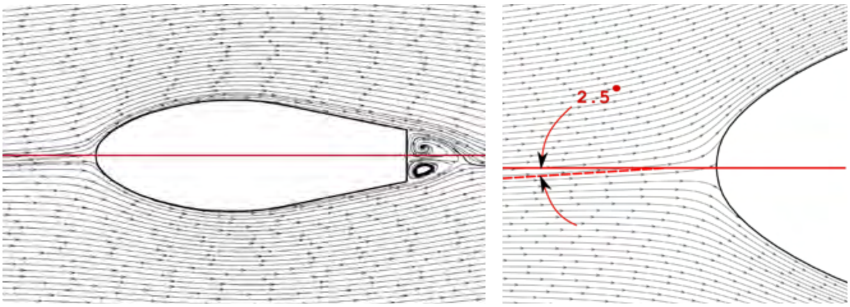

(a) (b)

Figure B.6: Effect of the propeller slipstream on the local angle of sideslip at the model sting (a) A top view of a cross sectional plane of the model sting close (O(0.1 [mm])) to the fuselage showing the local streamlines. As a reference the symmetry line of the sting is shown (b) The same as (a) but focused near the nose of the model sting

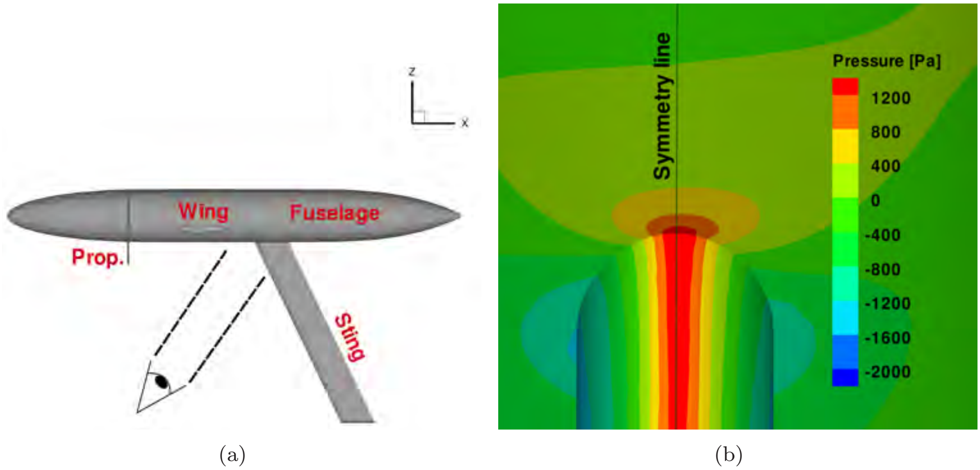

Figure B.7: Effect of the propeller slipstream on the local pressure distribution at the model sting and fuselage. The viewpoint is from upstream looking downstream at the leading edge of the sting at the bottom of the aircraft fuselage as given in (a). Contours of relative pressure level are plotted in (b). The pressure is taken relative to a freestream reference

excluding the support) the wing section pressure distribution is calculated at various spanwise stations. Integrating these distributions leads to a spanwise distribution of the lift $c_l(y)$. Subtracting these lift distributions then leads to the support influence on the local lift distribution. It can now be said that:

$$\Delta c_l(y) = c_{l_\alpha}(y)\Delta\alpha(y) + c_l\frac{\Delta q(y)}{q_\infty} \tag{B.2}$$

In Equation (B.2) the local disturbance is related to a change in angle of attack and dynamic pressure resulting from the disturbance of the support. The local lift slope c_{l_α} is approximated by a 2-dimensional inviscid airfoil calculation in the freeware code $XFOIL$ by Drela [76]. For the local value of the lift-coefficient the undisturbed value is taken. For a number of spanwise stations, the value of $\frac{\Delta q(y)}{q_\infty}$ can be determined by subtracting the values of the static pressures in the airfoil stagnation points of both configurations (including- and excluding the support). Applying the law of Bernoulli on the stagnation streamlines and assuming an equal total pressure in the undisturbed flow field upstream of the configurations it is seen that the disturbance in dynamic pressure of the airfoil is related to this change in stagnation pressure. The stagnation points of the sections are the only usable points whereas at these points the flow is not affected by a change in angle of attack due to the action of the airfoil. When these values are known, the spanwise disturbances in angle of attack can be calculated using Equation (B.2).

This same exercise is carried out for the power-on case. Subtracting the spanwise distributions of $\Delta\alpha$ and $\frac{\Delta q}{q_\infty}$ of the power-off case from the power-on case leads to the engine power effects on these far-field disturbance parameters. The results are given in Figure B.8.

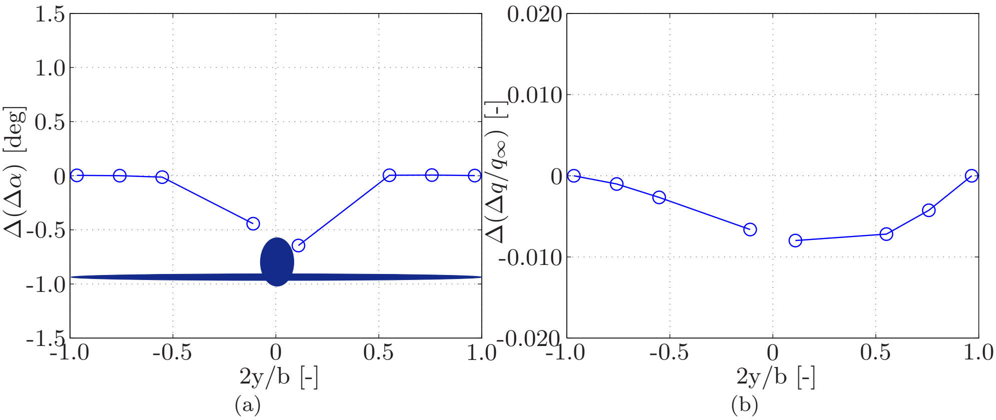

Figure B.8: The change in spanwise distribution of the disturbance parameters (a) $\Delta\alpha$ (b) $\frac{\Delta q}{q_\infty}$ due to engine power effects. The spanwise coordinate is non-dimensionalized using the wing span b

It is seen in Figure B.8 that due to the change in disturbance ability caused by engine power effects, the local values of the disturbance in angle of attack and dynamic pressure are affected to quite some extent:

- For the disturbance $\Delta\alpha$ (Figure B.8(a)) it is seen that changes of nearly 0.65° are found close to the fuselage. Because the local stagnation point on the sting near the fuselage shifts to the port side of the sting by the slipstream induced velocity field, the sting's effectivity in increasing the angle of attack locally is reduced. This reduction is mostly noticeable at the starboard side where it is seen that the engine power effect reaches a maximum value. This causes the distribution of the engine power effects on the value of $\Delta\alpha$ to be asymmetric,

- Regarding Figure B.8(b) and B.7, this asymmetric effect is also expressed in the disturbance in $\frac{\Delta q}{q_\infty}$. The local engine power effects on $\frac{\Delta q}{q_\infty}$ reach a maximum value at the starboard side of approximately -0.010. These negative values originate from the fact that due to the shift in stagnation points to the sting side, the flow locally sees a more blunt object causing the local dynamic pressure to decrease.

In Figure B.8 it is seen that the engine power effects go to zero at the wing tips. Close to the fuselage, these effects are significant. Combined with the local aerodynamic properties of the wing the net engine power effects of the propellers are negligible for this configuration.

Conclusions that can be drawn from this are:

1. The displacement effect of the engine slipstream puts the model sting locally at an angle of sideslip deviating from the freestream value. This is caused by the fact that two co-rotating propellers are discretized in the calculations. When contra-rotating propellers would be discretized the slipstream would induce a local change in angle of attack at the sting leading edge. Such changes are not thought to affect the model support near-field and far-field effects to a significant amount,

2. The local change in angle of sideslip induces a change in disturbance ability of the model sting,

3. This change is noticeable studying the pressure distribution at the model sting and its carry-over to the fuselage,

4. The engine power effects on the near-field disturbances are found as a change in sting pressure carry-over onto the fuselage. The net result of the engine power effects on the value of the near-field disturbance **for this configuration** is approximately zero,

5. The far-field disturbances are also affected. The extent of the engine power effects on the far-field disturbances is significant when evaluated locally. Combined with the local aerodynamic properties of the wing however these effects have a net negligible effect **for this configuration**.

In these conclusions the dependency of the final results on the selected configuration is stressed. It is thought that when this configuration changes, the net engine power effects on the values of the near-field and far-field disturbances might become significant: this would for instance be the case when the configuration is set at an angle of sideslip such that the propeller slipstream interacts directly with the sting.

The magnitude of these effects is also likely to depend on the placement of the sting with respect to the model and the local aerodynamic properties of the wing. Placing the sting in regions of adverse pressure gradients (e.g. at the backbody of the fuselage) increases the risk of considerable engine power effects on the near-field disturbances once the flow is unable to reattach on the fuselage aft of the model sting. The far-field disturbances are also affected by this. Their net effect might become considerable when combined with local aerodynamic wing characteristics showing high values in the distribution of e.g. lift (due to the deflection of flaps for instance).

Above mentioned considerations are not verified by additional calculations. This is left for future research.

In future experiments care should be taken in the setup of wind tunnel tests involving model engines. The magnitude of engine power effects on support disturbances can be decreased by ensuring that the engine slipstream maintains a maximum distance from the model support parts. Besides this, the sensitivity of the near-field and far-field disturbances to engine power effects must be minimized by choosing an appropriate placement of the support parts with respect to the wind tunnel model. This is realized by choosing a placement of the sting that is removed as far from the wing as possible while still attached to the cylindrical (constant cross-sectional) part of the fuselage.

Appendix C

Boundary layer sensitivity upstream the model sting

C.1 Introduction

Static pressure measurements on the fuselage upstream the sting discussed in section 4.3.2 reveal a difference with the Navier-Stokes results. This difference is reflected by the difference in local boundary layer velocity profile. Boundary layer measurements are performed to assess this.

C.2 Boundary layer measurements

Boundary layer measurements are performed using a flat mouth total pressure probe (schematized in Figure C.1) with a thickness of 0.5 [mm] connected to an electronic pressure scanner with a range of 1 [Psi] leading to an accuracy of 0.7% at $M_\infty = 0.179$. The probe is positioned close to the fuselage using a Taylor-Hobson scope with an accuracy of 0.02 [mm]. The boundary layer probe is positioned approximately half a sting chord in front of the support on the fuselage (closer to the support is not possible due to the probe geometry and the interference between probe and support in that case). A typical experimental result of a boundary layer traverse compared to the computational result is shown in Figure C.2.

In Figure C.2 the streamwise boundary layer velocity u is non-dimensionalized with the freestream velocity outside the boundary layer V_∞. The traversing distance from the fuselage, h, is non-dimensionalized by the 99% height of the velocity boundary layer δ_{99}. Just in front of the support, the experimental boundary layer seems more susceptible to the adverse pressure gradient (the experimental result shows a “less full” velocity profile) than shown by numerical results. This is indicative of the impact of the measured pressure gradient that proves to be larger than calculations reveal.

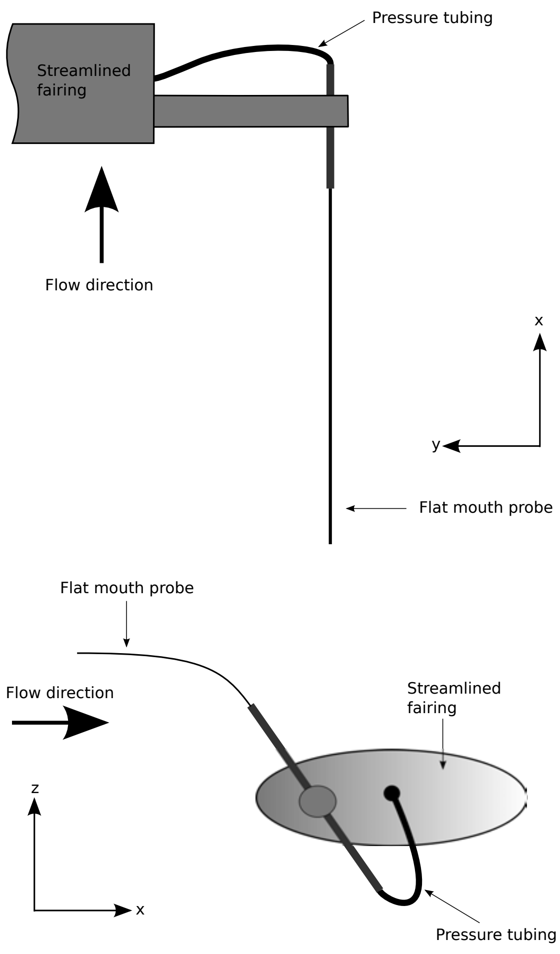

Figure C.1: A schematic of the setup used to probe the fuselage boundary layer

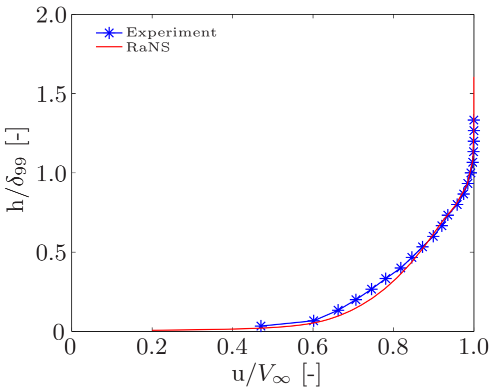

Figure C.2: Comparison of calculated and measured velocity boundary layers on the fuselage for a boundary layer traverse half a sting chord in front of the support on the fuselage

References

[1] J.B. Barlow, W.H. Rae JR. and A. Pope, *Low-Speed Wind Tunnel Testing*. Wiley-Interscience, 3rd ed., 1999.

[2] D.D. Baals and W.R. Corliss, *Wind Tunnels of NASA*. NASA SP-440, Washington, D.C.: Scientific and Technical Information Branch, National Aeronautics and Space Administration, 1981.

[3] S. Rolston, "High Reynolds number tools and techniques for civil aircraft design," in *Proceeding of the 19th Applied Aerodynamics Conference*, AIAA-2001-2411, (Anaheim, California, United States), American Institute of Aeronautics and Astronautics, June 2001.

[4] K. Pettersson and A. Rizzi, "Aerodynamic scaling to free flight conditions: Past and present," *Progress in Aerospace Sciences*, vol. 44, pp. 295–313, 2008.

[5] "AGARDograph 336: Wind Tunnel Wall Corrections," in *AGARD-AG-336*, AGARD, 1998.

[6] P.R. Ashill, "Boundary-Flow Measurement Methods for Wall Interference Assessment and Correction - Classification and Review," in *AGARD-CP-535*, AGARD, 1994.

[7] F. Steinle and E. Stanewsky, "Wind Tunnel Flow Quality and Data Accuracy Requirements," in *AGARD-AR-184*, AGARD, 1982.

[8] R.P. Luijendijk, "Prediction of Far Field Ventral Support Interference in a Subsonic Windtunnel by Means of a Second-Order Panel Method," Masters Thesis, Delft University of Technology, Faculty of Aerospace Engineering, August 1995.

[9] G. Krentz and B. Ewald, "Accuracy Problems in Wind Tunnels During Transport Aircraft Development," in *AGARD-CP-429*, AGARD, 1987.

[10] G.J. Carlin Jr. and D. Bevan, "Prediction of subsonic wind-tunnel mounting system interference," *Journal of Aircraft*, vol. 24, no. 5, pp. 317–321, 1987.

[11] B.J.C. Horsten and L.L.M. Veldhuis, "Experimental and Numerical Results on Cavity Effects in Juncture Flow," in *Proceeding of the 38th Fluid Dynamics Conference and Exhibit*, AIAA-2008-4178, (Seattle, Washington, United States), American Institute of Aeronautics and Astronautics, June 2008.

[12] L.L.M. Veldhuis, "Support Interference Effects of a Ventral Sting on a Body of Revolution. A Brief Description of Phase 1," Technical Report LSW 89-2, Delft University of Technology, Department of Aerospace Engineering, April 1988.

[13] B.J.C. Horsten and L.L.M. Veldhuis, "Engine Power Effects on Support Interference," in *Conference Proceeding of the World Congress on Science, Engineering and Technology 2009*, World Academy of Science, Engineering and Technology, October 2009.

[14] R.J.D. Poole and R.D. Galway, "Interference Corrections for a Centre-Line Plate Mount in a Porous-Walled Transonic Wind Tunnel," in *AGARD-CP-535*, AGARD, 1994.

[15] D.A. Kirby, "Phase II Report of Garteur Action Group AD(AG06): Model Support Interference in Large Low-Speed Wind Tunnels," Technical Report TP-052, RAE, March 1989.

[16] A. Elsenaar and S.O.T.H. Han, "A Break-Down of Sting Interference Effects," in *DGLR/DNW symposium Model Support Corrections in Wind Tunnels*, (Marknesse, The Netherlands), 1991.

[17] F.T Lynch, R.C. Crites and F.W. Spaid, "The Crucial Role of Wall Interference, Support Interference, and Flow Field Measurements in the Development of Advanced Aircraft Configurations," in *AGARD-CP-535*, AGARD, 1994.

[18] D. Eckert, "Correction of Support Influences on Measurements with Sting Mounted Wind Tunnel Models," in *AGARD FDP Conference*, (Brussels, Belgium), 1993.

[19] L.E. Ericsson, "Another Look at High-Alpha Support Interference in Rotary Tests," *Journal of Aircraft*, vol. 28, no. 9, pp. 584–591, 1991.

[20] G. Lee and J.L. Summers, "Effects of Sting-Support Interference on the drag of an Ogive-Cylinder Body With and Without a Boattail at 0.6 to 1.4 Mach Number," Technical Report RM A57I09, NACA, Washington, United States, December 1957.

[21] D.L. Loving and A.A. Luoma, "Sting-Support Interference on Longitudinal Aerodynamic Characteristics of Cargo-Type Airplane Models at Mach 0.70 to 0.84," Technical Report TN D-4021, NASA, Langley Research Center, Hampton, Virginia, United States, July 1967.

[22] W.E. Dietz Jr. and M.C. Altstatt, "Experimental Investigation of Support Interference on an Ogive Cylinder at High Incidence," *Journal of Spacecraft*, vol. 16, no. 2, pp. 67–68, 1979.

[23] T.N. Canning and J.N. Nielsen, "Influence of Support Systems on the Aerodynamics of an Inclined Ogive Cylinder," *Journal of Spacecraft*, vol. 19, no. 3, pp. 205–210, 1982.

[24] C. Quémard, "Phase II Report of Garteur Action Group AD(AG06): Model Support Interference in Large Low-Speed Wind Tunnels," Technical Report TP-052, ONERA and Aerospatiale, March 1989.

[25] X. Vaucheret, "Vortex Lattice Code For Computation of Any Wind Tunnel and Support Effects on Models," *La Recherche Aerospatiale*, vol. 1, no. 2, pp. 39–51, 1991.

[26] M. Mokry, "Evaluation of Combined Wall- and Support-Interference on Wind Tunnel Models," in *AGARD-CP-535*, AGARD, 1994.

[27] J. Willaume, C. Quémard and A. Bonnet, "Interaction d'Un Support de Type 3 Mâts Sur les Caractéristiques Aérodynamiques d'Une Maquette D'Avion Civil," in *AGARD-CP-535*, AGARD, 1994.

[28] D. Almosnino, "Calculation of Support Interference in Dynamic Wind-Tunnel Tests," in *AGARD-CP-535*, AGARD, 1994.

[29] D. Steinbach, "Calculation of Wall and Model Support Interference in Subsonic Wind Tunnel Flows," *Z.Flugwiss. Weltraumforsch.*, vol. 17, pp. 370–378, 1993.

[30] S.P. Fiddes and J.H. Gaydon, "A Hybrid Panel/Image Method for Calculating Wall Constraint Effects in Subsonic Wind Tunnels," in *ICAS-94-3.3.2*, 1994.

[31] D. Steinbach, "Calculation of support interferences on the aerodynamic coefficients for a windtunnel calibration model," *Aeronautical Journal*, vol. 95, no. 942, pp. 55–63, 1991.

[32] J. Amtsberg, "Prediction of Interference Effects Between Model and Sting Support in a Windtunnel by Panel Method," *Journal of Wind Engineering and Industrial Aerodynamics*, vol. 16, no. 2, pp. 351–360, 1984.

[33] K. Pettersson and A. Rizzi, "Estimating Reynolds number scaling and windtunnel boom effects with the help of CFD methods," in *Proceedings of the 24th Applied Aerodynamics Conference*, AIAA-2006-3162, (San Francisco, California, United States), American Institute of Aeronautics and Astronautics, June 2006.

[34] C.P. Britcher and C.W. Alcorn, "Interference-Free Measurements of the Subsonic Aerodynamics of Slanted-Base Ogive Cylinders," *AIAA Journal*, vol. 29, no. 4, pp. 520–525, 1991.

[35] H. Higuchi, H. Sawada and H. Kato, "Sting-free measurements on a magnetically supported right circular cylinder aligned with the free stream," *Journal of Fluid Mechanics*, vol. 596, pp. 49–72, 2008.

[36] P. Jackson, *Introduction to Expert Systems.* Addison-Wesley, 3rd ed., 1999.

[37] D. Eckert, H.G. Hegen and W. Kühn, “DNW’s Method to Correct for Support and Wall Interference Effects on Low Speed Measurements With a Large Propeller Powered Transport Aircraft Model,” in *Conference Proceeding of the 25th International Congress of the Aeronautical Sciences*, (Hamburg, Germany), 2006.

[38] B.J.C. Horsten, “The far-field disturbances of the LLF-support at DNW: Comparison between probe measurements and RaNS calculations,” Technical Report, Delft University of Technology, Faculty of Aerospace Engineering, March 2006.

[39] B. Goedegebuure, “Analysis of T2616.” DNW Internal Note, April 2002.

[40] C.H. Sung and C.W. Lin, “Numerical Investigation on the Effect of Fairing on the Vortex Flows Around Airfoil/Flat-Plate Junctures,” in *Proceeding of the 26th Aerospace Sciences Meeting*, AIAA-88-0615, (Reno, Nevada, United States), American Institute of Aeronautics and Astronautics, January 1988.

[41] W.J. Devenport, N.K. Agarwal, M.B. DeWitz, R.L. Simpson and K. Poddar, “Effects of a Fillet on the Flow Past a Wing Body Junction,” *AIAA Journal*, vol. 28, pp. 2017–2024, December 1990.

[42] W.J. Devenport, R.L. Simpson, M.B. DeWitz and N.K. Agarwal, “Effects of a Strake on the Flow Past a Wing-Body Junction,” in *29th Aerospace Sciences Meeting*, AIAA-91-0252, (Reno, Nevada, United States), American Institute of Aeronautics and Astronautics, January 1991.

[43] W.J. Devenport and R.L. Simpson, “Flow Past a Wing-Body Junction - Experimental Evaluation of Turbulence Models,” *AIAA Journal*, vol. 30, pp. 873–881, April 1992.

[44] W.J. Devenport, R.L. Simpson, M.B. DeWitz and N.K. Agarwal, “Effects of a Leading-Edge Fillet on the Flow Past an Appendage-Body Junction,” *AIAA Journal*, vol. 30, pp. 2177–2183, September 1992.

[45] S.M. Ölçmen and R.L. Simpson, “Influence of Wing Shapes on Surface Pressure Fluctuations at Wing-Body Junctions,” *AIAA Journal*, vol. 32, pp. 6–15, January 1994.

[46] D.D. Apsley and M.A. Leschziner, “Investigation of Advanced Turbulence Models for the Flow in a Generic Wing-Body Junction,” *Flow, Turbulence and Combustion*, vol. 67, pp. 25–55, September 2001.

[47] M.J. Khan and A. Ahmed, “Topological Model of Flow Regimes in the Plane of Symmetry of a Surface-Mounted Obstacle,” *Physics of Fluids*, vol. 17, January 2005.

[48] D.A. Jones and D.B. Clarke, “Simulation of a Wing-Body Junction Experiment Using the Fluent Code,” Technical Report DSTO-TR-1731, Australian Government, Department of Defence, Defence Science and Technology Organisation, Maritime Platforms Division, June 2005.

[49] R. Paciorri, A. Bonfiglioli, A. Di Mascio and B. Favini, "RANS Simulations of a Junction Flow," *International Journal of Computational Fluid Dynamics*, vol. 19, pp. 179–189, February 2005.

[50] S.C. Dickinson, "Appendage Hull Junction Flows and their Application to Sailboat Keels," in *Proceedings of the Second International Symposium on Performance Enhancement for Marine Applications*, pp. 47–58, October 1990.

[51] L. Bernstein and S. Hamid, "On the Effect of a Swept-Wing-Plate Junction Flow on the Lift and Drag," *Aeronautical Journal*, vol. 99, pp. 293–305, August-September 1995.

[52] L. Bernstein and S. Hamid, "On the Effect of a Strake-Like Junction Fillet on the Lift and Drag of a Wing," *Aeronautical Journal*, vol. 100, pp. 39–52, February 1996.

[53] B.W. van Oudheusden, C.B. Steenaert and L.M.M. Boermans, "Attachment-Line Approach for Design of a Wing-Body Leading-Edge Fairing," *Journal of Aircraft*, vol. 41, pp. 238–246, March-April 2004.

[54] L.R. Kubendran and W.D. Harvey, "Juncture Flow Control Using Leading-Edge Fillets," in *AIAA Paper*, AIAA-85-4097, American Institute of Aeronautics and Astronautics, 1985.

[55] L.R. Kubendran, A. Bar-Sever and W.D. Harvey, "Flow Control in a Wing/Fuselage-Type Juncture," in *Proceeding of the 26th Aerospace Sciences Meeting*, AIAA-88-0614, (Reno, Nevada, United States), American Institute of Aeronautics and Astronautics, January 1988.

[56] B.E. Green and J.L. Whitesides, "Method for Designing Leading-Edge Fillets to Eliminate Flow Separation," *Journal of Aircraft*, vol. 40, pp. 282–289, March-April 2003.

[57] C.V. Seal and C.R. Smith, "The Control of Turbulent End-Wall Boundary Layers Using Surface Suction," *Experiments in Fluids*, vol. 27, pp. 484–496, 1999.

[58] G. Constantinescu and M. Koken, "Time Dependent and Time Averaged Turbulence Structure of Flow Past a Surface Mounted Cylinder," in *Proceedings of the 4th International Conference on Computational Heat and Mass Transfer*, (Paris-Cachan, France), May 2005.

[59] R.J. Pattenden, N.W. Bressloff, S.R. Turnock and X. Zhang, "Unsteady Simulations of the Flow Around a Short Surface-Mounted Cylinder," *International Journal For Numerical Methods in Fluids*, vol. 53, no. 6, pp. 895–914, 2007.

[60] I.M.M.A. Shabaka and P. Bradshaw, "Turbulent Flow Measurements in an Idealized Wing/Body Junction," *AIAA Journal*, vol. 19, pp. 131–132, February 1981.

[61] R.D. Mehta, "Effect of Wing Nose Shape on the Flow in a Wing/Body Junction," *Aeronautical Journal*, vol. 88, pp. 456–460, December 1984.

[62] F.J. Peirce, G.A. Frangistas and D.J. Nelson, "Geometry Modification Effects on a Junction Vortex Flow," in *Proceedings of the Symposium on Hydrodynamic Performance Enhancement for Marine Applications*, pp. 37–44, October-November 1988.

[63] R.L. Simpson, "Junction Flows," *Annual Review of Fluid Mechanics*, vol. 33, pp. 415–443, 2001.

[64] E. Dobbinga and J.A. van Ghesel Grothe, "De Lage-Snelheids Windtunnel van de Sub-Afd. Vliegtuig Bouwkunde Der Technische Hogeschool," *De Ingenieur*, vol. 38, 1955.

[65] O. Brodersen, "Computation of engine-airframe installation drag," in *Notes on Numerical Fluid Mechanics And Multidisciplinary Design* (N. Kroll and J.K. Fassbender, ed.), vol. 89, pp. 151–161, 2005.

[66] I. Samuelsson, "Low Speed Wind Tunnel Investigation of Propeller Slipstream Aerodynamic Effects on Different Nacelle/Wing Combinations," Technical Note FFA TN 1990-24, Flygtekniska Försöksanstalten, 1990.

[67] AMI ANALYTICAL METHODS, *www.am-inc.com/VSAERO.shtml*. VSAERO, May 2011.

[68] J.K. Nathman, *VSAERO, A Code for Calculating the Nonlinear Aerodynamic Characteristics of Arbitrary Configuration*. Analytical Methods, Inc., 2133-152nd Avenue NE, Redmond, Washington, 98052, United States, Version 7.0 ed., May 2003.

[69] NUMECA INT., *www.numeca.com/index.php?id=23*. FINE/HEXA: Unstructured CFD technology, May 2011.

[70] NUMECA INT., *www.numeca.com/index.php?id=23*. FINE/HEXA: Unstructured CFD technology, May 2011.

[71] ANSYS, *www.ansys.com/Products/Simulation+Technology/Fluid+Dynamics*. ANSYS FLUENT, May 2011.

[72] Fluent Inc., Centerra Resource Park, 10 Cavendish Court, NH 03766, Lebanon, *FLUENT 6.3 User's Guide*, 6.3 ed., 2006.

[73] F.T.M. Nieuwstadt, *Turbulentie: theorie en toepassingen van turbulente stromingen*. Epsilon Uitgaven, 1998.

[74] G.B. Deng and M. Visonneau, "Computation of a wing-body junction flow with a new Reynolds-stress transport model," in *Proceedings of the 22nd Symposium on Naval Hydrodynamics*, (Washington DC, United States), pp. 691–707, 1999.

[75] W. Rodi, "Comparison of LES and RANS calculations of the flow around bluff bodies," *Journal of Wind Engineering Industrial Aerodynamics*, vol. 69-71, pp. 55–75, 1997.

[76] M. Drela and H. Youngren, *http://web.mit.edu/drela/Public/web/xfoil/*. XFOIL: Subsonic Airfoil Development System, May 2011.

[77] A.L. Treaster and A.M. Yocum, “The Calibration and Application of Five-hole Probes,” in *Proceeding of the Aerospace Industries/Test Measurement Divisions Symposium*, (Albuquerque, United States), 1978.

[78] D. Sons, “Initial development of an Expert System for support and wall interference,” Masters Thesis, Delft University of Technology, Faculty of Aerospace Engineering, May 2010.

[79] M. Drela and H. Youngren, “AVL 3.26 User Primer,” Manual, April 2006.

[80] J.D. Anderson, Jr., *Fundamentals of Aerodynamics*. McGraw-Hill, Inc., Second Edition ed., 1991.

[81] M. Drela and H. Youngren, *http://web.mit.edu/drela/Public/web/AVL/*. Athena Vortex Lattice, May 2011.

[82] R.W. Thomas, “Analysis of Aircraft Stability and Control Design Methods,” Technical Report AFWAL-TR-84-3038 Vol. II, App. B., Evaluation of Aerodynamic Panel Methods, by John Koegler, May 1984.

[83] M. Drela and H. Youngren, “XFOIL 6.9 User Primer,” Manual, November 2001.

[84] L.L.M. Veldhuis, *Propeller Wing Aerodynamic Interference*. PhD thesis, Delft University of Technology, 2005.

Curriculum Vitae

September 30, 1980	Born in Montfoort, the Netherlands.
1993-1999	Pre-university education (Gymnasium) at the Dr. F.H. de Bruijne Lyceum in Utrecht, the Netherlands.
1999-2005	Master's degree in Aerospace Engineering at Delft University of Technology, the Netherlands. Specialized in Aerodynamics. Graduated with a thesis entitled: "A Numerical Study on Laminar and Turbulent Flow over Sharp and Blunt Sawtooth Riblets. Viscous Drag Reduction Mechanisms Reviewed".
2005-2010	Ph.D. researcher at the Aerodynamics Department of Aerospace Engineering at Delft University of Technology. The title of the dissertation: "Low-Speed Model Support Interference. Elements of an Expert System". This research was funded by the German-Dutch Wind Tunnel Organization (DNW).